Abstract

Our aim in this thesis is to use the clustering of QSOs to investigate large-scale structure and cosmology. We are particularly concerned with estimating the cosmological parameters which govern the evolution of structure in the Universe.

We first investigate how QSOs trace the distribution of 'normal' galaxies by measuring the correlation between a sample of ~ 150 QSOs and faint, $b_{\rm J} < 23$ galaxies. At $z < 1.5$ we find that the cross-correlation amplitude is marginally negative. This low signal clearly rules out models in which QSOs inhabit rich environments. The environments of QSOs are more similar to those of *average* galaxies. The slight negative correlation can be explained by gravitational lensing, but this has no effect on our conclusions concerning QSO environments.

We determine the clustering properties of a combined sample of > 1500 QSOs including the LBQS and Durham/AAT QSO surveys. This data set has a clustering amplitude $\bar{\xi}(10\ h^{-1}\ \mathrm{Mpc}) = 0.83 \pm 0.29$ for $\Omega_0 = 1$ at $\bar{z} = 1.27$. On $\sim 100 - 1000\ h^{-1}$ Mpc scales the limit on detected signals in ξ is ± 0.025. A model of clustering evolution which includes the effect of bias was used to compare QSO clustering to the clustering of low redshift galaxies and Seyfert galaxies. If Seyferts and QSOs are similarly clustered, then the data prefer a low Ω_0 or high bias for QSOs and galaxies. In contrast, comparisons to the CMB measurements of *COBE* assuming a CDM-type power spectrum suggest low bias. This might be taken as evidence for low Ω_0, but the data is still consistent with $\Omega_0 = 1$ and $b_{{\rm q}\rho} \simeq b_{{\rm g}\rho} \simeq 2$. We consider the possibility that nearby galaxy clusters can gravitationally lense background QSOs. We apply the lensing hypothesis to the result of Boyle et al., (1988) and find that cluster masses required are too large. A small dust component could retrieve the lensing model and allow more reasonable mass estimates for clusters from this method.

The requirement for a new, deep, wide-field, QSO survey is clear. We discuss the construction of the candidate catalogue for the 2dF QSO Redshift Survey, which will contain ~ 25000 QSOs. We calibrate the photographic plates used for the candidate catalogue and assess the sources of errors and incompleteness. From preliminary spectroscopic observations we conclude that the completeness of the 2dF catalogue is $\sim 71.1 \pm 7.1\%$, compared with an estimated completeness of $\sim 80\%$. We propose to substantially increase the catalogue completeness (to $\sim 90\%$), by the introduction of UKST r plates into our candidate catalogue.

Preface

The work described in this thesis was undertaken between 1993 and 1997 whilst the author was a research student under the supervision of Dr. T. Shanks in the Department of Physics at the University of Durham. This work has not been submitted for any other degree at the University of Durham or at any other University.

The majority of the work contained in this thesis is the authors own. The research contained in Chapters 4 and 6 was carried out as part of the 2-degree Field Quasar Redshift Survey in collaboration with R.J Smith, T. Shanks, B.J. Boyle, L Miller and M.A. Read.

A number of the results presented here have appeared in the following papers :

Croom, S.M., Shanks, T., Boyle, B.J., (1995), in Maddox, S.J., Aragon-Salamanca, A., eds, *Wide-Field Spectroscopy and the Distant Universe (35th Herstmonceux Conf.)*, World Scientific.

Croom, S.M., Shanks, T., (1996), *MNRAS*, 281, 893.

Acknowledgements

I must first thank my supervisor, Dr. Tom Shanks, for his encouragement, enthusiasm and time over the last three and a half years. His many suggestions and comments on this thesis have greatly improved the final result. I should also thank Dick Fong, Shaun Cole, Ian Smail, Gavin Dalton, Steve Maddox and many others for useful discussions. I acknowledge the support given to me by a Durham University Research Studentship. The use of STARLINK computing facilities during my research has been vital, I would like to thank Alan Lotts for his continuous work to keep the computing network up and running.

My thanks must go to all the members of the 2dF QSO Redshift Survey team: Tom Shanks, Brian Boyle, Lance Miller, Mike Read, and most of all Robert Smith. It has been a pleasure to work with such a group of people. Mike Irwin at the APM facility must be thanked for his constantly helpful responses to my continuing demands for plates to be scanned. 2-degree Field instrument is a great technological achievement, my thanks and continued admiration goes to Keith Taylor, Karl Glazebrook, Ian Lewis and the many others on the 2dF team.

I have been fortunate to be surrounded by so many good colleagues while working here at the Department of Physics. My thanks go to all my friends that are past and present members of the department: Jane, Gillian, Roger, Andrew, Omar, Vince, Doug, Dave, Claire, Steve, Ali, Henry, Katherine, Harald, Scott ... (apologies to anyone I've missed out!). In particular, Andrew Ratcliffe, Omar Almaini, Doug Burke, Claire Halliday, Harald Kuntschner and Katherine Gunn deserve a mention for surviving sharing several offices with me. I am particularly indebted to Katherine for reading the drafts of this thesis.

I also have to thank my friends who allowed me to escape the world of Durham and astronomy from time to time, thanks to Paul O'Neill, Mark Watson, Martin Brockington, Hugh Bradley, Sam El Jouzi, Michael Sutton and Paul Bryant.

Finally, and most importantly, I must thank my family for their support over the many years that I have been a student. It is good to know that whatever I do and wherever I go they are behind me one hundred per cent.

Scott

21 August 1997

Contents

Chapter 1

Introduction

1.1 A Standard View of Cosmology

The field of cosmology addresses fundamental questions concerning our Universe. Observations made over the last 70 years have vastly increased our understanding of the physical processes involved, and this is particularly true of the last decade. Most cosmologists agree on a 'Standard Model' which provides the framework for further observational tests.

The standard cosmological model is founded on three key observational results. The first of these is the measured expansion of the Universe, determined from the recessional velocities of galaxies (Hubble, 1929). This expansion suggests that the Universe was previously more dense, and so at a higher temperature. The remnants of this hot, dense phase can be observed today and provide us with more evidence. At very early times, at temperatures of $\sim 10^9$K, nuclear reactions occurred producing the light elements (mainly hydrogen and helium). Measurements of the relative amounts of these light elements provide us with our second piece of evidence (Schramm, 1991). When the temperature falls below ~ 4000K protons and electrons combine to form hydrogen atoms and the radiation field decouples from the matter. This radiation field can then freely propagate through the Universe. The detection of this 'Cosmic Microwave Background Radiation' (Penzias & Wilson, 1965) is the last of the three key observations.

Underpinning these observations is the assumption of the 'Cosmological Principle'. This states that on large enough scales the Universe is both homogeneous and isotropic. The combination of this assumption and the observational evidence listed above gives us the standard picture of the 'Hot Big Bang'.

Assumption of the Cosmological Principle implies a specific type of metric to describe our Universe. This is the Friedmann-Robertson-Walker (FRW) metric,

$$d\tau^2 = c^2dt^2 - a^2(t)\left[\frac{dr^2}{1-kr^2} + r^2(d\theta^2 + \sin^2\theta d\phi^2)\right] \tag{1.1}$$

where both k, which defines the curvature of the space, and $a(t)$, the expansion factor, depend on the matter content of the Universe. The parameters r, θ and ϕ define a *comoving* coordinate system. Applying this metric to the Einstein field equations we obtain the two Friedmann equations:

$$8\pi G\rho = \frac{3}{a^2}(kc^2 + \dot{a}^2) - \Lambda c^2, \tag{1.2}$$

$$\frac{8\pi Gp}{c^2} = -\frac{2\ddot{a}}{a} - \frac{\dot{a}^2}{a^2} - \frac{kc^2}{a^2} + \Lambda c^2 \tag{1.3}$$

G is the gravitational constant, ρ is the mean density, p is the pressure and Λ is the cosmological constant. We now introduce $H = \dot{a}/a$, the Hubble parameter; $q = -\ddot{a}/aH^2$, the deceleration parameter; $\Omega = 8\pi G\rho/3H^2$, the density parameter and $\lambda = \Lambda c^2/3H^2$, the normalized cosmological constant. Parameters with subscript zero e.g. Ω_0, denote values at the present. With the assumption of zero pressure Equations 1.2 and 1.3 can then be reduced to

$$\lambda = \frac{\Omega}{2} - q \tag{1.4}$$

and

$$\frac{kc^2}{a^2H^2} = \Omega + \lambda - 1 \tag{1.5}$$

k can take the values $1, 0, -1$, corresponding to closed, flat and open geometries respectively. It is therefore obvious that for a flat Universe, $\Omega_0 + \lambda_0 = 1$. Expansion causes the wavelength of light emitted from an object at time t_e to be *redshifted* when observed at the present (t_0). The cosmological redshift, z, is defined as

$$1 + z = \frac{\lambda_{\rm obs}}{\lambda_{\rm e}} = \frac{a_0}{a(t_{\rm e})} \tag{1.6}$$

where $\lambda_{\rm obs}$ and $\lambda_{\rm e}$ denote the wavelength of the observed and emitted light.

1.2 Structure in the Universe

Our observations of the Universe locally show that the distribution of matter is not perfectly homogeneous. Structure is found over a huge range of scales. Galaxies are formed from an inhomogeneous mixture of stars, gas and 'dark matter', and galaxies themselves tend to clump together into groups, clusters, filaments and walls to scales $> 100\ h^{-1}$ Mpc (throughout this thesis we shall use a Hubble constant, $H_0 =$

$100h$ kms^{-1}Mpc^{-1}). How this structure was produced is a fundamental question in cosmology. The generally accepted picture is of a spectrum of primordial density perturbations which grow via gravitational instability. These tiny inhomogeneities could be produced from quantum fluctuations in the very early universe, during a period of *inflation* (Guth, 1981; Kolb & Turner, 1990). Measurements of the fluctuations in the Cosmic Microwave Background (CMB) tell us the amplitude of the perturbations at the time of matter-radiation decoupling. The CMB is observed to be smooth to better than one part in 10^4 and only recently have experiments, such as the *COBE* satellite (Bennett et al, 1994), detected anisotropies at $\sim 10^{-5}$. These fluctuations continue to grow from the decoupling era, and at present the fluctuations are of order unity on scales of a few h^{-1} Mpc.

The field of density fluctuations in the Universe can be described as follows; we can define the density contrast such that

$$\delta(\mathbf{x}, t) = \frac{\rho(\mathbf{x}, t) - \bar{\rho}}{\bar{\rho}} \tag{1.7}$$

If the density perturbations are in the form of a Gaussian random field they can be completely defined by the two-point auto-correlation function, ξ, which is related to the density contrast via

$$\xi(\mathbf{r}) = \langle \delta(\mathbf{x} + \mathbf{r}) \delta(\mathbf{x}) \rangle \tag{1.8}$$

or equivalently we can use the Fourier transform of the auto-correlation function, which defines the power spectrum of density fluctuations,

$$P(k) = |\delta_k|^2 = V \int \xi(\mathbf{r}) \exp(i\mathbf{k}.\mathbf{r}) d^3r \tag{1.9}$$

The exact form of the linear power spectrum is dependent on both cosmology and the type of matter which is dominant in the Universe. The simplest inflationary models predict a *scale invariant* primordial power spectrum, $P(k) \propto k$. This spectrum of fluctuations grows via gravitational instability and is also distorted from its original shape by several physical processes which occur in the early Universe. In the Cold Dark Matter (CDM) model, which fits a number, but not all, of current observations, growth is paused by acoustic oscillations on scales which become smaller than the Hubble length ($\sim c/H$) before the epoch of matter-radiation equality. After recombination the perturbations continue to grow with a power spectrum which now has the form $P(k) \sim k^{-3}$ at large k (small scales) while keeping the scale invariant form on the largest scales. In all models the power spectrum is also distorted at late times by non-linear processes when the density contrast becomes large.

The measurement of the power spectrum of density fluctuations gives us an insight into the physical processes occurring in the early Universe. The measurement of the evolution of clustering is also of vital importance. The rate at which density perturbations grow depends on the cosmology of the Universe. In a high density Universe growth is faster than in a low density Universe. Linear perturbation theory

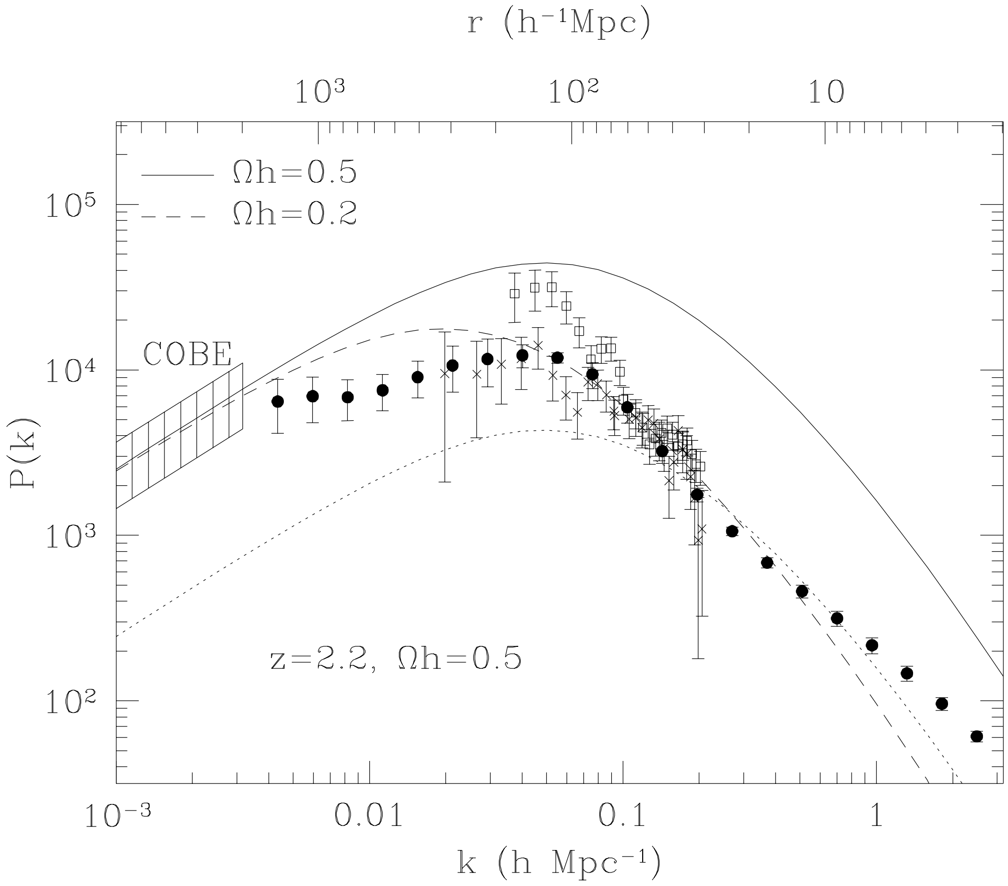

Figure 1.1: The power spectrum of density fluctuations. We plot Linear theory CDM power spectra (Efstathiou et al., 1992), which we normalize to the *COBE* CMB fluctuations and then multiply by a factor of 4 to match the galaxy clustering observations. Two models are shown, one with $\Omega h = 0.5$ at $z = 0$ (solid line) and $z = 2.2$ (dotted line), the other with $\Omega h = 0.2$ at $z = 0$ (dashed line). The data points show various estimates of $P(k)$. The filled circles show the power spectrum derived from the inversion of the angular two-point correlation function of the APM Galaxy Survey (Baugh & Efstathiou, 1993). The open squares are from the APM-Stromlo Redshift Survey (Tadros & Efstathiou, 1996), while the crosses are a combination of the QDOT and 1.2Jy IRAS redshift surveys (Tadros & Efstathiou, 1995).

can be used to find the rate of the growing mode of perturbations for different cosmologies. For $\lambda_0 = 0$ the change in density contrast is given by

$$\frac{\partial^2 \delta}{\partial t^2} + 2\frac{\dot{a}}{a}\frac{\partial \delta}{\partial t} = 4\pi G \rho \delta \qquad (1.10)$$

(Peebles, 1980). Solving this for a flat $\Omega_0 = 1$ Universe gives

$$\delta \propto \frac{1}{1+z} \qquad (1.11)$$

For an open Universe with $\lambda_0 = 0$ the growth rate is slower than in the $\Omega_0 = 1$ case. Here the growth rate (normalized to the growth in the $\Omega_0 = 1$ case) is

$$D(z) = 1 + \frac{3}{x} + \frac{3(1+x)^{1/2}}{x^{3/2}} \ln\left[(1+x)^{1/2} - x^{1/2}\right] \qquad (1.12)$$

where

$$x = |\Omega_0^{-1} - 1| \frac{1}{1+z} \tag{1.13}$$

The general solution for a flat Universe is given in Chapter 3 (Eq. 3.31) and other solutions for open and closed Universes are given by Peebles (1980). The major advantage of Quasi-Stellar Objects (QSOs or quasars) is that their high intrinsic luminosity means that they can be observed at very great distances, and so we have a long baseline in look-back time from which to measure evolution. In fact, QSOs allow us to study the 4-dimensional structure of the Universe. As the growth of perturbations is dependent on cosmology, we have a route to estimating Ω_0 via the evolution of QSO clustering. Fig 1.1 shows a CDM power-spectrum at a redshift, $z = 2.2$, the effective limit of the 2dF QSO Survey, assuming linear evolution with $\Omega_0 = 1$ (Eq. 1.11). There is an order of magnitude growth in clustering amplitude from $z = 2.2$ to $z = 0$.

The measurement of the cosmological parameters (Ω_0, λ_0, H_0) and the shape of the power spectrum of density fluctuations are the key aims for observational cosmology. The two are related, in so much as the shape of $P(k)$ for a given type of matter will depend on the cosmological parameters. The CDM model, which postulates that the majority of matter in the Universe consists of cold, non-baryonic particles which only interact via gravity, has been successful at fitting various observational data. However, the 'standard' CDM model, with $\Omega_0 = 1$ and $h = 0.5$, is inconsistent with the power spectrum measured on large scales by a number of surveys including the APM Survey (Baugh & Efstathiou, 1993), the IRAS QDOT and 1.2Jy Surveys (Tadros & Efstathiou, 1995) and the APM-Stromlo Survey (Tadros & Efstathiou, 1996). This can be seen in Fig. 1.1 where the shape of the observed power spectrum is clearly better fit by an $\Omega h = 0.2$ model. It should be noted that the amplitudes of neither model, when normalized to *COBE* measurements of the CMB fluctuations, fit the data, implying that the galaxy distribution may be *biased* with respect to the density field (see Section 1.4 below). The CMB measurements are vital, as they describe the density fluctuations in the early Universe. The galaxy observations, by comparison, describe the fluctuations in the galaxy distribution, which do not necessarily exactly follow those in the density distribution, in the local Universe. The large volume sampled by QSOs affords the possibility of measuring the power spectrum on the scales probed by *COBE*.

Large-scale structure can also be used to make more direct measurements of cosmological parameters. For example, distortions between the measured clustering in real- and redshift-space can be used to estimate Ω_0, from non-Hubble flow peculiar velocities (Kaiser, 1987). Distortions in clustering can also be caused by assuming the wrong cosmology when measuring large-scale structure, because the distances parallel and perpendicular to the line-of-sight have different dependences on cosmology. This effect can be used to determine cosmological parameters, and is particularly sensitive to the cosmological constant, λ_0 (Phillipps, 1994; Ballinger et al., 1996).

1.3 QSO Formation and the Relationship Between QSOs and Galaxies

It is evident that the QSO distribution contains a wealth of cosmological information. However, interpretation of this information is not necessarily a trivial problem. This is mainly due to the problem of relating the QSO distribution to the mass distribution, which drives cosmic evolution via gravitational instability. This is similarly a problem when using galaxies to study large-scale structure, although galaxies are far more numerous in the local Universe allowing us a clearer picture of the present day galaxy distribution. This is a vital starting point from which to look at the problem of cosmic evolution, and as such we are also required to understand the relation between QSOs and 'normal' galaxies. Possible answers to these problems may be found from a combination of theoretical and empirical investigation.

The discovery of the first QSO, 3C273 (Schmidt, 1963), initiated a considerable industry in the theoretical modelling of the QSO phenomenon. The substantial QSO flux (typically $\sim 10^{45}\mathrm{ergs}^{-1}$) is thought to be due to accretion of hot gas onto super-massive black holes of mass $\sim 10^{6} - 10^{10} M_{\odot}$. Detailed reviews of the unified black hole model for QSOs and Active Galactic Nuclei (AGN) are given in Antonucci (1993) and Rees (1984) . These black holes form at high redshift with the most distant QSOs presently known having $z \sim 5$.

The mechanisms required to form these super-massive black holes are qualitatively similar to the processes which are likely to occur in the formation of galaxies at early epochs. In both cases clouds of gas cool and collapse in the peaks of the matter distribution. The eventual fate of the collapsing gas is largely dependent on the angular momentum of the system. Efstathiou & Rees (1988) investigate the formation of QSOs in the CDM cosmogony and find that luminous QSOs could only form within galaxy-sized dark matter halos because of the small fraction of baryonic matter in the halo and the fact that only a fraction of baryons will collapse to the centre of the halo, while some will be expelled via a supernova driven wind. Loeb (1993) discusses the angular momentum considerations in the collapse of quasi-spherical gas clouds. Tidal torques from neighbouring density perturbations provide angular momentum to collapsing clouds, which then become rotationally supported and fragment into stars. In order to collapse to the Schwarzschild radius of the system, the specific angular momentum must be reduced by several orders of magnitude. One possibility is that QSOs are associated with rare peaks which obtain low angular momentum from tidal torques. Alternatively at very high redshifts, $z > 100$, Compton interactions between free electrons and the CMB can effectively extract angular momentum from a system.

The physical processes which occur once the black hole has formed are understood far better than the formation process. A large amount of gas needs to continue to fall into the system to fuel the QSO luminosity and will usually form a stable disk. The centre of the gaseous disk will be stable for black hole masses $\sim 10^{6} M_{\odot}$ or greater (Loeb & Rasio, 1994). The black hole then continues to grow at the Eddington rate (the rate at which radiation pressure balances the inflow of gas) assuming a sufficient supply of gas, so that the luminosity approaches the Eddington limit

$$L_{\rm E} = \frac{Mc^2}{t_{\rm E}} \tag{1.14}$$

where $t_{\rm E}$ is the Eddington time, the time needed for an object to radiate away its total rest mass at $L_{\rm E}$. The Eddington time is

$$t_{\rm E} = \frac{\sigma_{\rm T} c}{4\pi G m_{\rm p}} \tag{1.15}$$

where $\sigma_{\rm T}$ is the Thompson cross-section and $m_{\rm p}$ is the proton mass. This occurs while the QSOs inhabit gas rich environments. However, a QSO will cease to radiate at this high luminosity when the rate of gas fuelling the central black hole slows down or stops. Small & Blandford (1992) and others use this mechanism to produce a strong density evolution in the QSO luminosity function with relatively short-lived QSOs.

The life-time of QSO activity is crucial to understanding their role in tracing large-scale structure. A model of short lived QSOs implies many generations, with QSO activity in a substantial fraction of all galaxies, while a life-time similar to the Hubble time ($\sim H_0^{-1}$) would imply that QSOs are intrinsically rare. A possible explanation of this rarity would be that QSOs only trace the very highest peaks in the density field. Observational evidence from a number of areas does now appear to point to QSOs being short-lived. While pure luminosity evolution was originally found to fit the evolution of the QSO luminosity function, recent evidence shows that this is not exactly the case (Goldschmidt & Miller, 1991). Obviously pure luminosity evolution would be strong circumstantial evidence for a long QSO lifetime, although with QSOs becoming brighter in the past this requires the evolution to be due to a change in fuelling rate rather than the continual growth of a black hole accreting at the Eddington limit. Observations of the cores of a number of nearby galaxies (Kormendy & Richstone, 1995) suggest that some contain black holes in the mass range $\sim 10^6 - 10^9 M_\odot$ and rule out substantially larger masses. A black hole which accreted at the Eddington limit for a Hubble time would have a mass considerably larger than these observed limits.

The observed comoving QSO number density evolves strongly with redshift, increasing rapidly to $z \sim 2$. Above this redshift, QSO detection is more difficult, particularly using optical techniques in which QSO colours become more similar to stars. However, several high redshift data sets show a likely decline in the space density of QSOs at $z \sim 3 - 5$ using optical and variability selection methods (Hawkins & Veron, 1996) and radio selected samples (Shaver et al., 1996). This evolution is comparable to estimates of star formation in high redshift galaxies found from ultra-deep imaging experiments. Madau et al., (1996) use data from the *Hubble Deep Field* (HDF) (Williams et al, 1996) recently observed using the *Hubble Space Telescope* (HST) to constrain star formation history up to $z \sim 4$. Combining the HDF data with data from the Canada-France Redshift Survey (Lilly et al., 1995) Madau et al., find that star formation increases dramatically from the present to at least $z \simeq 1$ and appears to decrease from $z \sim 3$ to $z \sim 4$. Metcalfe et al., (1996) use data from both the HDF and the Herschel Deep Field imaged with the *William Herschel Telescope* (WHT) to show that the large population of 'faint blue galaxies' is most likely to lie at $z \sim 2$. It therefore appears that the 'Epoch of Galaxy Formation', the period in cosmic history when the bulk of stars were formed, occurred at $z \sim 2$, which coincides with the period at which the QSO space density reached a maximum. This is not altogether surprising when we consider that both star formation and QSO activity are heavily reliant on the supply of gas. Indeed the sharp fall off in both the QSO density and star formation rate to low redshift does imply that the amount of gas available in galaxies declines dramatically from $z \sim 2$ to the present. This picture suggests that QSOs and galaxy evolution are closely related.

1.4 Aims: QSOs as Cosmological Probes

The main aim of this thesis is to investigate the clustering of QSOs via objectively selected, complete, QSO catalogues. We wish to use clustering properties of QSOs to infer the form and evolution of the spectrum of density fluctuations in the Universe. This will allow us to make estimates of cosmological parameters, and give us a new insight into the underlying cosmological model.

The first question we should ask when using QSOs as tracers of large-scale structure is: how do we relate QSOs to the underlying mass distribution? and second, how do we relate QSOs to galaxies, the other main tracers of large-scale structure? Direct evidence for the manner in which QSOs trace the galaxy distribution can be found from deep imaging of QSO environments. There is much evidence that radio-loud QSOs appear to exist in rich environments (Ellingson et al., 1991; Hintzen et al., 1991), in some cases with similar richness to Abell class 1 galaxy clusters. Observations of radio-quiet QSOs find them in generally poorer surroundings at low ($z < 0.3$) (Smith et al., 1995) and intermediate ($z \sim 1$) (Boyle & Couch, 1993) redshift. The majority of optically selected QSOs ($\sim 90\%$) are found to be radio-quiet, and so are expected to exist in poor environments. In Chapter 2 we investigate the environment of a large sample of optically and X-ray selected QSOs in an attempt to confirm that such objects do not live in rich cluster-like environments.

The relationship between the mass, galaxy and QSO distributions can be understood in terms of *biasing*. Our lack of knowledge concerning the complex physical processes which occur during galaxy and QSO formation can be parameterized by a bias parameter, the simplest version of this being a linear bias such that

$$\xi_{\mathrm{q}}(r) = b^2 \xi_\rho(r) \tag{1.16}$$

where the bias parameter b relates the QSO correlation function (ξ_{q}) and the mass correlation function (ξ_ρ). Bardeen et al., (1986) use the peaks-bias formalism to determine the number density of peaks at a given threshold in a Gaussian random field. This shows that rare high peaks will be more strongly clustered than peaks at lower thresholds. The physical motivation for biasing is that primordial density peaks might be more likely to collapse if they already exist in an overdense region (Kaiser, 1984). Other effects such as the re-ionization of the inter-galactic medium by the first generation of stars or QSOs might well prevent the collapse of perturbations which have not already collapsed. Biasing is an observed fact; we see that the clustering of galaxy clusters with scale length $r_0 \sim 15\ h^{-1}$ Mpc (e.g. Dalton et al., 1994) is stronger than the clustering of galaxies with $r_0 \sim 6\ h^{-1}$ Mpc (e.g. Loveday et al., 1995; Ratcliffe et al., 1996). Different populations of galaxies have also been shown to have significantly different clustering properties; for example, the results from the APM-Stromlo Redshift Survey show that late and early type galaxies have significantly different correlation-functions (Loveday et al., 1995), while Park et al. (1994) have found that the amplitude of the power spectrum in the Extended CfA Galaxy Redshift Survey is dependent on luminosity. It is therefore obvious that at least a large sub-sample of galaxies cannot exactly trace the mass distribution. Bias, and particularly the possible evolution of bias with redshift, is then an important parameter to include when studying large-scale structure in QSO samples. In Chapter 3 we use a number of previous QSO catalogues to study the evolution of QSO clustering as a function of redshift, using the evolution to try and constrain the density parameter Ω_0. We include a model for the evolution of bias with redshift in order to relate the QSO evolution to the mass evolution which is dependent on Ω_0.

We will see in Chapter 3 that to make accurate measurements of QSOs clustering and clustering evolution a large, deep, QSO survey is required. For example, the present catalogues are not able to constrain the shape of the QSO clustering power spectrum. To improve the statistics of the measured QSO clustering we start the process of producing a large homogeneous QSO catalogue. The 2-degree Field (2dF) instrument at the Anglo-Australian Telescope (AAT) allows spectra for up to ~ 400 objects to be obtained at one time. This huge multiplex gain enables surveys to be constructed with many times more QSOs than previously possible. The 2dF QSO Redshift Survey will obtain redshifts for ~ 25000 QSOs, an order of magnitude more redshifts than the present largest QSO sample. The construction of the ultra-violet excess (UVX) catalogue used for candidate selection in the Southern half of this survey is discussed in Chapter 4. We take particular care to quantify the source and amount of incompleteness expected in the sample. Chapter 6 contains the results of preliminary spectroscopic data from the 2dF QSO Redshift Survey. In this chapter we compare the measured QSO densities to the expected values and suggest some possible improvements that could be made to the input QSO candidate catalogue.

Another use of QSO catalogues is to use the two-dimensional UVX catalogue to place constraints on gravitational lensing from foreground galaxy clusters by carrying out a cross-correlation with the clusters. Boyle et al., (1988) found a significant anti-correlation between UVX objects and galaxy clusters. In Chapter 5 we interpret this result in terms of gravitational lensing and then extend our investigation to the 2dF UVX catalogue. We also consider the effect of lensing on the measured cross-correlation between QSOs and faint galaxies in Chapter 2.

Chapter 7 contains a discussion of the general conclusions of this thesis and includes a look at the future prospects of using QSOs to increase our understanding of the Universe with particular reference to the 2dF QSO Redshift Survey.

Chapter 2

Cross-Correlation of QSOs and Faint, $b_{\mathrm{J}} = 23$, Galaxies

2.1 Introduction - QSO Environments

Relating QSOs to the underlying mass distribution and to other tracers of that distribution is a vital step in the process of using QSOs to measure large-scale structure in the Universe. In order to determine cosmological quantities, such as the density parameter Ω_0, from the evolution of large-scale structure we are required to know the evolution of the *mass* distribution. Therefore, knowledge of the biasing of QSOs with respect to this mass distribution is of the utmost importance, and the relationship between galaxies and QSOs is an essential step in understanding this bias. The local environments of QSOs also give important clues to the physical processes which form these objects and control their evolution.

Direct imaging of the regions around QSOs is the most obvious way to investigate their environments. Yee & Green (1984) imaged $3' \times 3'$ fields centred on individual QSOs over a wide range in redshift, ($0.05 < z < 2.05$). They found significant numbers of excess galaxies (to a limiting magnitude of ~ 21 in the Gunn r band) associated with QSOs at $z < 0.5$. The luminosity distribution of the excess galaxies strongly suggested that these QSOs are associated with galaxies at the distance implied by their cosmological redshift. Further investigations (Yee & Green, 1987) showed that at $z \simeq 0.6$ some radio-loud QSOs are found in environments as rich as those of Abell class 1 clusters. Significant evolution was also detected from $z = 0.4$ to $z = 0.6$ in this radio-loud sample, with the QSO-galaxy covariance amplitude increasing by a factor of ~ 3. An extension of this work (Ellingson et al., 1991) found that radio-quiet QSOs by contrast exist in significantly poorer environments than their radio-loud counter-parts. The results concerning radio-loud QSOs have been confirmed by several other independent studies (e.g. Hintzen et al., 1991) which found significant numbers of excess galaxies associated with QSOs out to $z \simeq 1.5$. However, observations of radio-quiet QSOs have found a range of results generally

Table 2.1: Details of the AAT photographic plates used in our QSO-galaxy cross-correlation

Field Name	Plate No.	R.A. (B1950)	Dec. (B1950)	Emulsion/filter
SGP2	J2801	00 49 39.4	-29 21 34	IIIaJ/GG385
SGP4	J1888	00 54 48.1	-27 54 45	IIIaJ/GG385
	R1996	00 54 48.7	-27 54 04	IIIaF/RG630
QSF3	J2719	03 40 18.0	-44 18 14	IIIaJ/GG385
F855	J1834	10 43 37.9	-00 04 48	IIIaJ/GG385
	R1835	10 43 37.9	-00 04 48	IIIaF/RG630
F864	J1836	13 41 14.0	-00 00 29	IIIaJ/GG385
	R1837	13 41 14.0	-00 00 29	IIIaF/RG630

consistent with these objects existing in poorer environments, similar to that of an average galaxy. Smith, Boyle & Maddox (1995) find that the cross-correlation function between low redshift ($z \leq 0.3$) X-ray selected QSOs and $b_J < 20.5$ galaxies from the APM Galaxy Survey (Maddox et al., 1990) is consistent with the auto-correlation function of the APM Galaxy Survey, suggesting that this population of QSOs is unbiased with respect to galaxies. Boyle & Couch (1993) have found no excess galaxy population associated with radio-quiet QSOs at $z \sim 1$, while Hutchings, Crampton & Johnson (1995) find that a number of radio-quiet QSOs exist in compact groups of star forming galaxies at $z = 1.1$. Clearly there is a difference between radio-loud and radio-quiet QSOs, with radio-loud QSOs inhabiting richer environments. Radio-quiet QSOs appear to inhabit environments similar to those of normal galaxies. This hypothesis is consistent with the currently available data from the clustering evolution of QSOs (See Chapter 3). In this Chapter we will further investigate the problem of QSO environments with a large (~ 150) sample of optically and X-ray selected QSOs covering a wide range in redshift.

2.2 Data and Methods

The faint galaxy samples were taken from deep AAT plates in five $40' \times 40'$ fields. Details of the plates are given in Table 2.1. Each field has a b_J plate and three fields also have r_F plates. The plates were scanned by the COSMOS measuring machine. Details of the analysis of the first 3 fields (SGP2, SGP4, QSF3), including star-galaxy separation and photometric calibration are given in Jones et al., (1991). Fields F855 and F864 (Roche et al., 1995; Roche, 1994) were similarly analysed. The plate scale for all five fields is 15.2 arcsec/mm. The magnitude limit for the b_J plates is $\simeq 24$ mag, the completeness limit is $b_J = 23.5$, we use the galaxies to a limiting magnitude of $b_J = 23.0$ which is comfortably brighter than the completeness

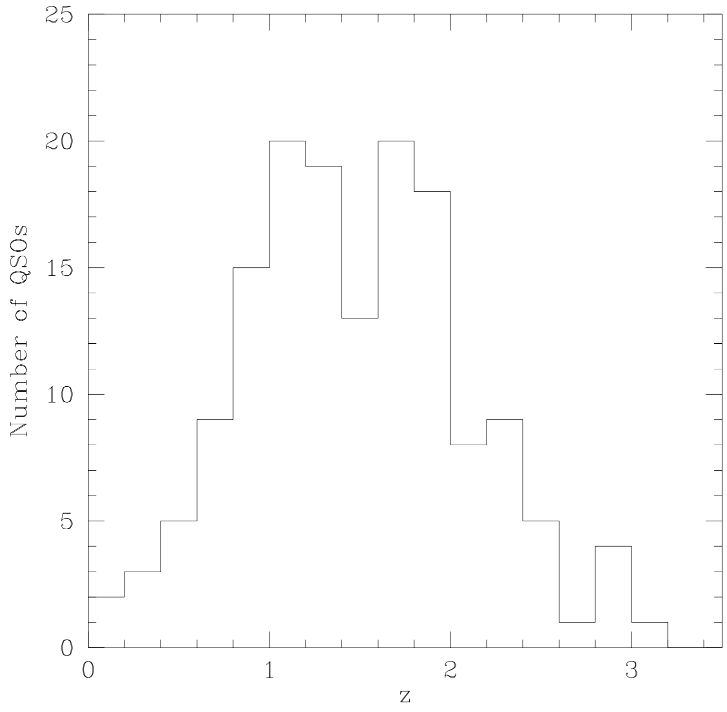

Figure 2.1: The redshift distribution of all the QSOs, optically and X-ray selected, used in this analysis. The total number of QSOs is 152.

limit. At this magnitude the errors in the star-galaxy separation are $\sim 5\%$.

The QSOs in this analysis are from both optically and X-ray selected samples. Fields SGP2, SPG4 and QSF3 contain QSOs from the Durham/AAT UVX selected sample (Boyle et al., 1990), limited to $B = 21$ mag. The F855 and F864 fields contain QSOs from the deeper ESO/AAT colour selected sample (Boyle et al., 1991; Zitelli et al., 1992) with a limiting magnitude of $B = 22.5$. Both these samples are also used in the clustering analysis of Chapter 3. The X-ray selected QSOs were taken from optical follow-up of a deep *ROSAT* survey (Almaini, 1996; Shanks et al., 1997). The QSOs are 4σ detections with the *ROSAT* Position Sensitive Proportional Counter (PSPC). Optical counterparts were identified from COSMOS and APM scans of UKST plates and the AAT plates used in this analysis. Spectroscopic identification was carried out with the AUTOFIB and LDSS instruments at the AAT. Details of the QSO samples used are given in Table 2.2, the redshift distribution of the combined sample of 152 QSOs is shown in Fig. 2.1. It should be noted that a large number of QSOs were selected independently using both optical and X-ray techniques.

The QSO coordinates (optical counterpart positions in the case of the X-ray selected objects) were transformed to the x,y system of the COSMOS scanned b_J plates using the Starlink ASTROM software, ~ 40 stars were used to produce the 6 coefficient transform. The RMS residuals for these transforms are shown in Table 2.2, all are less than $1''$. The five fields are plotted in Fig 2.2, showing all galaxies

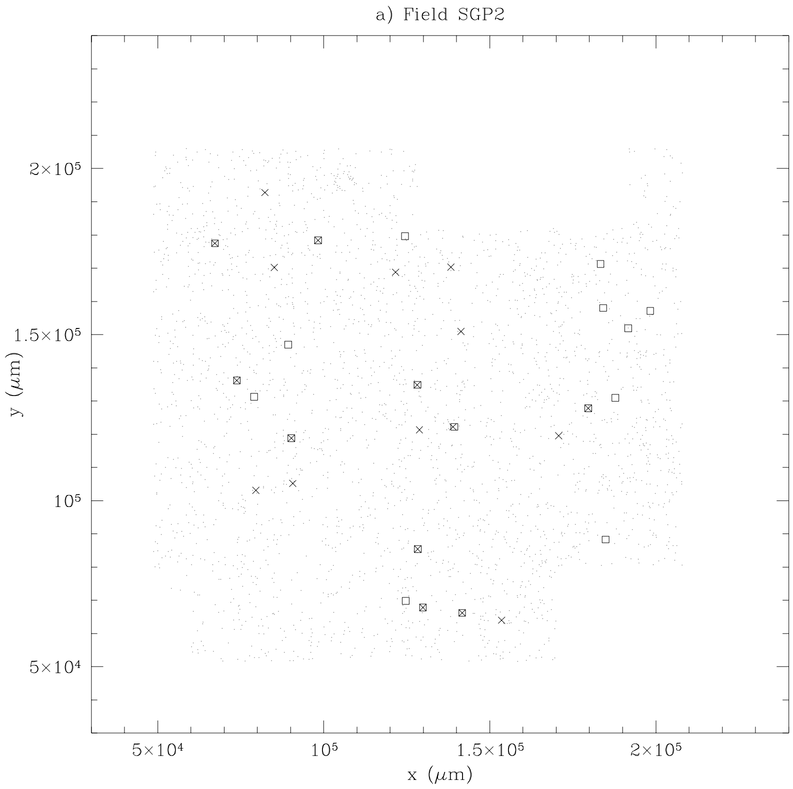

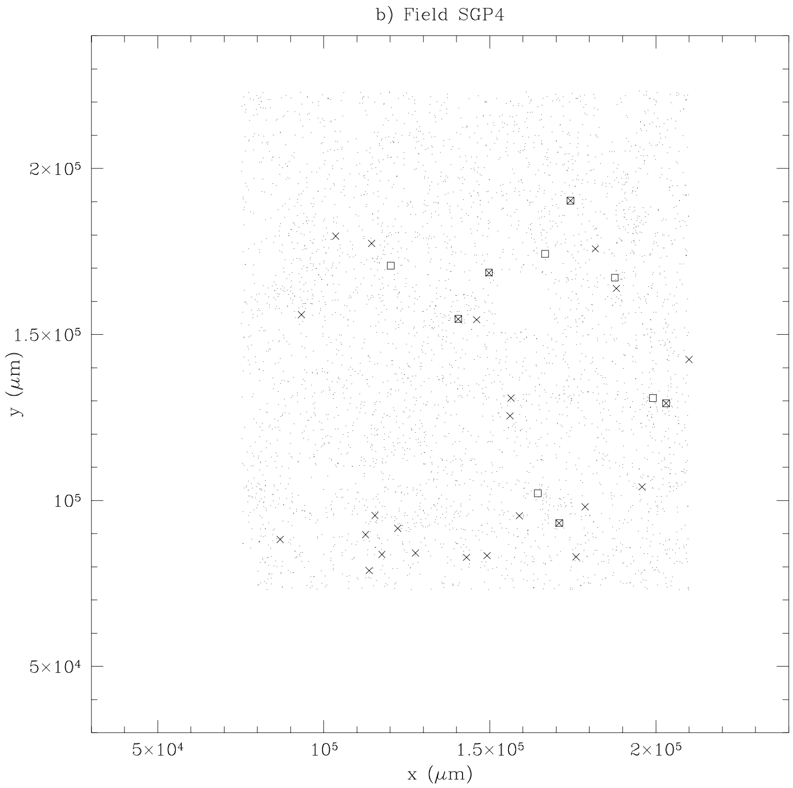

Figure 2.2: The x,y positions of galaxies to $b_J = 23$ from COSMOS scans of AAT photographic plates, together with the positions of the QSOs. a) Field SGP2, b) field SGP4, c) field QSF3, d) field F855, e) field F864. Open squares are the optically selected QSOs while crosses are the X-ray selected QSOs, The regions removed due to plate defects and bright stars can be seen.

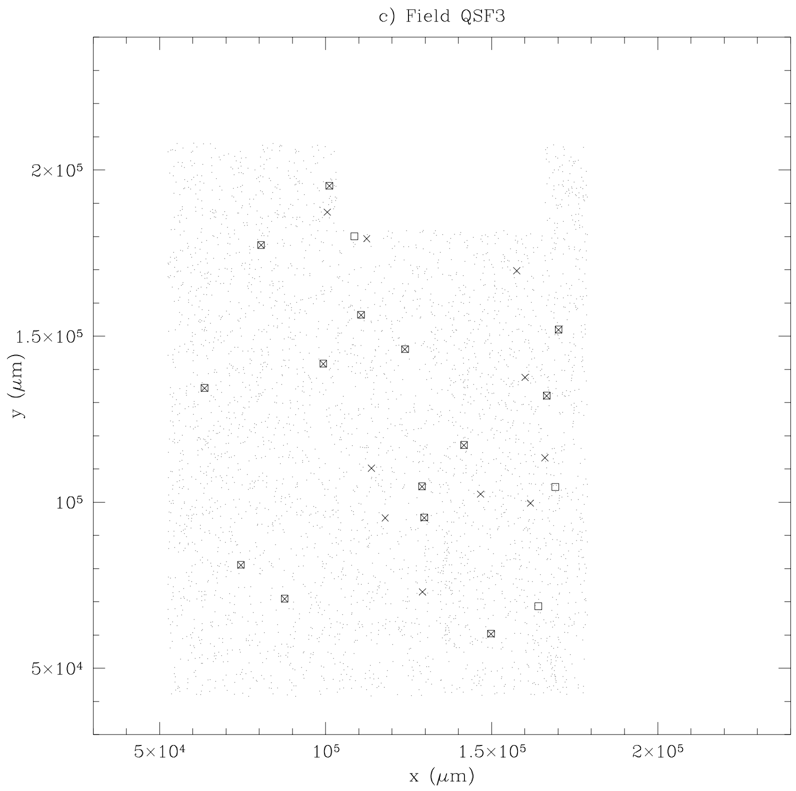

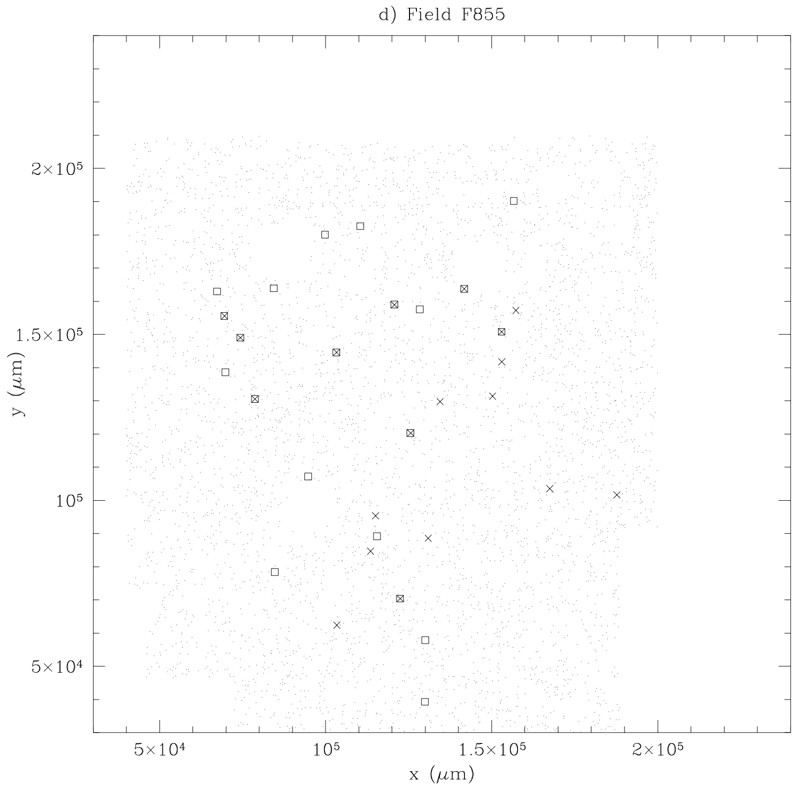

Figure 2.2: Galaxies and QSOs: continued

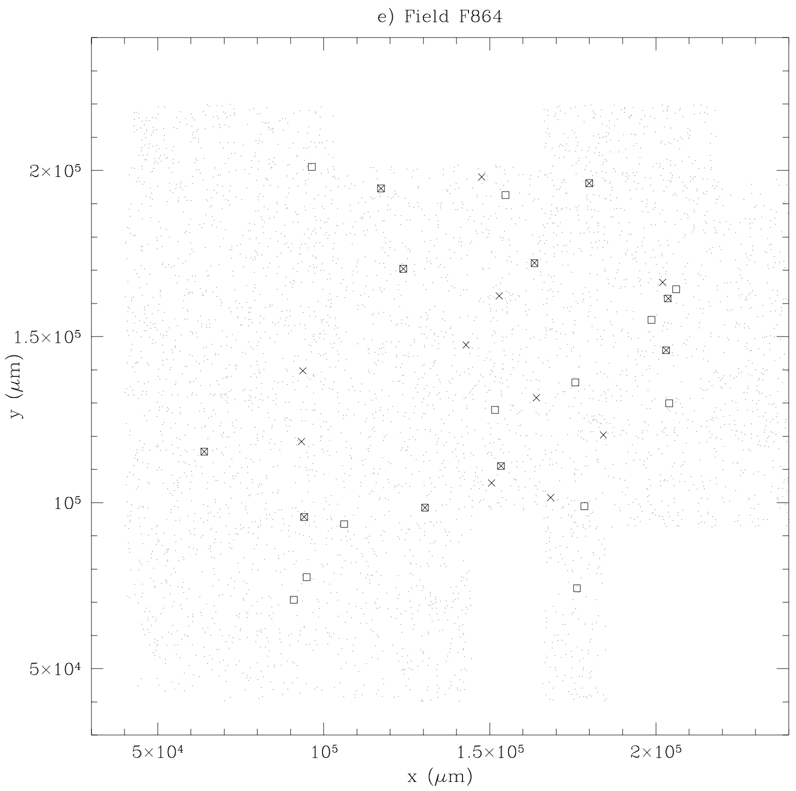

Figure 2.2: Galaxies and QSOs: continued

to $b_J = 23$ with the positions of the QSOs overlaid on top of this.

The cross-correlation was carried out in the standard manner, with the galaxy distribution being compared to a random distribution of points with the same angular selection function (that is avoiding holes) as the galaxies. The number density of randoms was 100 times the density of galaxies. So the angular cross-correlation function, $\omega_{\rm qg}(\theta)$, is defined as

$$\omega_{\rm qg}(\theta) = \frac{N_{\rm qg}(\theta) N_{\rm r}}{N_{\rm qr}(\theta) N_{\rm g}} - 1 \tag{2.1}$$

where $N_{\rm r}$ is the total number of random points, $N_{\rm g}$ is the total number of galaxies, and $N_{\rm qg}$ and $N_{\rm qr}$ are the number of QSO-galaxy and QSO-random pairs with separation $\theta \pm \delta\theta/2$ respectively. This was calculated in concentric annuli of width $30''$. The inner $5''$ is removed to avoid any confusion between very near companions and the QSOs themselves, and any QSOs which might have been classified as galaxies on the COSMOS scans. The errors shown in the figures below are Poisson errors:

$$\Delta\omega = \frac{\omega(\theta) + 1}{\sqrt{N_{\rm qg}}} \tag{2.2}$$

To test the Poisson error estimates we carry out two tests; the first is to replace the QSOs with a random selection of galaxies and carry out a cross-correlation between these random galaxies and the rest of the galaxy sample. A variance is calculated

Table 2.2: Details of the QSO samples used in this analysis. It should be noted that many QSOs were selected by both optical and X-ray methods.

Field Name	No. of Optical QSOs	No. of X-ray QSOs	Total No. of QSOs	RMS astrom. ($''$)
SGP2	20	20	30	0.86
SGP4	10	27	33	0.43
QSF3	17	24	26	0.39
F855	21	19	31	0.26
F864	22	20	32	0.69

from 100 realisations of this process. The second test calculates the cross-correlation between the QSOs and a bootstrap re-sampled galaxy distribution, again using 100 realisations to find a variance. For all QSOs with $z < 1.5$ the Poisson error on the amplitude within $120''$ is ± 0.020 (see Section 2.3 below), the error estimated from replacing QSOs with random galaxies is ± 0.026 while the bootstrap estimator gives ± 0.020. The excess variance from the first test is likely to be due to the positive galaxy auto-correlation which increases the variance. The bootstrap method uses the QSO-galaxy cross-correlation which, as we show below, has no significant clustering signal.

The background density of galaxies is determined from each field separately which forces the integral of $\omega(\theta)$ to be zero at the largest scales studied. This is the well known 'integral constraint', which is simply due to the fact that there is still appreciable clustering of galaxies on the scale of our fields. In our case we do not know *a priori* that there will be a significant signal on scales of $\sim 20'$, therefore an accurate estimate of the integral constraint is not possible. Given this, we can still determine a possible integral constraint correction in order to investigate its possible effect on our results. The angular correlation function determined in an area Ω is biased low by the amount

$$I = \frac{1}{\Omega^2} \int \int \omega(\theta_{12}) \mathrm{d}\Omega_1 \mathrm{d}\Omega_2 \tag{2.3}$$

We then assume the standard power-law for the cross-correlation function, $\omega(\theta) = A\theta^{-0.8}$. We find the following integral constraint for the five fields: $3.29A$ (SGP2), $3.42A$ (SGP4), $3.36A$ (QSF3), $3.04A$ (F855) and $2.89A$ (F864). The auto-correlation function amplitude for $b_J \sim 23$ galaxies is ~ 0.002. If we were to assume that this value was a reasonable estimate of the QSO-galaxy cross-correlation then the integral constraint in our fields would be ~ 0.006. We will demonstrate below that the addition of an integral constraint of this amplitude has no significant effect on our conclusions.

2.3 Cross-Correlation Results

We now present the results of the cross-correlation analysis between both the optically and X-ray selected QSOs and the galaxy catalogues. First, we look at the angular cross-correlation function for each field individually; these are shown in Fig. 2.3a-e while Fig. 2.3f shows a combination of all five fields. We show the results for all the known QSOs within each field (X-ray and optically selected QSOs combined). From these plots it is clear that there is a significant *anti-correlation* in the F855 and F864 fields while the SGP4 field is the only one which appears to show a positive correlation. The combined cross-correlation function therefore shows a small negative signal on small scales. Fig. 2.3 was derived using all the QSOs in each field (including the whole range of redshifts and both X-ray and optically selected objects). In order to look in detail at the source of the signal we calculate below a clustering amplitude for each individual QSO.

We calculate the individual cross-clustering amplitude for each QSO in a non-parametric fashion, simply using the integrated excess of galaxies out to a defined radius which we choose to be $120''$, giving $\omega(\theta < 120'')$ (still using an inner limit of $5''$). A radius of $120''$ is equivalent to $0.5\ h^{-1}$ Mpc in proper co-ordinates at a redshift of $z \sim 1$. We can relate this measure of clustering to a parametric clustering amplitude assuming the simple power-law form for the angular cross-correlation function:

$$\omega_{\rm qg}(\theta) = A_{\rm qg}\theta^{1-\gamma} \tag{2.4}$$

The number of QSO-galaxy pairs between θ_1 and θ_2 is

$$N_{qg}(\theta_1 \leq \theta \leq \theta_2) = \frac{2N_{\rm g}}{\theta_2^2 - \theta_1^2}\int_{\theta_1}^{\theta_2} \theta(1+\omega_{qg}(\theta))\mathrm{d}\theta \tag{2.5}$$

where $N_{\rm g}$ is the number of galaxies. This can then be used to relate the non-parametric $\omega(\theta < 120'')$ to the clustering amplitude $A_{\rm qg}$ via Eq. 2.1 for $5'' \leq \theta \leq 120''$. We assume a power-law slope with $\gamma = 1.8$.

In Fig. 2.4 we show the clustering amplitudes for individual QSOs within $120''$ as a function of redshift for each field. These show that the positive correlation in the SGP4 field is mainly due to three QSOs with strong positive signals. One of these is at $z = 2.861$ and has $\omega(\theta < 120'') = 0.62 \pm 0.20$ (equivalent to $A_{\rm qg} = 0.025 \pm 0.008$). We do not expect to see any galaxies brighter than $b_{\rm J} = 23$ at this redshift and hence this is either a chance alignment or the effect of gravitational lensing on the QSO. Examination of this object by eye confirms that there is a concentration of faint objects close to the QSO which could be a cluster of galaxies. Another of the three objects is only separated from the $z = 2.861$ QSO by $\sim 1'$. The third also shows a number of faint objects very close to the QSO. By contrast, the negative signal in fields F855 and F864 is seen to be due to a large number of objects with $\omega(\theta < 120'') \sim -0.2$ to -0.5. There is no measurable correlation between redshift and clustering amplitude, with objects over the entire range in redshift contributing to the negative signal.

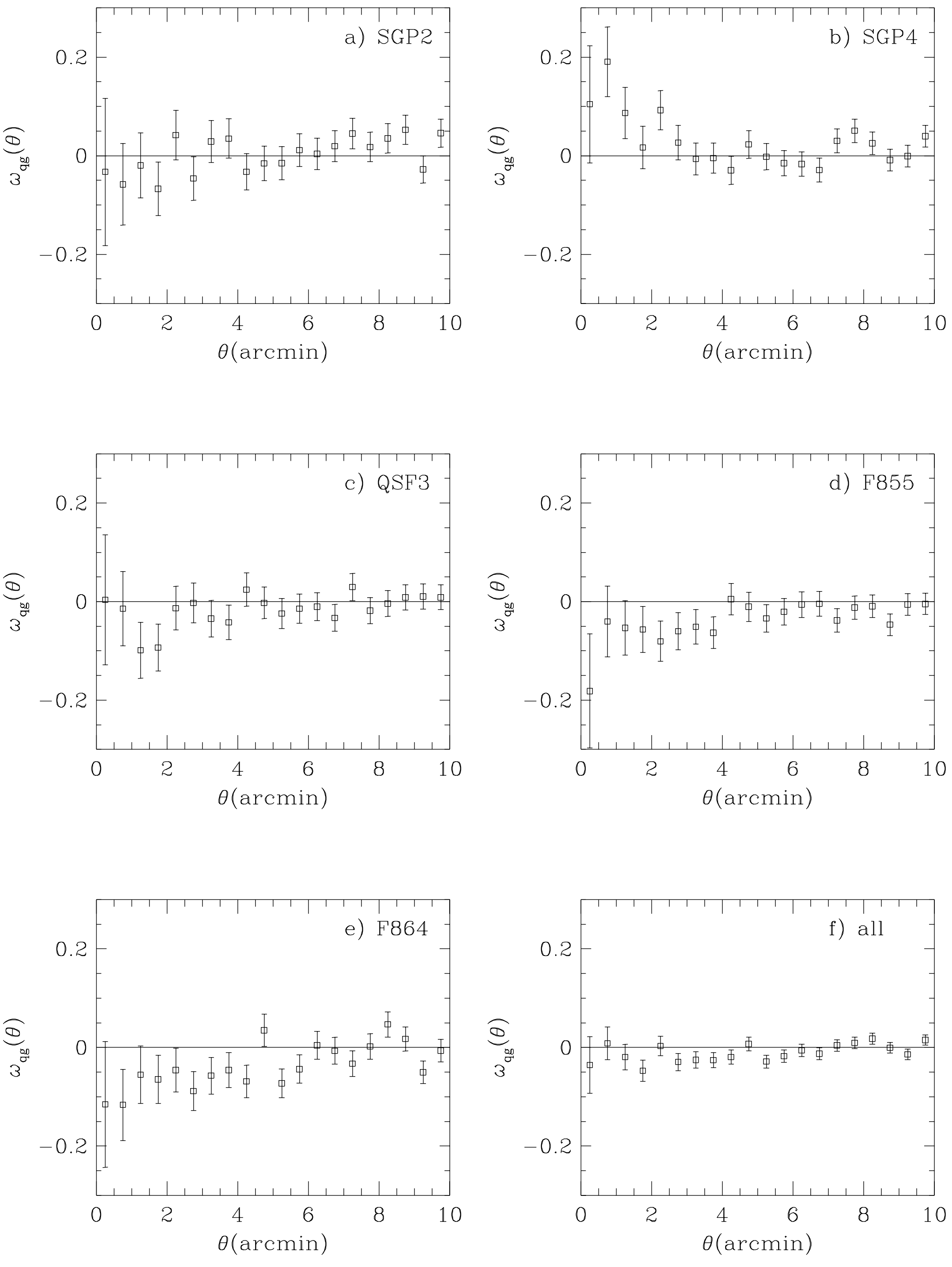

Figure 2.3: The QSO-galaxy angular cross-correlation function for each of the five AAT fields individually, including all QSOs. f) shows a pair weighted combination of all five fields.

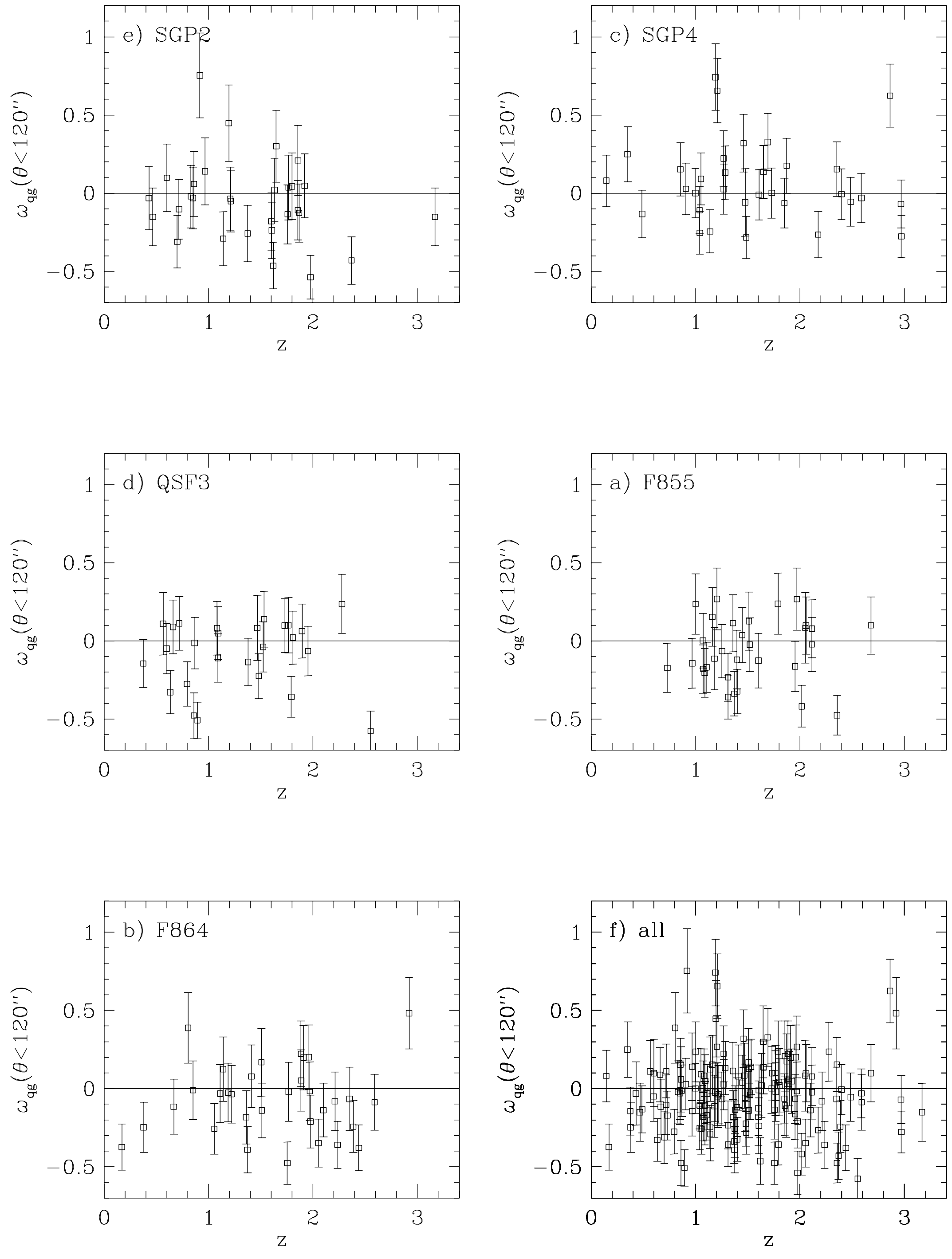

Figure 2.4: The QSO-galaxy clustering amplitude for individual QSOs in each AAT field (both optically and X-ray selected QSOs) as a function of redshift. f) shows all fields combined. Individual clustering amplitudes are measured within a radius of 120″.

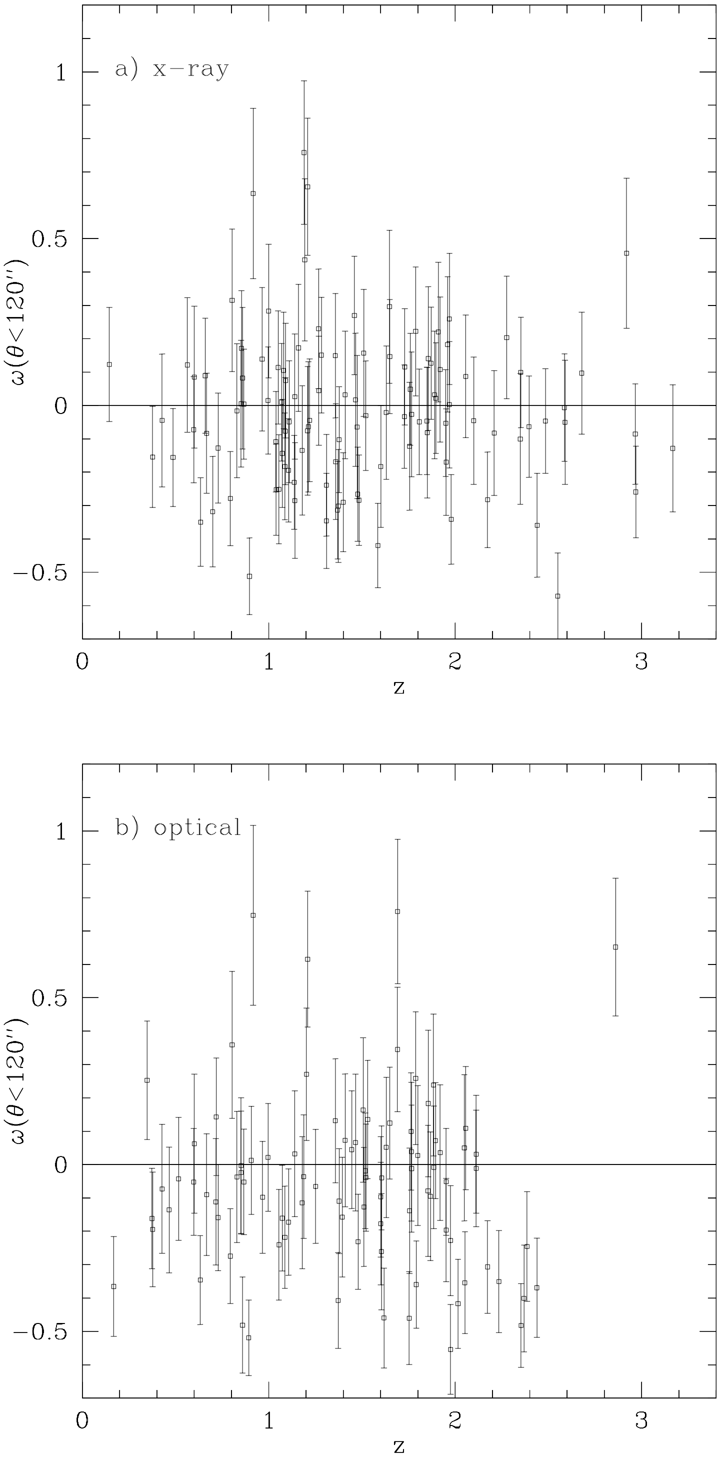

Figure 2.5: QSO-galaxy clustering amplitudes within $120''$ for individual QSOs as a function of redshift. a) X-ray selected QSOs and b) optically selected QSOs. Note that a large fraction of QSOs were selected using both X-ray and optical techniques.

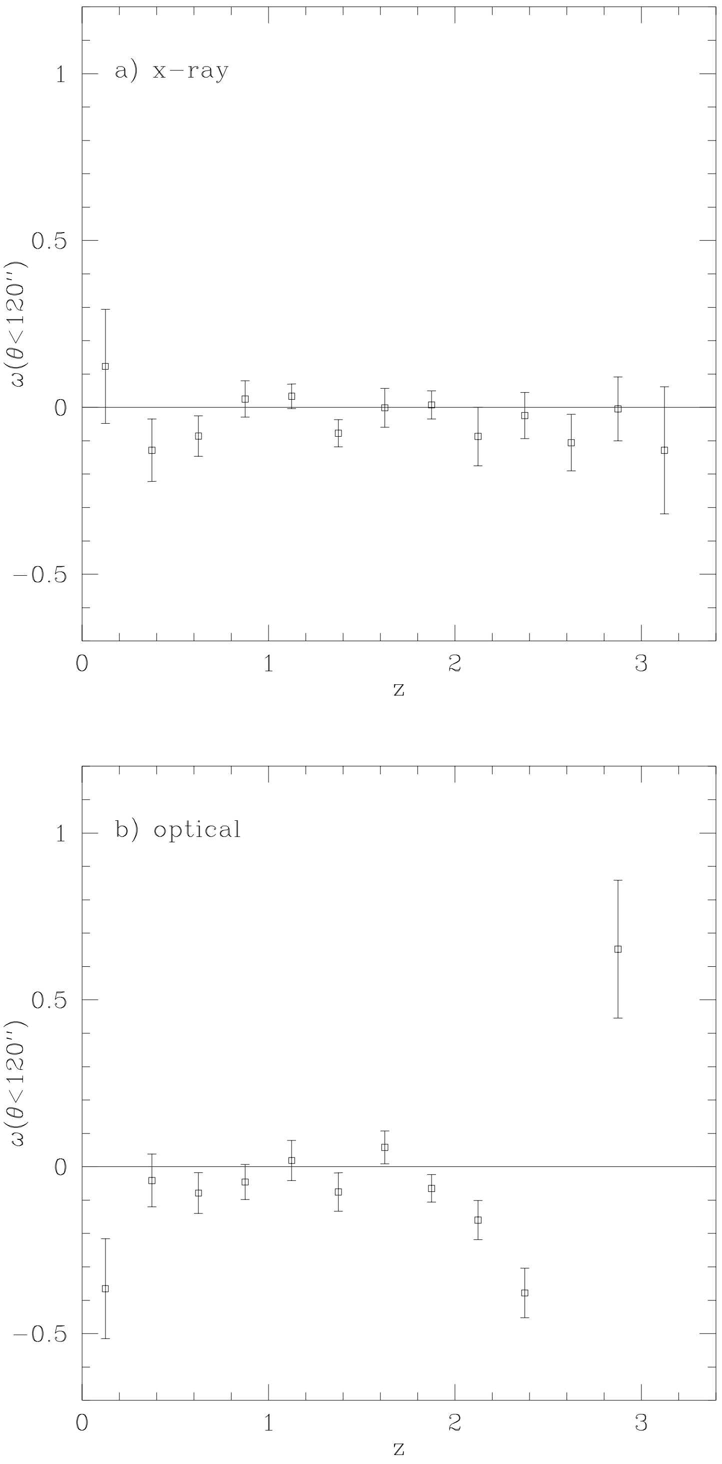

Figure 2.6: QSO-galaxy clustering amplitudes within $120''$ as a function of redshift, binned in $\Delta z = 0.25$ redshift intervals. a) X-ray selected QSOs and b) optically selected QSOs.

We should note that using galaxies from the AAT plates to the plate limit of $b_J \sim 24$ does not have any effect on the results presented here. The clustering amplitudes are not significantly altered, although obviously the Poisson errors are somewhat reduced by the increased number of galaxies. Considering that at this magnitude limit the sample is incomplete and the star-galaxy separation is ill-defined, a limit of $b_J = 23$ affords a more robust and reliable result.

The clustering amplitudes for individual QSOs separated on the basis of their selection (X-ray or optical) are shown in Fig. 2.5. It should be noted that a large fraction of the QSOs were selected independently by both X-ray and optical techniques. Of course the X-ray selected sample also has an implicit optical selection imposed on it due to the need to identify an optical counterpart to the X-ray source on which to carry out follow-up spectroscopy. Fig. 2.5 shows that almost all of the QSOs show zero or negative correlation amplitudes, while there are a small number of outlying objects with significant positive signal. The only difference between the X-ray and optically selected QSOs is a possible anti-correlation in the optical sample at high, $z > 1.8$, redshift. This can be seen more clearly if the results are combined in redshift intervals, as shown in Fig. 2.6. Here we combine the galaxy counts around each QSO in $\Delta z = 0.25$ intervals. The X-ray selected sample (Fig. 2.6a) shows no significant signal or trend as a function of redshift. The optically selected sample (Fig. 2.6b) shows a significant anti-correlation at redshifts greater than $z \sim 1.8$, with the other significant points (in the first and last redshift bins) both due to individual QSOs. At low redshift, where any signal due to real associations would be expected, none is detected; at $z < 1.5$, $\omega(\theta < 120'') = -0.018 \pm 0.022$ for the X-ray selected sample and -0.051 ± 0.027 for the optical sample. For the combined sample of all QSOs with $z < 1.5$ we obtain $\omega(\theta < 120'') = -0.027 \pm 0.020$. In the next section these results are compared to the expected values for given clustering amplitudes and clustering evolution.

We have colour information in several fields, with SGP4, F855 and F864 all containing r_F plates. The r_F plate in the SGP4 field has a bright $r_F \sim 21.5$ completeness limit, therefore we do not include this field in our analysis. However the plates in the other two fields are sufficiently deep for our purposes. The colour distribution of the galaxies peaks at $b_J - r_F \simeq 1.25$ so we use this limit to define red and blue galaxy populations. Fig. 2.7 shows the results of this analysis, with Figs. 2.7a and 2.7b showing the angular correlation functions for all QSOs. The red galaxies appear to contribute more to the anti-correlation seen in the F855 and F864 fields. When we look at the clustering amplitudes of individual QSOs at $\theta < 120''$ we see no obvious trend (Figs. 2.7c, d), but binning these results as a function of redshift we see that the blue galaxies show no strong correlation or anti-correlation at any redshift, while the red galaxies appear to show generally negative correlations (similar to that seen in the correlation of all galaxies with the optically selected QSOs, Fig. 2.6b). At $z < 1.5$ the correlations for the red and blue populations are $\omega(\theta < 120'') = -0.093 \pm 0.043$ and -0.057 ± 0.048 respectively. Further dividing the sample into X-ray and optically selected QSOs we see no significant differences, this is mostly due to the increased errors from a smaller number of QSOs.

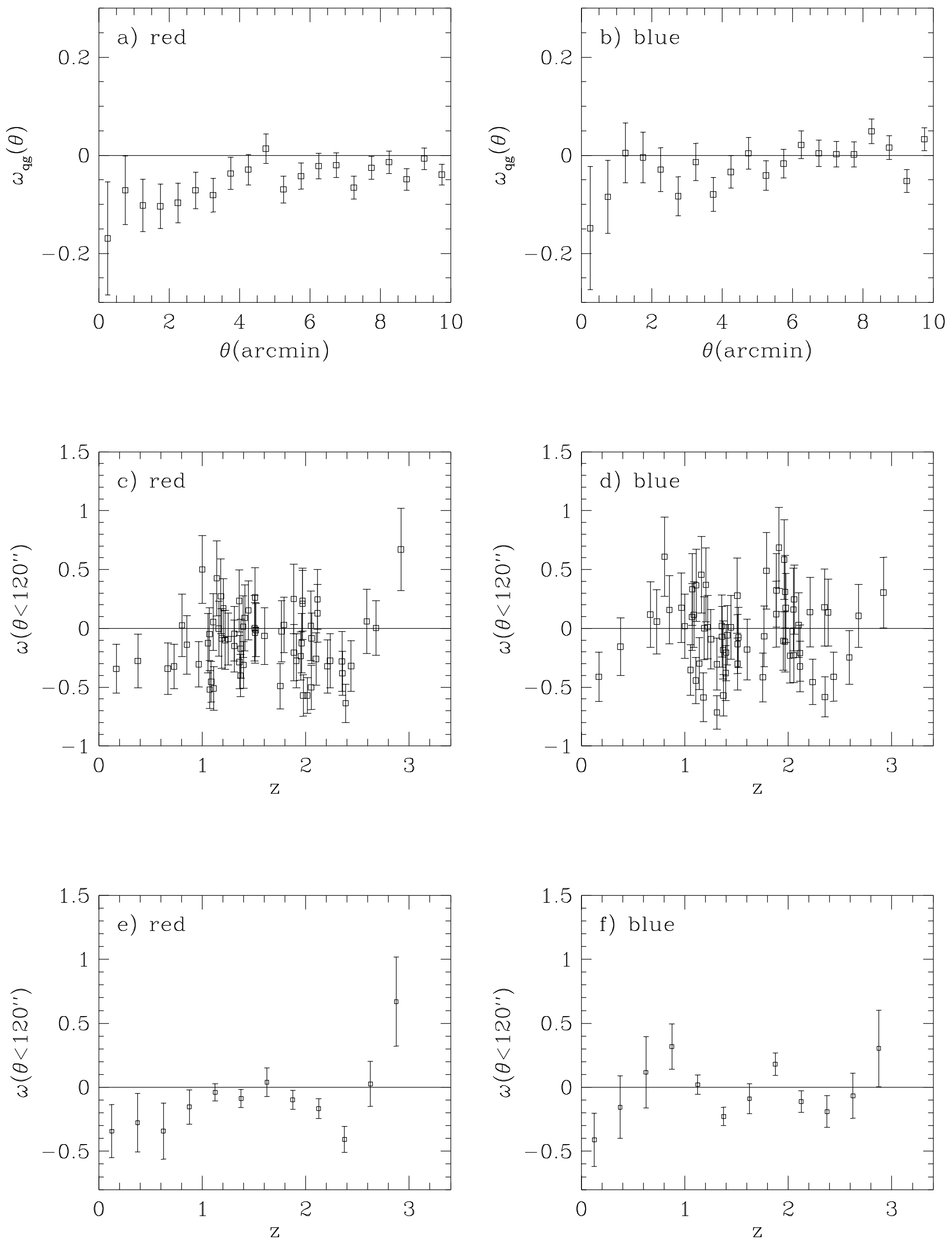

Figure 2.7: Results for the QSO cross-correlation with colour selected galaxies (with $b_J < 23$). The angular cross-correlation function for a) red and b) blue galaxies. The clustering amplitude within 120″ for individual QSOs with c) red and d) blue galaxies as a function of redshift, and the redshift binned clustering amplitude for e) red and f) blue galaxies.

We therefore see tentative evidence for a difference in the cross-clustering properties of red and blue galaxies with QSOs. Any physical process which would cause this effect will be largely due to the fact that red and blue galaxies tend to inhabit different environments. Red galaxies are found in richer environments and are more strongly clustered than blue galaxies, which tend to inhabit the field rather than clusters. Below we make some estimates of the expected QSO-galaxy cross-correlation and relate them to the results found here.

2.4 Modelling QSO Environments

2.4.1 Limber's equation

The angular cross-correlation function, $\omega_{\rm ab}(\theta)$, between two populations, a and b, can be related to the spatial cross-correlation function $\xi_{\rm ab}(r,z)$ by Limber's equation (Limber, 1953; Peebles, 1980) which can be written as:

$$\omega_{\rm ab}(\theta) = \frac{2\int_0^\infty \int_0^\infty x^4 F^{-2} \phi_{\rm a}(x)\phi_{\rm b}(x)\xi_{\rm ab}(r,z){\rm d}x{\rm d}u}{\int_0^\infty x^2 F^{-1}\phi_{\rm a}(x){\rm d}x \int_0^\infty x^2 F^{-1}\phi_{\rm b}(x){\rm d}x} \tag{2.6}$$

under the assumption that the integral is dominated by objects at almost equal cosmic distance. The F term accounts for varying cosmological geometries and is given by:

$$F = \left[1 - \left(\frac{H_0 a_0 x}{c}\right)^2 (\Omega_0 - 1)\right]^{1/2} \tag{2.7}$$

Unless otherwise stated we will assume a flat cosmology with $\Omega_0 = 1$, that is $F = 1$. The comoving distance to a point midway between a and b is given by x (assuming that the separation of a and b is small compared to x). The small angle approximation is also assumed so that the proper separation between a and b is

$$r = \frac{1}{1+z}\left(\frac{u^2}{F^2} + x^2\theta^2\right)^{1/2}, \qquad u = x_b - x_a \tag{2.8}$$

$\phi_{\rm a}(x)$ and $\phi_{\rm b}(x)$ are the selection functions for the two populations and satisfy

$$\int_0^\infty x^2\phi(x){\rm d}x = \int_0^\infty N(z){\rm d}z \tag{2.9}$$

where $N(z){\rm d}z$ is the number of objects per unit surface area in the redshift interval $[z, z+{\rm d}z]$.

We parameterize the spatial cross-correlation function in the conventional power-law form:

$$\xi_{\rm ab}(r,z) = \left(\frac{r}{r_0}\right)^{-\gamma}(1+z)^{-(3+\epsilon)} \tag{2.10}$$

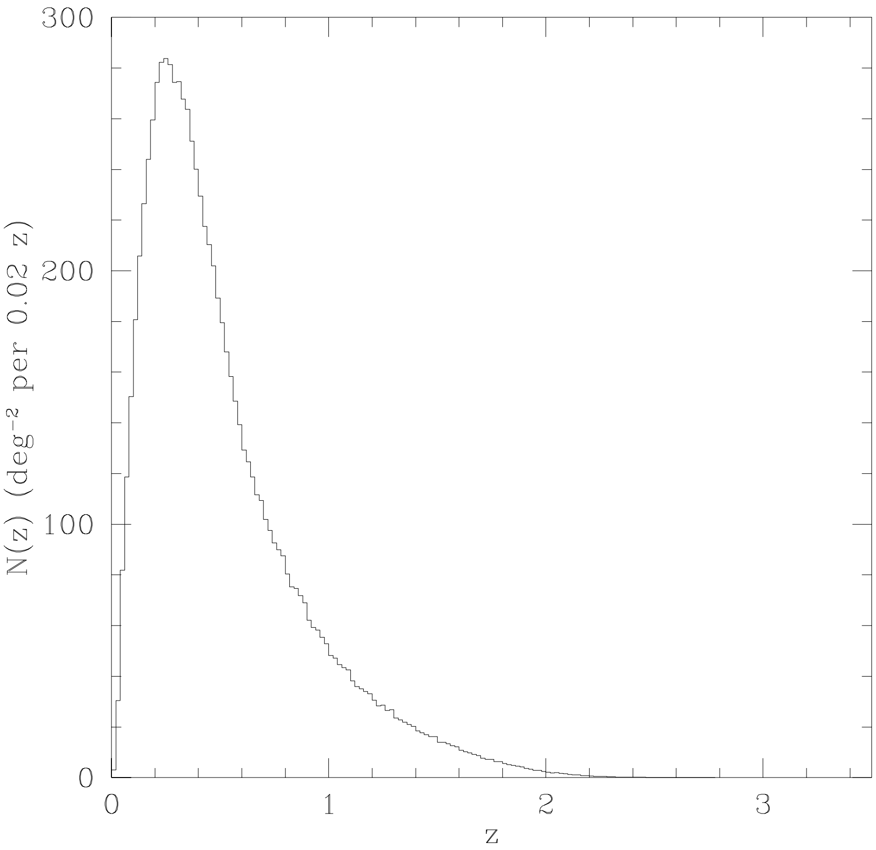

Figure 2.8: The model redshift distribution from Metcalfe et al., (1996) for a limiting magnitude of $b_J = 23$.

where r is the proper separation of two objects and r_0 is the correlation scale length at $z = 0$. Evolution is parameterized by ϵ, with various values of this parameter corresponding to the following cases: $\epsilon = 0$ is equivalent to constant clustering in proper coordinates, so called *stable clustering*; $\epsilon = \gamma - 3$ implies clustering which is constant in comoving coordinates; $\epsilon = \gamma - 1$ implies clustering which grows according to linear theory (for $\Omega_0 = 1$). We adopt the standard locally measured galaxy auto-correlation power-law slope of $\gamma = 1.8$. Although this is not necessarily correct at high redshift or in the case of QSO-galaxy cross-correlations, the measured QSO auto-correlation is consistent with this slope (Chapter 3). We investigated the effect of altering the slope and found that a change in slope of ~ 0.2 did not significantly alter our conclusions.

The conversion from spatial to angular cross-correlation function is obviously strongly dependent on the radial selection functions, $\phi(x)$, of the two populations. For the QSOs we simply use the redshift distribution of the QSOs used in our analysis above (Section 2.3), that is, we integrate Limber's equation for each QSO in the sample. To model the galaxy selection function we use the $N(z)$ derived from the galaxy evolution models of Metcalfe et al., (1996) which are consistent with the redshift distribution of galaxies in the deep Keck Telescope galaxy redshift survey

Table 2.3: Clustering amplitudes, $\omega(\theta < 120'')$ and A_{qg} (assuming the given value of γ), for $z < 1.5$ QSOs and $b_J < 23$ galaxies in a number of different models. σ gives the significance of the difference between the models and the observed clustering for all QSOs with $z < 1.5$. No correction is made for the integral constraint.

r_0	γ	ϵ	$\omega(\theta < 120'')$	A_{qg}	σ
6.0	1.8	-1.2	0.0430	0.00170	3.5
6.0	1.8	0.0	0.0245	0.00099	2.6
6.0	1.8	0.8	0.0175	0.00071	2.2
14.0	1.8	-1.2	0.1976	0.00797	11.2
14.0	1.8	0.0	0.1128	0.00454	7.0
14.0	1.8	0.8	0.0805	0.00324	5.4
8.8	2.2	-1.2	0.3179	0.00233	17.2
8.8	2.2	0.0	0.1867	0.00136	10.7
8.8	2.2	0.8	0.1360	0.00010	8.2

to $B = 24$ (Cowie et al., 1995). These models contain an exponential rise in star formation with look-back time and use the evolutionary tracks of Bruzual & Charlot, (1993). The $N(z)$ distribution from this model is shown in Fig. 2.8. It should be noted that the luminosity evolution produces a considerable high redshift tail to the distribution, as found in the sample of Cowie et al., where significant numbers of galaxies were found above $z = 1$.

Therefore, the only free parameters we have are the clustering correlation length r_0 and the evolutionary parameter ϵ, which we attempt to constrain from the QSO-galaxy cross-correlation results.

2.4.2 A comparison of models and data

We calculate the expected clustering amplitude for a number of different cases which are shown in Table 2.3. We first use the known present day galaxy-galaxy auto-correlation function with $r_0 = 6\ h^{-1}$ Mpc and $\gamma = 1.8$. With clustering evolution which is stable in comoving coordinates this model is inconsistent with the data for all $z < 1.5$ QSOs at the 3.5σ level. Clustering which is stable in proper coordinates is rejected at the 2.6σ level and clustering evolution which is consistent with linear theory is rejected at the 2.2σ level. If we allow for an integral constraint of ~ 0.006, which of course assumes a clustering amplitude similar to the auto-correlation amplitude of $b_J < 23$ galaxies, the significance of the results are only changed by $\sim 0.3\sigma$. If we use the measured cross-correlation amplitude to estimate an integral constraint then this correction would be considerably smaller. In fact the integral constraint would be negative, increasing the significance of the above rejections. Results from two other sets of parameters are also shown in Table 2.3. With a clustering amplitude similar to that of the cluster-cluster auto-correlation function $r_0 = 14\ h^{-1}$ Mpc

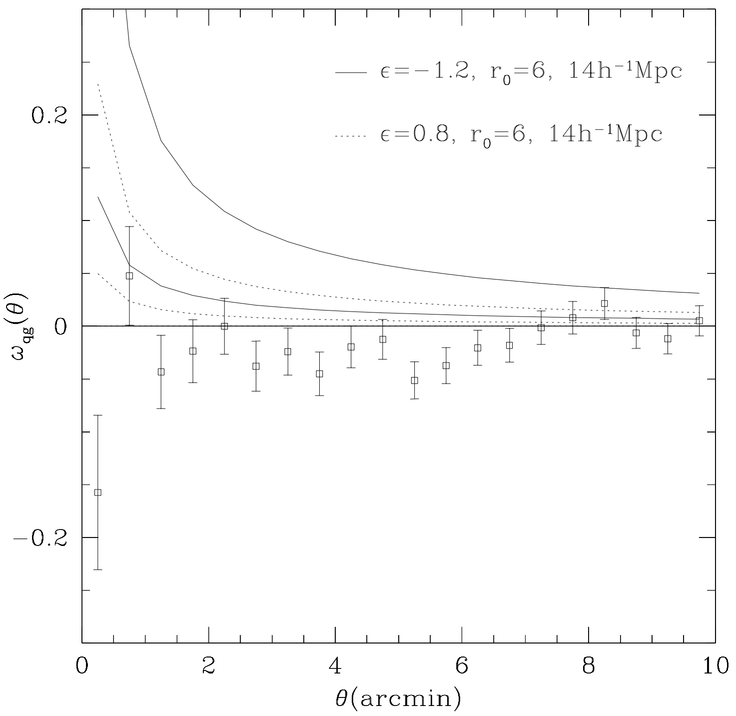

Figure 2.9: $\omega(\theta)$ calculated from the models discussed in the text compared to the results from all QSOs with $z < 1.5$ correlated with $b_{\rm J} < 23$ galaxies. The solid curves show models with comoving clustering evolution ($\epsilon = -1.2$) and amplitudes of $r_0 = 14\ h^{-1}$ Mpc (upper) and 6 h^{-1} Mpc (lower). The dotted curves show models with linear theory clustering evolution ($\epsilon = 0.8$) and amplitudes of $r_0 = 14\ h^{-1}$ Mpc (upper) and 6 h^{-1} Mpc (lower).

and $\gamma = 1.8$ (Dalton et al., 1994), the lowest amplitude found (assuming linear theory growth) is 5σ too high compared with the data. We then try a model which fits the galaxy-cluster cross-correlation function, $r_0 = 8.8\ h^{-1}$ Mpc and $\gamma = 2.2$, (Lilje & Efstathiou, 1988). This model, which might be a better estimate of our expected signal if QSOs were found only in rich clusters, is comfortably rejected for any reasonable rate of evolution. Ideally we would attempt to find the best fit values for r_0 and ϵ using maximum likelihood techniques. However, as the measured cross-clustering amplitude is marginally negative, these best fit values would have no physical meaning. We therefore follow the above method to constrain particular models.

2.5 Discussion

It is clear that there is strong disagreement between the clustering results presented here and a range of models. This is demonstrated by Fig. 2.9 which shows the cross-correlation function between QSOs at $z < 1.5$ and $b_{\rm J} < 23$ galaxies compared to a number of the models described above. We found a significant rejection of a number of the models within $2'$. From Fig. 2.9 it is clear that the disagreement is also severe on scales up to $\sim 8'$. The cross-correlation is, on average, negative up to this scale and inclusion of an integral constraint of the magnitude discussed above (Section 2.2) has no significant effect on this statement. At $z < 1.5$ the correlation within $120''$ is $\omega(\theta < 120'') = -0.027 \pm 0.020$, and at $z > 1.5$, the combined X-ray and optically selected sample has a clustering amplitude of $\omega(\theta < 120'') = -0.028 \pm 0.021$, almost identical to that found at lower redshift. If we assume that a non-zero cross-correlation is only produced by physically associated QSOs and galaxies then the above results give us strong constraints on the environments of radio-quiet QSOs up to $z \sim 1.5$. Out to this redshift we still expect to see significant numbers of galaxies with a limiting magnitude of $b_{\rm J} = 23$. The local luminosity function has $M^*_{\rm J} \simeq -19.7$ (e.g. Ratcliffe, 1996) which is equivalent to $b_{\rm J} = 23$ and 24 for $z = 1.0$ and $z = 1.5$ without K-corrections. A combination of K-correction and reasonable luminosity evolution (Pozzetti et al., 1996) leaves these values largely unchanged (particularly for late type galaxies) and thus at $z = 1$ we reach $\sim M^*$ and at $z = 1.5$ about 1 mag brighter than M^*. We can firmly reject the hypothesis that the QSOs in our data set exist in rich environments similar to galaxy clusters. This is true for a wide range of evolutionary rates (parameterised by ϵ). A scenario in which QSOs have poorer environments, similar to 'normal' galaxies, is a more acceptable alternative, although this still gives a clustering amplitude which is inconsistent with the data at the $2 - 3\sigma$ level.

We see a significant anti-correlation in our data, which cannot be explained by the conventional clustering models used above, but the data give us various clues as to the source of this signal. First, we find that the optically selected QSOs show more anti-correlation than the X-ray selected samples, particularly at high redshift. Second, when we sub-divide the galaxy samples on the basis of colour (for only two fields), we find that the red galaxies show a much stronger anti-correlation than the blue galaxies. It has been established that the auto-correlation amplitude for faint red galaxies is significantly higher than for faint blue galaxies (Roche et al., 1996). This is easily understood if the redder galaxies lie predominantly at low redshift while the high redshift tail of the galaxy distribution is composed of the blue population. Of course, early type galaxies are also more numerous in rich structures such as galaxy clusters. It therefore appears that QSOs tend to show an anti-correlation with galaxies in rich environments at low redshift.

The possible causes of this signal are either obscuration by high densities of dust in rich structures or gravitational lensing which can cause an anti-correlation if the QSO number-counts slope is flat (see Chapter 5). The optical QSOs in the sample are in the magnitude range where the number counts are flat, ~ 0.3, compared to the critical slope of 0.4 which is the slope required for zero-correlation. The X-ray selected QSOs, in contrast, have a $\log N - \log S$ slope of 2.52 ± 0.3 at bright magnitudes turning over to 1.1 ± 0.9 (Georgantopoulos et al., 1996). The critical $\log N - \log S$ slope is 1.0 so we expect no anti-correlation (although it should be noted that the errors in the slope at faint fluxes are large). In Chapter 5 we show that even extreme estimates of galaxy masses could only produce anti-correlations ~ -0.02 to -0.03. This extreme model can just account for the anti-correlation measured at $z < 1.5$. Lensing could reduce the inconsistency between our results and the lowest amplitude clustering models to only $\sim 1\sigma$, while the inconsistency with the strongly clustered models is still very significant. Lensing does not appear to explain the larger anti-correlation found at $z > 1.8$ between the $b_{\rm J} < 23$ galaxies and optical QSOs, although it should be noted that this signal is due to a relatively small number of QSOs. A final possibility is that QSOs at low redshift might avoid rich environments. However, we have only a small number of QSOs at low redshift which are in fields that contain colour information (7 QSOs at $z < 1$), and also, other observations (Smith et al., 1995) find a low but positive correlation between QSOs and galaxies at low redshift.

2.6 Conclusions

We have carried out an investigation of the environments of a large sample of QSOs (~ 150), using deep AAT photographic plates in 5 independent areas. The QSOs were selected by optical colour techniques and using deep X-ray exposures from *ROSAT*. We draw the following conclusions:

1. Only a small number of QSOs ($\sim 4-5$) show significant positive correlation with $b_{\rm J} \leq 23$ galaxies; most QSOs show zero or negative correlations. For a combination of all QSOs at $z < 1.5$ we find $\omega(\theta < 120'') = -0.027 \pm 0.020$.

2. Optically and X-ray selected QSOs show marginally different properties, with the optical sample being more anti-correlated than the X-ray sample; for $z < 1.5$ $\omega_{\rm x}(\theta < 120'') = -0.018 \pm 0.022$, while $\omega_{\rm o}(\theta < 120'') = -0.051 \pm 0.027$. At high, $z > 2$, redshift the optical QSOs become more anti-correlated with galaxies.

3. Analysis of two fields with colour information suggests that the anti-correlation is stronger in the red galaxy population than the blue population.

4. The cross-correlation results are compared with models including clustering evolution. Models which have clustering amplitudes similar to that of galaxy clusters ($r_0 \sim 14\ h^{-1}$ Mpc) with a wide range of evolutionary rates are ruled out. The data are more consistent with a low clustering amplitude, similar to that of the galaxy auto-correlation function, although $r_0 = 6\ h^{-1}$ Mpc combined with linear theory evolution still gives too high an amplitude at the 2σ level. If gravitational lensing causes some of the measured anti-correlation, the disagreement with the low amplitude clustering model could be reduced to $\sim 1\sigma$.

5. We suggest that the anti-correlation found could be due to gravitational lensing, which is particularly suggested by the fact that optical QSOs and red galaxies show the strongest anti-correlation. This is investigated further in Chapter 5. An extreme lensing model could account for most of the measured anti-correlation at $z < 1.5$. However, even this extreme lensing model does not significantly affect our conclusions when comparing the data to clustering models.

The results presented here clearly reject the notion that radio-quiet QSOs exist in rich cluster-like environments up to $z \sim 1.5$. Beyond this redshift we require deeper images to determine the environments of QSOs. Our results are consistent with those of Boyle & Couch (1993) who find no correlation between $R \sim 23$ galaxies and QSOs in the redshift range $0.9 < z < 1.5$. Ellingson et al., (1991) find a marginal positive signal at $z < 0.6$, which is consistent with our data (although we have a small number of QSOs at these low redshifts). Our data appear to be inconsistent with those of Hutchings et al., (1995) who find that a sample of 14 QSOs are associated with compact groups of star forming galaxies. We conclude that our results continue to uphold the hypothesis that QSOs are not strongly biased with respect to the galaxy population, but are more likely to trace the distribution of 'normal' galaxies.

Chapter 3

Evolution of QSO Clustering

3.1 Introduction

In this chapter we present an analysis of various QSO surveys. In particular we look at the clustering properties of four recent QSO samples. Much of the motivation for this analysis has been described in Chapter 1. At present, it is technically impossible to obtain spectra (and therefore redshifts) for large, statistically complete samples of high redshift ($z > 1$) galaxies. However, the statistics of QSO samples can be used to study the Universe at these high redshifts.

We have two entwined problems to resolve: Firstly we need to know how the QSO distribution samples the underlying density field. This relationship can generally be both a function of redshift and scale. We can introduce the concept of *bias* to describe this relation between the observable tracers of large-scale structure (in our case, QSOs) and the density perturbations in the mass distribution. Once this first, highly non-trivial, problem is overcome we can use the statistics of QSO clustering and its evolution over time to constrain cosmological parameters, in particular the density parameter, Ω_0, and the cosmological constant, λ_0. In reality these two problems are closely associated and difficult to separate. We therefore use methods of analysis which allow for both biasing and cosmology.

The first QSO survey to show clustering in a well defined sample was the Durham/AAT QSO survey (Boyle, 1986; Boyle et al., 1990). This showed clustering on scales of $< 10\ h^{-1}$ Mpc (Shanks et al., 1987). A large scale QSO 'supercluster' was found in the CFHT survey of 215 QSOs (Crampton et al., 1985; Crampton et al., 1987; Crampton et al., 1989) at $z = 1.1$ which has dimensions $\simeq 50\ h^{-1}$ Mpc in comoving coordinates. However, no significant clustering was found in the remainder of the survey. Shanks & Boyle (1994) (henceforth SB94), combined the completed Durham/AAT UVX sample (Boyle et al., 1990) with the CFHT survey and the ESO/AAT sample (Boyle et al., 1991; Zitelli et al., 1992) of 83 UVX/colour selected QSOs to obtain statistics on a sample of ~ 700 QSOs, finding significant clustering on scales $< 10\ h^{-1}$ Mpc.

Georgantopoulos (1991) (see also Georgantopoulos & Shanks, 1994), carried out a similar analysis on the low redshift Seyferts in the IRAS Point Source Catalogue (de Grijp et al., 1987) and a 2σ clustering signal was found on scales less than 10 h^{-1} Mpc. Boyle & Mo (1993) obtained clustering statistics for the QSOs at low redshift ($z < 0.2$) in the Einstein Extended Medium Sensitivity Survey (EMSS) but did not find a significant clustering signal at small scales. Both of these low redshift results are consistent with the amplitude of QSO clustering at $z = 1.4$ if there is no evolution of the clustering in comoving coordinates. This previous work suggests only a small amount of evolution from a redshift of $z = 0.1$ to $z = 1.4$ if we can assume that the low and high redshift samples come from the same parent population.

Below we describe the QSO samples that are used in this analysis and then in Section 2.3 discuss in detail the techniques used to calculate the auto-correlation function for QSOs, paying particular attention to the effects of cosmology and estimates of errors. Section 2.4 contains the results obtained from the correlation analysis of the QSO surveys and the rest of the chapter is devoted to interpreting these clustering results, in particular looking at clustering evolution and biasing.

3.2 Data

3.2.1 The QSO samples

The largest of the four surveys used in this analysis is the Large Bright Quasar Survey (LBQS) (Hewett et al., 1995). This consists of 18 United Kingdom Schmidt Telescope (UKST) field areas, each $6° \times 6°$, eleven along the equator ($\delta = 0°$), four in the direction of the Virgo Cluster, and three in the South. QSOs were selected using UKST objective prism plates, and broad band fluxes were obtained from direct plates in the $b_{\rm J}$ band. Both sets of plates were scanned by the Automatic Plate Measuring (APM) machine. The bright magnitude limit for the survey is $b_{\rm J} = 16.0$ and the faint magnitude limit varies from field to field in the range $18.41 < b_{\rm J\ lim} < 18.85$. A conservative error of $\Delta m = 0.15$ (Foltz et al., 1987) is suggested for the QSO magnitudes. Follow-up spectroscopy was obtained from the Multiple Mirror Telescope (MMT) and the Las Campanas Du Pont Telescope. The survey contains a total of 1053 QSOs and their redshift distribution can be seen in Fig. 3.1.

The Durham/AAT QSO survey (Boyle et al., 1990) is a colour selected QSO catalogue, using the Ultra-Violet Excess (UVX) technique. Colours were obtained from COSMOS measurements of eight sets of UKST plates in the $b_{\rm J}$ and u bands and QSO candidates were selected from their blue $u - b$ colours. The faint limiting magnitude is $b = 21$. Spectroscopy was carried out using the FOCAP system at the Anglo-Australian Telescope (AAT) in 34 $40'$ diameter fields randomly placed within the UKST plate areas. The sample contains 392 QSOs with redshifts in the range

$0.3 < z < 2.2$ (the effective range of the UVX selection technique).

The third survey used is the Canada-France-Hawaii Telescope (CFHT) Survey (Crampton et al., 1989). This is an objective prism/colour selected sample based on four CFHT plate areas. One of the sub-fields within these plate areas may not be representative of the underlying QSO distribution as observations in this field (at $12^{\mathrm{h}}48^{\mathrm{m}} + 27°$) were concentrated on a previously known QSO 'supercluster' at $z = 1.1$. When considering this survey we will quote results both with and without the region $0.9 < z < 1.2$ in this field included in our analysis (removing this region rejects 30 QSOs from the sample). The faint limit for this survey is $B = 20.5$. At this limit there are 215 QSOs within the same redshift range as the Durham/AAT survey.

Lastly, the ESO/AAT survey (Boyle et al., 1991; Zitelli et al., 1992) is a smaller colour/UVX selected survey using AAT and European Southern Observatory (ESO) 3.6m telescope plates to a fainter limiting magnitude of $B = 22.5$. Spectroscopy was carried out using FOCAP and EFOSC. The sample contains 83 QSOs in the range $0.3 < z < 2.2$.

3.2.2 Comparison of LBQS and other surveys

The LBQS has a considerably brighter magnitude limit than the three other surveys used in this work, which raises particular problems when considering clustering analysis. The number-magnitude relation for QSOs is particularly steep over the range covered by the LBQS and only flattens at $B \simeq 19.15$,

$$n(< B) \propto 10^{0.86B} \ (B < 19.15) \tag{3.1}$$

$$n(< B) \propto 10^{0.28B} \ (B > 19.15) \tag{3.2}$$

(Boyle et al., 1988b). The LBQS therefore has a much lower surface density of QSOs than the three other surveys. At a limiting magnitude of $b_{\mathrm{J}} = 18.41$ the LBQS has an effective area of 453.8 deg^2 and 667 QSOs (Hewett et al., 1993) implying a surface density of 1.47 QSOs deg^{-2}. By comparison, the Durham/AAT survey has a surface density of 33.05 QSOs deg^{-2}. The accuracy of the two-point correlation function, $\xi(r)$, defined in Eq. 1.8, is strongly dependent on the number of QSO-QSO pairs at a scale r. It is only when we reach large scales ($\sim 100\ h^{-1}$ Mpc) that the LBQS has more pairs per bin in r than the Durham/AAT sample which is less than twice the size of the LBQS. Thus while at small scales the Durham/AAT, ESO/AAT and CFHT surveys contribute most of the signal, the LBQS is dominant at the largest scales. The shape of the LBQS redshift distribution is also significantly different from that of the other three samples (see Fig. 3.1), peaking at a much lower redshift, so weighting any results towards low redshift. The UVX selection technique can only be used to a redshift of $z = 2.2$, so we shall generally carry out our analysis below this redshift limit.

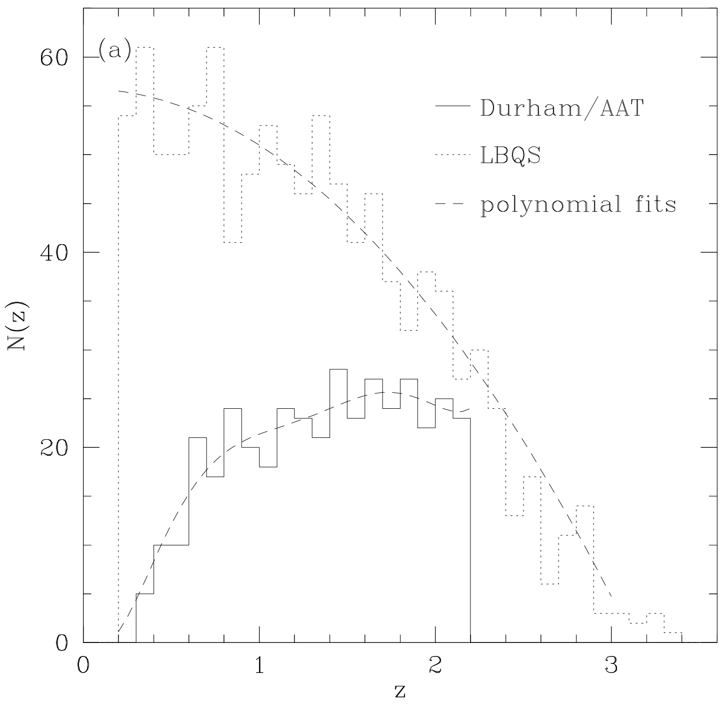

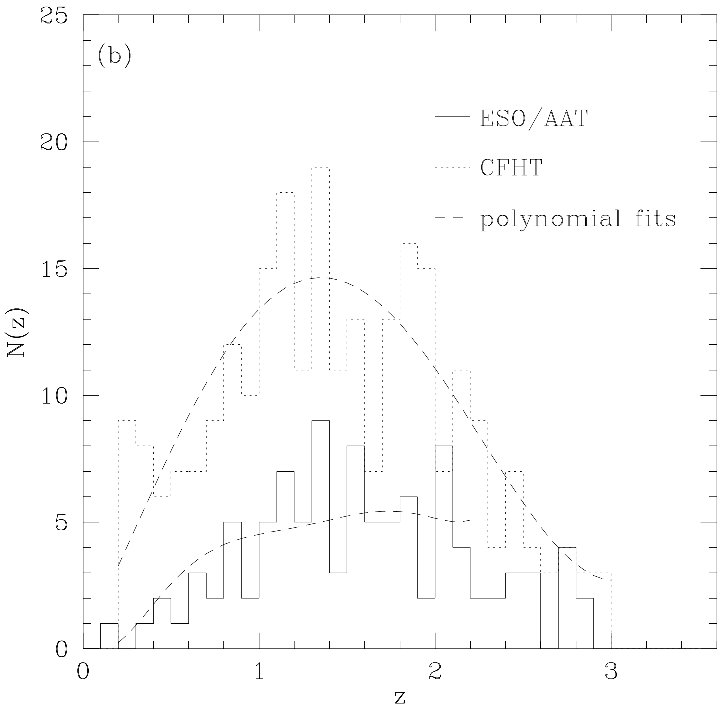

Figure 3.1: The redshift distributions, $N(z)$, for the surveys used in this analysis. (a) The Durham/AAT and LBQS samples, and (b) the CFHT and ESO/AAT samples. Each is plotted with a fitted polynomial, the first three samples using individual fits and the ESO/AAT using a normalized Durham/AAT fit. These polynomials are used in producing the random samples for our calculations of the correlation function.

3.3 Techniques

3.3.1 Correlation function estimates

We use the two-point correlation function as our main estimator of the clustering properties of the above QSO samples. This is defined in Eq. 1.8, but when studying a distribution of point sources rather than a density field this can be defined as

$$\xi(\mathbf{r}) = \langle \delta n(\mathbf{x}+\mathbf{r})\delta n(\mathbf{x})\rangle \tag{3.3}$$

where $n(\mathbf{x})$ is the number density of sources.

On the scales probed with the QSO correlation function, separation is a strong function of cosmology. We use the method of Osmer (1981) which uses the coordinate transformation in the Friedmann-Robertson-Walker metric (Eq. 1.1),

$$\mathbf{X}' = \mathbf{X} + \mathbf{a}[\sqrt{1-k\mathbf{X}^2} - (1-\sqrt{1-k\mathbf{a}^2})(\mathbf{X}.\mathbf{a}/\mathbf{a}^2)] \tag{3.4}$$

(Weinberg, 1972) where $\mathbf{a} = (0, 0, -s_1)$ and $\mathbf{X} = (s_2\sin(\theta), 0, s_2\cos(\theta))$. s_1 and s_2 are the dimensionless comoving distances to QSOs 1 and 2 respectively, and θ is their angular separation on the sky. This is a relatively simple transformation, however, the values s_1 and s_2 depend on the cosmological model used. Taking Eq. 1.1, with $d\tau = 0$ for a photon and assuming the photon travels along a radial path, we have

$$c^2dt^2 = \frac{a^2(t)dr^2}{1-kr^2} \tag{3.5}$$

Integrating this equation from the time of emission of the photon (t_e) to the present (t_0) gives,

$$\int_0^r \frac{\mathrm{d}r}{\sqrt{1-kr^2}} = \int_{t_e}^{t_0} \frac{c\mathrm{d}t}{a(t)} = \int_{a_e}^{a_0} \frac{\mathrm{d}a}{a\dot{a}} \tag{3.6}$$

Writing this equation in terms of redshift (using Eqs. 1.2 and 1.6) we can find the comoving distance to an object with redshift, z. This distance is given by

$$x = \frac{c}{H_0a_0}\int_0^z \frac{\mathrm{d}z}{\sqrt{\Omega_0(1+z)^3 - (\frac{3}{2}\Omega_0 - q_0 - 1)(1+z)^2 + \frac{\Omega_0}{2} - q_0}} \tag{3.7}$$

and

$$s = \begin{cases} \sin(x) & k=1 \\ x & k=0 \\ \sinh(x) & k=-1 \end{cases} \tag{3.8}$$

When we are considering the case of $\lambda_0 = 0$, Eq. 3.7 reduces to

$$x = \frac{c}{H_0a_0}\int_0^z \frac{\mathrm{d}z}{(1+z)\sqrt{\Omega_0 z + 1}} \tag{3.9}$$

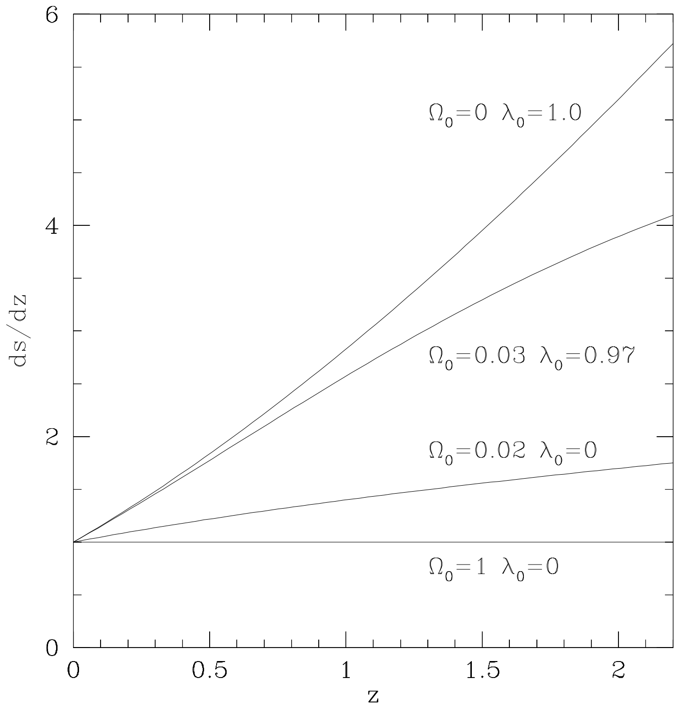

Figure 3.2: $\mathrm{d}s/\mathrm{d}z$ as a function of redshift, normalized to $\mathrm{d}s/\mathrm{d}z$ for $q_0 = 0.5$, where s is the comoving distance. This is plotted for some of the cosmologies used in our analysis, namely $q_0 = 0.5$ and $q_0 = 0.01$ with $\lambda_0 = 0$, and flat low Ω_0 models with $\lambda_0 = 0.97$ and 1.0.

and we can solve exactly, obtaining

$$s = \frac{zq_0 + (q_0 - 1)(\sqrt{2zq_0 + 1} - 1)}{(1 + z)q_0^2} \tag{3.10}$$

For $\lambda_0 \neq 0$ the integral can only be solved numerically, however an approximation (Peebles, 1984) can be used for inflationary (i.e. flat, $k = 0$) Λ models,

$$s = z \text{ for } 1 + z < (\Omega_0^{-1} - 1)^{1/3} \tag{3.11}$$

The correlation function is a difference of two comoving distances, so an assumed cosmology will affect ξ via $\mathrm{d}s/\mathrm{d}z$. In Fig. 3.2 we plot the relative $\mathrm{d}s/\mathrm{d}z$ compared to a $q_0 = 0.5$ universe for a number of different cosmologies. The above approximation for inflationary Λ is only exact for $\Omega_0 = 0$ and $\lambda_0 = 1$. For $\Omega_0 = 0.03$ (with $\lambda_0 = 0.97$) the approximation deviates from the true value by 10 per cent at $z = 1$ and 34 per cent at $z = 2$. In this analysis we shall integrate Eq. 3.7 numerically for $\lambda_0 \neq 0$ cosmologies. The comoving separation is then given by

$$r = \frac{c}{H_0 a_0} \begin{cases} \arcsin(|\mathbf{X}'|) & k = 1 \\ |\mathbf{X}'| & k = 0 \\ \operatorname{arcsinh}(|\mathbf{X}'|) & k = -1 \end{cases} \tag{3.12}$$

We use the following estimator to obtain the two-point correlation function:

$$\xi(r) = \frac{N_{\rm qq}(r)}{N_{\rm qr}(r)} \frac{2n_{\rm r}}{(n_{\rm q} - 1)} - 1 \tag{3.13}$$

where $N_{\rm qq}$ is the number of QSO-QSO pairs at a separation $r \pm \delta r/2$ and $N_{\rm qr}$ is the number of QSO-random pairs in the same interval. The $2n_{\rm r}/(n_{\rm q} - 1)$ term normalizes the number of randoms to the number of QSOs, $n_{\rm q}$ being the number of QSOs and $n_{\rm r}$ the number of random points. We use $n_{\rm r} = 100 n_{\rm q}$ within each field. As the magnitude limits for each LBQS field differ, the number of random points is normalized to the number of QSOs in the individual fields. We give each point a random RA, declination and a random redshift weighted by the overall $N(z)$ for the QSO sample. Other estimators for the two-point correlation function have been suggested, such as

$$\xi(r) = \frac{N_{\rm qq}(r) N_{\rm rr}(r)}{N_{\rm qr}^2(r)} - 1 \tag{3.14}$$

(Hamilton, 1993). These other methods were tested but they were not found to be significantly different from the estimator in Eq. 3.13, which was used as it requires significantly less computational time (as no $N_{\rm rr}(r)$ term is needed).

A comment is required concerning the variable effective area in different LBQS fields. All the LBQS fields cover $5.8^\circ \times 5.8^\circ$. However, each field has different regions removed due to overlapping spectra, step-wedges and bright images (Hewett et al., 1995). We calculate $\xi(r)$ for the LBQS by two different methods, the first is to simply take the $5.8^\circ \times 5.8^\circ$ area (apart from those fields which overlap, where the overlaps are removed from one of the fields) and distribute randoms within this region with no regard to any holes in the effective area. The second is to use the real positions of the LBQS QSOs for our random points, but randomly shuffle their redshifts. We then use 1000 realisations of this process to obtain a mean number of QSO-random pairs. When we compare the two processes we find no significant difference; the r.m.s.difference between the two estimates is 0.26σ where σ is the error on the first estimator. This is not altogether unexpected as the LBQS survey regions are much more extended in the radial direction than in the angular direction. Holes in the field would only be expected to contribute to any signal at large scales, and at large scales the redshift component of the distance dominates the signal. Throughout this analysis we will use the first estimator as this should give a less biased estimate of clustering on small scales.

No correlation between fields is attempted, as any systematic magnitude calibration error between fields would mean a considerable QSO density variation. If we use a form for the bright counts such that $N(<B) \propto 10^{0.8B}$ then a ~ 0.1 mag error in the zero point magnitude produces a 20 per cent variation in the QSO surface density. Our normalization is such that it forces the integral correlation function to zero on the very largest scales probed. On small scales we also use the integrated correlation function, $\bar{\xi}(r)$, where

$$\bar{\xi}(r) = \frac{3}{r^3} \int_0^r \xi(x) x^2 {\rm d}x \tag{3.15}$$

To estimate this we simply use the same estimator in Eq. 3.13, but for pairs at separation 0 to r.

3.3.2 Error analysis

Field-to-field variation of number density

We look at the field-to-field variance of the number of QSOs in the LBQS, taking the 18 fields and considering the number counts of QSOs to a limiting magnitude of $b_\mathrm{J} = 18.41$ mag. A χ^2 test is carried out on the hypothesis that the fields are derived from the same population. The result is $\chi^2 = 33.92$ for 17 degrees of freedom, which is a rejection of the hypothesis at a 99 per cent significance level. Most of this variation comes from three fields, two equatorial, $01^\mathrm{h}00^\mathrm{m}$ $00°00'$, $22^\mathrm{h}40^\mathrm{m}$ $00°00'$, and one southern, $00^\mathrm{h}53^\mathrm{m}$ $-28°00'$, with 56, 24 and 57 QSOs respectively. Without these fields a χ^2 test gives $\chi^2 = 16.47$ on 14 degrees of freedom, only significant at the 70 per cent level. A possible cause of this effect could be residual magnitude errors after calibration, although CCD sequences were used to obtain zero-points and linearize the APM magnitudes. Hewett et al., (1995) suggests that there could still be systematic variations across individual fields of up to 0.1 mag. This justifies our decision not to correlate QSOs between individual fields.

Correlation function errors

Analysis of errors in the two-point correlation function is an area of some debate. In the case of QSOs we have the particular problem that at small scales there are only a small number of pairs, while at the largest scales we can probe, $\xi(r)$ has an intrinsically lower amplitude causing any signal to be close to the noise. To determine our errors, particularly on larger scales, we have carried out an analysis of several different error estimators to find the most accurate and consistent errors for our estimates of the QSO $\xi(r)$. We consider Poisson errors, field-to-field errors, simulations and bootstrap methods (Barrow et al., 1984) to produce estimates for the error on the QSO correlation function.

The Poisson noise due to the number of pairs in the sample is

$$\Delta\xi = \frac{1+\xi}{\sqrt{N_\mathrm{qq}}} \tag{3.16}$$

This estimate should be valid at small scales if the signal is still relatively low. The number of pairs is small so most pairs are independent and contribute independent information to the correlation function. At large scales QSO pairs become less independent, and one might expect that n_q would be a more realistic error estimate than N_qq.

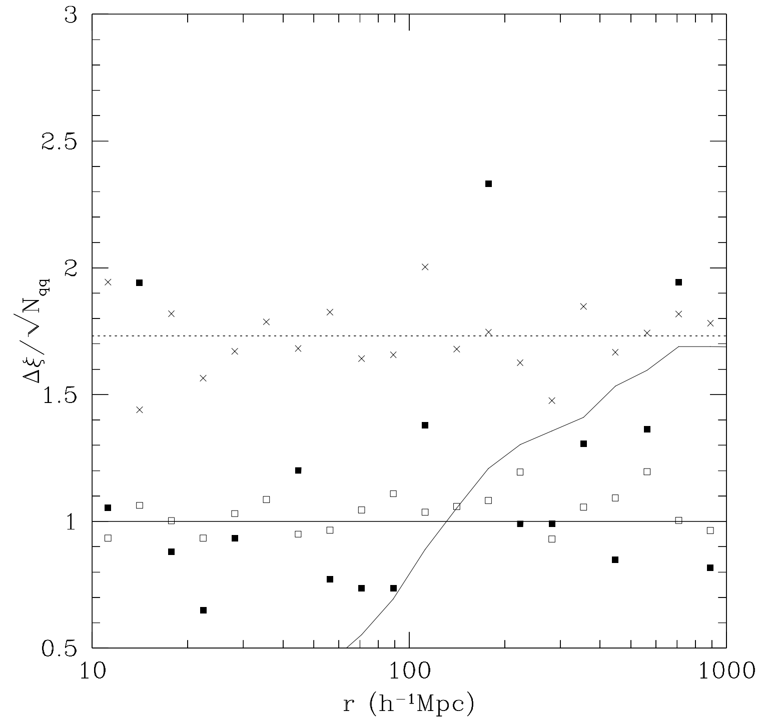

Figure 3.3: Relative estimates of the errors in the 2-point correlation function from simulations (open squares), field-to-field variation (filled squares), bootstrap re-sampling (crosses), and $n_{\rm q}^{1/2}$ (solid line), normalized to $N_{\rm qq}^{1/2}$ for the LBQS sample. The dotted line is $\Delta\xi = (3N_{\rm qq})^{1/2}$, the expected relative error from bootstrap estimates.

For field-to-field errors we have split the LBQS survey up into five regions, each containing ~ 170 QSOs, calculating the variance between these five different correlation function estimates. We produced multiple random (a good approximation to the survey due to the small number of correlated pairs) simulations of the LBQS survey region and found the variance from the estimates of $\xi(r)$ from these simulations. The bootstrap re-sampling was carried out by randomly selecting a sample of n QSOs from a total of n QSOs *with replacement.* For both the simulations and bootstrap re-sampling 100 realisations were used.

In Fig. 3.3 we plot the error estimates normalized to the Poisson ($\sqrt{N_{\rm qq}}$) error for the LBQS sample. The field-to-field variance has a large scatter over all scales probed by the LBQS $\xi(r)$, but $\Delta\xi_{\rm field-field}$ is approximately consistent with $\sqrt{N_{\rm qq}}$ at all these scales. The variance calculated from simulations is also consistent with Poisson errors on all scales. The errors resulting from the bootstrap method are 1.7 times larger than the $\sqrt{N_{\rm qq}}$ at all scales. This is consistent with a suggested analytical expression for the bootstrap error (Mo et al., 1992),

$$\sigma^2_{\rm boot}(r) \simeq 3N_{\rm qq}(r) + \frac{4N^2_{\rm qq}(r)}{n_{\rm q}} \tag{3.17}$$

This expression was formulated assuming a large contiguous region in which the edge effects are negligible. This is obviously not the case for any of the QSO surveys.

As a result the second term in the above expression is always small, particularly as there is no attempt to correlate QSOs between fields. Hence $\Delta\xi_{\rm boot}/\sqrt{N_{\rm qq}} \simeq \sqrt{3}$ at all scales.

At small scales we know that the bootstrap errors overestimate the true errors (Mo et al., 1992). We should therefore use $\sqrt{N_{\rm qq}}$ errors on these scales as they are consistent with both field-field and simulation errors. On larger scales ($> 100\ h^{-1}$ Mpc) the choice is not so obvious. Bootstrap errors should be more realistic on these scales but still overestimate the field-to-field and simulated errors by a factor of $\sqrt{3}$. $n_{\rm q}$ errors are consistent with $N_{\rm qq}$ errors at $\sim 100\ h^{-1}$ Mpc and consistent with bootstrap estimators at $\sim 1000\ h^{-1}$ Mpc. For these reasons (and because of the large amount of time needed to run simulations for every case) the correlation function for the QSOs will be plotted using $\sqrt{N_{\rm qq}}$ errors until $N_{\rm qq} = n_{\rm q}$, then with $\sqrt{n_{\rm q}}$ at larger scales. It should be noted that the majority of our analysis will be carried out below 50 h^{-1} Mpc and in this region it is clear that $\sqrt{N_{\rm qq}}$ is the best choice. When looking for low amplitude signals at larger scales the simulations will be used to obtain a reliable estimate of the uncertainty.

3.4 Results at Small Scales

Correlation functions out to $r = 100\ h^{-1}$ Mpc are shown in Fig. 3.4. Figs. 3.4a and 3.4b show the correlation functions for LBQS and Durham/AAT on log-log plots for $q_0 = 0.5$. The LBQS in particular does not have a strongly significant signal at small scales due to the small number of QSO-QSO pairs at $< 10\ h^{-1}$ Mpc (only five) in the survey. Within the large errors the two surveys both appear to be consistent with the power law,

$$\xi(r) = \left(\frac{r}{r_0}\right)^{-\gamma} \tag{3.18}$$

with $r_0 = 6\ h^{-1}$ Mpc and $\gamma = 1.8$. A χ^2 test on the hypothesis that the data fit this power law gives $\chi^2 = 6.852$ (6 degrees of freedom) and $\chi^2 = 1.608$ (4 degrees of freedom) for the Durham/AAT and LBQS samples respectively, hence the probabilities of the hypothesis being rejected are small, 0.665 and 0.193. This test was carried out below 30 h^{-1} Mpc. The pair-weighted combined QSO $\xi(r)$ for the ESO/AAT and CFHT samples is plotted in Fig. 3.4c. This plot is corrected from the previous version in SB94, which contained an error producing more small scale power and an anti-correlation on scales of $\sim 40 - 100\ h^{-1}$ Mpc. The corrected version of this plot shows excess power over that expected from the $r_0 = 6\ h^{-1}$ Mpc power law at the 30 h^{-1} Mpc scale. This excess power is from the QSO 'supercluster' in the CFHT sample. When the region around the 'supercluster' is removed, the data are consistent with the above power law. Fig 3.4d shows the four surveys combined, using a simple pair weighting. The errors are obtained from Eq. 3.16 and are significantly improved by combining the data. It is possible to find a best fit power law to these data, using a minimum χ^2 fit. For $q_0 = 0.5$ the best fit (without

Table 3.1: The integrated QSO clustering, $\bar{\xi}$, within 10 h^{-1} Mpc and 25 h^{-1} Mpc, for the LBQS and for all surveys combined (excluding the CFHT 'supercluster'). The results are listed for various cosmologies.

Ω_0	$\lambda_\circ$	LBQS $\bar{\xi}(10)$	All $\bar{\xi}(10)$	All $\bar{\xi}(25)$
1	0	1.86 ± 1.28	0.83 ± 0.29	0.16 ± 0.08
0.1	0	1.06 ± 1.45	1.09 ± 0.47	0.21 ± 0.11
0.02	0	1.09 ± 1.48	1.01 ± 0.50	0.28 ± 0.12
0.2	0.8	2.42 ± 2.42	1.01 ± 0.58	0.35 ± 0.14
0.03	0.97	1.54 ± 2.55	0.76 ± 0.79	0.74 ± 0.23

the CFHT 'supercluster') is $r_0 = 4.00 \pm 1.14$ and $\gamma = 1.59 \pm 0.46$ ($r_0 = 4.96 \pm 1.13$ and $\gamma = 1.40 \pm 0.30$ with the CFHT 'supercluster'), (see Fig. 3.4d). The fit is made between the scales 2 and 32 h^{-1} Mpc. It should be noted that varying the range of scales over which this fit is made makes a considerable difference to the best fit parameters, demonstrating that a significantly larger sample is required to obtain a robust result.

Another measure of the clustering amplitude on small scales is the value $\bar{\xi}(r)$ (Eq. 3.15). We calculate this at two scales, $r = 10$ h^{-1} Mpc and $r = 25$ h^{-1} Mpc, the results of this are shown in Table 3.1. Shanks & Boyle (1994) find $\bar{\xi}(10\ h^{-1}\ \mathrm{Mpc}) = 0.93 \pm 0.34$ for Durham/AAT, CFHT (without cluster) and ESO/AAT combined. With the corrected analysis for CFHT and ESO/AAT this becomes $\bar{\xi}(10) = 0.74 \pm 0.30$. For the LBQS individually, $\bar{\xi}(10) = 1.86 \pm 1.28$ (there are only 5 QSO-QSO pairs within 10 h^{-1} Mpc), and combining this with the other surveys, $\bar{\xi}(10) = 0.83 \pm 0.29$. These results and those for other cosmologies are shown in Table 3.1.

Formally the significance of a rejection of a Poisson random distribution is 3.8σ (by comparing 39 pairs found to 21.3 expected). In cosmologies with low Ω_0, we generally find a higher amplitude but larger errors, as pairs move out to larger scales. For $q_0 = 0.01$, $\bar{\xi}(10) = 1.01 \pm 0.50$ (considering the whole sample without the CFHT cluster) and for $\Omega_0 = 0.2$ and $\lambda_0 = 0.8$ we find $\bar{\xi}(10) = 1.01 \pm 0.58$, representing a formal detection of clustering at the 2.8σ and 2.5σ levels respectively.

If the sample ($q_0 = 0.5$) is split into redshift bins then for $0.3 < z < 1.4$, $\bar{\xi}(10) = 0.97 \pm 0.43$ and for $1.4 < z < 2.2$, $\bar{\xi}(10) = 0.68 \pm 0.40$. Although the high redshift signal is lower there is no significant evolution between the two redshift bins. Similarly, the best fit power laws for the low and high redshift bins respectively are $r_0 = 4.48 \pm 1.36$, $\gamma = 2.00 \pm 0.92$ and $r_0 = 4.08 \pm 2.27$, $\gamma = 1.32 \pm 0.60$ which show that although the high redshift correlation function appears to be lower it is not significantly so.

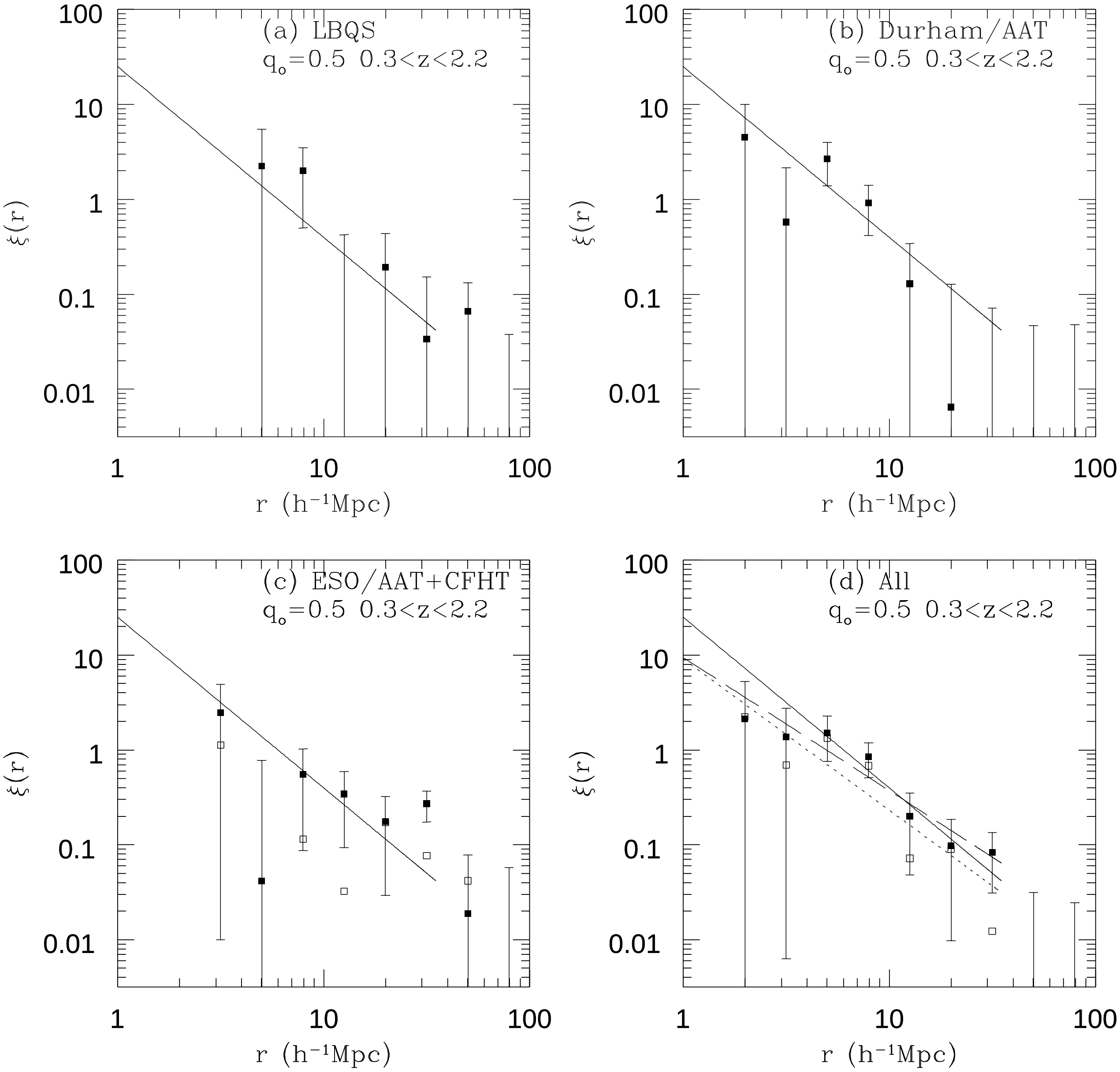

Figure 3.4: QSO correlation functions on small scales for $\Omega_0 = 1.0$ in the redshift range $0.3 < z < 2.2$. (a) The LBQS, (b) the Durham/AAT sample, (c) the corrected ESO/AAT and CFHT combined (open squares with the redshift range $0.9 - 1.2$ removed in the $12^{\rm h}48^{\rm m} + 27^\circ$ field) and (d) all surveys combined (again the open symbols are with the CFHT 'supercluster' removed). The solid line in all the plots is a power law with $r_0 = 6\ h^{-1}$ Mpc and $\gamma = 1.8$. Dashed and dotted lines in (d) are the best fit power laws with and without the CFHT 'supercluster' respectively. The data is binned with $\Delta\log(r) = 0.2$.

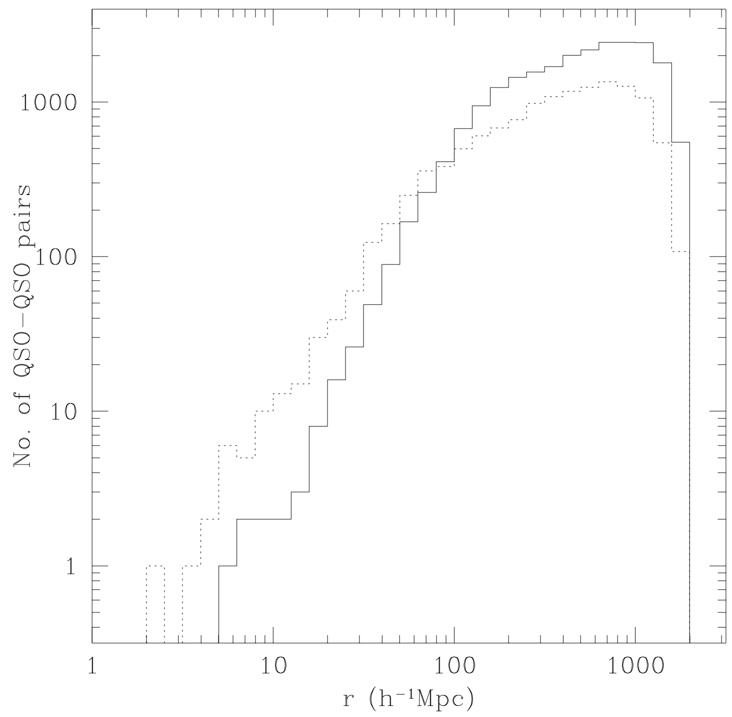

Figure 3.5: The number of QSO-QSO pairs as a function of scale (for $\Omega_0 = 1$) for the LBQS (solid line) and the Durham/AAT sample (dotted line).

3.5 Results at Large Scales

3.5.1 Clustering in the LBQS at large scales

Below we present the results of QSO clustering analysis at larger scales ($r > 20\ h^{-1}$ Mpc). The combined QSO sample of the LBQS, Durham/AAT, CFHT and ESO/AAT surveys gives a total of over 1500 QSOs between $z = 0.3$ and $z = 2.2$.

In Section 3.4 it was pointed out that the LBQS makes very little contribution to clustering statistics on scales less than $\sim 10\ h^{-1}$ Mpc. However, on larger scales the LBQS is an important new probe of structure. The count of QSO pairs peaks at around $800 - 900\ h^{-1}$ Mpc and Fig. 3.5 shows this pair distribution as a function of scale (for $0.3 < z < 2.2$). The Durham/AAT survey has a higher pair count below $100\ h^{-1}$ Mpc, but above this scale the LBQS starts to dominate the signal.

First, we have calculated $\xi(r)$ for the LBQS over the entire redshift range of the sample, $0.2 < z < 3.4$ (Fig. 3.6). This will actually be heavily weighted towards low redshift due to the shape of the LBQS number-redshift relation. The LBQS does not show a significant deviation from $\xi = 0$ on any scale probed, and at scales larger than $100\ h^{-1}$ Mpc the error on $\xi(r)$ is only ± 0.03. In order to compare the LBQS to the other samples we have also calculated $\xi(r)$ for the LBQS in the range $0.3 < z < 2.2$. This is shown in Fig. 3.7a, again there is no significant signal at these large scales.

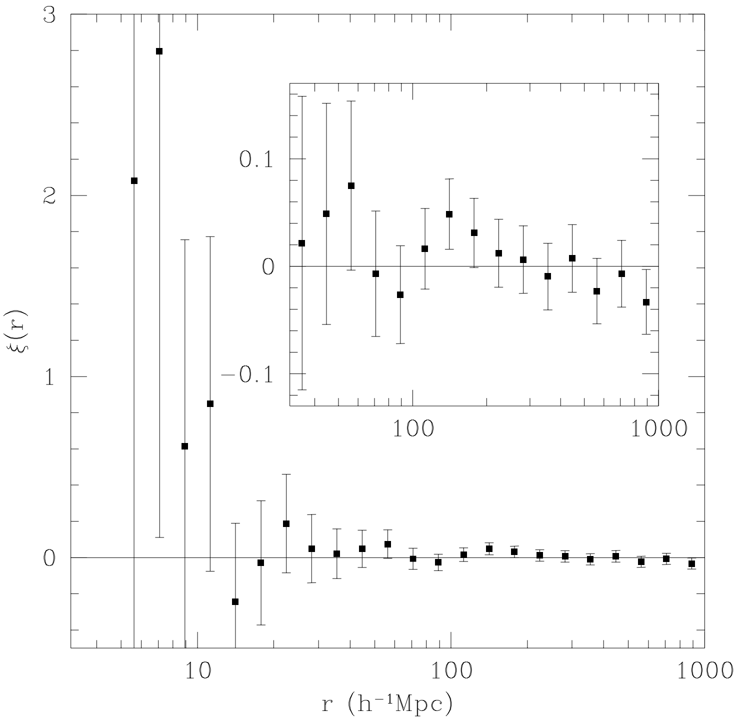

Figure 3.6: The two-point correlation function for the LBQS in the redshift range $0.2 < z < 3.4$. Inset is an expanded version of the plot from 30 to 1000 h^{-1} Mpc. The bins have width $\Delta \log(r) = 0.1$.

Results from the Durham/AAT, ESO/AAT and CFHT are also shown on this plot. Shanks & Boyle (1994) show an anti-correlation in the Durham/AAT survey on scales $40 - 100\ h^{-1}$ Mpc, significant at the 2σ level, which is not seen in the LBQS. The signal in the Durham/AAT sample is $\xi(40 - 100\ h^{-1}\ \mathrm{Mpc}) = -0.084 \pm 0.036$ (SB94) with errors from simulations. The corresponding signal in the LBQS is $\xi(40 - 100\ h^{-1}\ \mathrm{Mpc}) = 0.00 \pm 0.034$, again using errors from simulations. These two values are consistent at the 2σ level. The revised $\xi(r)$ for the CFHT and ESO/AAT samples also show no anti-correlation on these scales: $\xi(40 - 100\ h^{-1}\ \mathrm{Mpc}) = -0.006 \pm 0.041$. Therefore there is no evidence in the LBQS, CFHT or ESO/AAT samples to support the claimed anti-correlation of Shanks & Boyle (1994), although the difference between the surveys is not strongly significant.

Next, the LBQS was split into redshift bins. For consistency we used the same bins as used by SB94, that is $0.3 < z < 1.4$ and $1.4 < z < 2.2$. The correlation functions for these are shown in Fig. 3.7b. In the $0.3 < z < 1.4$ case there are 556 QSOs, and no significant deviations from zero are seen at any scale. By contrast, in the Durham/AAT sample the anti-correlation seen at $40 - 100\ h^{-1}$ Mpc is seen largely in the lower redshift range. The high redshift sub-sample of the LBQS shows only one point that significantly deviates from zero. The lack of significant deviations from $\xi = 0$ at large scales is a strong constraint on the inhomogeneity of the Universe.

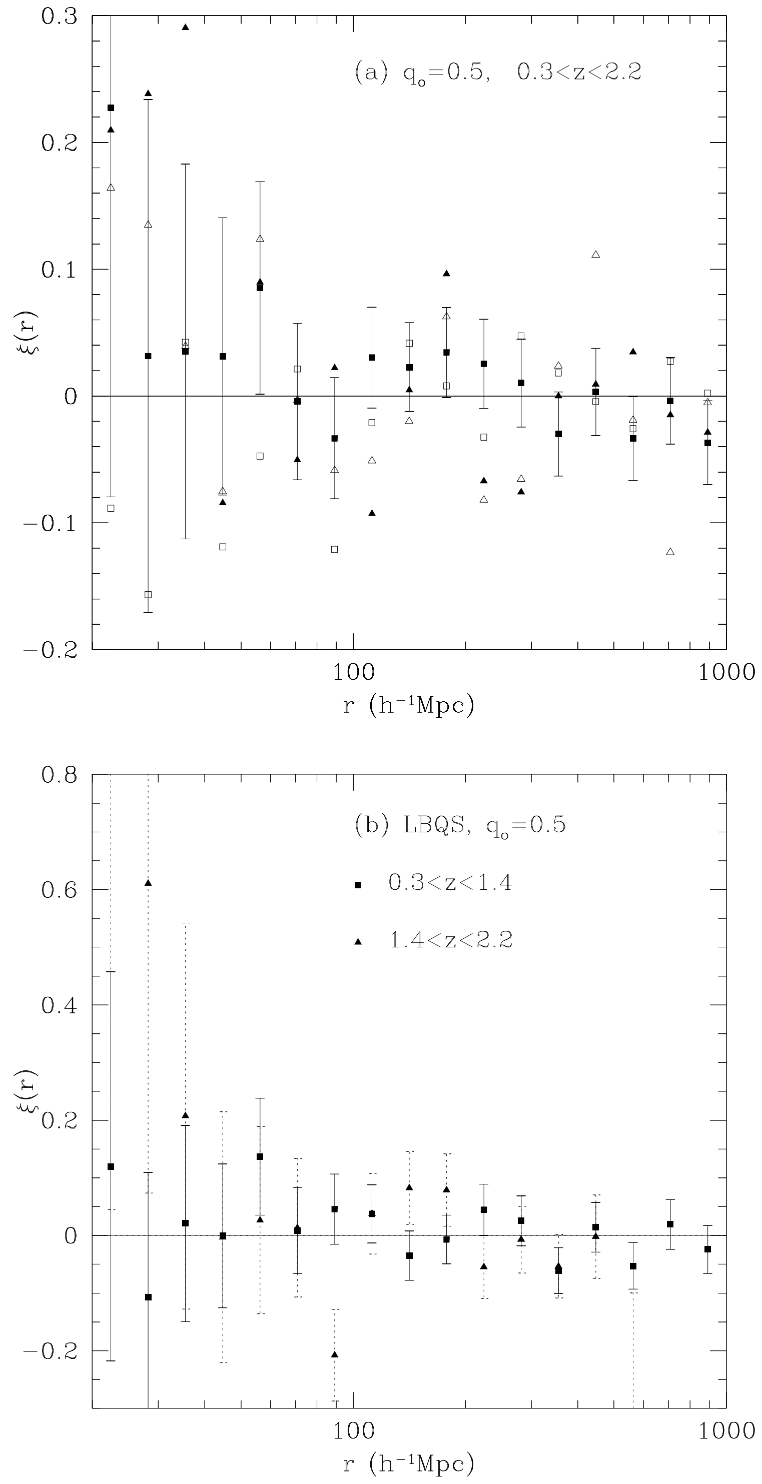

Figure 3.7: QSO Correlation functions with $q_0 = 0.5$ and $0.3 < z < 2.2$. (a) the LBQS (filled squares with errors), Durham/AAT (open squares) and re-analysed CFHT and ESO/AAT (filled triangles, open triangles with CFHT 'supercluster' removed). (b) $\xi(r)$ for LBQS in redshift bins $0.3 < z < 1.4$ (filled squares) and $1.4 < z < 2.2$ (filled triangles).

3.5.2 Large-scale structure in the combined sample of QSOs

The $\xi(r)$ for the combined sample at large scales is shown in Fig. 3.8a, and constitutes one of the most accurate available representations of large-scale structure on scales in excess of 50 h^{-1} Mpc. Removing the CFHT 'supercluster' makes little difference on scales $> 30\ h^{-1}$ Mpc. In the region at $40 - 100\ h^{-1}$ Mpc that caused interest in the Durham/AAT sample, the mean correlation function is now $\xi(40 - 100\ h^{-1}\ \mathrm{Mpc}) = -0.026 \pm 0.022$ (this error is obtained from simulations, note that $\sqrt{n_\mathrm{q}}$ would give a similar error, ± 0.024). Looking more closely at the region around 100 h^{-1} Mpc there are points at 89 and 177 h^{-1} Mpc that are marginally $(1.5 - 2\sigma)$ non-zero, so only tentative evidence of a feature on this scale. Positive signals near these scales have been seen in pencil-beam galaxy surveys (Broadhurst et al., 1990), and it should be remembered that all the QSO surveys are effectively pencil beams, so there is some observational precedent for a signal of this kind. On scales greater than 200 h^{-1} Mpc there are no deviations away from a Poisson distribution. Splitting the combined sample into redshift bins, Fig. 3.8b, we see that both redshift bins contribute to the signal at $\sim 100\ h^{-1}$ Mpc but no distinctive features are seen. In the combined sample, we therefore have even tighter constraints on inhomogeneity in the Universe. The upper limits at $r > 100\ h^{-1}$ Mpc are at the ~ 0.025 level.

Galaxy redshift surveys show impressive amounts of structure when the galaxy distribution is mapped out (e.g. Ratcliffe 1996) . This produces a significant signal in the correlation function at scales of $\sim 20 - 30\ h^{-1}$ Mpc, as demonstrated by the Durham/UKST Galaxy Redshift Survey (Ratcliffe et al., 1997), the Las Campanas Galaxy Redshift Survey (Tucker et al., 1997) and others. The galaxy auto-correlation functions for these two surveys are compared to the QSO auto-correlation function in Fig. 3.9. The Las Campanas data are consistent with the QSO data while the Durham/UKST result has a slightly higher amplitude on large scales. We should, of course, remember that galaxy clustering measurements are at $z \sim 0$ while the QSOs have a mean redshift of $\bar{z} = 1.27$. Nevertheless, the similarities between the galaxies and QSOs are clear.

3.5.3 QSO $\xi(r)$ in low q_0 and $\Lambda \neq 0$ models

The combined QSO correlation functions for $q_0 = 0.01$ ($\lambda_0 = 0$) and $\Omega_0 = 0.03$, $\lambda_0 = 0.97$ are shown in Fig 3.10. Fig. 3.2 has shown how the differential comoving distance varies with cosmology. This effect can be used to discriminate between cosmologies if it is possible to observe linear features in the correlation function at low redshift. Linear theory predicts that features should not change scale as they evolve, their only evolution being in amplitude. Hence, if a linear feature is observed at low redshift in the correlation function then a corresponding feature should be observable at high redshift, only if the correct cosmology is assumed. Effectively we are using features in the correlation function as standard rods. Both low q_0 and positive Λ increase the average separation between pairs of QSOs.

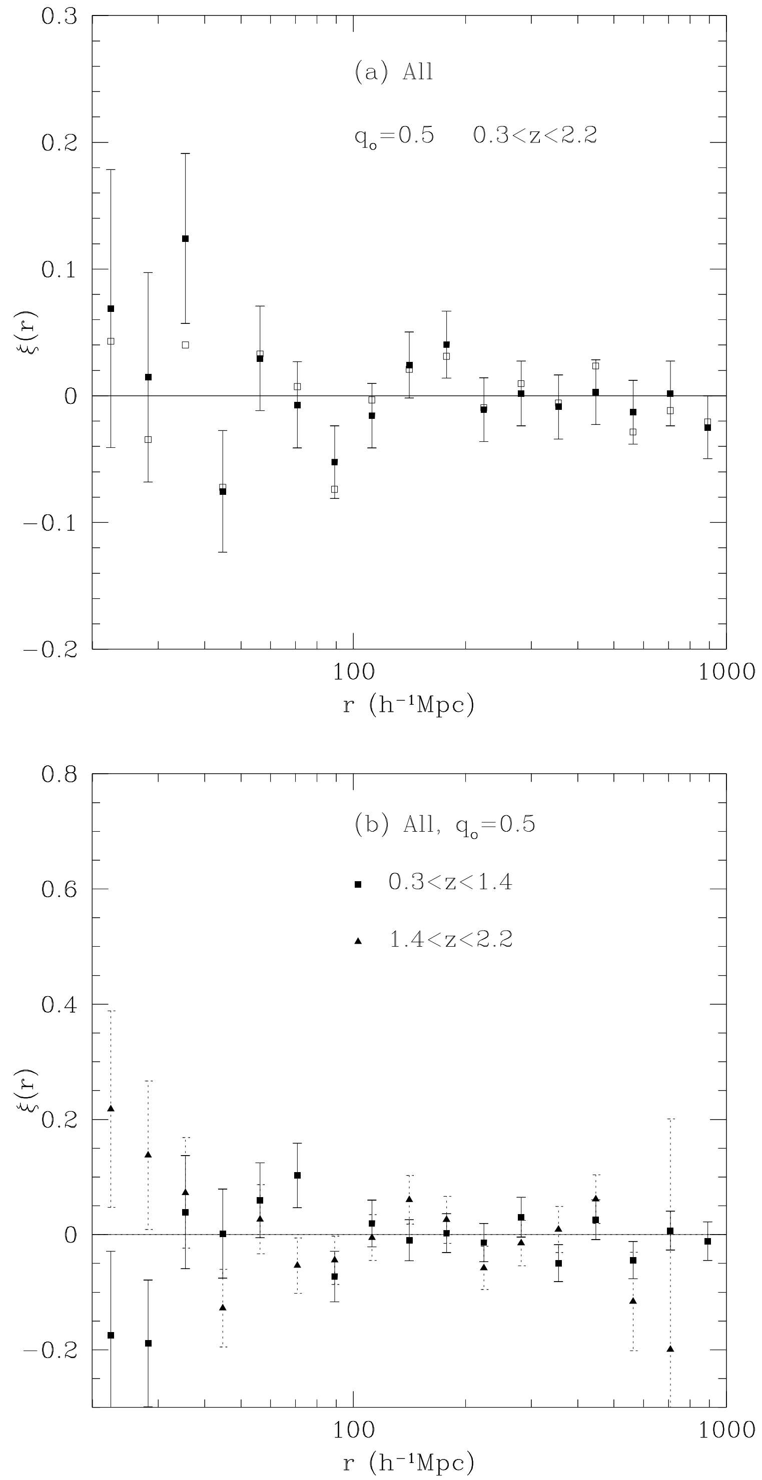

Figure 3.8: The QSO correlation function for the combined sample at large scales, for $q_0 = 0.5$. (a) Redshift range $0.3 < z < 2.2$ (open squares with the CFHT 'supercluster' removed), (b) $0.3 < z < 1.4$ without CFHT 'supercluster' (filled squares) and $1.4 < z < 2.2$ (filled triangles).

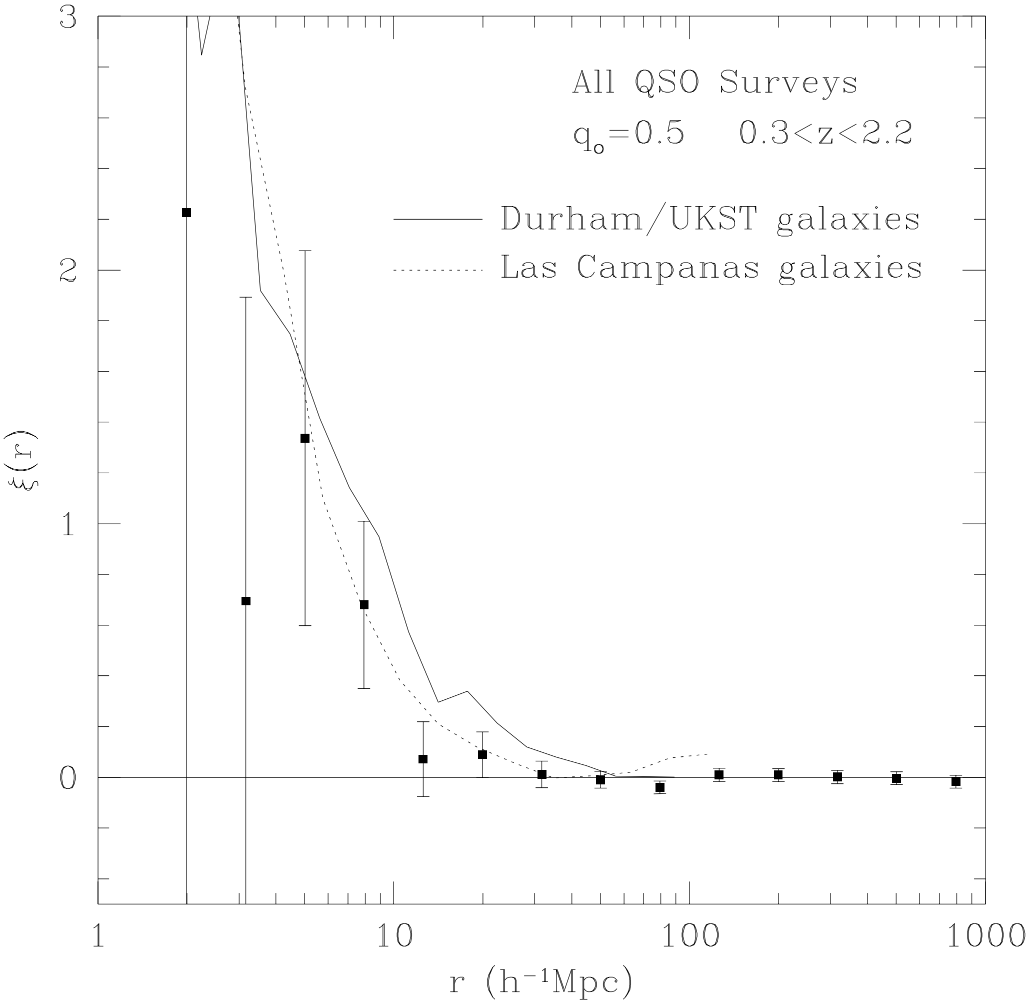

Figure 3.9: The QSO correlation function for the combined sample (with $q_0 = 0.5$ and $0.3 < z < 2.2$) over the entire range of scales probed. The data are binned with $\Delta\log(r) = 0.2$. For clarity only the data without the CFHT 'supercluster' are used. The data are compared to local galaxy correlation functions from the Durham/UKST Redshift Survey (solid line) and the Las Campanas Redshift Survey (dotted line).

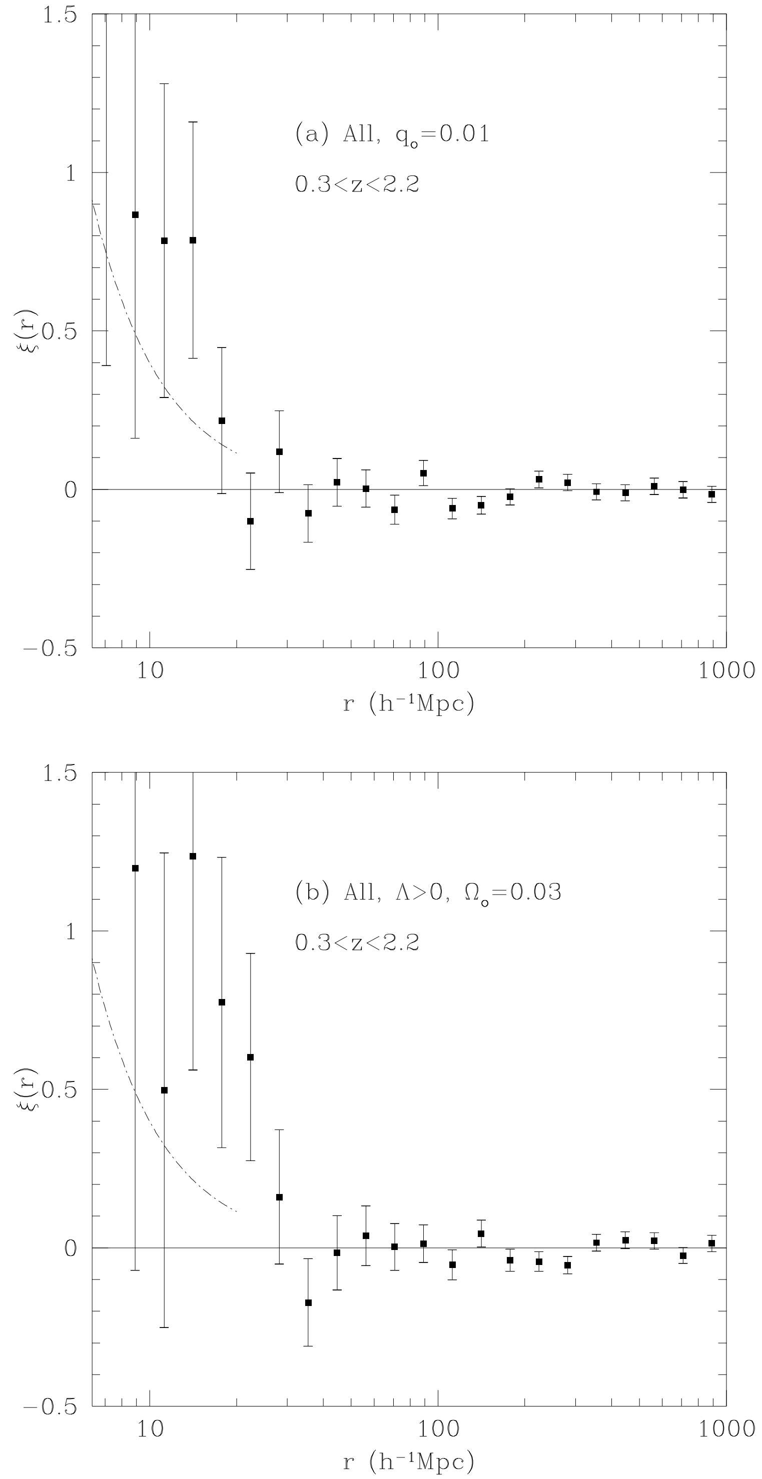

Figure 3.10: The QSO correlation function for the combined sample with (a) $q_0 = 0.01$ and (b) inflationary Λ, $\Omega_0 = 0.03$, $\lambda_0 = 0.97$. For clarity we only plot points excluding the CFHT 'supercluster'. The dot-dashed line is $\xi = (r/6)^{-1.8}$.

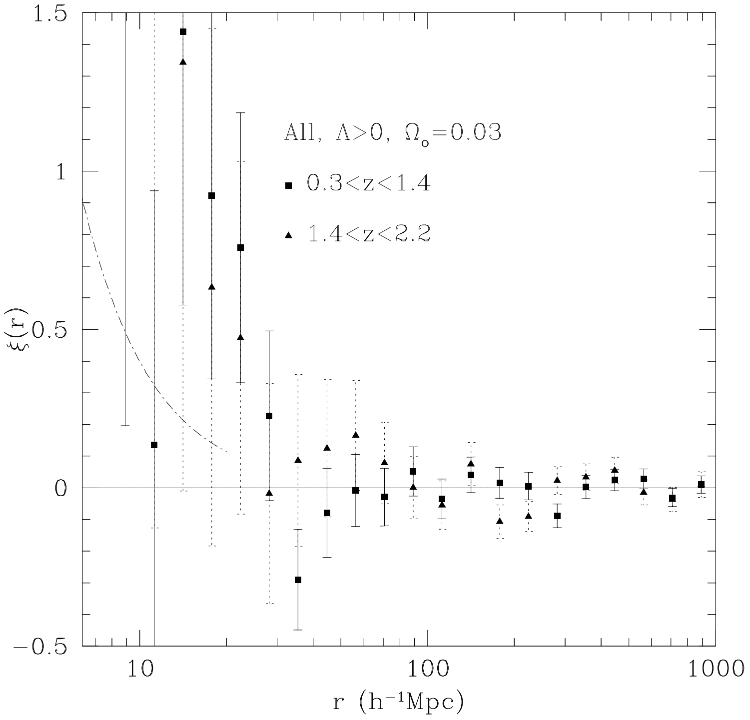

Figure 3.11: The QSO correlation function for $\Omega_0 = 0.03$, $\lambda_0 = 0.97$ in the redshift intervals $0.3 < z < 1.4$ (filled squares) and $1.4 < z < 2.2$ (filled triangles).

In Fig. 3.11 we plot the QSO $\xi(r)$ for $\Omega_0 = 0.03$ and $\lambda_0 = 0.97$ in the two redshift bins used above. From low to high redshift we expect a doubling of the scale of any real feature, if $q_0 = 0.5$ is the correct cosmology. At some level this will be watered down by the angular separation of the QSOs, but all the samples considered in this chapter are of a geometry which is much more extended in the radial direction. There are marginal anti-correlations seen, at $\sim 280\ h^{-1}$ Mpc at low redshift, and at $\sim 200\ h^{-1}$ Mpc at high redshift. Unfortunately these signals are not significant enough to use as convincing 'standard rods'.

To quantify the effect of cosmology (at a somewhat smaller scale), we calculate $\bar{\xi}(25\ h^{-1}$ Mpc) (see Table 3.1). With an inflationary Λ cosmology this quantity is $\bar{\xi}(25) = 0.74 \pm 0.23$, and is larger than for other cosmologies without significant contributions from Λ. We can compare this measurement in the Λ cosmology to a power law with $r_0 = 6\ h^{-1}$ Mpc and slope of -1.8 (making the simplifying assumption that this power law extends to $\sim 25\ h^{-1}$ Mpc). These two correlation functions are inconsistent at the 2.9σ (4σ with CFHT 'supercluster') level. If QSOs randomly sample the galaxy distribution (see arguments below), this is a rejection of the Λ model. This test assumes ξ is approximately stable in comoving coordinates as a function of z. If ξ did in fact evolve faster the rejection would be stronger. Similarly if the power law turned over before $25\ h^{-1}$ Mpc then the present day clustering amplitude would be lower, again increasing the significance of the rejection. The same analysis is attempted for a low q_0 cosmology ($q_0 = 0.01$) but no significant rejection is found.

3.6 The Evolution of QSO Clustering in a Biased Model

At scales of $\sim 10\ h^{-1}$ Mpc the amplitude of the QSO correlation function is such that it is possible to start discriminating between evolutionary models of large-scale structure. In particular, the redshift evolution of the mass correlation function depends strongly on Ω_0. If QSOs are biased with respect to the overall mass distribution, this biasing will also play a major role in the evolution of QSO clustering. SB94 argue that, because the QSO clustering amplitude at high redshift is similar to that of nearby galaxies and Seyferts, QSO clustering evolution is approximately stable in comoving coordinates. This comoving picture is based on the assumption that QSOs, Seyferts and galaxies all have similar clustering properties. However, SB94 do not give any quantitative statements on the cosmological implications of their result. In contrast, Mo & Fang (1993) have used the same data (Durham/AAT and CFHT samples), which give the same clustering result at high redshift, to estimate a large present day correlation length for QSOs compared to the present day galaxy population. They find $r_0(z=0) = (18 \pm 2)\ h^{-1}$ Mpc, by assuming *unbiased* linear theory evolution from the high redshift clustering result; that is $\xi(z) = \xi(0)/(1+z)^2$. This leaves us with a paradox: the high present day amplitude suggests that the QSOs are highly biased with respect to present day galaxies and hence to the mass distribution, yet the result is obtained by assuming that the QSOs are unbiased.

Below, we have constructed a simple and consistent model of QSO clustering evolution, that can be used to compare high redshift QSO clustering and the low z Seyfert clustering amplitude (Georgantopoulos & Shanks, 1994; Boyle & Mo, 1993). To simplify the model we will consider clustering in the linear regime, using the peaks-bias formalism (Bardeen et al., 1986). This formalism is not used in the sense that QSOs are rare, therefore very high peaks, and therefore strongly clustered. It is simply stating that above a given threshold QSOs are able to form, but may only form in a *random fraction* of the peaks that are above that threshold. Bardeen et al (1986) defines the bias parameter b as,

$$b = \frac{\langle \bar{\nu} \rangle}{\sigma(t)} + 1 \tag{3.19}$$

where $\sigma(t)$ is the r.m.s. fluctuation in the mass distribution and $\langle \bar{\nu} \rangle$ defines some threshold above which QSOs/galaxies can form. If we assume that $\langle \bar{\nu} \rangle$ is a constant then the dependence of b on redshift is contained in $\sigma(t)$. This will scale as $\delta\rho/\rho$ and hence for $\Omega_0 = 1$

$$b(z) = (b(0) - 1)(1+z) + 1 \tag{3.20}$$

This evolution of bias can also be derived using a simple physical model where the QSOs are formed at a specific time by a mechanism which produces biasing and are then allowed to move under the influence of gravity. Fry (1996) shows that, to first order, the galaxy density contrast,

$$\delta_g(\mathbf{x}, t) = \frac{n(\mathbf{x}, t) - \bar{n}}{\bar{n}} \tag{3.21}$$

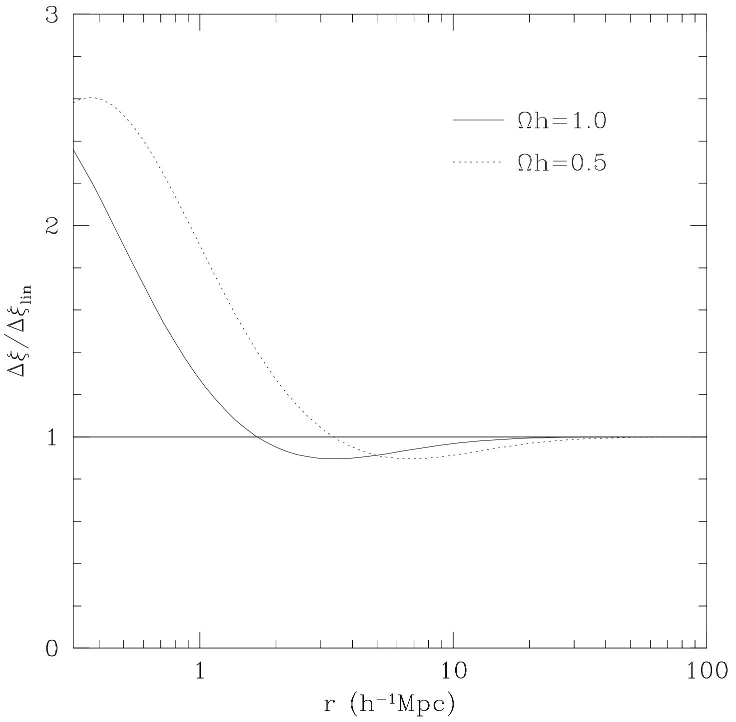

Figure 3.12: Growth of CDM $\bar{\xi}(r)$ for $\Omega_0 = 1$ and $h = 0.5, 1$ in the quasi-linear regime, from $z = 1.27$ to the present. The growth rate is normalized to linear theory evolution, $(1+z)^2$.

satisfies the relation

$$a\frac{\partial \delta_g}{\partial t} = -\theta = a\delta_0 \tag{3.22}$$

where δ_0 is the density contrast (Eq. 1.7) at some initial time, θ is the velocity divergence and a is the cosmological scale factor. Then as the linear bias factor is

$$b(t) = \frac{\delta_g(t)}{\delta(t)} = \frac{\delta_g(t)}{\delta_0 a(t)} \tag{3.23}$$

the solution to Eq. 3.22 shows exactly the same form of evolution as Eq. 3.20.

The average redshift of the combined QSO sample is $\bar{z} = 1.27$. The best comparisons and the tightest constraints will be available from comparing this to clustering at the present day (presently there is no gain from splitting the high redshift QSOs into redshift bins because of the increased errors on the points). We first compare the amplitude of QSO clustering at high redshift to present day galaxy clustering, then go on to make comparisons with the clustering of low redshift Seyfert galaxies. As an estimate of the $z = 0$ galaxy clustering we use $\xi_{\rm gg} = (r/6)^{-1.8}$, which gives $\bar{\xi}_{\rm gg}(10) = 1.00$. This can also be thought of as an estimate of the present mass correlation function, $\xi_{\rho\rho}$, if we include a term for the biasing of galaxies. The QSO correlation function can be related to the mass correlation function via

$$\xi_{\rm qq}(r,z) = [B(1+z)+1]^2\xi_{\rho\rho}(r,z) \tag{3.24}$$

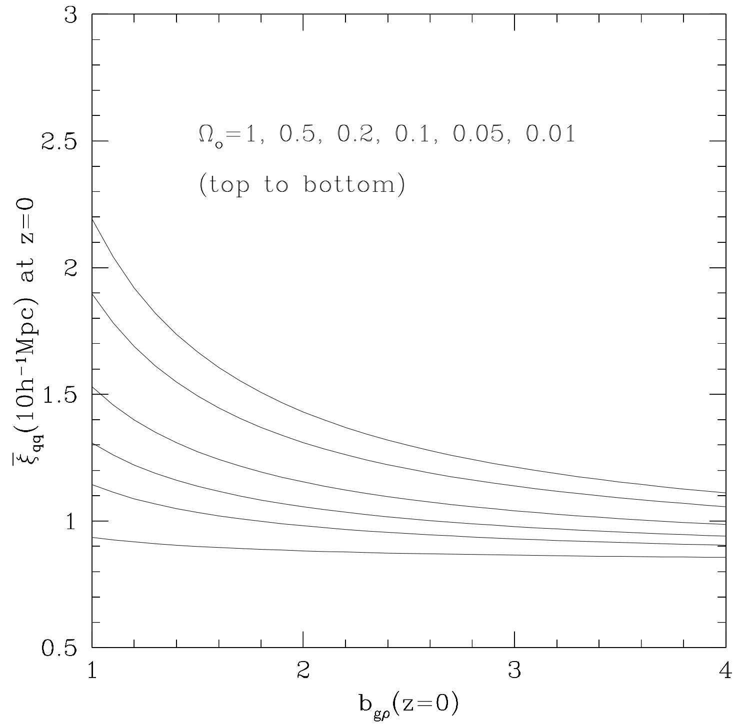

Figure 3.13: Amplitude of $\bar{\xi}_{qq}(10\ h^{-1}\ \mathrm{Mpc})$ at $z = 0$, estimated from the high redshift ($z = 1.27$) QSO clustering amplitude using our biasing model. This is shown as a function of Ω_0 and the present day galaxy bias. It can be seen that both high bias and low Ω_0 reduce the rate of evolution, to give low QSO clustering amplitudes at the present day.

where $B = b(0) - 1$. For $\Omega_0 = 1$

$$\xi_{\rho\rho}(r, 0) = (1 + z)^2 \xi_{\rho\rho}(r, z) \tag{3.25}$$

The biasing of the observed galaxy distribution can be taken into account using

$$\xi_{\mathrm{gg}} = b^2_{\mathrm{g}\rho} \xi_{\rho\rho} \tag{3.26}$$

where $b_{\mathrm{g}\rho}$ is the biasing of the galaxies with respect to the mass at $z = 0$. Combining these equations we obtain an estimate for $b_{\mathrm{q}\rho}$, the estimated present day biasing for QSOs,

$$b_{\mathrm{q}\rho}(z = 0) = B + 1 = \left[\frac{\xi_{\mathrm{qq}}(z)}{\xi_{\mathrm{gg}}(0)}\right]^{1/2} b_{\mathrm{g}\rho} - \frac{1}{1 + z} + 1 \tag{3.27}$$

In the following analysis we will use $\bar{\xi}(10\ h^{-1}\ \mathrm{Mpc})$ as an estimate of the QSO clustering amplitude, which has the advantage of giving a significant signal while at the same time not being affected by large non-linear effects. Hamilton et al (1991) find an empirical fit to the non-linear growth of the CDM correlation function. This is used to predict the deviation away from linear theory expected over the range of scales that we are interested in. Fig. 3.12 shows the relative growth of $\bar{\xi}$ from $z = 1.27$ to $z = 0$ for two CDM type correlation functions ($\Omega_0 = 1$ and $h = 0.5, 1.0$).

Table 3.2: Estimates of $b_{q\rho}$, $\bar{\xi}_{qq}(10)$ and the QSO clustering scale length, r_0, at $z = 0$. These are predicted using our biasing model and $\bar{\xi}(10)$ at $z = 1.27$.

Ω_0	$b_{g\rho}$	$b_{q\rho}(z=0)$	$\bar{\xi}_{qq}(10, z=0)$	$r_0(z=0)$
1	1	1.47 ± 0.16	2.16 ± 0.47	9.23 ± 1.11
1	2	2.38 ± 0.32	1.42 ± 0.38	7.30 ± 1.08
0.1	1	1.27 ± 0.23	1.62 ± 0.57	7.85 ± 1.54
0.1	2	2.31 ± 0.45	1.34 ± 0.52	7.08 ± 1.53
0.02	1	1.09 ± 0.25	1.19 ± 0.54	6.62 ± 1.68
0.2(Λ)	1	1.42 ± 0.29	2.00 ± 0.82	8.84 ± 2.00

The non-linear effects are at the 3 per cent level at 10 h^{-1} Mpc for $h = 1$ and at the 9 per cent level for $h = 0.5$. The CDM correlation function used here is normalized to fit a -1.8 power law at $z = 0$.

So at $\sim 10\ h^{-1}$ Mpc the linear approximation is close to the true mass evolution and in particular the error which might be caused by non-linearity is very much smaller than the errors for the QSO clustering amplitude. At smaller scales it would be possible to extrapolate the biasing model and use the non-linear evolution of $\bar{\xi}$ (Hamilton et al., 1991), but to use the linear biasing process at these scales would involve making very large assumptions about the mechanism of biasing, particularly when reaching scales where the clustering is strongly non-linear. The results of this analysis will be much more robust if only the linear regime is considered. Linear theory predictions can also be made in a general case with any value of Ω_0, so instead of $(1 + z)$ there is a general growth factor, $G(z, \Omega_0)$,

$$b_{q\rho}(z=0) = \left[\frac{\bar{\xi}_{qq}(z)}{\bar{\xi}_{gg}(0)}\right]^{1/2} b_{g\rho} - \frac{1}{G(z,\Omega_0)} + 1 \tag{3.28}$$

3.7 Predicted and Observed QSO Clustering at $r \sim 10\ h^{-1}$ Mpc

We wish to use the above model to find the equivalent present day clustering amplitude for QSOs, which can then be compared to the clustering amplitude of low redshift AGN as well as that of galaxies and other tracers of large-scale structure. Fig. 3.13 shows how the predicted $\bar{\xi}_{qq}(10)$ at $z = 0$ (based on the measured $\bar{\xi}_{qq}(10)$ at $z = 1.27$) varies as a function of $b_{g\rho}$ and Ω_0. Each result will correspond to a value of $b_{q\rho}$. Table 3.2 shows the calculated values of $b_{q\rho}(z = 0)$, $\bar{\xi}_{qq}(10, z = 0)$ and $r_0(z = 0)$ for $b_{g\rho} = 1$ and 2 and various Ω_0. With $\Omega_0 = 1$ and $b_{g\rho} = 1$, the present day QSO bias is $b_{q\rho} = 1.47 \pm 0.16$ but with $b_{g\rho} = 2$ this increases to $b_{q\rho} = 2.38 \pm 0.32$. These correspond to $\bar{\xi}_{qq}(10) = 2.16 \pm 0.47$ and 1.42 ± 0.38 respectively at $z = 0$. Higher

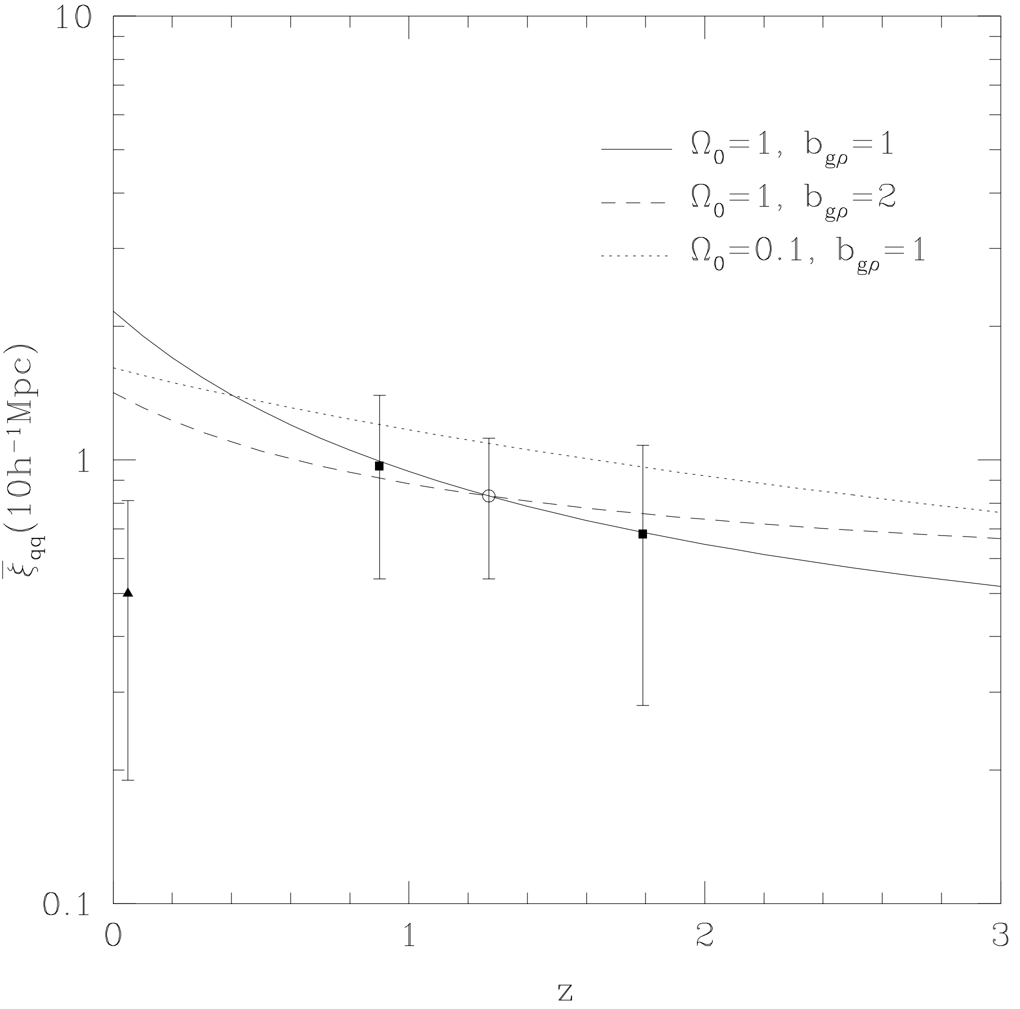

Figure 3.14: The expected evolution in our biasing model for $\Omega_0 = 1$, $b_{g\rho} = 1$ (solid line), $\Omega_0 = 1$, $b_{g\rho} = 2$ (dashed line) and $\Omega_0 = 0.1$, $b_{g\rho} = 1$ (dotted line). The points are the combined QSO clustering result $0.3 < z < 2.2$ (open circle), combined QSO clustering in two redshift bins $0.3 < z < 1.4$ and $1.4 < z < 2.2$ (filled squares), all assuming $\Omega_0 = 1$, and the low redshift AGN clustering amplitude (Georgantopoulos & Shanks 1994; Boyle & Mo 1993) (filled triangle). The $\Omega_0 = 0.1$ model is above the QSO data points as the measured QSO clustering assuming $\Omega_0 = 0.1$ is larger than that found when assuming $\Omega_0 = 1$.

biasing of galaxies (that is, a lower effective mass correlation function) or low Ω_0 reduces the amplitude of $\bar{\xi}_{\rm qq}(10, z = 0)$. Therefore the clustering amplitude of QSOs at the present is a maximum when $\Omega_0 = 1$ and $b_{\rm g\rho} = 1$. Taking these parameters and assuming a -1.8 power law gives a scale length $r_0(z = 0) = 9.23 \pm 1.11\ h^{-1}$ Mpc. This value is obviously significantly smaller than the value of $18 \pm 2\ h^{-1}$ Mpc discussed above (Mo & Fang, 1993); the difference is that we infer a QSO bias with respect to the mass distribution, which produces a slower rate of evolution, while Mo & Fang assume that the QSOs are unbiased. The QSO amplitude lies close to that of the galaxies for all but the $\Omega_0 = 1$, $b_{\rm g\rho} = 1$ case, and in all cases is significantly lower than the clustering amplitude associated with galaxy clusters, e.g., $r_0 = 14.3 \pm 2.35\ h^{-1}$ Mpc (Dalton et al., 1994).

By making the assumption that AGN at both high and low redshift belong to the same population it is possible to constrain further the evolutionary history of QSOs. Fig. 3.14 compares the clustering amplitude for a combination of the IRAS Seyferts (Georgantopoulos & Shanks, 1994) and EMSS QSOs (Boyle & Mo, 1993) at low redshift, with high redshift QSOs. The low redshift ($z \simeq 0.05$) data have $\bar{\xi}(10) = 0.50 \pm 0.31$. The $\Omega_0 = 1$, $b_{\rm g\rho} = 1$ model above gives $\bar{\xi}(10) = 2.16 \pm 0.47$ for high z QSOs evolved to the present day and these two values are inconsistent at the 2.9σ level. This then can be interpreted as a rejection of the $\Omega_0 = 1$, $b_{\rm g\rho} = 1$ scenario. Fig. 3.14 also shows that the $\Omega_0 = 1$, $b_{\rm g\rho} = 2$ case is only rejected at the 1.9σ level, as the predicted QSO amplitude at $z = 0$ is lower. For $\Omega_0 = 0.1$ and $b_{\rm g\rho} = 1$ the present day QSO clustering is estimated to be $\bar{\xi}(10) = 1.62 \pm 0.57$ which is only inconsistent with the low z clustering at the 1.7σ level. Therefore the slow evolution of QSO clustering is consistent to better than 2σ with either $\Omega_0 = 1$, $b_{\rm g\rho} = 2$ or $\Omega_0 = 0.1$, $b_{\rm g\rho} = 1$.

3.8 The QSO Clustering Amplitude Compared to *COBE* Normalized CDM

Using the combined QSO sample it is also possible to compare the QSO correlation function to the amplitude of CMB fluctuations from *COBE*, using parametric models of the mass correlation function to extrapolate from *COBE* scales to the region between 8 and 50 h^{-1} Mpc. In a sense, we are deriving the QSO bias directly from estimates of the mass fluctuations at very high redshift ($z \sim 1500$), using linear evolution and CDM to relate these fluctuations to our data. In the previous section, we derived values for the QSO bias by making comparisons to low redshift galaxies and Seyferts. We use the $8 - 50\ h^{-1}$ Mpc range, as at this scale, clustering is approximately linear, various different CDM type correlation functions show significant differences and the QSO $\xi(r)$ has relatively small errors. In particular we use the Fourier transform of the generic CDM power spectrum (Efstathiou et al., 1992) which is a good fit to a wide range of cosmologies in the linear regime,

$$P(k) = \frac{Bk}{\{1 + [ak + (bk)^{3/2} + (ck)^2]^{\nu}\}^{2/\nu}} \qquad (3.29)$$

where $a = (6.4/\Gamma)\ h^{-1}$ Mpc, $b = (3.0/\Gamma)\ h^{-1}$ Mpc, $c = (1.7/\Gamma)\ h^{-1}$ Mpc, and $\nu = 1.13$. The shape parameter Γ is equivalent to $\Omega_0 h$ for $\Omega_0 = 1$ CDM and flat CDM with a non-zero cosmological constant. The amplitude of the power spectrum, B, is normalized to the *COBE* two year quadrupole, $Q_{\rm rms} = 17.6 \pm 1.5\mu$K (Bennett et al., 1994). To convert this value to the power spectrum amplitude, B, we use the fact that the coefficients for the spherical harmonic expansion of the temperature fluctuations of the CMB are given by,

$$\langle |a_l^m|^2 \rangle = 4\pi^2 \left(\frac{H_0}{c}\right)^4 \left(\frac{\Omega_0}{D_0}\right)^2 \int_0^\infty P(k) j_l^2(kr) \frac{dk}{k^2} \tag{3.30}$$

(Peebles, 1993), where $P(k)$ is the present day power spectrum (Eq. 3.29), j_l is the spherical Bessel function of order l, r is the angular size distance defined in Eq. 3.8 and D_0 is the growth rate of mass perturbations normalized to an Einstein-de Sitter universe at $z = 0$. The comparison of the CDM models to the QSO correlation function is made at a mean redshift of $\bar{z} = 1.27$ so D_0 is replaced with $D(z = 1.27)$. D is a function of z and Ω_0 and is described by

$$D = \left(\frac{x}{x_0}\right) (x^3 + 1)^{1/2} \int_0^1 \frac{dy}{(1 + x^3 y^{6/5})^{3/2}}$$

$$x = \frac{(\Omega_0^{-1} - 1)^{1/3}}{1 + z} \tag{3.31}$$

for a universe with zero curvature (Peebles, 1984) (for other cosmologies this is given in Peebles (1980)). Assuming a scale invariant spectrum on *COBE* scales, that is $P(k) = Bk$, then

$$Q_{\rm rms} = \left(\frac{5C_2}{4\pi}\right)^{1/2} T_0 \tag{3.32}$$

where $C_2 = \langle |a_2^m|^2 \rangle$ and $T_0 = 2.735 \pm 0.006$K (Mather et al., 1990), so

$$B = \left(\frac{Q_{\rm rms}}{T_0}\right)^2 \frac{12}{5\pi} \left(\frac{c}{H_0}\right)^4 \left(\frac{D}{\Omega_0}\right)^2 \tag{3.33}$$

Once the power spectrum is normalized, it is a simple process to produce a corresponding $\xi(r)$, via

$$\xi(r) = 4\pi \int_0^\infty k^2 P(k) \frac{\sin(kr)}{kr} dk \tag{3.34}$$

To fit the above models for ξ to the QSO data there are two free parameters, Γ (the shape of $P(k)$) and the QSO bias. For this comparison we will be fitting the QSO data at $z = 1.27$, but will convert the bias measured at this redshift to the value of the QSO bias at the present, using the model described in Section 3.6. The rate of evolution, which is dependent on Ω_0, has to be assumed. Below, two cases are considered, one with $\Omega_0 = 1.0$, the second assuming $\Omega_0 = 0.2$ and $\lambda_0 = 0.8$. We

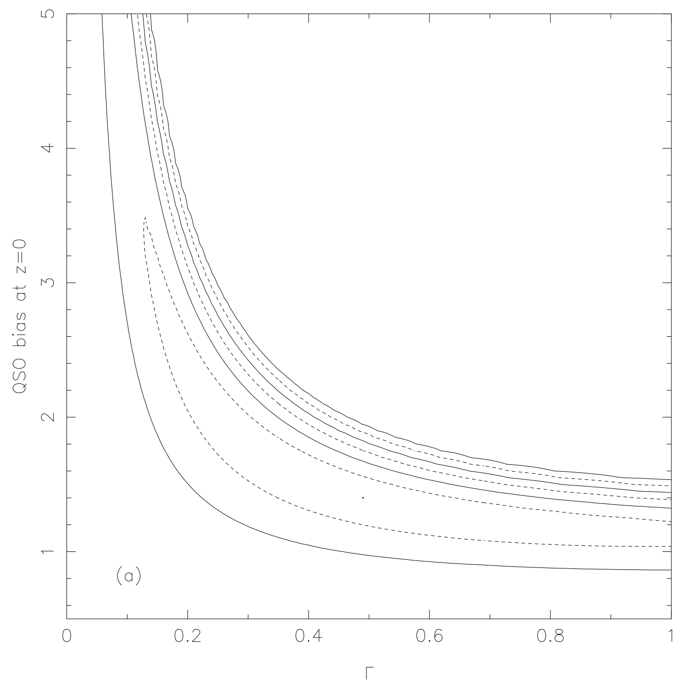

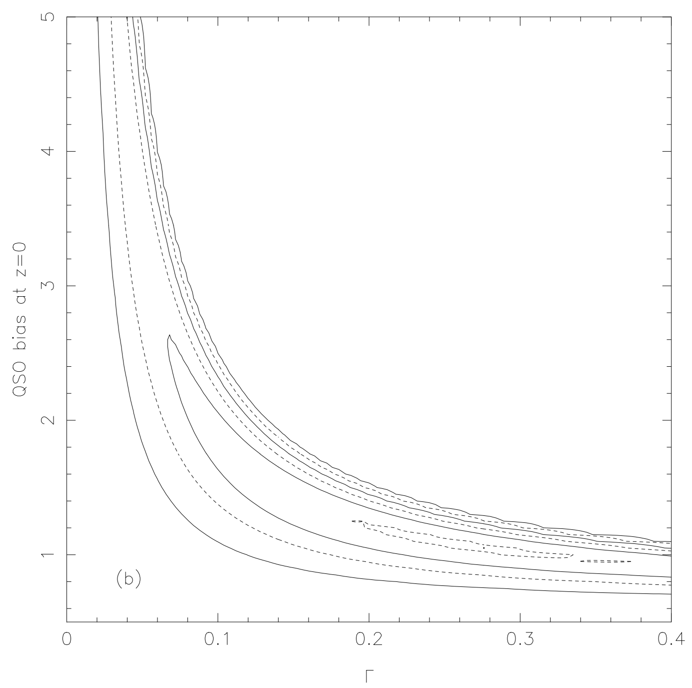

Figure 3.15: Confidence levels for fits of CDM type correlation functions to the combined QSO ξ with free parameters Γ and $b_{q\rho}$ for (a) $\Omega_0 = 1$, and (b) $\Omega_0 = 0.2$, $\lambda_0 = 0.8$. Dotted lines are 0.5σ intervals, solid lines are 1σ intervals.

search the parameter space in Γ and $b_{q\rho}$ to find the set of parameters which best fits the QSO clustering data on scales ~ 8 to $50\ h^{-1}$ Mpc. In all cases we fit the data without the CFHT 'supercluster'.

Fig. 3.15a shows the confidence contours for the $\Omega_0 = 1$ (so $\Gamma \sim h$) case. It is clear that it is not possible, with present statistics, to constrain both the amplitude and shape of the linear correlation function if both are allowed to vary freely. If Γ is constrained to a particular value then a statistically significant result for the bias can be obtained. Taking the value for standard CDM ($\Gamma = 0.5$), the best value of the present day QSO bias is $1.40^{+0.28}_{-0.43}$ and the 3σ upper limit is 1.93.

The same analysis with a different cosmology is shown in Fig. 3.15b which shows the confidence contours and best fit for the case of $\Omega_0 = 0.2$ and $\lambda_0 = 0.8$; here Γ only varies from $0 - 0.4$ (as $\Gamma = 0.2h$). Again, without first fixing one of the two parameters, the range of possible values for both parameters is not well constrained. A currently popular model is CDM with $\Gamma = 0.2$ and a cosmological constant (ΛCDM). Assuming this model, it is possible to obtain $b_{q\rho}(z=0) = 1.2^{+0.13}_{-0.18}$ and a 3σ upper limit of 1.53. In our discussion below we will compare the results found in this section with those of Section 3.6.

3.9 Discussion

3.9.1 Small scale clustering

Assuming a $\gamma = 1.8$ power law the value of $\bar{\xi}(10) = 0.83 \pm 0.29$ (for $\Omega_0 = 1$) implies $r_0 = 5.4 \pm 1.1\ h^{-1}$ Mpc. The best fit power law to the combined QSO data gives $r_0 = 4.00 \pm 1.14\ h^{-1}$ Mpc and $\gamma = 1.59 \pm 0.46$. These results are fully consistent with the present day galaxy value. This also agrees with the value found by Mo & Fang (1993) of $r_0 = 6.6 \pm 0.5\ h^{-1}$ Mpc, but is lower than the Andreani & Cristiani (1992) value of $r_0 \sim 10\ h^{-1}$ Mpc. It is not clear why this last result is higher. Andreani & Cristiani also find little evidence for evolution of clustering in comoving coordinates, consistent with the slow evolution described here.

The natural conclusion from assuming that Seyferts and QSOs come from a similarly clustered population is that their clustering does not evolve in comoving coordinates. The clustering amplitude of both populations is consistent with present day galaxy clustering, which suggests that QSOs randomly sample a comoving galaxy distribution on the scales that have been tested in this analysis, $\sim 10\ h^{-1}$ Mpc. Recent results from the cross-correlation of low redshift EMSS QSOs with APM galaxies (Smith et al., 1995), where the cross-correlation amplitude is found to be similar to the galaxy auto-correlation amplitude, also support the idea that QSOs randomly sample galaxies.

Section 3.6 describes a biasing model to test further the clustering evolution of QSOs. Assuming $\Omega_0 \leq 1$ this model gives an upper limit to the present day clustering of QSOs of $r_0(z=0) = 9.23 \pm 1.11\ h^{-1}$ Mpc. When we postulate that the low redshift Seyferts and the high redshift QSOs are clustered in the same way a strong constraint on the evolution of clustering is obtained, and hence a constraint on a combination of biasing and Ω_0. The case of $\Omega_0 = 1$, $b_{g\rho} = 1$ is ruled out at almost the 3σ level. $\Omega_0 = 1$, $b_{g\rho} = 2$ and $\Omega_0 = 0.1$, $b_{g\rho} = 1$ are consistent to better than 2σ with the QSO evolution. For very low Ω_0 ($\simeq 0.02$) we find consistency to $\sim 1\sigma$. Thus the evolution of QSO clustering over this redshift range seems to imply a low value of Ω_0 or a strongly biased galaxy distribution (and therefore a biased QSO distribution). It is difficult to argue that QSOs can be strongly biased compared to normal galaxies. The above biasing model shows that as biasing is increased, the rate of evolution is reduced, forcing the QSOs to have a similar amplitude to galaxies at the present time. A similar level of biasing is then required for both galaxies and QSOs.

3.9.2 Intermediate scale clustering

The QSO ξ is compared to a correlation function produced via a Fourier transform of the generic CDM power spectrum (Efstathiou et al., 1992) normalized to the CMB results from the two-year *COBE* data (Bennett et al., 1994). Because the shape of our correlation function is not well constrained, we are effectively comparing the QSO clustering amplitude to the CMB anisotropy amplitude. To do this we use a linear model power spectrum to extrapolate from *COBE* scales, to scales where we have a QSO clustering signal ($\sim 8 - 50\ h^{-1}$ Mpc). *COBE* normalized standard CDM, with $\Omega_0 = 1$ and $\Gamma = 0.5$, gives a best fit of $b_{q\rho}(z=0) = 1.40^{+0.28}_{-0.43}$; while for CDM plus a cosmological constant, $\Omega_0 = 0.2$, $\lambda_0 = 0.8$ and $\Gamma = 0.2$ we find $1.20^{+0.13}_{-0.18}$. The 3σ upper limits for these two models are 1.93 and 1.53 for standard CDM and ΛCDM respectively. From these values of the QSO bias we can calculate a present day QSO clustering amplitude, with which to compare the results found in Section 3.6, $\bar{\xi}(10, z=0) = 2.30^{+1.87}_{-1.22}$ and $\bar{\xi}(10, z=0) = 3.54^{+2.80}_{-2.46}$ for standard CDM and ΛCDM respectively. These values are higher than the low redshift AGN clustering result ($\bar{\xi}(10, z \simeq 0) = 0.50 \pm 0.31$), although the increased errors result in no significant inconsistency with the low redshift clustering of the AGN, or the $z = 0$ clustering of QSOs estimated from our biasing models.

Thus the fits to the intermediate scale QSO correlation function (at $z = 1.27$) prefer a low bias for $\Omega_0 = 1$ CDM with $\Gamma = 0.5$. This is in contrast to the small scale evolution results of Section 6 where a high bias is required for the $\Omega_0 = 1$ case. These data might be taken as evidence for low Ω_0, but the errors are still large, and there exists a narrow range where the two bias estimators overlap for $\Omega_0 = 1$. For ΛCDM we find a similar result, which also suggests fast evolution of clustering, again in contradiction (although not significantly) to the small scale evolution results. These results show that new surveys, such as the 2-degree Field QSO survey are vitally important, in order to reduce the large errors that exist presently.

3.9.3 Large scale clustering

The addition of the LBQS survey to the data used in Shanks & Boyle (1994) greatly increases our statistics at large scales, as the number of pairs per bin in the LBQS becomes greater than in the Durham/AAT sample at scales $> 100\ h^{-1}$ Mpc. On these scales the combined sample has errors of ± 0.025. This can be compared to previous estimates, for example, $\pm 0.1 - 0.15$ for a sample of 125 QSOs at $1.5 < z < 3.0$ (Osmer & Hewett, 1991). Looking at the region at $40 - 100\ h^{-1}$ Mpc, where an anti-correlation was seen in the Durham/AAT sample, there is no evidence that the LBQS (and similarly the CFHT and ESO/AAT surveys) shows this signal on these scales. The Durham/AAT is still found to have a negative signal in this region, in particular at $\simeq 89\ h^{-1}$ Mpc. A direct comparison between the LBQS and Durham/AAT samples produces a 2σ inconsistency at scales $40 - 100\ h^{-1}$ Mpc.

A combined sample of all surveys for $0.3 < z < 2.2$ gives us a ξ which is to first order consistent with a Poisson distribution on all scales larger than $40\ h^{-1}$ Mpc. There is a marginal signal at $\sim 100\ h^{-1}$ Mpc which could be tested by larger samples. The errors at large scales are such that we can provide the most accurate measurements of large-scale structure available at $> 100\ h^{-1}$ Mpc from redshift survey data.

Changing our assumed cosmology, some changes are seen in the correlation function. For $q_0 = 0.01$ the negative region at $\simeq 89\ h^{-1}$ Mpc moves out past $100\ h^{-1}$ Mpc and similarly for the $\Omega_0 = 0.03$, $\lambda_0 = 0.97$ case, this moves to $\sim 200\ h^{-1}$ Mpc. The Λ model, if incorrect, should be rejected by the change of scale of linear features in the correlation function. There are negative regions in the correlation function for this cosmology in both low and high redshift bins, but these features are at low signal to noise and do not appear to correspond to the same scale.

We compare the QSO clustering amplitude, $\bar{\xi}(25)$, in a cosmology with a cosmological constant, $\Omega_0 = 0.03$, $\lambda_0 = 0.97$, to a power law with $\gamma = 1.8$ and $r_0 = 6\ h^{-1}$ Mpc. These are inconsistent at the 2.9σ level. In this cosmology the linear growth rate from $z = 1.27$ to $z = 0.0$ is low, only a factor of 1.26, compared to 2.27 for $\Omega_0 = 1$. Therefore the evolution is approximately stable in comoving coordinates. So, if QSOs do randomly sample the galaxy distribution then this result rejects the above cosmology with a large cosmological constant.

3.10 Conclusions

We have analysed a total sample of > 1500 QSOs with $0.3 < z < 2.2$. In particular we have looked at the clustering in the LBQS survey and used a simple but self consistent model for biased clustering evolution. From this analysis the following conclusions can be drawn:

1. At small scales there is a marginal detection of clustering in the LBQS; $\bar{\xi}(10) =$

1.86 ± 1.28 (assuming $\Omega_0 = 1$). With $\Omega_0 = 0.1, 0.02$ and cases with cosmological constants there is no significant clustering in the LBQS. The combined sample has $\bar{\xi}(10) = 0.83 \pm 0.29$ for $\Omega_0 = 1$ (including re-analysed CFHT and ESO/AAT data). The results for other cosmologies are shown in Table 3.1. The LBQS is not an efficient sample to use for clustering at this scale due to its sparsely sampled nature.

2. At large scales the LBQS makes a significant contribution to clustering statistics. The LBQS does not support the anti-correlation found in the Durham/AAT survey at scales $40 - 100\ h^{-1}$ Mpc by SB94, but is only inconsistent at the 2σ level. At $> 100\ h^{-1}$ Mpc the upper limit on a detected signal is now at the ± 0.025 level, which constitutes the best limit so far on the homogeneity of the Universe on large scales (other than measurements from CMB experiments).

3. A model for biased clustering evolution based on the peaks-bias formalism (Bardeen et al., 1986) was used to derive a present day clustering amplitude for QSOs. In the case of $\Omega_0 = 1$ with an unbiased galaxy distribution, $\bar{\xi}(10) = 2.16 \pm 0.47$ for QSOs at $z = 0$. Assuming a -1.8 power law this is equivalent to $r_0 = 9.23 \pm 1.11$. If Ω_0 is decreased or galaxy biasing is increased this value will decrease. Hence this value of r_0 is an upper limit on the present day QSO clustering amplitude. This value is significantly lower than the clustering amplitude of rich galaxy clusters, and lower than a value for the present day clustering of QSOs calculated by Mo & Fang (1993) using evolution that assumes that QSOs trace the mass distribution.

4. If the low redshift AGN population and the high redshift QSO population are both clustered in the same way, then the clustering evolution is best fit by a slowly evolving model. The $\Omega_0 = 1$, unbiased galaxies model (see above) is then inconsistent with the clustering evolution at the $\sim 3\sigma$ level. The slow development of QSO clustering therefore implies low Ω_0 and/or high biasing.

5. Comparing the QSO ξ to linear theoretical predictions of CDM correlation functions, normalized to the CMB anisotropy (Bennett et al., 1994) with two free parameters (biasing and Γ), it is not possible to obtain a significant constraint on QSO biasing. Assuming a value of Γ this does become possible. For $\Omega_0 = 1$, $\Gamma = 0.5$ (standard CDM), $b_{q\rho}(z = 0) = 1.40^{+0.28}_{-0.43}$. For $\Omega_0 = 0.2$, $\lambda_0 = 0.8$, $\Gamma = 0.2$ (ΛCDM) the value found is $1.20^{+0.13}_{-0.18}$.

6. For a flat cosmology with $\lambda_0 = 0.97$, $\Omega_0 = 0.03$, the amplitude at $25\ h^{-1}$ Mpc is $\bar{\xi}(25) = 0.74 \pm 0.23$. This is inconsistent with $\xi = (r/6)^{-1.8}$ at the 2.9σ level, confirming the result obtained in Shanks & Boyle (1994). Assuming that high redshift QSOs randomly sample the galaxy population, this is a significant rejection of this inflationary $\Lambda > 0$ cosmology.

The small scale evolution and intermediate scale comparisons to the CMB (via CDM) could be used to imply low Ω_0. However, the data allow a range of acceptable values for bias in $\Omega_0 = 1$ CDM around $b_{q\rho} \simeq b_{g\rho} \simeq 2$. With the advent of new QSO samples with order of magnitude improvements in numbers, a combination of small scale evolution and comparison to the CMB will give us a great opportunity to independently discriminate between different values of biasing and Ω_0. For example, measuring the QSO power spectrum to *COBE* scales and comparing it to anisotropy in the CMB will give a direct measurement of QSO bias.

Chapter 4

A New UVX Catalogue for the 2-degree Field QSO Survey

4.1 Introduction - the need for a new QSO survey

As discussed in Chapter 1, QSOs are fundamental probes of the Universe at high redshift. Clustering statistics of present surveys (Chapter 3) are beginning to answer important cosmological questions. The ability to measure clustering at different epochs allows us to make estimates of the density parameter Ω_0, while geometric tests can be used to measure Λ, both of these parameters being fundamental to cosmology. Chapter 3 clearly showed that significantly larger QSOs surveys are required to obtain certain measurements of these parameters, in particular, a survey with a high number density of QSOs. It is the production of a large, deep, wide-field QSO survey that we turn to in this chapter.

The past decade has seen a vast increase in the number of known QSOs. These have been found using a variety of optical and non-optical selection methods. Optical selection methods can be divided into three areas, the first being selection based on low dispersion spectra obtained from objective prism plate surveys. This process allows a measure of the shape of the QSO candidate continuum, effectively an estimate of the colour, as well as the identification of broad emission lines, the latter being particularly useful for identifying high redshift, $z > 2$, QSOs in which the continuum is becoming redder. The advantages of this method include well defined selection for a given flux and spectral type and low levels of contamination by galactic stars. There are two main disadvantages; the first is that objective prism spectra from nearby objects will overlap, making the measurement of the continuum or lines difficult or impossible. The second disadvantage is that present objective prism surveys cannot expect to reach magnitudes fainter than $b_J \sim 19 - 20$, due to both the large relative sky flux in such observations and the increase in number density leading to overlapping spectra. However this method remains the most effective for detection of bright QSOs in samples such as the Hamburg/ESO survey

(Wisotzki et al., 1996) covering the magnitude range $13 \leq B \leq 17.5$, and the LBQS (Hewett et al., 1995) over the range $16 \leq b_{\rm J} \leq 18.5$.

Alternatively the selection process can be based solely on broad band colours. The first method of this type to be employed was the ultra-violet excess (UVX) technique (Schmidt & Green, 1983; Shanks et al., 1983b), which uses the extremely blue colour ($U - B < -0.3$) of QSOs to differentiate them from ordinary galactic stars. This has been applied in the Homogeneous Bright QSO Survey (Cristiani et al., 1995) to a depth of $B \simeq 18.75$, the Durham/AAT QSO survey (Boyle et al., 1990) to a depth of $B \simeq 21$, as well as many other samples. UVX selection has the advantage of being able to reach fainter magnitudes, although with a higher fraction of contaminating stars than in the objective prism method. For example, the Durham/AAT QSO sample contains a total of 420 QSOs along with 57 narrow emission line galaxies, spectroscopy of the candidates also found 824 galactic stars (including a number of white dwarfs), the best possible photometric accuracy is required to reduce this level of contamination. As well as the relatively high rate of contamination there are several selection effects to consider when using the UVX technique. As objects are only selected if they have a stellar point spread function (PSF), QSOs at low redshift can be rejected if their host galaxy is sufficiently bright to create a non-stellar PSF. At redshifts higher than $z = 2.2$ the Lyα emission line moves into the B band so that the QSOs generally have redder $U - B$ colours. The UVX selection can therefore only be complete below this redshift. Within these constraints the UVX selection technique is consistent in selecting the vast majority ($> 95\%$) of QSOs detected via other selection methods. To reach higher redshifts multi-colour selection procedures are used, such as $B - R$ vs. $U - B$ (Shanks et al., 1983a; Warren et al., 1987; Boyle et al., 1991). Multi-colour photometry also further reduces stellar contamination, as an increase in the number of bands observed allows tighter constraints to be placed on the spectral energy distribution (SED) of the QSOs. A detailed discussion of multi-colour QSO selection is given by Warren et al., (1991).

A third optical selection process is based on QSO variability. QSO luminosities are known to vary over a large range of time scales. By using the long baseline provided by photographic plate archives it is possible to detect these variations (Koo et al., 1986; Veron & Hawkins, 1995). Problems with this method lie in the luminosity dependence of the variability (Cristiani et al., 1996) and the uncertain completeness, with surveys based on variability generally producing lower number densities of QSOs than the UVX selection method. QSO variability will also have an effect on colour selection methods, which we will discuss further in Section 4.3.

The very first QSOs discovered were found on the basis of their strong radio flux (Schmidt, 1963). However it was soon apparent that the majority of QSOs ($> 90\%$) did not show this radio emission but were radio-quiet. New deep radio surveys such as the FIRST Bright QSO survey (Gregg et al., 1996) reach to deeper flux levels and are starting to find *radio-quiet* objects. 50% of the QSOs in the FIRST sample are radio-quiet (as opposed to radio silent), that is $L_{\rm 21cm} < 10^{32.5}{\rm ergs}^{-1}$. All-sky X-ray surveys have also produced significant numbers of QSOs, these include the Einstein

Extended Medium Sensitivity Survey (EMSS) (Stocke et al., 1991) and the ROSAT All-Sky Survey (Bade et al., 1995). There are also a number of deeper ROSAT pointings in particular regions of the sky (Shanks et al., 1991; Boyle et al., 1993).

This combination of selection techniques has provided a total of ~ 9000 QSOs (Veron-Cetty & Veron, 1996), a collection of QSOs which is, of course, completely inhomogeneous, and as such cannot be used as a whole for a range of statistical tests. To carry out tests on clustering in particular it is imperative to start with a homogeneous sample. Clustering studies are also highly dependent on the space density of QSOs. It was noted in Chapter 3 that the LBQS was not an ideal sample with which to study clustering, the surface density of QSOs in this sample being a factor of ~ 20 lower than in the Durham/AAT QSO survey. It is therefore imperative that the depth of any QSO survey to be used for clustering analysis reaches at least the magnitude of the turnover in the number-magnitude relation for QSOs, (Eqs. 3.1 and 3.2), at $B \sim 19.5^m$. A large contiguous area is also important for measurements of large-scale structure, allowing the complete sampling of a large volume, and the matching of photometry across the catalogue.

The new 2-degree Field (2dF) instrument on the Anglo-Australian telescope is a multi-object fibre-fed spectrograph, which can obtain spectra for ~ 400 objects at a time over a field of view fully 2 degrees in diameter. This huge multiplexing gain opens the door to a new generation of redshift surveys an order of magnitude larger in size than previously possible. To take advantage of this instrument a large wide-field catalogue of QSO candidates was needed. Not only this, but to obtain maximum scientific gain from the survey, this catalogue should be uniform, complete and photometrically accurate. To obtain a sufficient number density of QSOs a colour selection process was required, and the only method available to cover sufficient area was the use of photographic plates. The UVX selection method was an obvious choice, being proven to select the overwhelming majority of QSOs at redshifts $z < 2.2$.

Below we describe the construction of the 2dF QSO survey input catalogue, in particular the southern strip at $\delta = -30°$. A similar northern strip was constructed by Robert Smith (IoA, Cambridge) using the same process. We paid particular attention to the correction for plate field effects and obtaining accurate and reliable CCD photometric sequences with which to calibrate and linearize our photographic magnitudes. We have also estimated the level of completeness we expect from the distribution of all the known QSOs which lie in our survey region. We will discuss several factors which may contribute to incompleteness.

Table 4.1: Details of the UKST III-aJ survey plates used in the Southern 2dF QSO survey.

UKST field	Plate No.	R.A.(B1950)	Dec. (B1950)	Date
f466	J5113c	21 51 00	-30 00 00	25/06/79
f467	J3514cc	22 14 00	-30 00 00	18/08/77
f468	J6436	22 37 00	-30 00 00	30/09/80
f469	J3508	23 00 00	-30 00 00	17/08/77
f470	J3525c	23 23 00	-30 00 00	18/08/77
f471	J6138	23 46 00	-30 00 00	17/07/80
f409	J2693c	00 00 00	-30 00 00	17/11/76
f410	J2696c	00 23 00	-30 00 00	18/11/76
f411	J4606c	00 46 00	-30 00 00	25/10/78
f412	J3516c	01 09 00	-30 00 00	18/08/77
f413	J3774c	01 32 00	-30 00 00	03/12/77
f414	J3579c	01 55 00	-30 00 00	15/09/77
f415	J4607c	02 18 00	-30 00 00	25/10/78
f416	J4608c	02 41 00	-30 00 00	25/10/78
f417	J3818c	03 04 00	-30 00 00	12/12/77

4.2 Producing a Homogeneous UVX Catalogue

For the reasons discussed above we wish to produce a deep, uniform UVX catalogue to use as a candidate list for the 2dF QSO survey. The selection procedure is based on scans of $6° \times 6°$ United Kingdom Schmidt Telescope (UKST) III-aJ and U plates scanned by the Automatic Plate Measurement (APM) facility at the Royal Greenwich Observatory (RGO), Cambridge. Table 4.1 gives details of the UKST III-aJ plates used. These are part of the 1st Epoch UKST Sky Survey and use the III-aJ emulsion in conjunction with a Schott GG395 filter to produce the blue photographic passband which we will denote as $b_{\rm J}$. The conversion between this band and the standard Johnson-Kron-Cousins photometric system is given by

$$b_{\rm J} = B - 0.28(B - V) \tag{4.1}$$

(Blair & Gilmore, 1982) where B and V denote the standard passbands. The U plates have mostly been obtained over a period of ~ 5 years, in preparation for this survey. A large number of these exposures have been taken on film, rather than glass plate. In both cases the UG1 filter was used, in conjunction with the III-aJ or 4415 emulsion for plates or films respectively. Blair & Gilmore also measure the colour transform from the standard photo-electric system to photographic u, finding

$$u = U - 0.03(U - B) \tag{4.2}$$

where u is the photographic system, although here this is defined by the IIa-O emulsion and the UG1 filter. The error on the colour term in this case is ± 0.05, so given that the colour term is not significant we shall define our photographic u-band magnitudes as $u = U$, where U is the standard photo-electric magnitude. Table 4.2 gives details of the u plates. Multiple plates were obtained in each survey area in order to, (i) ensure at least one good quality plate reaches the depth of the survey and (ii) allow us to use co-addition of the image intensities, in order to reduce the intrinsic r.m.s. scatter of the magnitudes at faint limits. As can be seen from Table 4.2 the depth of the plates is varied, from $u = 19.4$ in the very worst case to $u = 21.6$ for the best two plates. A small number of plates (four in all) were not scanned, due to trailing and other plate defects.

Table 4.2: Details of the UKST u plates used in the Southern 2dF QSO survey. Exposures labelled (f) are films, those marked * are poor quality and were not scanned

UKST Field	Plate No.	R.A.(B1950)	Dec. (B1950)	Date	Exposure time	Plate limit
f466	U15162(f)	21 51 00	-30 00 00	17/09/92	1800	20.7
	U15167(f)	21 51 00	-30 00 00	18/09/92	1800	20.3
	U15222(f)	21 51 00	-30 00 00	20/10/92	1800	20.4
	U15226	21 51 00	-30 00 00	21/10/92	1800	21.5
f467	U15706	22 14 00	-30 00 00	18/08/93	1800	21.2
	U15718(f)	22 14 00	-30 00 00	20/08/93	1800	21.4
f468	U15169(f)	22 37 00	-30 00 00	20/09/92	1800	20.8
	U15170	22 37 00	-30 00 00	20/09/92	1800	20.9
	U15750	22 37 00	-30 00 00	07/09/93	1800	21.4
	U16781*	22 37 00	-30 00 00	20/09/95	900	-
	U16840(f)	22 37 00	-30 00 00	23/10/95	1000	21.2
f469	U15231	23 00 00	-30 00 00	22/10/92	1800	21.6
	U15235(f)	23 00 00	-30 00 00	01/11/92	1225	19.8
	U15642(f)	23 00 00	-30 00 00	26/07/93	1800	21.2
f470	U1776	23 23 00	-30 00 00	14/08/75	900	20.1
	U15654(f)	23 23 00	-30 00 00	28/07/93	1800	19.4
	U15724	23 23 00	-30 00 00	21/08/93	1800	21.6
	U16730(f)*	23 23 00	-30 00 00	21/08/95	670	-
	U16838(f)	23 23 00	-30 00 00	22/10/95	900	19.8
	U16843(f)	23 23 00	-30 00 00	27/10/27	900	20.9
f471	U15733	23 46 00	-30 00 00	22/08/93	1800	21.4
	U15738(f)	23 46 00	-30 00 00	23/08/93	1800	21.0
f409	U1833	00 00 00	-30 00 00	04/10/75	900	19.8
	U16247(f)	00 00 00	-30 00 00	14/08/94	900	20.4
	U16812(f)	00 00 00	-30 00 00	14/10/95	900	20.8
f410	U16743(f)	00 23 00	-30 00 00	25/08/95	900	20.5
	U16813(f)	00 23 00	-30 00 00	14/10/95	900	20.8
	U17246(f)	00 23 00	-30 00 00	13/09/96	900	20.6
f411	U14503	00 46 00	-30 00 00	01/09/91	1800	20.3
	U15202(f)	00 46 00	-30 00 00	01/10/92	900	20.6
	U15223(f)	00 46 00	-30 00 00	20/10/92	900	20.5
	U15227(f)	00 46 00	-30 00 00	21/10/92	900	20.7

Table 4.2: u plates: continued

UKST Field	Plate No.	R.A.(B1950)	Dec. (B1950)	Date	Exposure time	Plate limit
	U15719(f)	00 46 00	-30 00 00	20/08/93	900	21.0
f412	U13970	01 09 00	-30 00 00	06/11/90	1800	19.3
	U16335(f)	01 09 00	-30 00 00	03/10/94	900	21.0
	U16340(f)	01 09 00	-30 00 00	05/10/94	900	21.3
	U16389(f)	01 09 00	-30 00 00	08/11/94	900	21.3
f413	U16751(f)	01 32 00	-30 00 00	17/08/95	900	20.5
	U16814(f)	01 32 00	-30 00 00	14/10/95	900	19.8
	U17263(f)	01 32 00	-30 00 00	15/09/96	900	20.9
f414	U16751(f)	01 55 00	-30 00 00	27/08/95	900	20.6
	U16782(f)	01 55 00	-30 00 00	21/09/95	900	20.6
	U16824(f)	01 55 00	-30 00 00	16/10/95	900	21.1
f415	U16427(f)	02 18 00	-30 00 00	02/12/94	900	20.9
	U16744(f)	02 18 00	-30 00 00	25/08/95	900	20.9
f416	U2830*	02 41 00	-30 00 00	19/01/77	900	-
	U7348	02 41 00	-30 00 00	22/11/81	900	20.3
	U16903(f)	02 41 00	-30 00 00	24/12/95	900	20.7
	U16905(f)	02 41 00	-30 00 00	25/12/95	900	20.9
	U17248(f)	02 41 00	-30 00 00	13/09/96	900	21.2
f417	U15251	03 04 00	-30 00 00	27/11/92	1173	20.8
	U15273	03 04 00	-30 00 00	28/12/92	1800	21.5
	U15274(f)	03 04 00	-30 00 00	29/12/92	1800	20.3
	U16839(f)*	03 04 00	-30 00 00	22/10/95	900	-

The APM is a high speed micro-densitometer which is combined with a computer system which performs on-line image detection and analysis. The scanning laser samples a plate on a grid of positions at $\sim 8\mu$m separation. The detection algorithm identifies groups of connected pixels with densities higher than a given threshold above the local sky. This sky value is obtained from a preliminary scan, in which groups of 64×64 pixels are taken and the modal value found, these values produce the background map. The image analysis software then calculates a number of parameters for each image, including position, isophotal intensity, areal profiles and intensity weighted moments. These parameters were used in the next stage of analysis, which utilized the standard APM reduction software written by Dr. M. Irwin. The program `STATS` takes the moments, area and intensity of each image and uses them to perform a classification of images into noise, stellar, non-stellar and merged objects. Program `APMCAL` was then used to linearize stellar magnitudes and check the classification process. Multiple plate scans from the same field area were then combined using `MERGE`, and the astrometry was matched to the B1950 coordinates of the PPM astrometric catalogue (Bastian & Roeser, 1993) using `CHECK`.

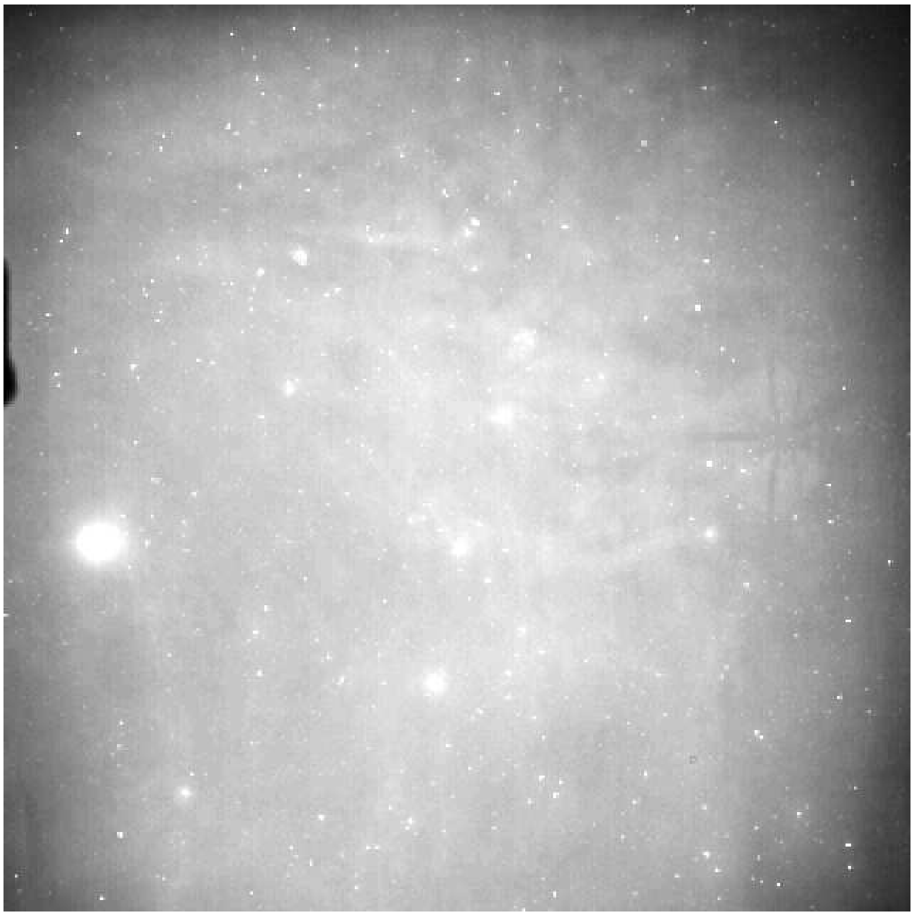

Figure 4.1: Background map for the APM scan of UKST plate $J4606c$ in the F411 field. On the far left the effect of a step wedge can be seen. A number of bright stars are also obvious.

4.2.1 Correcting field effects on photographic plates

The APM measures a $\sim 5.8° \times 5.8°$ region of each UKST plate or film. Ideally we would use the whole of this area to construct the UVX catalogue, however, various *field effects* which are a function of position on the plate make this impossible; we use the central $5° \times 5°$ in construction of the catalogue. These field effects have two main sources, the first is the geometric vignetting of the telescope, causing a decrease in throughput for images which are progressively further off-axis. The second contribution is from *variable desensitisation* (Dawe & Metcalfe, 1982); the III-aJ emulsion is hypersensitized by soaking in hydrogen and nitrogen gases, a process which is gradually reversed by the action of water vapour and oxygen in the atmosphere. The UKST plate holder allows greater circulation of air at the plate edges, and so desensitisation occurs preferentially at these edges. The plate holder was modified in 1982, so that the plate surface was flushed with nitrogen gas during exposures. However, all the J plates used for the Southern UVX catalogue were taken before this upgrade.

The threshold for each scan is set to a constant value above the local sky value.

Therefore, in areas of strong vignetting, objects begin to fall below this threshold (a more correct method would be to define the threshold as a fractional value above the local sky, if the true sky intensity did not vary appreciably across the plate), and intensities are systematically reduced. Therefore a correction to the image intensities as a function of plate position needs to be made. This was done in the case of the APM Galaxy Survey (Maddox, 1988) by using the correlation between sky intensity (from background maps) and object numbers averaged over a large number of plates. A background map of an APM scan clearly shows the field response function. Fig. 4.1 shows the background map for plate J4606c in the f411 field, where the vignetting towards the corners is particularly obvious.

The final catalogue will only contain objects classified as stellar by the APM software. To correct the b_J stellar magnitudes for the field response function we have developed a method based on that of Maddox (1988). Below I will outline this process which was produced in collaboration with Robert Smith at the Institute of Astronomy, Cambridge, who developed a large fraction of the software for this correction procedure:

1. The number density of stellar objects increases as magnitudes become fainter, fitting this function allows us to relate the change in number density to a magnitude correction. We fit a quadratic function to the data in magnitude-Log(number) space, where the magnitudes are APM instrumental magnitudes, $m_{\rm APM} = 2.5 \log(\text{APM intensity})$. At the plate edges the number-magnitude relation will be altered by the field effects that we are trying to correct, so only the central $4° \times 4°$ of each plate is used for finding the relation.

2. There are several regions on each plate which could not be used, mostly due to the halos of bright stars. Data in these areas were cut out of the sample and not used at any stage in the analysis, as they would be likely to have both erroneous magnitudes and background densities.

3. Each scan of our III-aJ plates was divided into a 32×32 grid. The number density of stellar objects in each of these grid cells was measured in magnitude bins (spaced logarithmically to obtain similar numbers of stars in each bin). The background density for the cell was also measured from a median filtered (to remove bright stars, see Fig. 4.1) background map of the scan. The number density was converted to a magnitude correction, relative to the centre of the plate using the number-magnitude relation.

4. The magnitude variation vs. background density data from each plate was then combined into one data set. This has the effect of removing any real structure in the stellar distribution, which, although less than that shown by galaxies (Maddox, 1988), would have a significant effect if the correction had been attempted on a plate by plate basis. A smooth surface is then fitted to the data, to obtain a correction which is dependent on both magnitude and background. All thirty III-aJ plates were combined in this process, 15 from the southern strip and 15 from the north. It was found that 3 plates in the Southern region (J5113, J6138 and J3818 in the f466, f471 and f417

fields respectively) showed a correlation that was significantly different from the plates in the rest of the sample. Data for these three plates were combined separately from the other 27 plates, and used to correct the plates in question.

5. The QSO candidates were to be selected on the basis of $u - b_J$ colour. To remove any residual vignetting and to correct any colour gradient in the plates we correct the u magnitudes, such that the distribution of colours over the area of the plate is uniform.

6. After the photographic magnitudes were calibrated (see below), the u magnitudes from individual plates were co-added, in order to reduce the r.m.s scatter in the u band photometry.

A detailed description of this process can be found in Smith (1997) .

4.2.2 CCD photometry of stellar sequences

Accurate photometric calibration is of vital importance in a survey of this kind, where colour is the basis of the selection procedure. In order to obtain this calibration we have observed a number of deep CCD sequences covering all of the Southern 2dF fields (similar data were obtained for the Northern survey area).

Observations of all the sequence fields were carried out using the Tek#3 CCD mounted at Cassegrain focus on the 0.9m telescope at Cerro Tololo Inter-American Observatory (CTIO) in two separate observing runs, from 23 – 27 August 1995 (observers: A. Ratcliffe and Q.A. Parker) and 15 – 20 September 1996 (observer: S.M. Croom). The Tek#3 CCD is a 2048×2048, thinned, AR coated device with low read noise and good QE in the U band. Readout is controlled by the ARCON system, which has four separate amplifiers allowing quad readout, giving quick readout times, $\sim$ 40s. The pixel scale is 0.396 arcsec pixel^{-1} giving a large $13.5' \times 13.5'$ field of view, allowing us to obtain magnitudes for a large number of stars $\sim$ 100 in each frame. The specific sequence areas were chosen to have a broad range of stellar magnitudes. During the first observing run B and R sequences were obtained for 14 of our 15 fields. During the second run we obtained $UBVR$ sequences in three fields including the one field previously unobserved, a list of fields observed is given in Table 4.3. Filters used for these observations were the standard CTIO $UBVR$ 3×3 inch filters, BVR being similar to the Harris BVR set, U uses a Copper Sulphate solution blocker. Magnitude zero-points, extinction and colour terms relating the instrumental magnitudes to the standard Johnson-Kron-Cousins system were obtained from frequent observations of standard stars from the E-field standards at $\delta = -45°$ (Graham, 1982). All observations of the sequence fields were made at low airmass, $\sec(z) \leq 1.34$.

Removal of the instrumental signature of the CCD from the images was carried out using the **ared.quad.quadproc** and **imred.ccdred.ccdproc** tasks in the IRAF package. **quadproc** is a variant of **ccdproc** specifically designed to reduce data from

Table 4.3: Data on all CCD sequence fields. $B_{\rm lim}$ is the limiting magnitude for 0.05mag photometric errors.

Field name	R.A.(B1950)	Dec. (B1950)	date	bands	$B_{\rm lim}$
f466-1	21 53 09.0	-29 33 46.0	24/08/95	BR	21.1
f467-1	22 06 17.0	-27 39 23.0	26/08/95	BR	20.7
f468-1	22 29 37.0	-31 27 40.0	25/08/95	BR	20.9
f469-1	23 03 00.0	-30 55 14.0	25/08/95	BR	21.2
f470-1	23 16 59.0	-29 47 52.0	25/08/95	BR	20.8
f471-1	23 45 03.0	-28 25 09.0	25/08/95	BR	21.2
f409-1	23 58 39.0	-27 50 31.0	25/08/95	BR	21.1
f410-1	00 34 16.0	-29 48 05.0	26/08/95	BR	21.0
f411-1	00 48 54.0	-28 46 39.0	26/08/95	BR	21.2
f412-1	01 14 27.0	-28 50 55.0	26/08/95	BR	20.8
f413-1	01 32 06.0	-31 53 51.0	26/08/95	BR	20.8
f414-1	02 04 19.0	-28 32 57.0	25/08/95	BR	21.2
f415-1	02 18 38.0	-32 07 57.0	24/08/95	BR	21.2
f417-1	03 10 24.0	-28 01 59.0	26/08/95	BR	21.2
f466-2	21 51 23.0	-30 05 00.0	15/09/96	$UBVR$	20.8
f409-2	00 00 23.0	-29 38 59.0	15/09/96	$UBVR$	20.8
f416-2	02 45 24.0	-30 31 00.0	15/09/96	$UBVR$	20.9

the multi-readout ARCON system. This software removes the instrumental bias and also corrects bad columns and pixels (of which there are a number in the Tek#3 CCD) as well as flat fielding each frame. In each passband we obtained both dome flats taken during the day and sky flats taken at twilight. It was found that both dome and sky flats adequately corrected small scale variations in pixel sensitivity. However, division by dome flats generally left a residual large scale gradient across the image. This gradient was at the 5% level in many cases, therefore we used the sky flats, which flattened the images to the 1% level. At least 5 separate exposures were used to generate each flat-field. These were median combined using 3σ clipping to remove cosmic ray events (CREs).

We used the IRAF task **digiphot.daophot.phot** to obtain photometry of all the E-field standard stars observed. We used 25-pixel ($10''$) radius apertures centred on each standard star to obtain their instrumental magnitudes, which we denote by $U_{\rm CCD}$, $B_{\rm CCD}$, $V_{\rm CCD}$ and $R_{\rm CCD}$; the instrumental magnitude is simply,

$$m_{\rm CCD} = -2.5\log(f) + 2.5\log(t) \tag{4.3}$$

where f is the flux and t the exposure time. The sky background value was obtained from the mode of an annulus between 35 and 50 pixels in radius. The IRAF task **digiphot.photcal.fitparams** was used to obtain the magnitude zero-points, colour and extinction terms. For the first set of data (BR sequences) we assumed standard extinction values for Cerro-Tololo: $A_{\rm B}$ = 0.209 mag airmass^{-1}, $A_{\rm R}$ = 0.108 mag airmass^{-1}. For these data the maximum airmass reached was 1.341 in $R_{\rm CCD}$ and 1.292 in $B_{\rm CCD}$, with over 50% of the observations obtained at airmasses of less than 1.1; therefore even in the most extreme cases this assumption would cause a zero-point error of less than 0.01 mag. For the second set of data ($UBVR$ sequences) we calculated the extinction terms from the standard observations made; these were $A_{\rm U}$ = 0.453 mag airmass^{-1}, $A_{\rm B}$ =0.232 mag airmass^{-1}, $A_{\rm V}$ = 0.131 mag airmass^{-1} and $A_{\rm R}$ = 0.113 mag airmass^{-1}. Inverse colour equations were fitted giving

$$\begin{aligned} B_{\rm CCD} &= B - 22.442 + 0.209\sec(z) + 0.095(B-R) \quad \text{r.m.s.} = 0.003 \\ R_{\rm CCD} &= R - 22.566 + 0.108\sec(z) + 0.006(B-R) \quad \text{r.m.s.} = 0.004 \end{aligned} \tag{4.4}$$

for the first set of observations while the second set of observations gave

$$\begin{aligned} U_{\rm CCD} &= U - 20.240 + 0.453\sec(z) - 0.035(U-B) \quad \text{r.m.s.} = 0.014 \\ B_{\rm CCD} &= B - 21.800 + 0.232\sec(z) + 0.110(B-V) \quad \text{r.m.s.} = 0.014 \\ V_{\rm CCD} &= V - 22.030 + 0.131\sec(z) - 0.019(B-V) \quad \text{r.m.s.} = 0.007 \\ R_{\rm CCD} &= R - 21.992 + 0.113\sec(z) - 0.002(V-R) \quad \text{r.m.s.} = 0.005 \end{aligned} \tag{4.5}$$

The sequence fields were combined using **imcombine** with the **crreject** algorithm used to reject CREs. In the case of single exposures on a field (as was the case for data from the first run), we used the image detection routines, and the matching of images in different bands to reject cosmic ray events. All images with peak counts higher than a 5σ threshold above the sky background were selected using **daofind**. Aperture photometry was obtained for these objects using **phot** within 10 and 25 pixel apertures. The larger aperture, corresponding to $10''$ radius, is the same as that used for our standard observations and defines the zero-point for our magnitude system. The median seeing during the observations was $1.5''$ and was rarely above $2.0''$. At faint fluxes the sky counts add considerable noise within an aperture of this size. For this reason we obtained magnitudes within a 10 pixel aperture and then corrected this magnitude to the 25 pixel magnitude scale using the brightest unsaturated stars (at least 8 per field) with no close companions in each field to define the aperture correction, which was typically $\sim$ 0.03 mag. The aperture corrected instrumental magnitudes were then converted to the standard $UBVR$ system using the **invertfit** task and the colour equations derived above. The Poisson photometric errors were plotted as a function of magnitude (e.g. Fig. 4.2) in order to estimate the effective limiting magnitude of the standard observations in each field (in this case the magnitude at which the photometric errors reach 0.05 mag). The limiting B band magnitudes are shown in Table 4.3.

The brightest 10 unsaturated stars in each field were matched to their positions on the APM scans of the UKST III-aJ survey plates which in turn have been matched to the PPM (B1950) (Bastian & Roeser, 1993) astrometric catalogue. These stars were then used to derive a transform from CCD (x, y) positions to (α, δ) using the STARLINK ASTROM software.

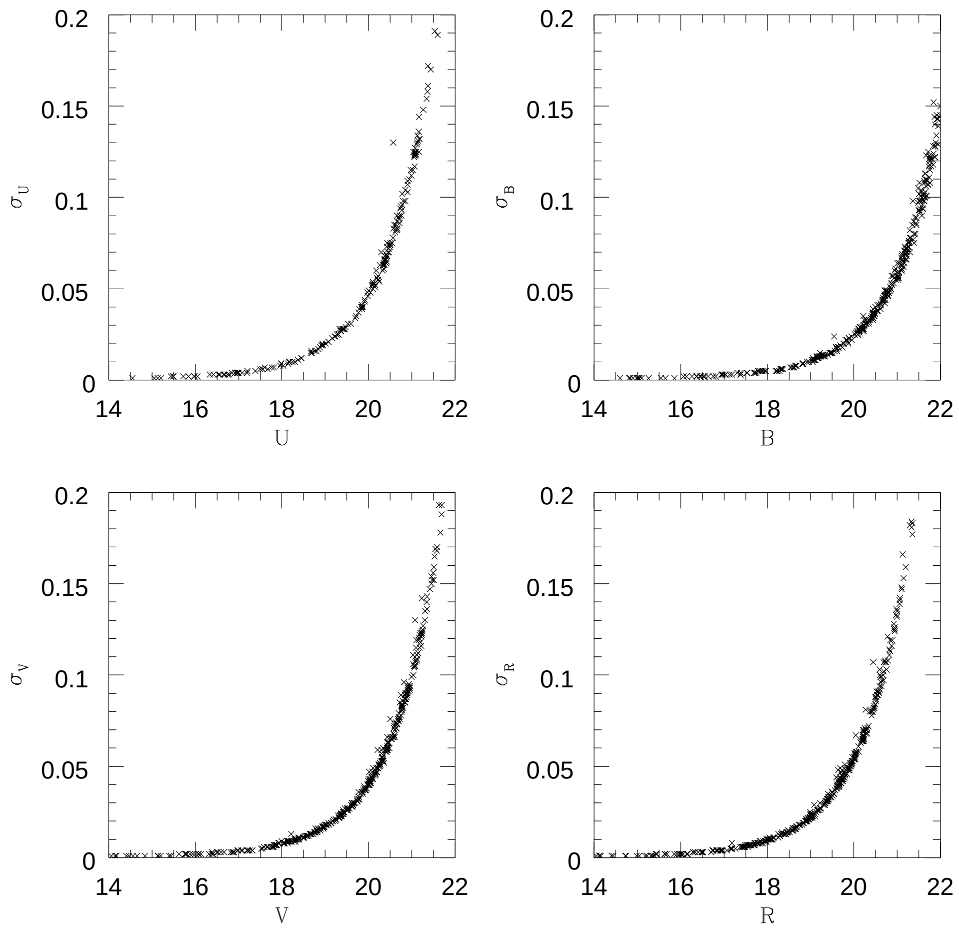

Figure 4.2: Poisson photometric errors for $UBVR$ bands in the f466-2 CCD field.

4.2.3 Calibrating photographic plates with CCD sequences

We obtain an equivalent calibrated b_J magnitude for each target CCD star using the colour equation in Eq. 4.1. In the case of data from the first run, in which we only observed in the B and R bands it was first necessary to convert the colour term from $(B-V)$ to $(B-R)$, which was done using the relation

$$(B-R) = 1.54(B-V) \tag{4.6}$$

(Metcalfe et al., 1991), which was derived from the Landolt (1983a,b) standard stars. Fig. 4.3 shows this relation plotted against the E-Field standards used in our observations. All the objects with b_J magnitudes in our CCD fields were matched to the APM scans of the III-aJ plates. The objects classified as stellar on the scans were taken and the relation between $m_{\rm APM}$ (after being corrected for field effects) and $b_J(CCD)$ was fitted with a quadratic function. This function was used to convert the non-linear instrumental photographic magnitudes to the linear magnitude system. The data and fits for all 15 Southern III-aJ plates are shown in Fig. 4.4. To obtain a

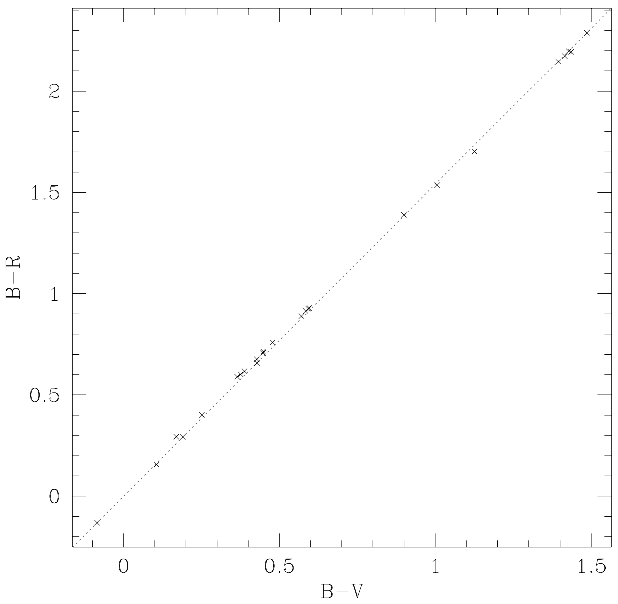

Figure 4.3: Plot of $(B-R)$ vs. $(B-V)$ colour for the E-Field standard stars used. The dotted line is the relation in Eq. 4.6.

uniform photometric system over each survey strip we then attempted to match the calibrated magnitudes in the overlaps between each plate, and correct the individual plate zero-points to obtain a zero-point defined by the f470/f471 plates which have the smallest offsets of any plate pairing. The zero-point offsets for all plates are listed in Table 4.4. It is possible that this process will actually add systematic errors to the survey photometry, as it utilizes the poorer areas of the photographic plates to obtain the relative plate zero-points. Below we shall make several checks to ascertain if this is the case, before deciding whether to use the overlap corrections or direct CCD calibration in the final catalogue. In the first instance we will simply use the direct CCD calibration.

Until now we have only discussed the photometric calibration of the III-aJ plates. It is obvious from Table 4.3 that we do not have U_{CCD} sequences in all of our survey fields. However, these are not necessary in order to calibrate the photographic u band photometry. In each field area we have several tens of thousands of stellar images with both u and b_{J} magnitudes. A large fraction of these images are blue galactic stars which follow a straightforward relation in the $(u-b_{\mathrm{J}})$ vs. b_{J} plane. This blue stellar ridge-line has been shown to remain at a constant $(u-b_{\mathrm{J}})$ colour as a function of b_{J} magnitude (Boyle, 1986). We shall assume $(u-b_{\mathrm{J}})_{\mathrm{ridge-line}}=0$; this is probably correct to ±0.2 mag. Fitting this relation allows us to bootstrap from our b_{J} magnitudes to obtain a photometric zero-point in our u band. It can be seen from Table 4.2 that we have several available u plates in each UKST field area. To improve the r.m.s. error in the photographic magnitudes, particularly at magnitudes near to the plate limit, we co-add the calibrated intensities of matched objects for all plates which reached a depth of at least $u=20.8$ in each field.

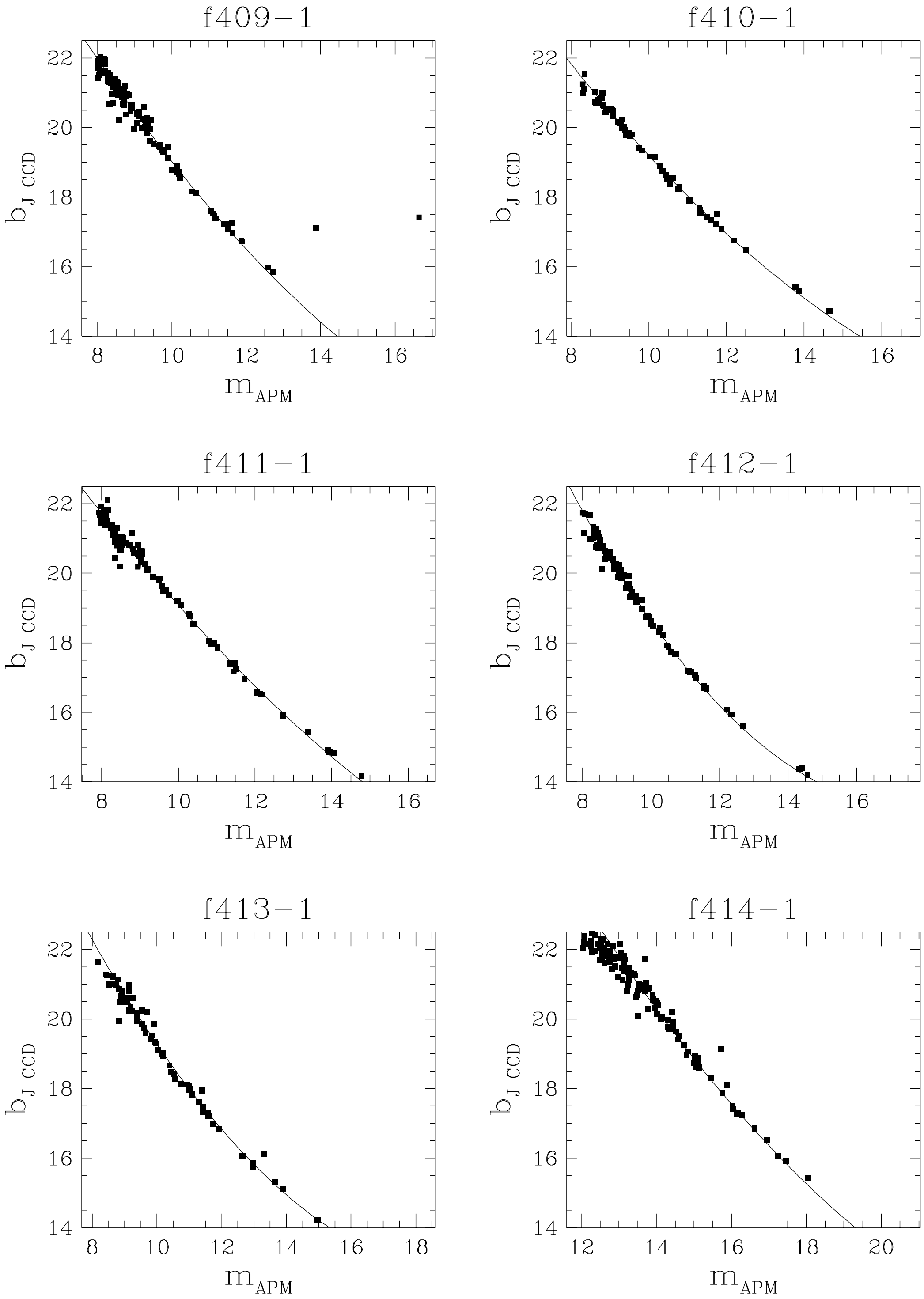

Figure 4.4: Plot of b_J CCD magnitude vs. APM instrumental magnitude for all the Southern b_J plates. The solid line shows the quadratic fit used to calibrate the APM magnitudes in each field.

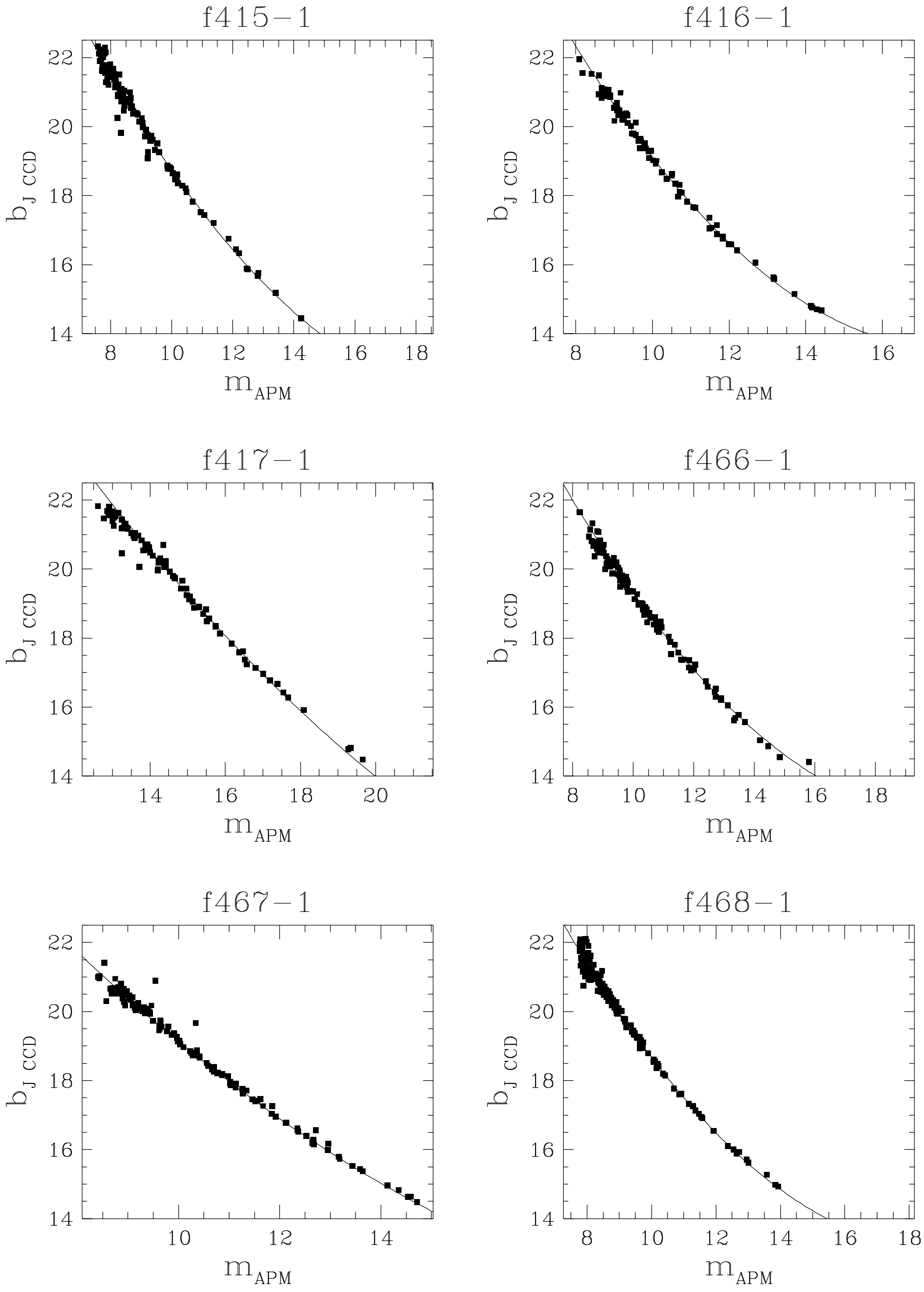

Figure 4.4: $b_{\mathrm{J\ CCD}}$ vs. m_{APM}: continued.

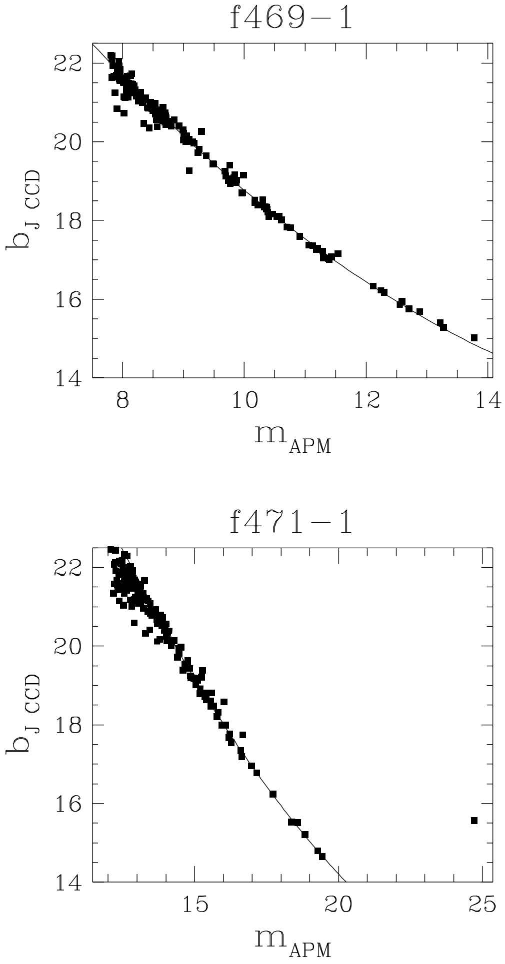

Figure 4.4: $b_{\rm J\ CCD}$ vs. $m_{\rm APM}$: continued.

4.2.4 Checks on the photometric calibration

In field f466 we have two sets of B CCD sequences. These allow us to directly confirm the accuracy of the zero-point used in this field, Fig. 4.5 shows a comparison of photographic magnitudes, calibrated by the f466-1 CCD sequence (i.e. not zero-point corrected using plate overlaps), with CCD magnitudes from the f466-2 field. The mean offset 0.048 ± 0.01 mag, is an estimate of the systematic variation of the photographic magnitudes in the f466 field. However, it should be noted that both f466-1 and f466-2 are situated towards the centre of the f466 field where systematic variations should be at a minimum. A more extensive program of CCD imaging would allow the systematic magnitude variations across the plates to be estimated before and after the field-effect correction procedure.

The U CCD photometry available allows us to test the accuracy of our u band zero-point and linearization obtained from the ridge-line fitting. We might expect that galactic reddening would cause the exact position of the ridge-line to vary

Table 4.4: The b_J offsets from plate-edge matching. The offsets were calculated from the mean offset of the stellar magnitudes matched in plate overlaps. Errors in the measured offsets are of the order ~ 0.004 mag.

Field name	b_J offset
f466	-0.062
f467	-0.101
f468	-0.043
f469	0.028
f470	0.000
f471	0.001
f409	-0.037
f410	0.038
f411	0.073
f412	-0.149
f413	0.084
f414	0.108
f415	0.270
f416	0.246
f417	-0.021

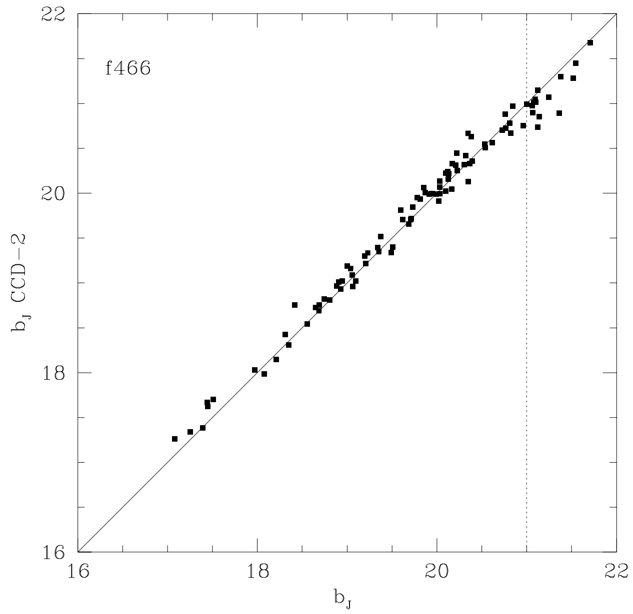

Figure 4.5: Comparison of the calibrated photographic b_J (from the CCD sequence f466-1) magnitudes in the f466 field and b_J magnitudes derived directly from the f466-2 CCD sequence.

systematically over our survey region. Using the simple relation of Woltjer (1975),

$$E(B-V) = 0.06\mathrm{cosec}|b_{\mathrm{II}}| - 0.06 \tag{4.7}$$

which relates reddening to galactic latitude, b_{II}, we expect a low level of reddening at both ends of the Southern strip. f466-2 ($b_{\mathrm{II}} = -51^{\circ}.22$) has $E(B-V) = 0.017$mag while f416-2 ($b_{\mathrm{II}} = -64^{\circ}.42$) has $E(B-V) = 0.007$mag. Reddening derived from HI and galaxy counts (Burstein & Heiles, 1982) also gives similar measures of $E(B-V) \simeq 0.01$mag. The reddening in $E(B-V)$ can be converted to a $(U-B)$ extinction using

$$\frac{E(U-B)}{E(B-V)} = 0.72 + 0.05E(B-V) \tag{4.8}$$

(Zombeck, 1990). It is clear that this gives a very small offset in the $(U-B)$ colours, with the difference in $E(U-B)$ from one end of the strip to the other being ~ 0.005 mag.

Fig 4.6 shows a comparison of ridge-line photometry with direct CCD photometry for two fields, f416 and f466, *without* zero-point corrections from plate-edge matching. The ridge-line photometry for both of these fields has almost exactly the same systematic zero-point offset with respect to the CCD photometry. The mean offset in the f466 field is 0.218 ± 0.018 mag, while f416 shows a 0.186 ± 0.020 mag offset. This therefore suggests that for these two fields the u ridge-line photometry is consistent to ± 0.03, with an offset of ~ 0.2 mag relative to the standard photoelectric U band. Further U CCD photometry will be required to confirm this over the rest of the survey area.

4.2.5 $u - b_{\mathrm{J}}$ selection of QSO candidates

The fully calibrated and flattened stellar catalogue was then used to select the final UVX catalogue which forms the candidate list for follow-up spectroscopy. For the reasons discussed above, and those outlined below, we did not use plate-edge matching to zero point the photometry in individual fields. Fig 4.7 shows colour-magnitude plots for all 15 of the fields in the Southern survey region. Also shown here are all the previously known QSOs (Veron-Cetty & Veron, 1996); we shall use these objects in Section 4.3 to make an estimate of the completeness of the survey. The 2dF survey limits are $18.25 < b_{\mathrm{J}} < 21.0$ (note, the FLAIR survey covers the range $17 < b_{\mathrm{J}} < 18.25$), and $(u-b_{\mathrm{J}}) \leq -0.36$. Within these limits there are ~ 22000 candidates covering an effective area of 355.4 deg^2. The colour limit was chosen to be the reddest limit possible given the faint limit of $b_{\mathrm{J}} = 21$ and a maximum surface density of candidates of $\sim 62 - 63$ per deg^2. This second constraint was a balance of practical observational considerations, and our desire to obtain a QSO catalogue with a high level of completeness. Below we will discuss the effectiveness of our chosen criteria and issues concerning the calibration of the survey.

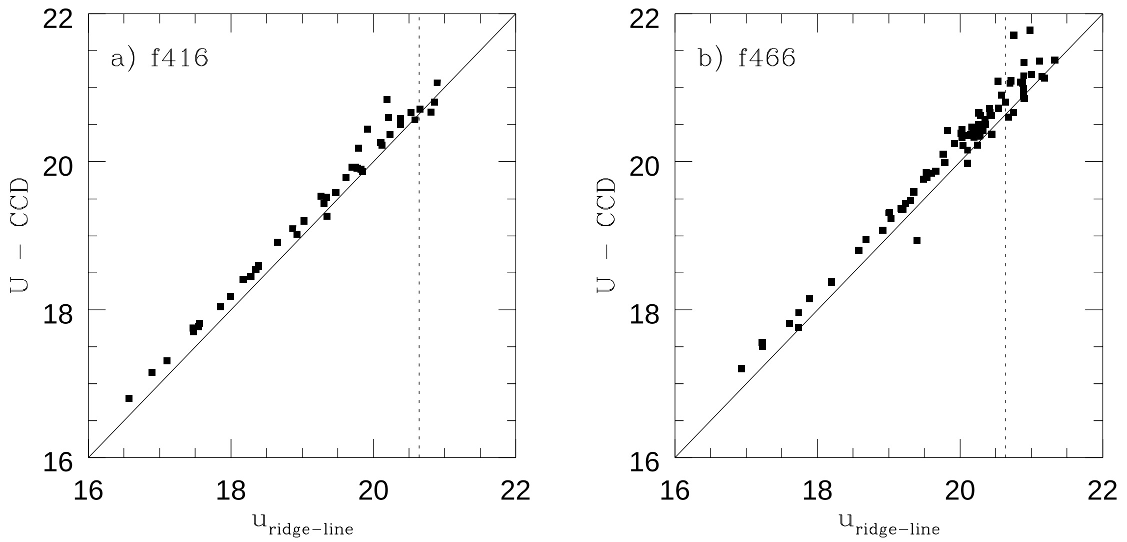

Figure 4.6: A comparison of U CCD photometry and u ridge-line photometry in two fields at opposite ends of the southern 2dF QSO survey strip, a) f416 and b) f466. The solid line is $U = u_{ridge-line}$, the dotted line corresponds to the chosen $u - b_{\rm J}$ selection limit of $u - b_{\rm J} = -0.36$ for $b_{\rm J} = 21$.

4.3 Testing the UVX Catalogue

We now come to discuss the properties of the UVX catalogue in the Southern strip which is shown in Fig. 4.8. The most obvious feature is a significant number gradient across the survey area. This is more clearly shown by a histogram of UVX number density for consecutive fields (Fig. 4.9). Several fields show higher than average candidate densities; in f410, f413 and f415 it is likely that we are seeing an increased number of stars being scattered into our selection limits due to the relatively bright limiting magnitudes of the u plates in these fields, which are $u = 20.8 - 20.9$. f466 also has a large excess, and although this might be expected of the field closest to the galactic bulge it is likely that a small zero-point error could also increase the number. Fig. 4.9 also shows the number densities for each field after using plate edge matching. There is obviously a much larger gradient across the strip in this case. The zero-point offsets shown in Table 4.4 have been plotted in Fig. 4.10. There is a clear correlation between number density and zero-point correction. Of particular interest is the f412 field which has an excess with respect to the surrounding fields of ~ 10 deg^{-2} with plate edge matching, but has a deep u plate ($u_{\rm lim} = 21.2$). An excess of $\simeq 10$ deg^{-2} implies a zero-point offset of $\simeq 0.2$ mag assuming the number-magnitude relation has a slope of $\simeq 0.28$ (that is $N(m) \propto 10^{0.28m}$), which is in fact the offset relative to the f411 and f413 fields listed in Table 4.4. This is further evidence to suggest that plate matching leaves residual $\sim 0.1 - 0.2$ mag zero-point differences between the survey fields, and so is additional justification for not using plate-edge matching.

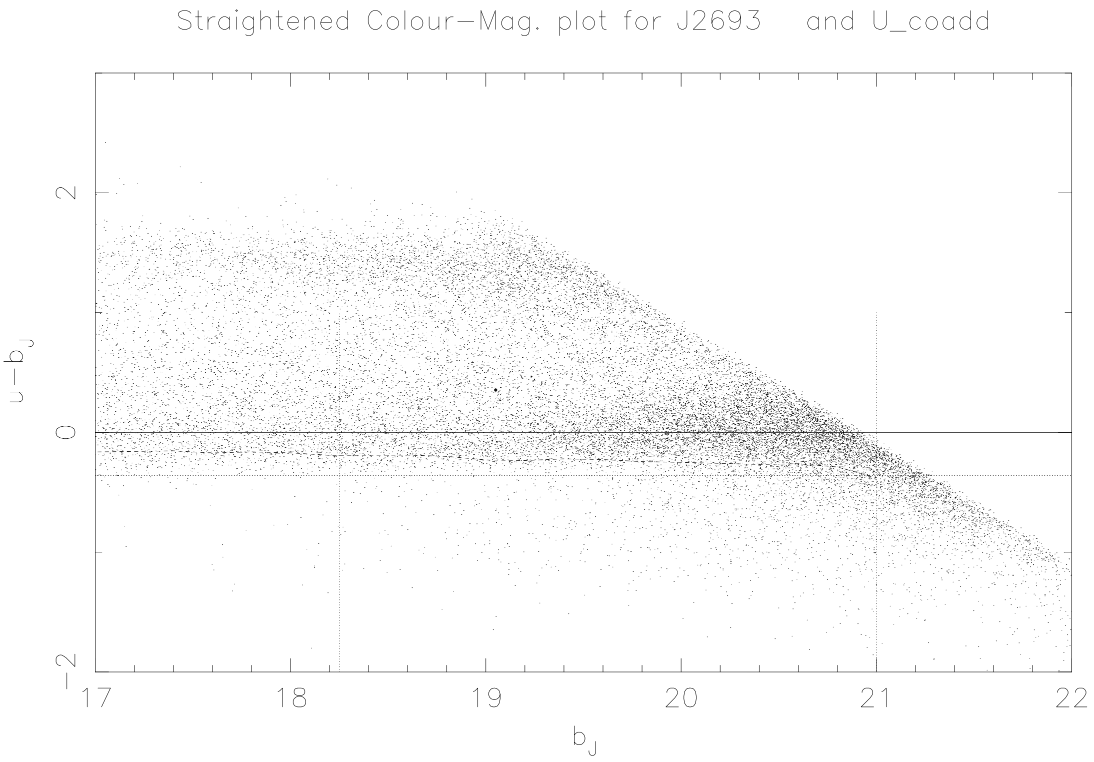

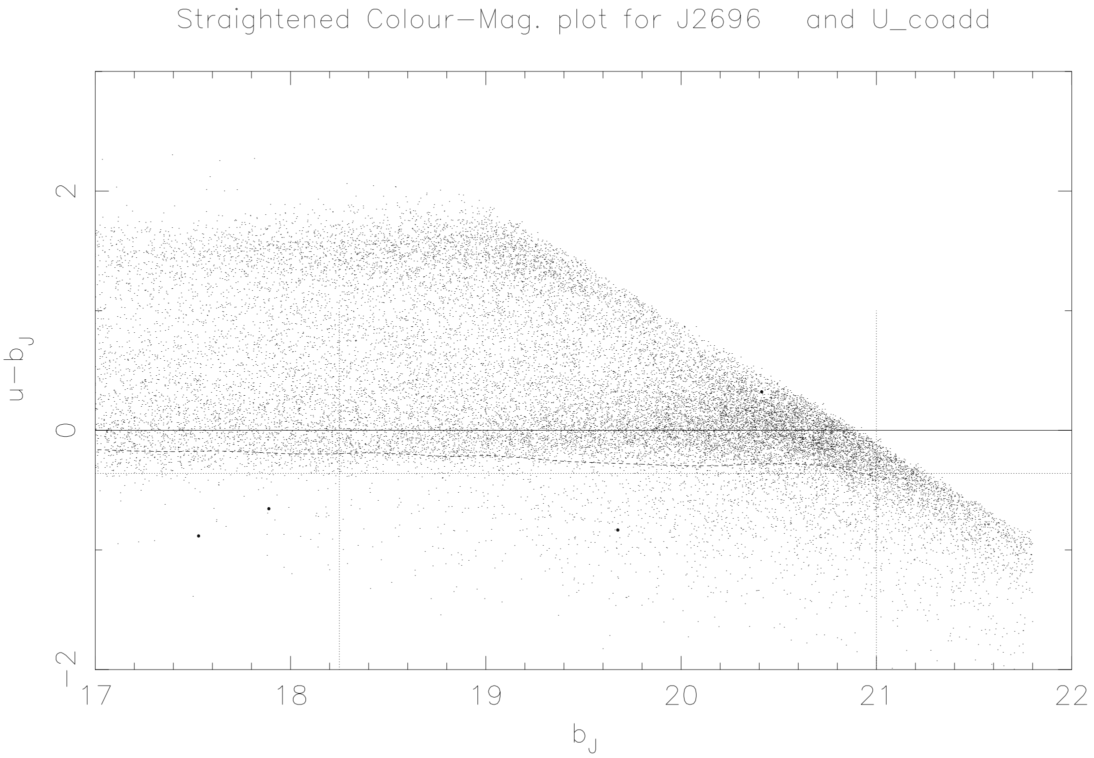

Figure 4.7: Colour-magnitude plots used to select UVX objects for each field in the Southern strip of the 2dF QSO survey. The solid lines show $u - b_J = 0$ and the survey limits of $u - b_J = -0.36$, $18.25 < b_J < 21.0$. The dotted line shows the FWHM of the stellar ridge-line. The large points show previously known QSOs.

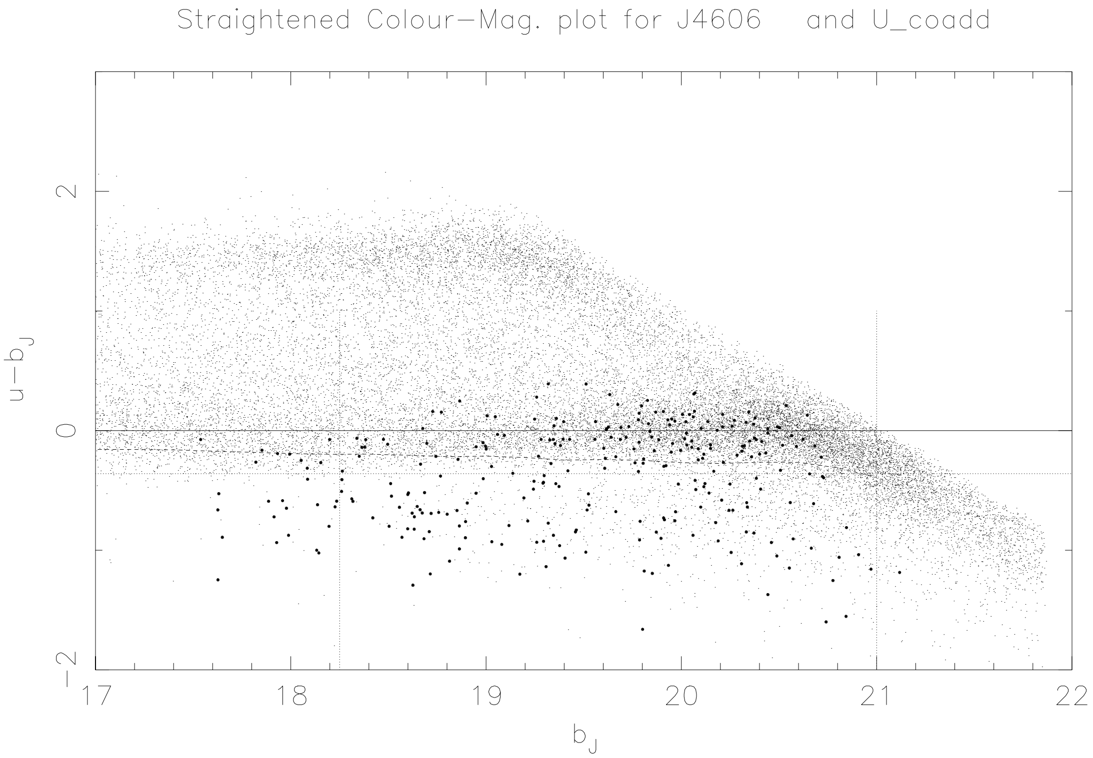

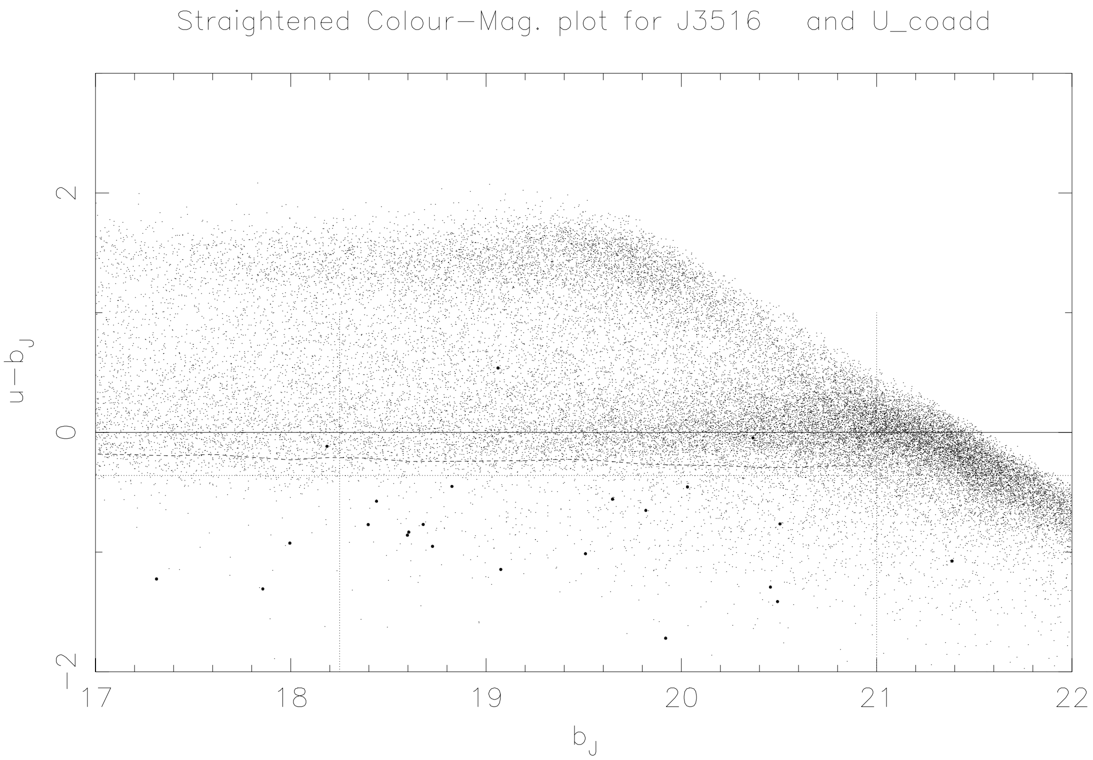

Figure 4.7: Colour-magnitude plots: continued

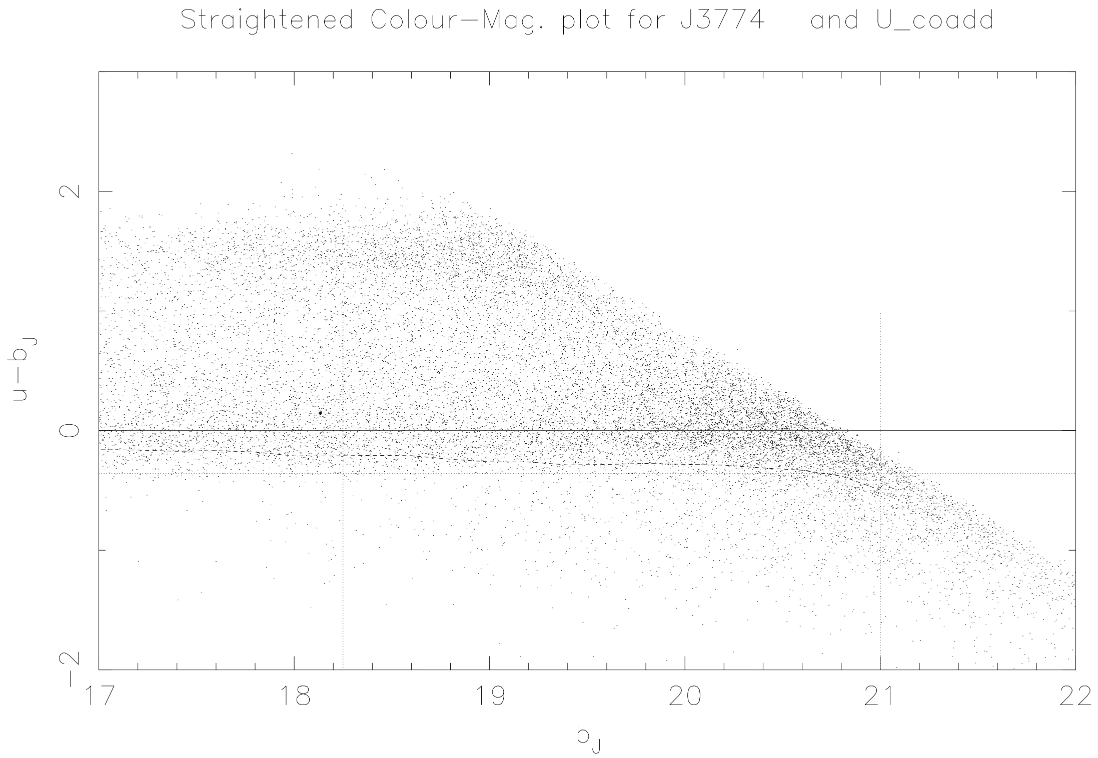

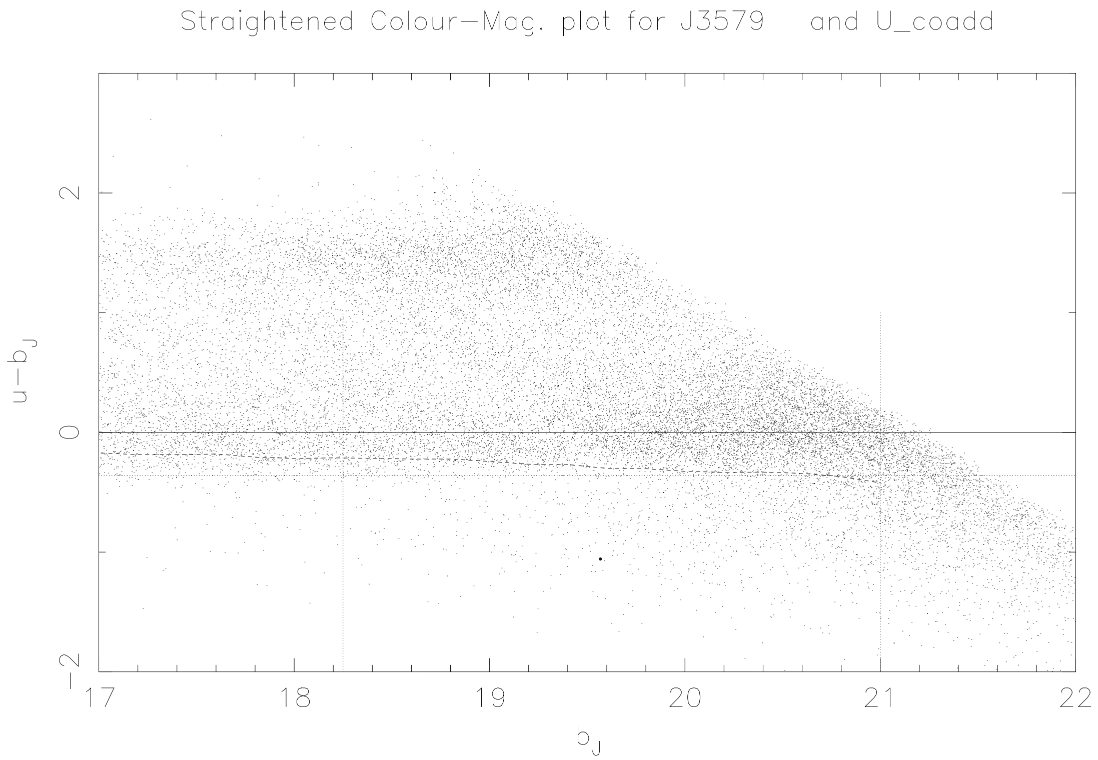

Figure 4.7: Colour-magnitude plots: continued

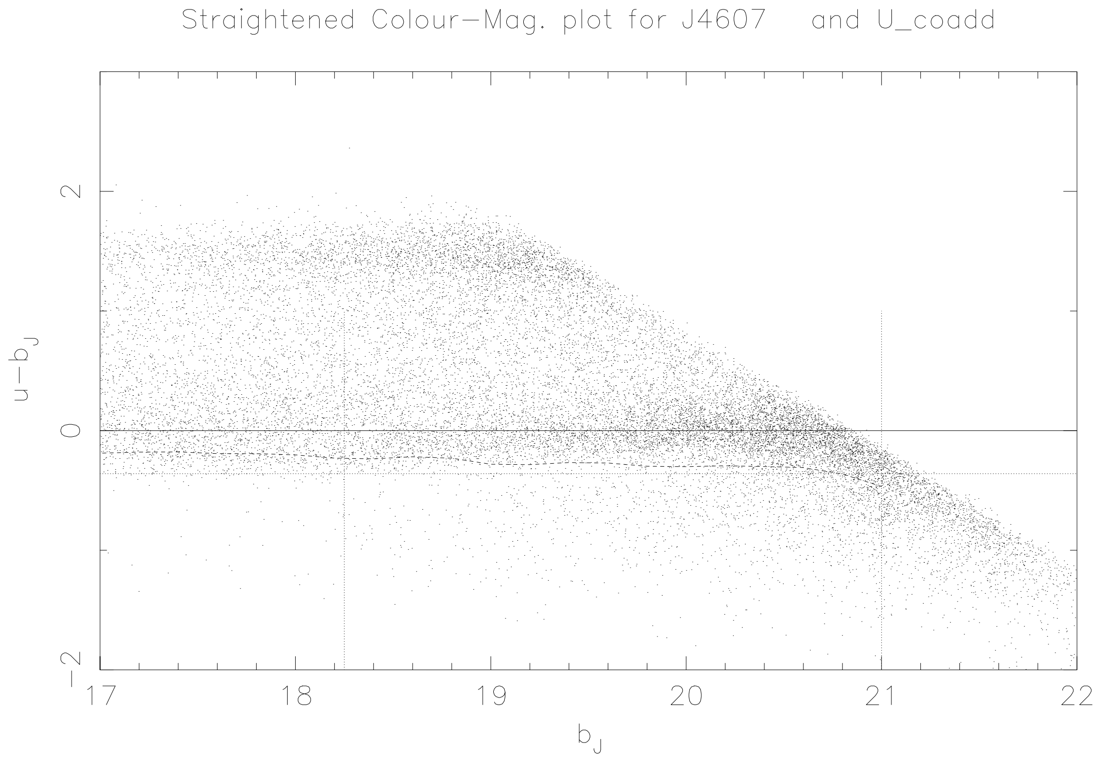

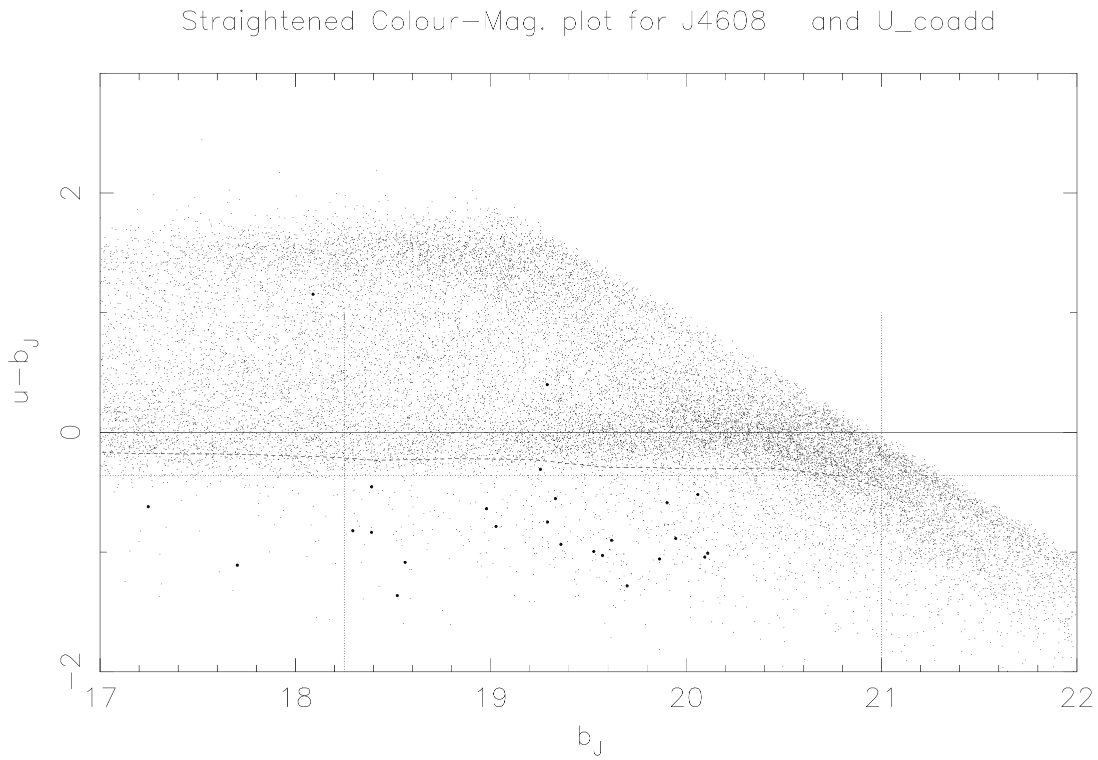

Figure 4.7: Colour-magnitude plots: continued

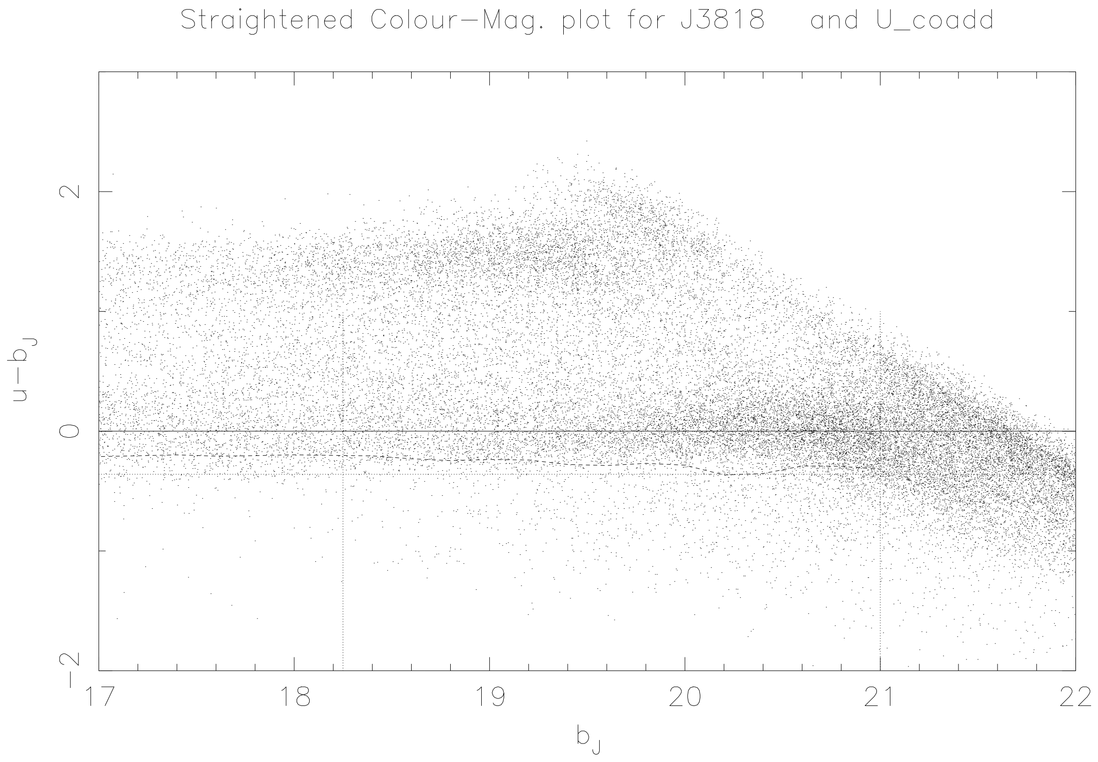

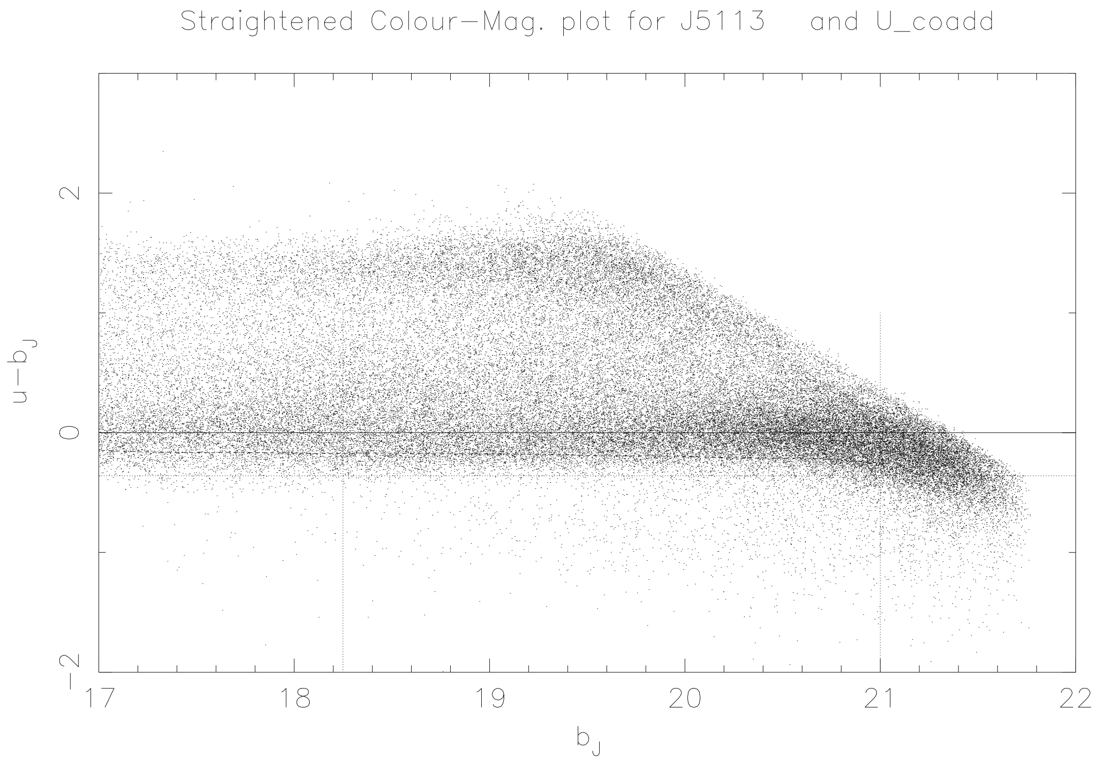

Figure 4.7: Colour-magnitude plots: continued

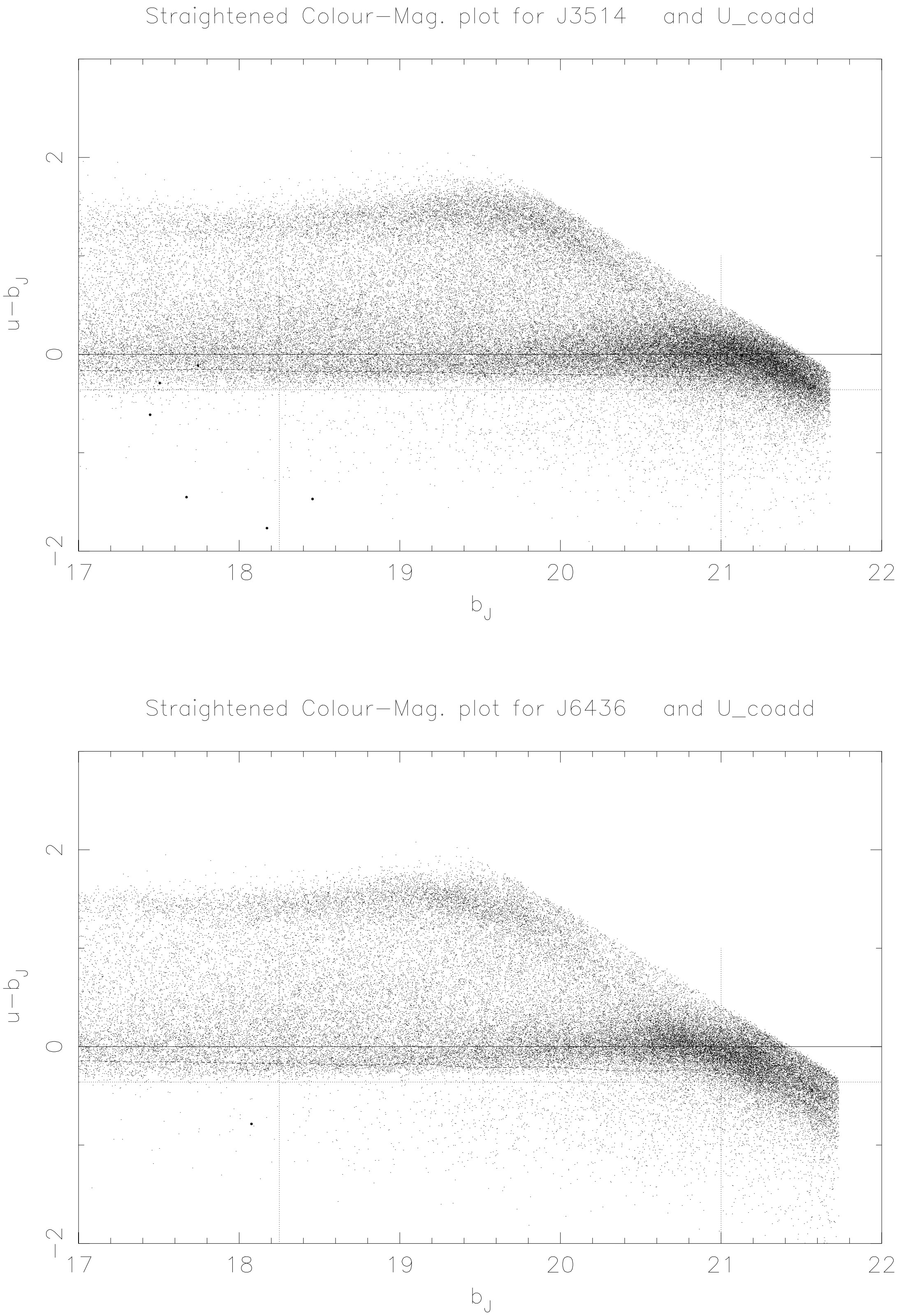

Figure 4.7: Colour-magnitude plots: continued

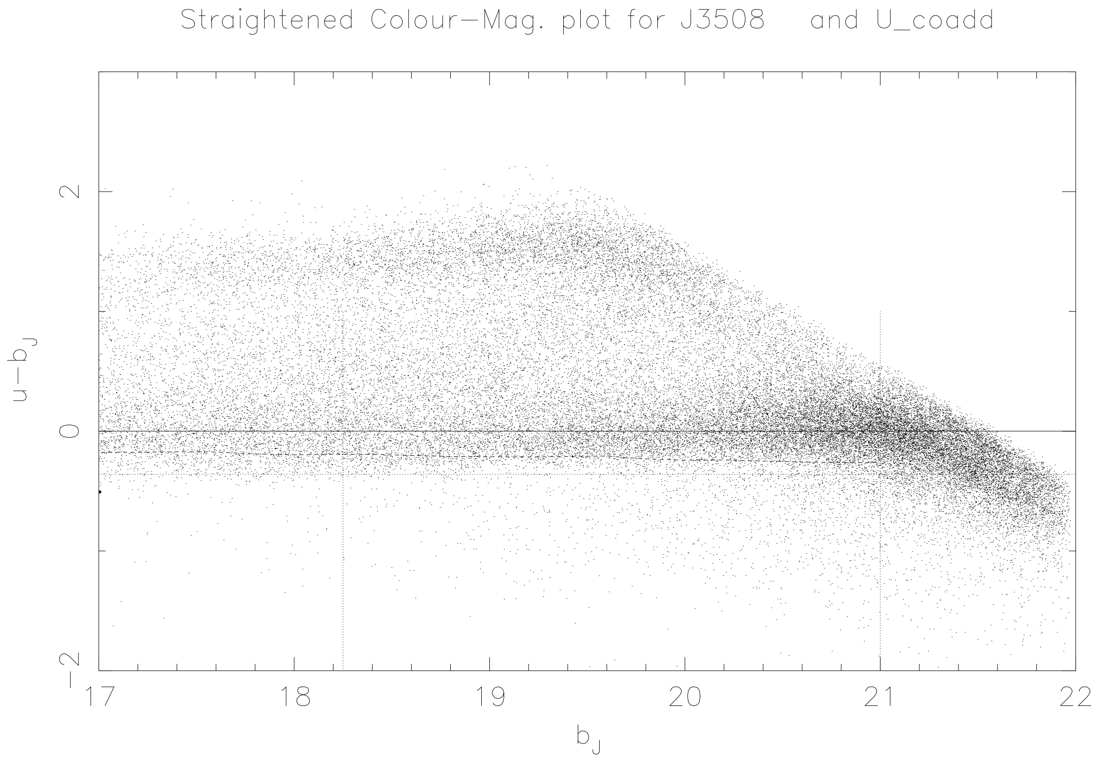

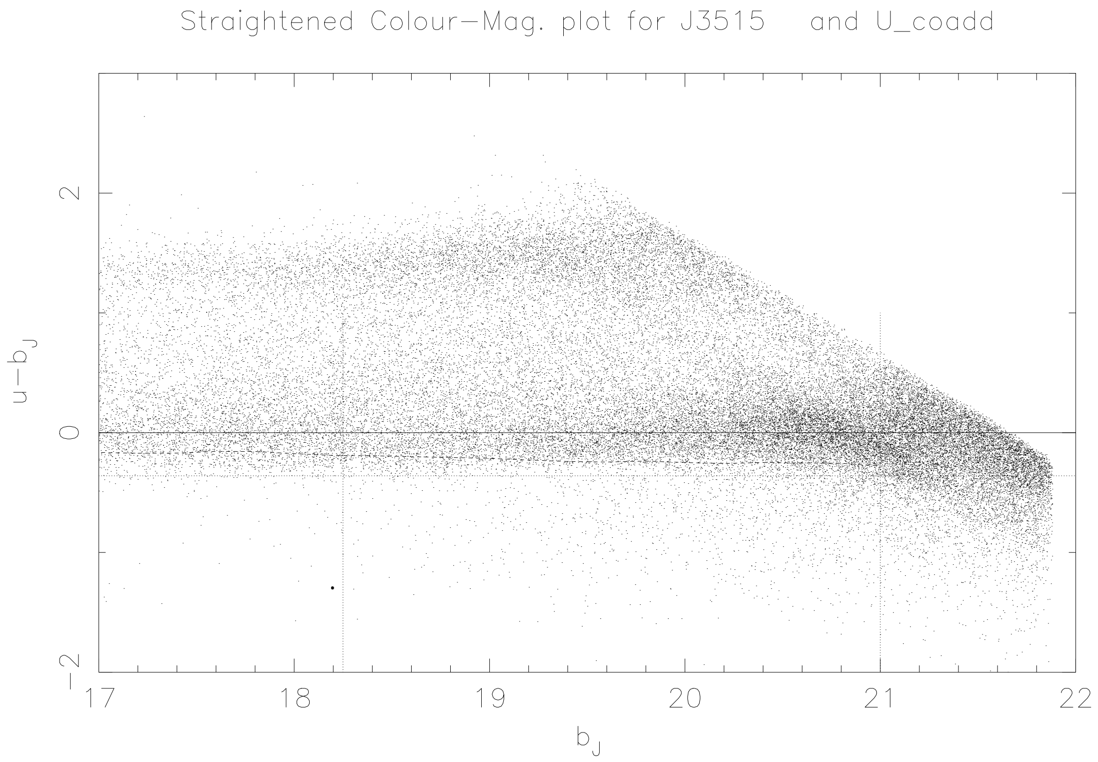

Figure 4.7: Colour-magnitude plots: continued

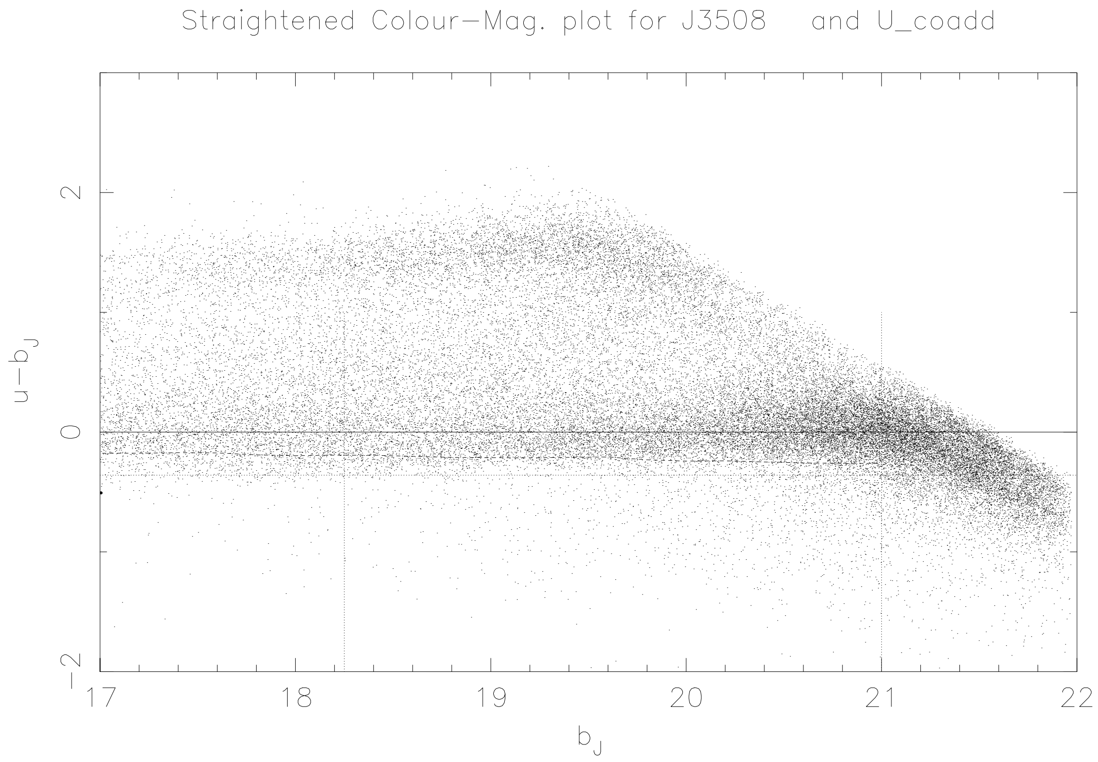

Figure 4.7: Colour-magnitude plots: continued

4.3.1 Photometric errors

Random photometric errors will have a significant effect on the completeness and contamination of the survey at our faintest limits. In order to quantify these we have carried out two tests. The first makes use of the large overlap at 00^{h} RA between f409 and f471. We match all stellar objects with both u and b_{J} magnitudes in this overlap (a total of $\sim$ 4200 images) and calculate the r.m.s. scatter of b_{J}, u and $u - b_{\mathrm{J}}$. Fig 4.11 shows that in the case of these plates the r.m.s. scatter in u and b_{J} are almost identical, $\simeq 0.18$ mag at $b_{\mathrm{J}} = 21$. As we move brighter the error on the b_{J} magnitudes drops below the u errors until $b_{\mathrm{J}} \simeq 19.2$. The error in the colour falls quickly from 0.25 at $b_{\mathrm{J}} = 21$ to 0.2 only 0.3 mag brighter, tending to ~ 0.1 at the brightest magnitudes. The f409 and f471 fields have u plate limits of u =20.8 and 21.4 respectively, so f409 will contribute a larger fraction of this error than f471. However a combination of the two plates should give an approximation to the errors from an average plate in the sample.

The second test is to measure the width of the stellar locus as a function of b_{J}. Fig. 4.12 shows the half-width of the stellar ridge-line, calculated from the peak of the ridge to the $u - b_{\mathrm{J}}$ value corresponding to half the maximum counts. This is only carried out on the blue side of the ridge, removing the effect of the large number of red stars at $u - b_{\mathrm{J}} > 0$. We have split the 15 fields into 4 groups, based on the depth of the u plates in each field. As well as plotting the widths for the individual fields

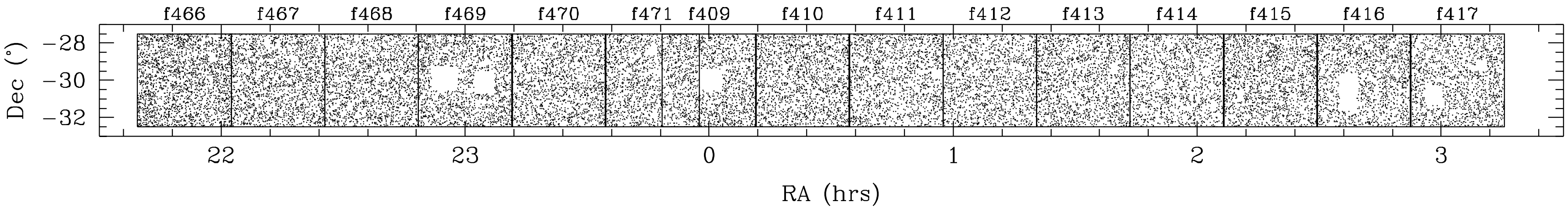

Figure 4.8: The Southern survey region of the 2dF QSO survey. Note the stellar gradient across the strip (due to increased contamination from galactic stars nearer the galactic bulge) and the hole regions cut out of the survey around bright stars.

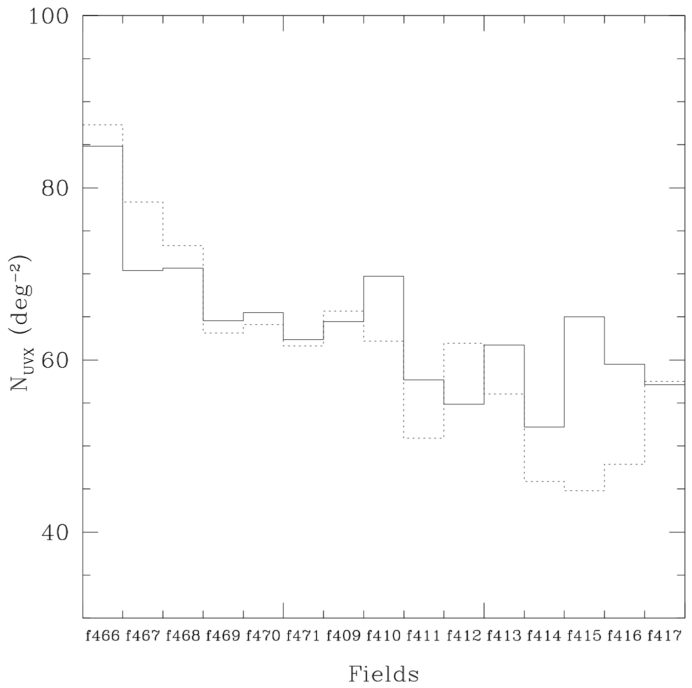

Figure 4.9: Histogram of the number density of UVX objects along the Southern strip, with the fields in order of Right Ascension. The solid line shows the number density of candidates without plate edge matching, while the dotted line includes plate edge matching.

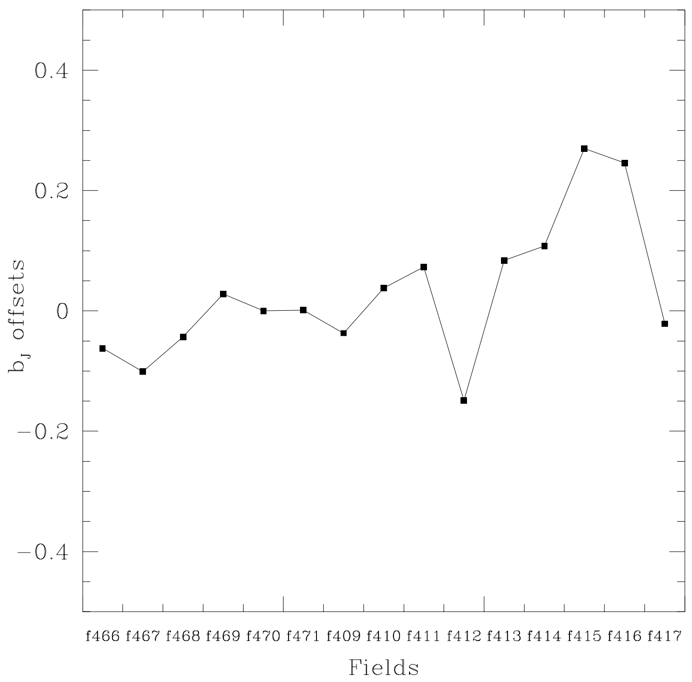

Figure 4.10: Plot of the plate-to-plate zero-point corrections as measured from matching plate-edge overlaps. The fields are in order of Right Ascension. Errors on each measured zero-point offset are $\sim 0.003 - 0.004$.

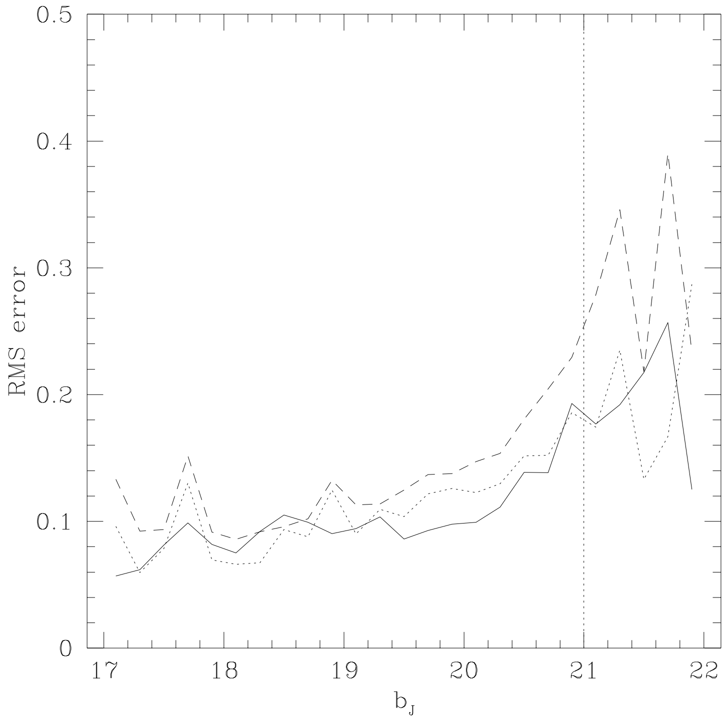

Figure 4.11: The RMS error on b_J (solid line), u (dotted line) and $u - b_J$ (dashed line) as a function of b_J measured from the overlap of the f409 and f471 fields. The vertical dotted line signifies our survey limit of $b_J = 21$.

we have also plotted an average of each of the groups. There are several points of note concerning these diagrams; first, the width at the faint end of the distribution is strongly dependent on the u plate limits, with the shallower plates having widths of ~ 0.4 at $b_J \simeq 21$. For deeper plates this is closer to 0.2. Over the magnitude range $18.5 < b_J < 20$ the ridge-line width is consistently at the $0.16 - 0.18$ level, for all 15 of the fields, suggesting that the photometry over this region is largely independent of the depth of our plates. At brighter magnitudes the smaller numbers of objects increases the noise of the width estimate, however a distinct increase in width is still observable, from ~ 0.18 to 0.25. There are two possible reasons for this increase at brighter magnitudes; either the photometric errors increase, for example due to the effects of increased saturation in the photographic plates, or there is an intrinsic broadening of the locus over this range. The r.m.s. errors from the f409/f471 overlap (Fig. 4.11) suggest that the increased width in the stellar locus is indeed an intrinsic property, and that the errors in both b_J and u tend to ~ 0.1 mag at bright magnitudes.

4.3.2 Measures of completeness from known QSOs

There are more than 200 known QSOs in the Southern strip survey region. These objects have been taken from the Veron-Cetty & Veron (1996) catalogue and have been identified using a variety of techniques. They include UVX, objective-prism,

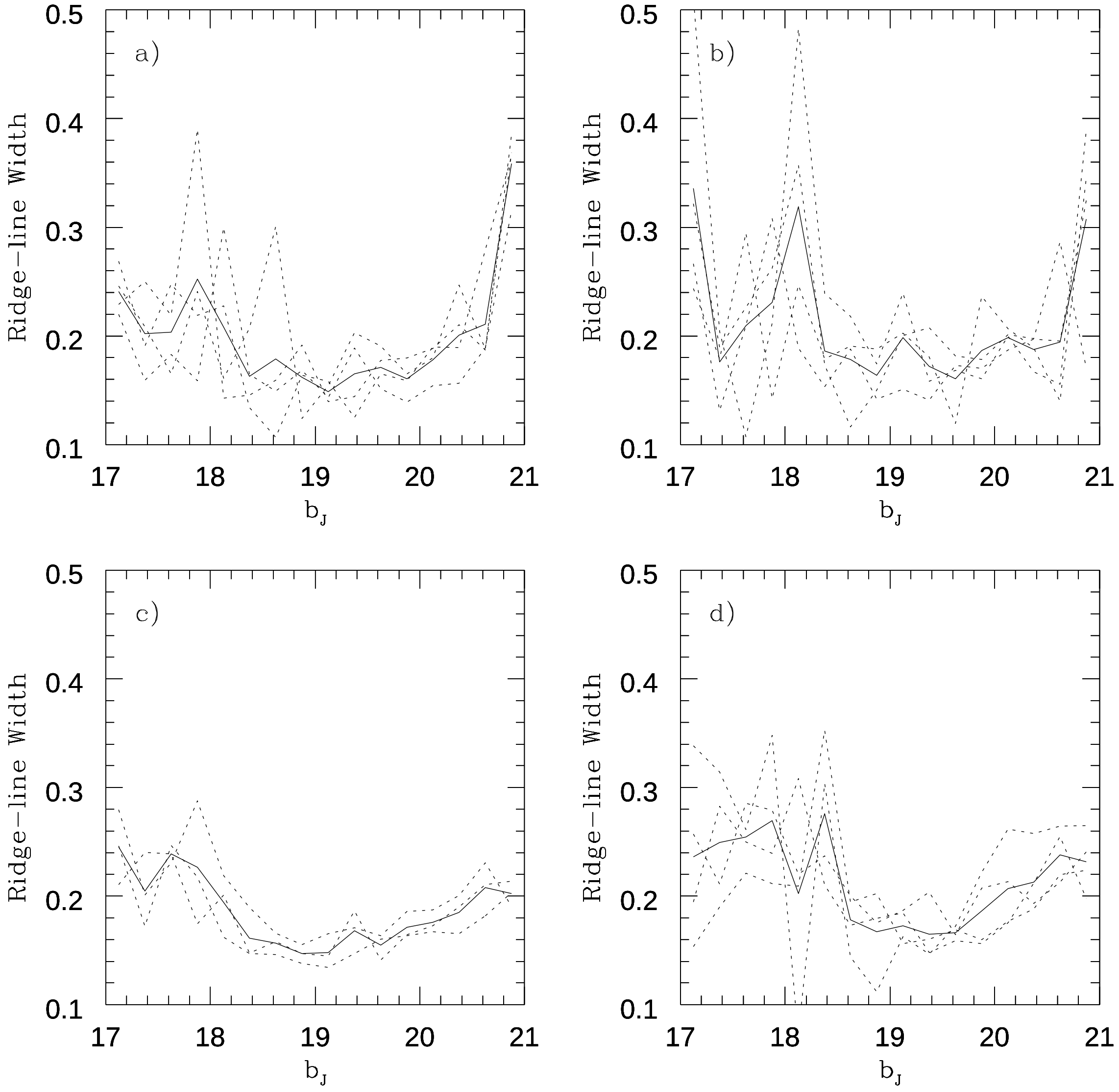

Figure 4.12: The ridge-line half-width as a function of b_J. Fields are grouped according to the limit of the deepest u plate in the field. a) The fields with the shallowest u plates, f409, f410, f413 and f415, $u_{\rm lim} = 20.8 - 20.9$; b) f411, f414, f416 and f412, $u_{\rm lim} = 21.0 - 21.3$; c) f467, f468 and f471, $u_{\rm lim} = 21.4$; d) the fields with the deepest u plates, f466, f417, f469 and f470, $u_{\rm lim} = 21.5 - 21.6$. The dotted lines are for individual fields while the solid lines denote the average of the 3 or 4 fields in each plot.

Table 4.5: Numbers of known QSOs in our survey region

Identification	Number
Total	224
Detected	213
Detected and selected	174
Not detected	11
Non-detections:	
Stellar	1
Galaxies	2
Mergers	8

X-ray and radio selected QSOs. Although the distribution is not homogeneous, the number of these QSOs which we select will tell us whether we are selecting a large fraction of the known QSO population.

We find a total of 224 previously known QSOs within our survey area, over the magnitude range $17.0 < b_{\rm J} < 21.0$ and the redshift range $0.3 < z < 2.2$. These are matched to the stellar catalogue (both UVX and non-UVX) with a maximum positional difference of $10''$. Details of this are shown in Table 4.5. We find that 11 of the known QSOs are not detected. These 11 comprise 8 objects which were classified as mergers, 2 which were classified as galaxies, and a single stellar object. Each of these was checked by eye using images from the Digitized Sky Survey (STScI), and the mergers and galaxies show nearby, $< 5''$, companions or faint extensions. The object classified as stellar has no matched u magnitude. We are then left with 213 known QSOs for which we have matches in our stellar catalogue. It should be noted that of these, 83 QSOs are UVX selected from the Durham/AAT sample (Boyle et al., 1990).

We take these 213 known QSOs and determine the fraction selected as UVX in our catalogue. Fig. 4.13a shows the number-magnitude relation for these objects. Although this is an inhomogeneous sample, this plot shows that we have significant numbers of QSOs over the range $17.5 < b_{\rm J} < 21$. Fig. 4.13b shows the colour histogram for the sample. Of the 213 detected QSOs we select 174, that is 82%. Inclusion of the unmatched QSOs reduces this to 78%. Below we try to determine the cause of this incompleteness.

From Fig. 4.13c it is clear that there are several QSOs which are extremely red, 13 QSOs (6%) have $u - b_{\rm J} \geq 0.0$. In the range $b_{\rm J} = 19 - 20$ there are a number of QSOs which lie just redward of our original colour selection limit, as well as those already discussed with $u - b_{\rm J} > 0.0$. In the range $b_{\rm J} = 20 - 21$ we see that there is a broader spread of QSOs with colours redder than the $u - b_{\rm J} = -0.36$ limit. This suggests that the incompleteness is at least partially due to photometric errors, although we note from our previous analysis that the photometric errors even

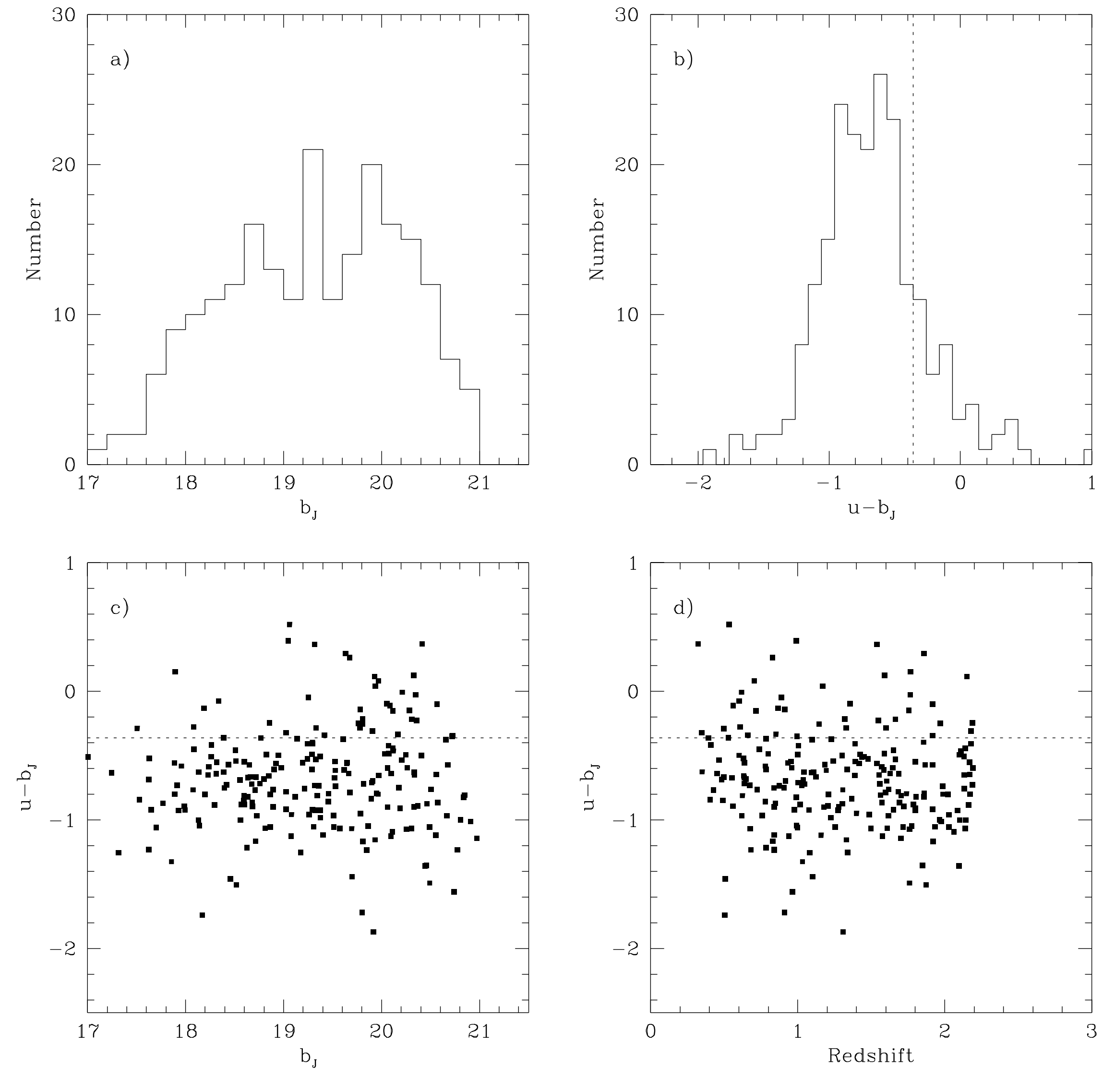

Figure 4.13: The previously known QSOs that have been matched to stellar objects in our survey region. a) the number magnitude relation for this sample, b) a histogram of the colour distribution, c) a colour-magnitude plot, d) a colour-redshift plot. The dotted lines in b), c) and d) show the $u - b_J < -0.36$ colour selection criterion.

at $b_J = 21$ are only at the 0.25mag level, or less for fields with deep u plates. The distribution of $u - b_J$ with redshift (Fig. 4.13d) appears to be reasonably uniform, but does not show the tight relation found by Hawkins & Veron (1995).

4.3.3 2dF vs. Durham/AAT

A possible test to ascertain the source of this incompleteness is to compare the 2df UVX catalogue colours of QSOs and stars found in the Durham/AAT sample. The SGP field from this survey overlaps with the f411 field of the current sample. Boyle et al., (1990) use plates J3721 and U6380 to obtain $u' - b$ colours (these magnitudes are defined below) for their QSO candidates (these plates were taken on the dates 4/11/77 and 15/09/80 respectively). In this section we aim to compare the magnitude systems of the two surveys, as well as compare the photometry of the QSOs and stars.

The magnitude system used by Boyle et al., is somewhat different from the one used in the present sample. b is defined as the photographic magnitude zero-pointed to the instrumental CCD magnitude of the photometric calibration sequences. It is related to the standard Johnson B via

$$b = B - 0.28(B - V - 0.9) \tag{4.9}$$

where $(B - V) = 0.9$ is the average colour of the calibrating stars. It should be noted that Boyle et al., (1990) use a different relation, replacing -0.28 with -0.23. Kron (1980) found a relation between photographic b_J and Johnson B which was $b_J = B - 0.23(B - V)$, but this was derived using the GC385 filter to define the b_J band. A preferable transform for the GC395 filter, used for the Durham/AAT and 2df samples, is that derived by Blair & Gilmore (1982), Eq. 4.1. This then gives a conversion from the b system used in the Durham/AAT catalogue to the b_J system used in the present sample,

$$b_J = b - 0.252 \tag{4.10}$$

This relation implies that the 2dF UVX sample, with its limit of $b_J = 21$, is slightly deeper that the Durham/AAT, which had an average limit of $b = 21$. The 2dF sample u magnitudes were derived using stellar locus fitting, while the Durham/AAT u' magnitudes use CCD calibration combined with an extrapolation, assuming a straight stellar locus. The U CCD photometry in the f416 and f466 fields show that locus straightening does indeed produce a linearized magnitude scale. However, there is a average zero-point offset between the 2dF ridge-line magnitudes and the CCD magnitudes of 0.20 mag. In contrast, Georgantopoulos (1991) found an offset between the u' magnitude scale and the standard Johnson U magnitude of -0.2 mag in the SGP field. We have no independent U photometry in the f411 field to confirm the u zero-point, but note that if the same u zero-point offset in f416 and f466 also applied to the f411 field we would expect that the u' and u magnitudes will have a difference of ~ 0.4 mag.

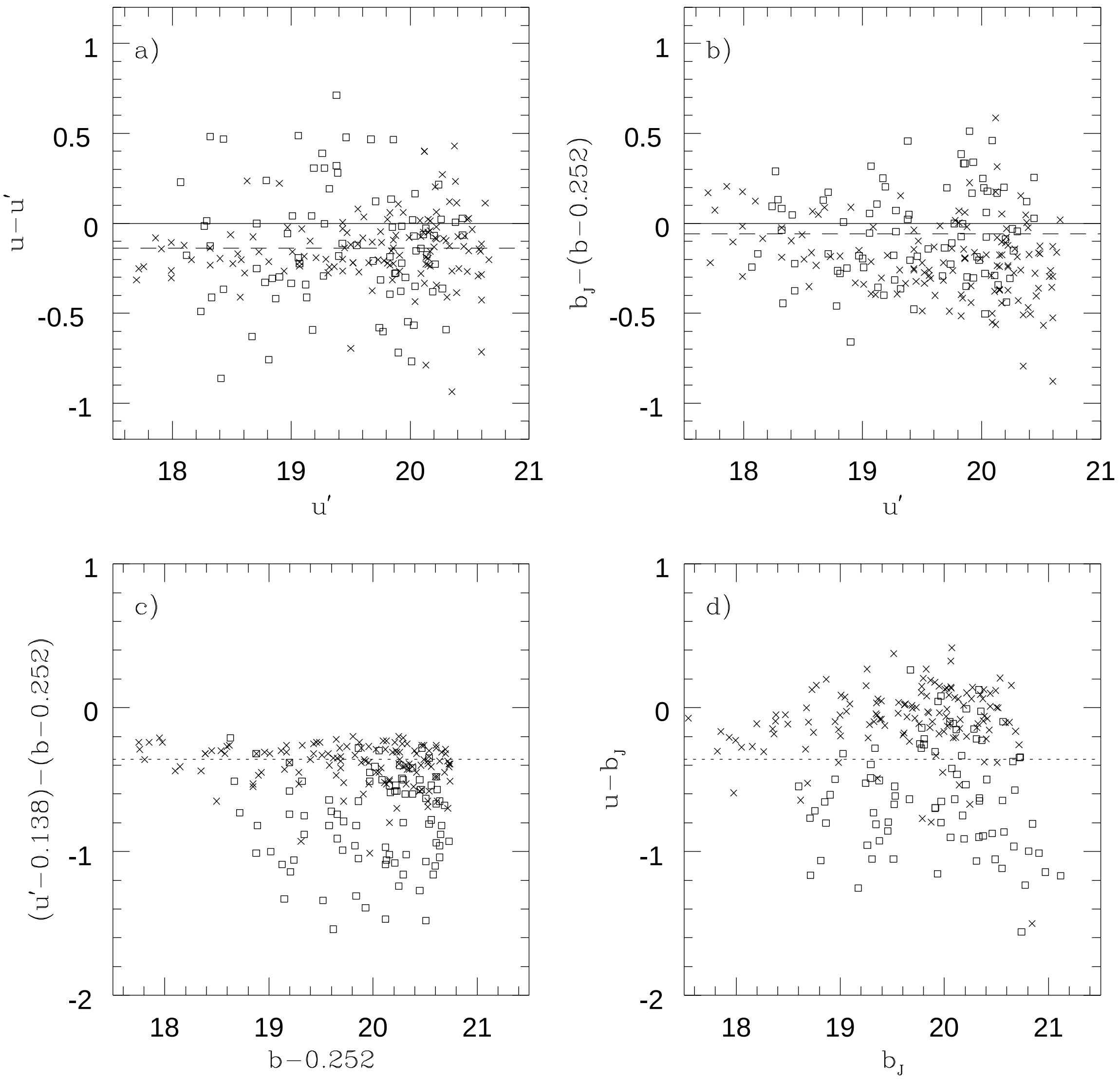

Figure 4.14: A comparison of photometry from the Durham/AAT and 2dF samples for QSOs (open squares) and UVX stars (crosses). a) $u - u'$ as a function of u', the solid line is $u - u' = 0$, the dashed line shows the mean offset for the QSOs. Note that the wider dispersion for QSOs is probably caused by variability. b) $b_{\rm J} - (b - 0.252)$ as a function of u', the dashed line is the mean offset for QSOs. c) colour-magnitude diagram for the Durham/AAT photometry corrected to the 2dF magnitude system. d) colour-magnitude diagram for the 2dF photometry. Dotted lines in c) and d) show $u - b_{\rm J}$ cut for the 2dF survey.

Table 4.6: The r.m.s. scatter between Durham/AAT and 2dF magnitudes for stars and QSOs.

	Stars			QSOs		
u	No.	r.m.s. $(u-u')$	r.m.s. (b_J-b)	No.	r.m.s. $(u-u')$	r.m.s. (b_J-b)
18–19	26	0.136	0.204	21	0.363	0.249
19–20	48	0.135	0.172	41	0.359	0.259
20–21	56	0.243	0.252	21	0.232	0.254
18–21	130	0.190	0.215	83	0.354	0.291

The plates used for candidate selection in the f411 field are J4606, U15202, U15227 and U15719 (exposure dates, 25/10/78, 1/10/92, 21/10/92 and 20/08/93 respectively). Clearly there is a significant interval between the epochs of the III-aJ and u plates. While the epochs of the III-aJ plates used in the two surveys are similar the epochs of the u plates for the two samples differ by $\sim$ 12 years. Fig. 4.14a shows a comparison of the u-band magnitudes for objects detected by both the Durham/AAT sample and the 2dF QSO survey. While the stellar magnitudes follow a tight relation, which broadens at faint magnitudes (due to increased photometric errors), the QSO distribution has a much larger scatter. The measured r.m.s. scatter for the stars is 0.19 mag, while for the QSOs this is 0.35 mag. When the r.m.s. is calculated as a function of magnitude the difference is even clearer; these data are listed in Table 4.6. Brighter than $u' = 20$ the QSO distribution is clearly broader than that of the stars, while in the $u' = 20 - 21$ bin the widths are similar. A similar plot is shown for the $b_J - (b - 0.252)$ magnitude difference in Fig 4.14b. Here is it clear that the scatter in the QSO distribution is considerably less than for the u-band, while the stellar distribution has more scatter. The r.m.s. scatter in magnitude bins is shown in Table 4.6. The QSO magnitude differences, while still larger than that of the stars, is consistently smaller than the u-band difference measured. This difference between stars and QSOs in the u photometry can most easily be explained as due to variability of the QSOs.

The mean offset between u magnitudes are -0.144 for the stars and -0.129 for the QSOs. There is therefore an average offset of -0.138 between the two sets of photometry, which is somewhat different from the expected -0.4 difference. This possibly suggests that there are other effects which we have not accounted for when comparing the zero-points of the two sets of photometry. The b_J and $b - 0.252$ magnitudes are offset by -0.198 mag in the case of the stars, but by only -0.060 mag in the QSOs. This will be largely due to the stars being scattered into the selection by photometric errors.

By making an approximate conversion from the old magnitude system to the one used in the 2dF catalogue, we produce Fig. 4.14c which can be compared directly to Fig. 4.14d, containing the new photometry for these objects. It should be noted that a correction to the u' magnitudes has been made which is the average offset of all objects between the u' and u systems. The comparison between the new and old photometry suggests that the colour selection limit for the Durham/AAT sample appears to be, at $u - b_{\rm J} \simeq -0.2$, somewhat redder than the 2dF survey limit.

4.3.4 A calculation of 2dF survey completeness

Now we compute the expected completeness of our catalogue due to photometric errors, variability and our $u - b_{\rm J}$ cut. The width of the QSO colour distribution is dependent on a number of effects. The intrinsic width is convolved with effects from variability and photometric errors. If we assume that the excess width in $u - u'$ exhibited by the UVX QSOs is due to variability, then variability adds an r.m.s error of 0.24 mag. We assume an intrinsic width for the QSO colour distribution ($0.3 < z < 2.2$) which is also 0.24 mag, measured from the variability selected sample of Hawkins & Veron (1995). A similar value is given by Veron (1983). We have removed the effect of photometric errors which are ~ 0.1 mag for the variability selected sample (Hawkins, 1986). We then combine this intrinsic width with our estimate for variability and the photometric errors in the $u - b_{\rm J}$ colour measured from the f409/f471 plate overlap. We generate a random QSO population of 100000 QSOs which has the measured number-magnitude relation (Eq. 3.1 and 3.2) and a Gaussian colour distribution with a mean of -0.68 (the mean colour of the known QSOs in our survey area), and a width defined from the above calculation. Integrating over this population we find that 79.4% of these QSOs are selected with $u - b_{\rm J} < -0.36$. This is consistent with the expected completeness measured from the known QSOs in the survey area of 78%. Without the variability component this percentage rises to 85.7%, suggesting that we are losing $\simeq 6\%$ of QSOs due to variability. If we also remove photometric errors the percentage completeness rises to 90.6%.

It is therefore clear that with the current UVX colour limit we miss a number of QSOs ($\sim 21\%$). However our main objective was to produce a catalogue which contained a low level of contamination as well as a high number density of QSOs. With this in mind we chose the limit of ~ 62.5 candidates per deg^2 (200 candidates per 2dF field) on average over the survey area. The expected number density of QSOs at our survey limit is 44 per deg^2. Allowing for the $\sim 21\%$ incompleteness, this leaves 35 QSOs per deg^2 and thus we expect over 50% of our candidates to be QSOs. This should be compared to the Durham/AAT sample in which only one third of candidates were successfully identified as QSOs.

4.4 Conclusions

In this Chapter we have discussed the production of a new UVX catalogue to be used as the candidate list for the 2dF QSO survey. We have limited our discussion to the Southern strip; a region of equal area near the North Galactic Cap has also been produced. This will be outlined along with further details of the plate flattening process in Smith (1997). In particular, we have looked in detail at the photometric properties of the catalogue, and carried out several tests to ascertain the levels of completeness expected from the spectroscopic follow-up of the candidate list. We draw the following conclusions:

1) The Southern catalogue consists of 22000 stellar UVX objects covering an effective area of 355 deg^2. Objects were selected from photographic $u - b_{\rm J}$ colours from UKST plates. We use a process which corrects the photographic plates for field effects. The corrected magnitudes in $b_{\rm J}$ were calibrated using independent CCD sequences in each UKST field. The u magnitudes were calibrated by defining the position of the galactic star ridge-line to be $u - b_{\rm J} = 0$.

2) In two fields U-band CCD photometry was available. This shows that the photographic u photometry from ridge-line straightening was linear, although with a possible zero-point offset of ~ 0.2 magnitudes.

3) The catalogue selection limit was chosen to be $u - b_{\rm J} < -0.36$ over the range $18.25 \leq b_{\rm J} \leq 21.0$. These limits give the required candidate densities defined by our observational constraints.

4) We measure the r.m.s. and systematic photometric errors present in the catalogue. The r.m.s. errors in colour are ~ 0.15, increasing to ~ 0.25 mag at the very faint end of the catalogue. When we attempt to match the photometry across plate edges we produce a systematic gradient across the survey area. This suggests that there still exist some low level systematic errors at the edges of the photographic plates which have not been removed by our field effect correction process. We do *not* use plate-edge matching to calibrate our catalogue.

5) We estimate the completeness of the survey from the previously known QSOs in our sample. Over the redshift range $0.3 < z < 2.2$ this estimate gives a completeness of 78%.

6) By comparing the 2dF survey photometry of QSOs and stars selected as UVX in the Durham/AAT catalogue, we determine that variability is a significant effect in our catalogue, accounting for $\sim 6\%$ incompleteness. Modelling the contributions from photometric errors, variability and intrinsic scatter we calculate an expected completeness of 79%.

The UVX catalogue with a completeness of $\sim 80\%$ should produce a QSO survey with a high number density, ~ 35 deg^{-2}, allowing us to make effective measurements of large-scale structure on a range of scales. The first spectroscopic observations of this catalogue will allow us to ascertain whether the estimates of completeness discussed here are indeed correct. Discussion of these observations, and a possible way to improve the survey completeness by utilizing UKST r plates can be found in Chapter 6.

Chapter 5

The Correlation of UVX QSOs with Foreground Galaxy Clusters

5.1 Introduction

The existence of associations between high redshift QSOs and low redshift galaxies has been controversial for a number of years; by some this association has been taken as evidence of the non-cosmological nature of QSO redshifts (Hoyle & Burbidge, 1996). However, there are more popular explanations which have been offered, that reconcile the observations with the standard cosmological world view. In particular, gravitational lensing can give a natural explanation for an association that is real but not physical; statistical lensing can be invoked to produce an excess or deficit in QSO counts around a particular lens. An excess can be produced in a flux limited sample because objects intrinsically fainter than the flux limit can be amplified and hence artificially added to the sample (Gott & Gunn, 1974). As lensing also produces a distortion in the expected 2-D image, reducing the real background area observed, a deficit in the number of background objects can also arise (Wu, 1994) if the intrinsic number-count slope of the source objects is sufficiently flat. Although it is hard to imagine other mechanisms which would produce an excess of QSOs near low redshift galaxies or galaxy clusters, this is not the case with anti-correlations. Dust in the intervening object could produce a deficit, though observations of galaxy groups and clusters do not show the presence of significant amounts of dust (Ferguson, 1993).

If correct, the lensing hypothesis allows important constraints to be placed on cosmology and large-scale structure. The excess or deficit of QSOs near a cluster can be used to weigh the cluster. This method has the advantage over other mass estimates in that it allows a measurement of the absolute mass of the cluster, while other estimators such as the measurement of velocity dispersions and the observation of shear due to strong lensing are effectively measuring the gradient of the cluster potential. Thus, in principle, it is possible to determine directly the fractional mass over-density of a cluster by comparing mass estimates from amplification by weak lensing and from shear by strong lensing. In practice the QSO density is too low to determine the mass for individual clusters (although faint galaxy counts may be able to do this) and so we use large samples of clusters to obtain a statistical measure of the mass in the cluster population.

There is a large amount of observational evidence for QSO-galaxy associations, a selection of results being given in Table 1 of Wu (1994). Most find a positive association of QSOs with foreground galaxies, using samples of bright QSOs (e.g. Tyson, 1986). In this Chapter we will first investigate the anti-correlation between faint UVX objects and galaxy clusters and groups found by Boyle et al., (1988) (BFS88), (see also Shanks et al., 1983). We shall then go on to use the 2dF QSO Survey UVX catalogue (Chapter 4) and the Abell-Corwin-Olowin (ACO) (Abell et al., 1989) and APM (Dalton et al., 1997) galaxy cluster catalogues to extend this investigation. In Chapter 2 we commented on the possible contribution of gravitational lensing to the correlation of faint galaxies and QSOs while trying to determine QSO environments. In this Chapter we will determine the level of this effect to ascertain whether gravitational lensing has any effect on the conclusions of Chapter 2. Finally we will discuss the cosmological implications of the results in our conclusions. However, first, we review some of the theoretical aspects of gravitational lensing, and discuss the components of the lensing models used.

5.2 Statistical Gravitational Lensing

Gravitational lensing is caused by the deflection of photons by large masses; the deflection angle, α, is given by

$$\alpha = \frac{4GM(<b)}{bc^2} = \frac{D_{\mathrm{s}}}{D_{\mathrm{ls}}}(\theta - \theta_{\mathrm{q}}) \tag{5.1}$$

where α, b, θ and θ_q are defined in Fig. 5.1 and D_s, D_l and D_{ls} are the angular diameter distances from the observer to the source, the observer to the lens and the lens to the source respectively (also shown in Fig. 5.1). $M(<b)$ is the mass contained within a radius b of the lens centre. Surface brightness is conserved, which implies the images will be amplified by a factor, A, which is defined by

$$A = \left| \frac{\theta}{\theta_{\mathrm{q}}} \frac{\mathrm{d}\theta}{\mathrm{d}\theta_{\mathrm{q}}} \right| \tag{5.2}$$

(Turner et al., 1984). A graphical representation of this is shown in Fig. 5.2. Clearly the amplification depends on the form of the mass distribution. We use two analytic mass profiles; the first, and simplest, of these being the single isothermal sphere (SIS), which has a mass surface density, Σ, defined by

$$\Sigma_{\mathrm{SIS}} = \frac{\sigma^2}{2Gr} \tag{5.3}$$

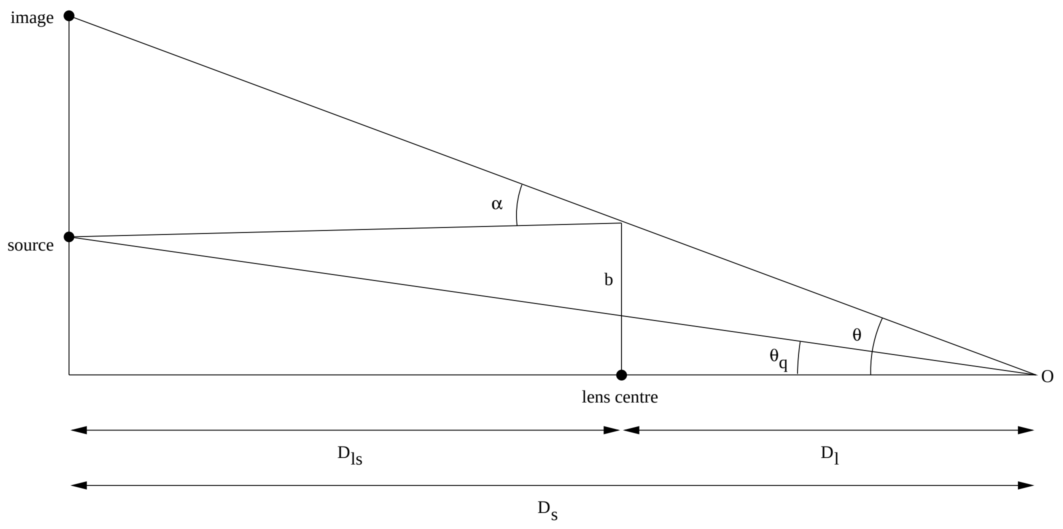

Figure 5.1: The geometry of gravitational lensing; light from the un-lensed source, which passes the lensing mass at a distance b, is deflected by an angle α into the line of sight of the observer.

where σ is the 1-D velocity dispersion of the isothermal sphere. When integrated from $r = 0$ to $r = b$ this gives

$$\alpha = 4\pi \frac{\sigma^2}{c^2} \tag{5.4}$$

which when combined with Eqs. 5.1 and 5.2 gives amplification as a function of θ,

$$A = \frac{\theta}{\theta - \theta_{\mathrm{E}}}, \qquad \theta > \theta_{\mathrm{E}} \tag{5.5}$$

where θ_{E} is the Einstein radius, the radius within which multiple images can occur. For the SIS case this is

$$\theta_{\mathrm{E}} = 4\pi \frac{D_{\mathrm{ls}}}{D_{\mathrm{s}}} \left(\frac{\sigma}{c}\right)^2 \tag{5.6}$$

In our second mass profile we add a uniform density plane to the isothermal profile (SIS+plane). This is a good approximation to the effects of clustering and large scale structure (as pointed out by Wu et al., 1996), because a distribution of isothermal spheres with an auto-correlation function of the form $\xi(r) \sim r^{-2}$ produces a uniform mass surface density. The true auto-correlation function slope is ~ -1.8, which produces a sheet of matter which is uniform to better than 10%. The total surface density then becomes

$$\Sigma = \Sigma_{\mathrm{c}} + \frac{\sigma^2}{2Gr} \tag{5.7}$$

where Σ_{c} is the mass surface density in the uniform plane. This mass distribution produces the amplification

$$A = \frac{\theta}{\theta - \theta_{\mathrm{E}}(1 - \Sigma_{\mathrm{c}}/\Sigma_{\mathrm{crit}})} \frac{1}{(1 - \Sigma_{\mathrm{c}}/\Sigma_{\mathrm{crit}})^2} \tag{5.8}$$

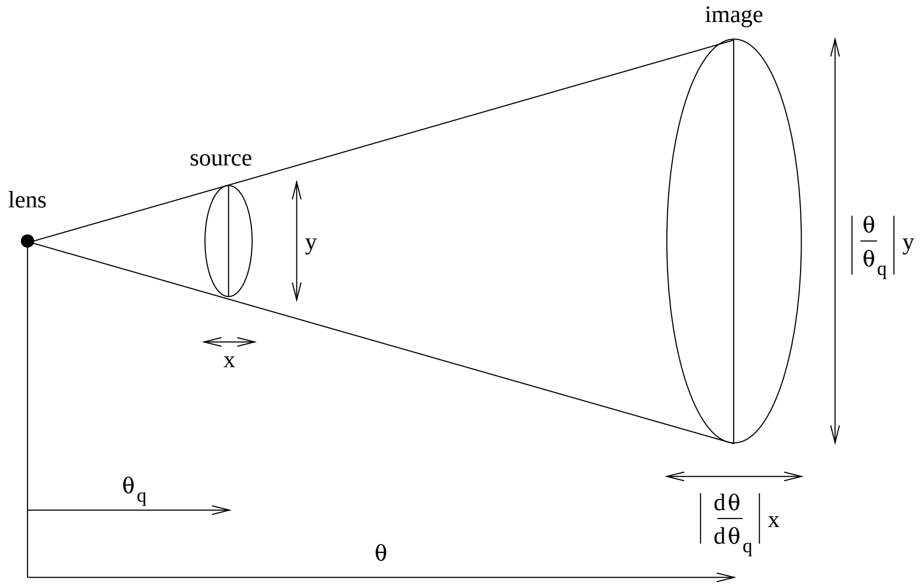

Figure 5.2: The amplification due to gravitational lensing; surface brightness is conserved to give the image a greater total brightness which depends on the distance that the image has been deflected.

where the critical surface density, $\Sigma_{\rm crit}$, is the average surface density required to create multiple images,

$$\Sigma_{\rm crit} = \frac{D_{\rm s} c^2}{D_{\rm ls} D_{\rm l} 4\pi G} \tag{5.9}$$

We now come to the question of how this amplification affects the relative distributions of lenses and sources. Looking at this problem from a statistical point of view, we see that it is possible for gravitational lensing to cause an over- or under-density of source objects near to the lens. The ratio of observed surface density to the true surface density (un-lensed) is the enhancement factor, q, given by

$$q = \frac{N(< m + 2.5\log(A))}{N(< m)} \frac{1}{A} \tag{5.10}$$

(Narayan, 1989), where A is the amplification factor and $1/A$ is the effective area distortion. $N(< m)$ is the integrated number count of source objects brighter than magnitude m. It is therefore obvious that the enhancement factor is strongly dependent on the form of the integrated number count. If we take a power law form for the counts, say $N(< m) \propto 10^{\beta m}$, the enhancement is given by

$$q = \frac{1}{A} \frac{10^{\beta(m+2.5\log(A))}}{10^{\beta m}} = A^{2.5\beta - 1} \tag{5.11}$$

If $A > 1$ we then have

$$q \begin{cases} < 1, & \beta < 0.4 \\ = 1, & \beta = 0.4 \\ > 1, & \beta > 0.4 \end{cases} \tag{5.12}$$

so q depends only on the amplification and the slope of the integrated source number count. We can then associate the enhancement factor q with the angular cross-correlation function $\omega(\theta)$. This gives

$$\omega(\theta) = q - 1 = A^{2.5\beta-1} - 1 \tag{5.13}$$

5.3 The Correlation of Durham/AAT QSOs and Galaxy Clusters

We first look at the result from the Durham/AAT UVX Survey (Boyle, 1986; Boyle et al., 1990) which shows an anti-correlation between UVX QSO candidates and galaxy clusters (BFS88). This cross-correlation was carried out within 7 UKST fields, using COSMOS scans of photographic plates. Three of these also had emission line objects selected from objective prism plates and two other fields contained only emission line selected objects. Extensive spectroscopy of the UVX catalogue (Boyle et al., 1987) suggested that with a colour limit of $u' - b < -0.4$ there was ~ 55 per cent contamination by Galactic stars. In the UVX sample used, the $u' - b$ selection criterion was tightened to $u' - b < -0.5$, reducing this contamination to 25 per cent while keeping 85 per cent of the spectroscopically identified QSOs. The UVX catalogue was then split into two magnitude limited samples, $17.9 < b < 19.9$ (bright) and $17.9 < b < 20.65$ (faint). The galaxy catalogue consists of all galaxies to a limit of $b_{\rm J} = 20.0$ and the cluster sample was created using a multiplicity algorithm (Gott & Turner, 1977; Stevenson, 1985). Groups of seven or more galaxies with density greater than 8 times the average for the field were classed as clusters, which amounted to 10 per cent of the total number of galaxies. The emission line catalogue was taken from various sources (Savage & Bolton, 1984; Clowes & Savage, 1983; Chen, 1984; Savage et al., 1984). Cross-correlation was carried out between the entire galaxy catalogue and the UVX sample but no correlation was found on any scale. Cross-correlation of cluster galaxies with the UVX catalogue resulted in negative correlations on scales $< 5'$ for both the bright and faint samples, the bright sample showing a marginally more negative clustering signal. This can be interpreted as due to the decrease in contamination from the smaller photometric errors at brighter magnitudes. A negative correlation was also found between the emission line objects and the cluster galaxies; however, we will not discuss the emission line catalogue any further as the selection process used (objective prism plates) may tend to introduce negative correlations with dense regions.

5.3.1 A comparison of lensing models and the data

The effect of gravitational lensing is strongly dependent on the slope of the QSO number-magnitude relation at faint magnitudes. We use the number counts from Boyle, Shanks & Peterson (1988) which give a faint end slope of $\simeq 0.28$. A flatter slope would reduce the lensing mass required. The separation of observer, lens

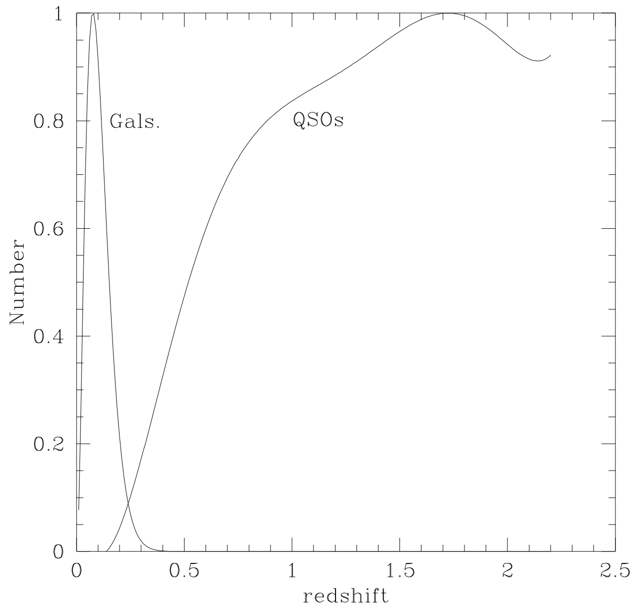

Figure 5.3: Redshift distributions assumed for the galaxy and QSO populations in the lensing models described in the text. The normalizations of the two curves are arbitrary.

and source also affects the lensing amplification. To take this into account in our model, we integrate the known QSO redshift distribution over the effective range of the Durham/AAT survey ($0.3 < z < 2.2$). This gives us an effective lensing amplification for a particular lens mass. For the galaxies we assume the analytic form of $N(z)$ given by Baugh & Efstathiou (1993):

$$\frac{\mathrm{d}N}{\mathrm{d}z} \propto z^2 \exp\left[-\left(\frac{z}{z_{\mathrm{c}}(m)}\right)^{3/2}\right] \tag{5.14}$$

where $z_{\mathrm{c}} = (0.016(b_{\mathrm{J}} - 17.0)^{1.5} + 0.046)/1.412$. This is shown integrated to $b_{\mathrm{J}} = 20$ in Fig. 5.3 along with a polynomial fit to the QSO $N(z)$. It is clear from this plot that the two populations occupy almost completely independent volumes, less than 1% of the QSOs are at $z < 0.3$ while less than 0.5% of the galaxies are at $z > 0.3$. We assume an $\Omega_0 = 1$ cosmology throughout this analysis, but it should be noted that when the lensing mass is at low redshift ($z \sim 0.1$) cosmology has a relatively small effect as $D_{\mathrm{s}} \sim D_{\mathrm{ls}}$.

We compare the SIS lens model (from Eqs. 5.5 and 5.13) to the cross-correlation results from the faint sample. Using a minimum χ^2 fit the velocity dispersion is $\sigma = 1165^{+76}_{-90}\mathrm{kms}^{-1}$ (reduced $\chi^2 = 1.40$). The equivalent Einstein radius for the fit is $0.58'$. The dotted line in Fig. 5.4 shows this model. The two component SIS+plane model (Eqs. 5.8 and 5.13) is shown as the dashed line in Fig. 5.4, the best fit in this case has velocity dispersion $\sigma = 1063^{+110}_{-142}\mathrm{kms}^{-1}$ (the equivalent Einstein radius for this is $0.46'$) and the surface density in the plane of $\Sigma_{\mathrm{c}} = 0.0569 \pm 0.0238h$ g cm^{-2}. The reduced χ^2 for this fit is 1.07. The confidence levels for this fit are shown in Fig. 5.5. As discussed above, even with an extreme $U - B$ selection there will be $\sim 25\%$ contamination. Allowing for this contamination in our models, assuming

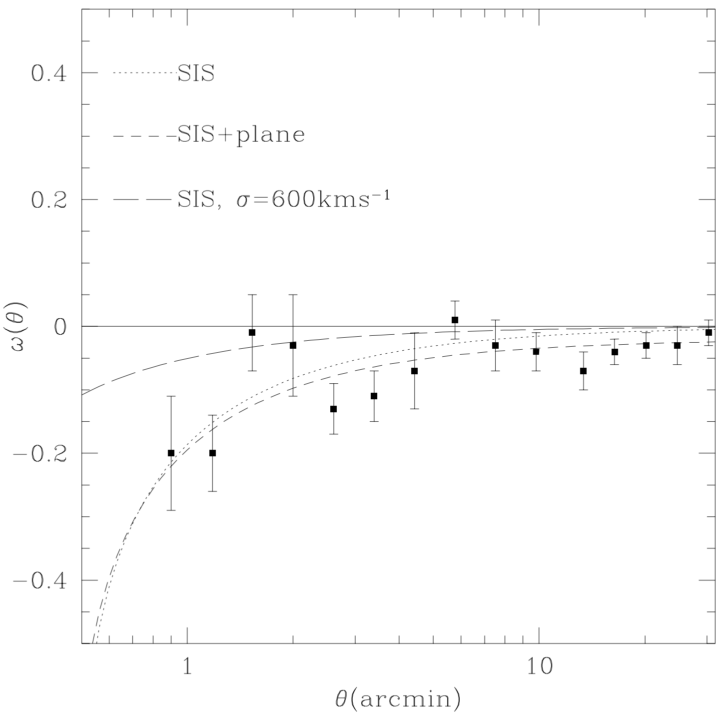

Figure 5.4: UVX-cluster cross-correlation for the faint UVX sample of BFS88 showing the best fit models; the dotted line shows the best fit single isothermal sphere model ($\sigma = 1165^{+76}_{-90}\mathrm{kms}^{-1}$), while the dashed line shows the isothermal sphere plus constant density plane. The long-dashed line shows a lensing SIS model with $\sigma = 600\mathrm{kms}^{-1}$.

that the cross-correlation between the stellar contamination and the galaxy clusters is zero, we find that the best fit parameters are increased. For the SIS model we find $\sigma = 1286^{+72}_{-91}\mathrm{kms}^{-1}$, and for the two component model $\sigma = 1205^{+85}_{-108}\mathrm{kms}^{-1}$ and $\Sigma_c = 0.0779 \pm 0.0232h$ g cm^{-2}. Confidence contours for this fit are also shown in Fig. 5.5.

The values found are significantly larger than directly measured velocity dispersions of poor clusters and groups. However, because BFS88 correlate cluster members with UVX objects, they effectively weight each cluster by the number of member galaxies. Stevenson et al., (1988) find the fraction of clusters, defined using the multiplicity algorithm, as a function of the number of members, which is an approximate power-law with a slope of -2.2. From this we can calculate the mean cluster membership, $\bar{n}$. Integrating the relationship between $n = 7$ and $n = 50$ gives $\bar{n} = 15$. However, we should also weight this mean by the number of members; when this is done, $\bar{n} = 20$. Thus, the BFS88 result is probing clusters which typically have ~ 20 members. The density on the sky of these clusters is ~ 0.8 deg^{-2}, which can be compared to the density of clusters in the APM Cluster Catalogue (Dalton et al., 1997, also see Section 5.4 below) of ~ 0.2 deg^{-2} and the density of richness class 0 or greater Abell clusters which is ~ 0.1 deg^{-2} (Abell et al., 1989). Thus an 'average' cluster used by BFS88 is significantly poorer than Abell richness clusters. In this context it appears that the velocity dispersions found assuming the lensing

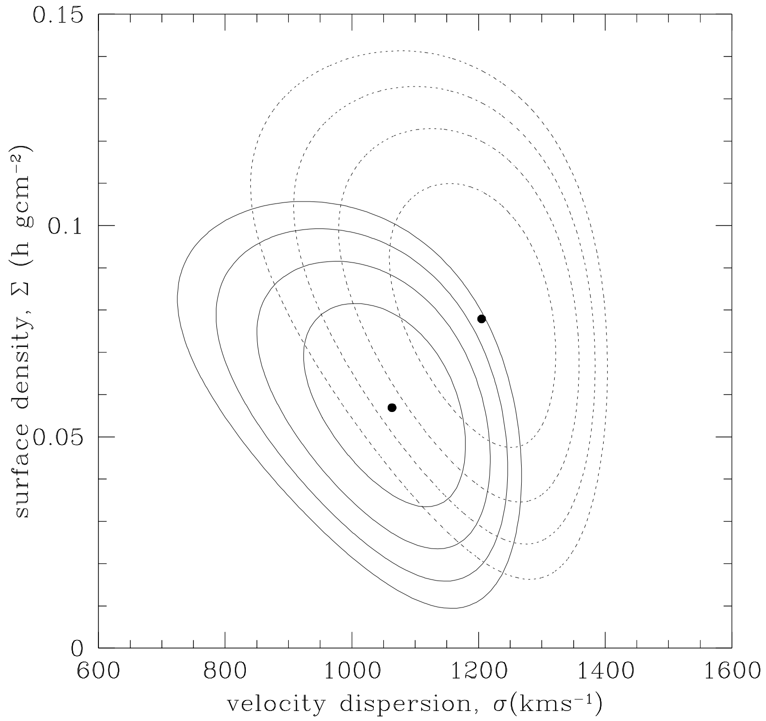

Figure 5.5: Confidence contours for the fit of the two component SIS+plane model to the cross-correlation result for the faint UVX sample. The solid contours show the results uncorrected for contamination, while the dotted lines are corrected for 25% stellar contamination. Contours are at $\Delta\chi^2 = 1, 2, 3, 4$.

models were too large, and we can make a similar argument in the case of the matter density in the uniform plane. Wu et al., (1996) find that the maximum mass likely to be associated with lenses from large-scale structure is $\sim 0.01 - 0.02h$ g cm^{-2}, which assumes that the matter density in clusters is near the critical density (i.e. $\Omega_{\rm clus} \sim 1$). A more conventional velocity dispersion for clusters of this richness is $\sigma \sim 600$kms^{-1}. The lensing model corresponding to this velocity dispersion is plotted in Fig. 5.4. Although this model is formally rejected at $> 5\sigma$, a possible error in the normalization of the BFS88 data on large scales, so that the real $\omega(\theta)$ was zero on $\sim 10'$ scales, would bring the low velocity dispersion model into agreement with the data.

BFS88 originally interpreted the UVX QSO-cluster anti-correlation as being due to absorption by dust present in clusters, the required amount of absorption being $A_{\rm B} \simeq 0.2$ mag. Ferguson (1993) used the relation between the Mg_2 index and $B-V$ colours for a large sample of elliptical galaxies in clusters to determine the reddening due to dust in these clusters. He finds no evidence for any reddening, and the 90% upper limit on the reddening is $E(B-V) = 0.06$, an upper limit which is just consistent with the required absorption, assuming $A_{\rm B} = 4.10E(B-V)$. It could be argued that dust is more likely to survive in poorer clusters and groups as the temperature of the intra-cluster medium will be lower. However, Ferguson finds no evidence for reddening in group environments either. Given the upper limits on dust in clusters, it is still possible that lensing and absorption could both play a part in the anti-correlation found. The cluster masses estimated from statistical lensing might then be brought into line with other estimates.

5.4 The Correlation of 2dF UVX QSOs and Rich Clusters

5.4.1 The data and methods

To further test the lensing hypothesis we turn to a much larger UVX sample, the candidate list for the 2dF QSO redshift survey which was discussed in detail in Chapter 4. This catalogue consists of $\sim$ 46000 UVX QSO candidates covering an area of 740 deg^2 in the magnitude range $18.25 < b_{\rm J} < 21.0$. We use a bluer UVX selection than is used for the full QSO survey in order to reduce the level of contamination, $u - b_{\rm J} \leq -0.5$ leaves only 25% contamination (estimated from the preliminary spectroscopic observations in Chapter 6) and a total of $\sim$ 30000 UVX objects.

We use two galaxy cluster catalogues which overlap our fields: the first is the ACO catalogue (Abell et al., 1989) which has 44 clusters within the bounds of the Northern strip and 158 clusters in the Southern strip (including the 'supplementary Southern clusters') which are richness class 0 or greater. The second sample is the APM Cluster Survey (Dalton et al., 1997) which has 59 clusters in the area of the Southern strip. The ACO catalogue was constructed on the basis of visual inspection of photographic plates and is therefore prone to systematic errors which are largely unquantifiable. This could cause potential problems if the errors introduce spurious clusters into the sample; so by also selecting clusters on the basis of richness we hope to reject the majority of these spurious clusters. The APM sample is selected using an automated algorithm from the APM Galaxy Survey (Maddox, 1988), so any contamination by spurious clusters is likely to be smaller and more uniform. Of course, we should also note that the cluster catalogue used in the BFS88 analysis is a catalogue of poorer clusters, and so more prone to contamination by chance alignments of galaxies along the line-of-sight. All the APM clusters have estimated distances from the photometry of member galaxies and $\sim$ 100 have reliable redshift determinations, which allows us to determine the cross-correlation function as a function of projected proper distance as well as angular distance. Table 5.1 contains the numbers of clusters within the two 2dF QSO survey strips at different richness levels. Different richness parameters are used in the APM and ACO samples. Fig 5.6 shows both the distribution of UVX objects with $u - b_{\rm J} \leq -0.5$ and the positions of the clusters used in this analysis.

The cross-correlation function was estimated in the standard manner, using the estimator in Eq. 2.1, counting the number of UVX objects and random points a distance $\theta \pm \delta\theta/2$ from the cluster centres. The random points were distributed

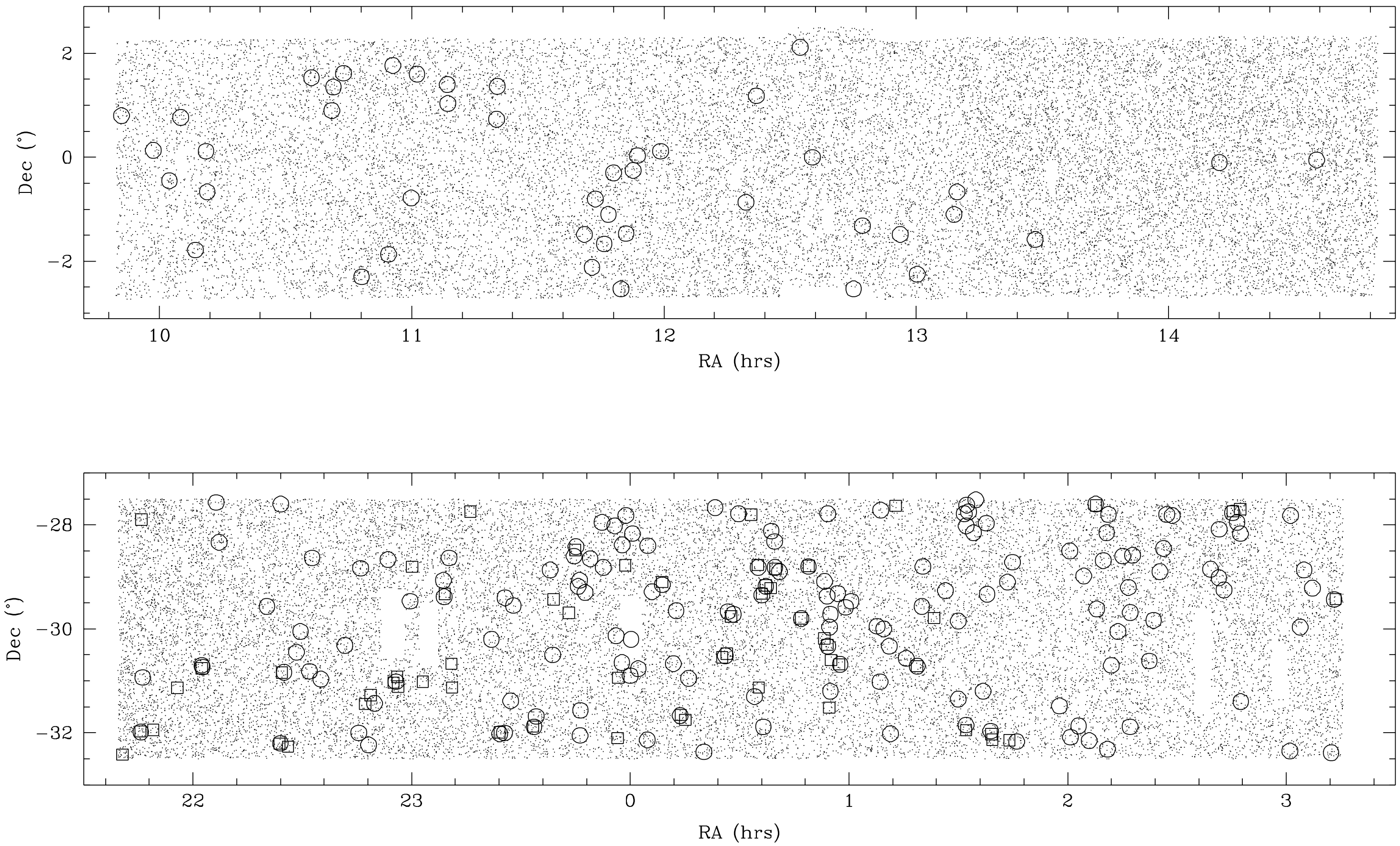

Figure 5.6: The 2dF UVX catalogues for the Northern ($\delta = 0°$) and Southern ($\delta = -30°$) strips with $18.25 \leq b_J \leq 21.0$ and $u - b_J \leq -0.5$. Open circles show the positions of ACO clusters while open squares show the positions of APM clusters. Note that the declination axis has been expanded in order to make these plots clearer.

Table 5.1: Details of the cluster samples used in the cross-correlation analysis with 2dF UVX objects, showing the number of clusters for different richness selections. Note that the APM sample uses a different richness criterion.

Cluster Sample	No. of Clusters $R_{\rm ACO} \geq 0$	$R_{\rm ACO} \geq 1$	$R_{\rm ACO} \geq 2$
ACO South	158	71	22
ACO North	44	28	11
	$R_{\rm APM} \geq 40$	$R_{\rm APM} \geq 45$	$R_{\rm APM} \geq 50$
APM	59	41	27

uniformly within the area of the 2dF UVX sample taking into account areas removed due to bright stars and plate defects. The random point density was 25 times the UVX density.

5.4.2 Results

Before carrying out the UVX-cluster cross-correlation we first measured the cross-correlation function of all the images classified as stellar in our survey area ($17.0 \leq b_{\rm J} \leq 21.0$), with the clusters. Fig. 5.7 shows the results of this cross-correlation. We clearly see a positive signal of amplitude ~ 0.05 from $\sim 1'$ to $40'$. Some fraction of this signal may be due to contamination of the stellar catalogue by galaxies. By comparing the amplitude of this clustering to the cluster-galaxy correlation function, we estimate that there is a possible $\sim 10-15\%$ contamination in the catalogue. In Chapter 6 we find that spectroscopic follow up of the UVX catalogue identifies 16% of the sample as narrow emission line galaxies. However most of these objects are both faint and red, with $b_{\rm J} \geq 20.6$ and $u - b_{\rm J} \geq -0.5$. With $u - b_{\rm J} \leq -0.5$ and $b_{\rm J} \leq 21$ the contamination is 7.7%, while with $u - b_{\rm J} \leq -0.5$ and $b_{\rm J} \leq 20.6$ only 4.9% of the UVX candidates are galaxies. Thus, by using a blue selection with $u - b_{\rm J} \leq -0.5$ we reduce this contamination to a minimum.

The cross-correlation functions for all the clusters in each sample are shown in Fig 5.8, correlated with UVX objects in the magnitude ranges $18.25 \leq b_{\rm J} \leq 21.0$ and $20.0 \leq b_{\rm J} \leq 21.0$. Neither of the cluster samples show a significant cross-clustering signal. The aim of using a fainter sub-sample of UVX objects was to use only objects inhabiting the regime where the QSO number counts are flat. Even this sample fails to show the expected negative correlation which would be the signature of gravitational lensing. We also attempted a cross-correlation of only bright QSOs, $17 \leq b_{\rm J} \leq 19$, (including the bright candidates with $b_{\rm J} < 18.25$ from the bright extension of the 2dF QSO survey which is being observed using the FLAIR instrument), as the steep counts slope over this range should produce strong positive correlations from lensing. However, the numbers of QSOs in this magnitude range is small and the fractional contamination increases to reduce the signal, and

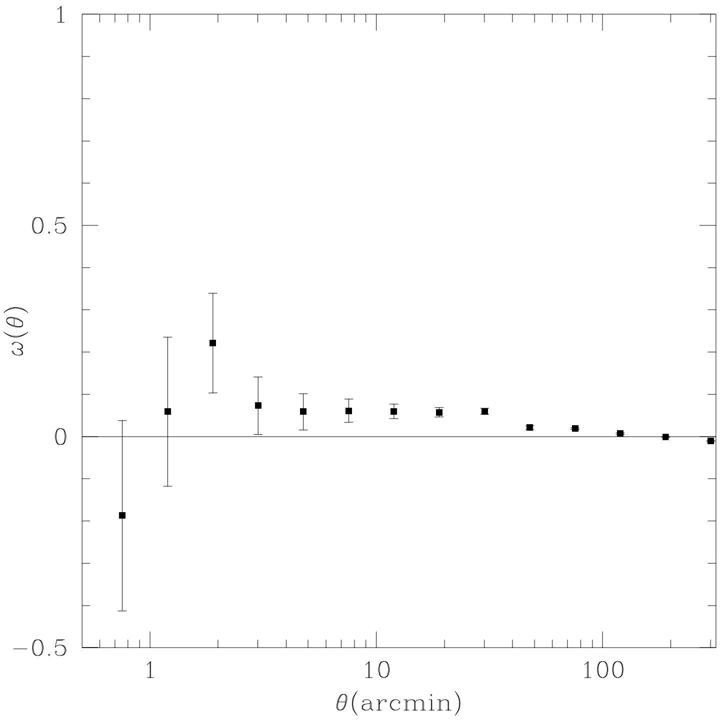

Figure 5.7: The cross-correlation function of all stellar objects ($17.0 \le b_J \le 21.0$) and APM galaxy clusters in the Southern 2dF catalogue area.

no positive correlation was seen in this regime.

We next look at the cross-correlation as a function of richness, demonstrated in Fig. 5.9. The cross-correlation with APM clusters shows a marginally significant anti-correlation on scales $\sim 3 - 20'$; for $R_{\rm APM} \ge 45$ we find $\omega(\theta < 24') = -0.115 \pm 0.061$ and for $R_{\rm APM} \ge 50$, $\omega(\theta < 24') = -0.104 \pm 0.075$. The ACO sample does not show this signal, with $\omega(\theta < 24') = -0.002 \pm 0.043$ ($R_{\rm ACO} \ge 1$) and $\omega(\theta < 24') = 0.077 \pm 0.076$ ($R_{\rm ACO} \ge 2$). At angular scales greater than $30'$ the cross-correlation function is zero in all cases, thus the constant density plane lensing model cannot be consistent with these results on large scales. This might be reasonable as the model is only valid in the regime where $\xi_{\rm cc}(r) \sim r^{-2}$. At larger scales the cluster auto-correlation function turns over, producing a cut-off. Fig. 5.10 shows the projected cross-correlation function for APM clusters ($R \ge 45$), using the photometric distance estimate, which demonstrates that this cut-off is actually at $\sim 1\ h^{-1}$ Mpc, the scale of galaxy clusters, rather than $\sim 20\ h^{-1}$ Mpc which is the scale at which the power-law in the cluster-cluster auto-correlation function breaks. The clustering amplitude within $1\ h^{-1}$ Mpc in Fig. 5.10 is $\omega(r < 1\ h^{-1}\ {\rm Mpc}) = -0.197 \pm 0.078$.

An isothermal sphere profile can be fit to this data, but only the richer APM selected clusters give a significant measure of the velocity dispersion. This is $\sim 2600 \pm 1000{\rm kms}^{-1}$ but is somewhat dependent on the range of scales fit as at small scales, close to the Einstein radius, the lensing model produces a quickly changing correlation function. Added to this problem, within the Einstein radius the model

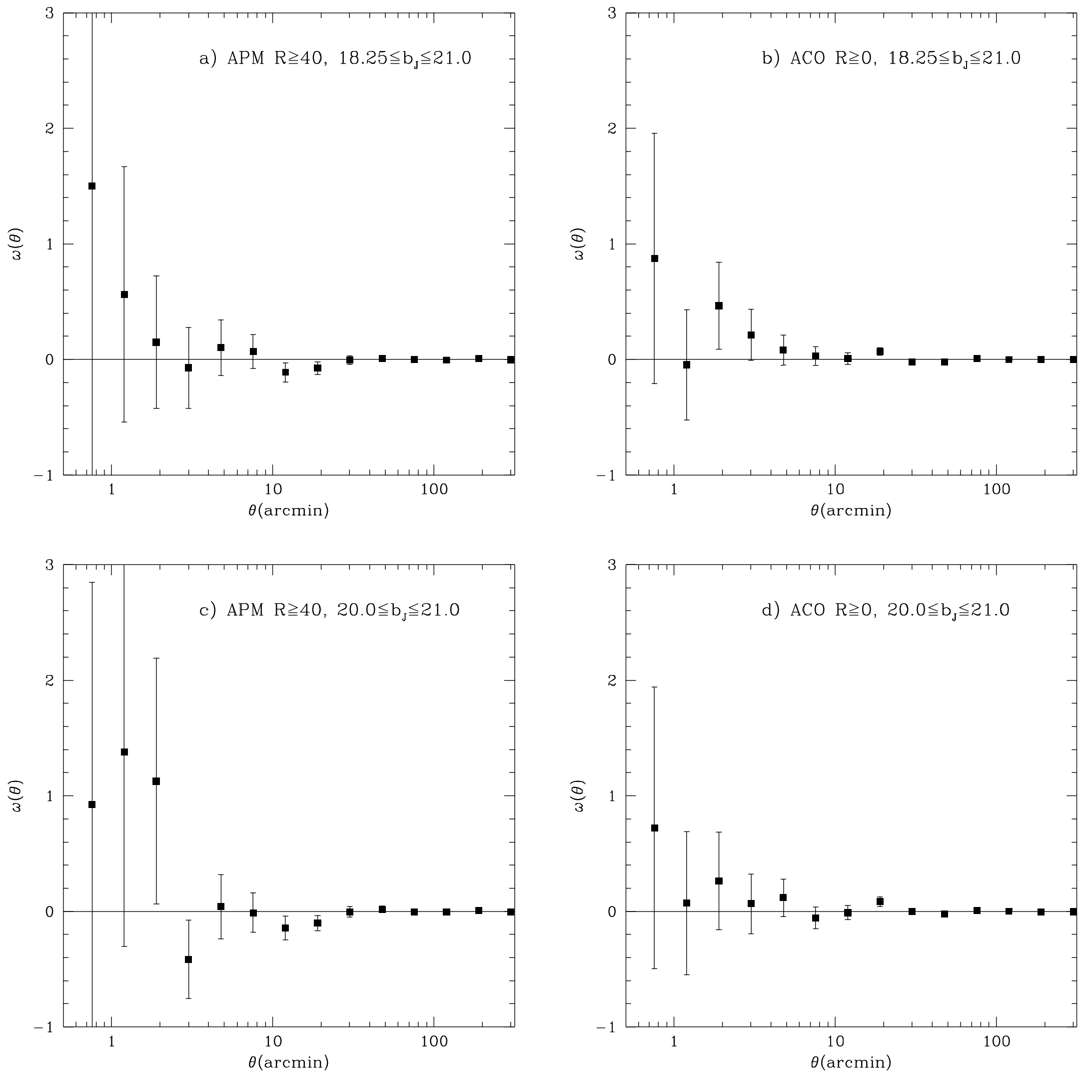

Figure 5.8: The results of angular cross-correlation between APM and ACO clusters and UVX objects ($u - b_{\rm J} \leq -0.5$). a) UVX objects in the range $18.25 \leq b_{\rm J} \leq 21.0$ and APM clusters with $R_{\rm APM} \geq 40$, b) UVX range: $18.25 \leq b_{\rm J} \leq 21.0$, ACO clusters: $R_{\rm ACO} \leq 0$, c) UVX range: $20.0 \leq b_{\rm J} \leq 21.0$, APM clusters: $R_{\rm APM} \leq 40$, d) UVX range: $20.0 \leq b_{\rm J} \leq 21.0$, ACO clusters: $R_{\rm ACO} \leq 0$.

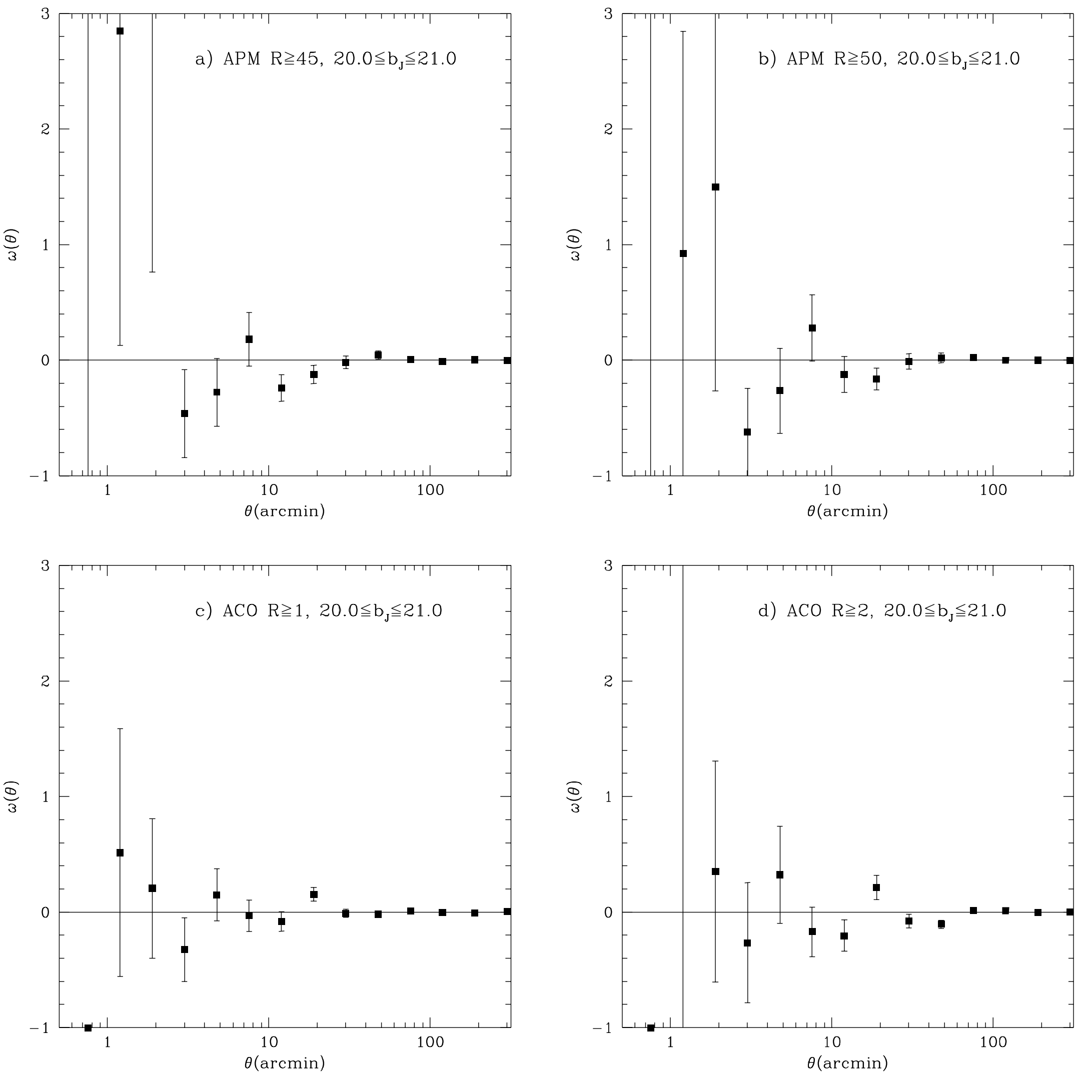

Figure 5.9: The results of angular cross-correlation between APM and ACO clusters and UVX objects ($20.0 \leq b_{\mathrm{J}} \leq 21.0$ and $u - b_{\mathrm{J}} \leq -0.5$) for a) APM $R_{\mathrm{APM}} \geq 45$, b) APM $R_{\mathrm{APM}} \geq 50$, c) ACO $R_{\mathrm{ACO}} \geq 1$ and d) ACO $R_{\mathrm{ACO}} \geq 2$.

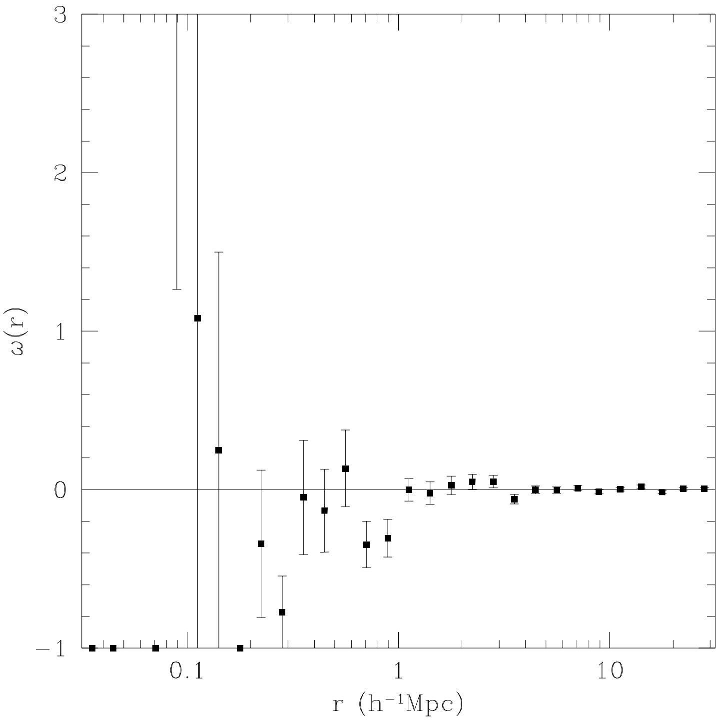

Figure 5.10: Projected cross-correlation function for UVX objects ($20.0 \leq b_{\rm J} \leq 21.0$ and $u - b_{\rm J} \leq -0.5$) and APM clusters $R_{\rm APM} \geq 45$

used for the amplification is no longer valid and multiple images can be produced. It is clear from the data presented here that we cannot obtain a robust result for the correlation between rich clusters and UVX objects, which is likely to be due to the small number of cluster centres, as compared to the result of BFS88 which used individual cluster member galaxies. To demonstrate this point we show a comparison of the two data sets in Fig. 5.11. Obviously, the errors are considerably smaller in the BFS88 data.

5.5 The Correlation of QSOs and $b_{\rm J} < 23$ Galaxies

Results from Chapter 2 suggested that there could be a lensing component to the cross-correlation of faint, $b_{\rm J} < 23$, galaxies and optically selected QSOs, as a small anti-correlation was measured between the two populations. Here we attempt to model the effect of the lensing contribution on this result. Using the redshift distributions of the galaxy and QSO populations in Chapter 2 we construct Monte-Carlo simulations to calculate the expected correlation signal as a function of redshift. These simulations model the individual galaxy potentials as isothermal spheres, and take into account the clustering of galaxies by also adding a constant density plane as discussed above. Wu et al., (1996) calculate that the maximum matter surface density contributed by large-scale structure is $\sim 0.01 - 0.02h$ g cm^{-2} assuming that the amount of matter in galaxies is $\Omega_{\rm g} \sim 1$. Typical velocity dispersions for galaxies

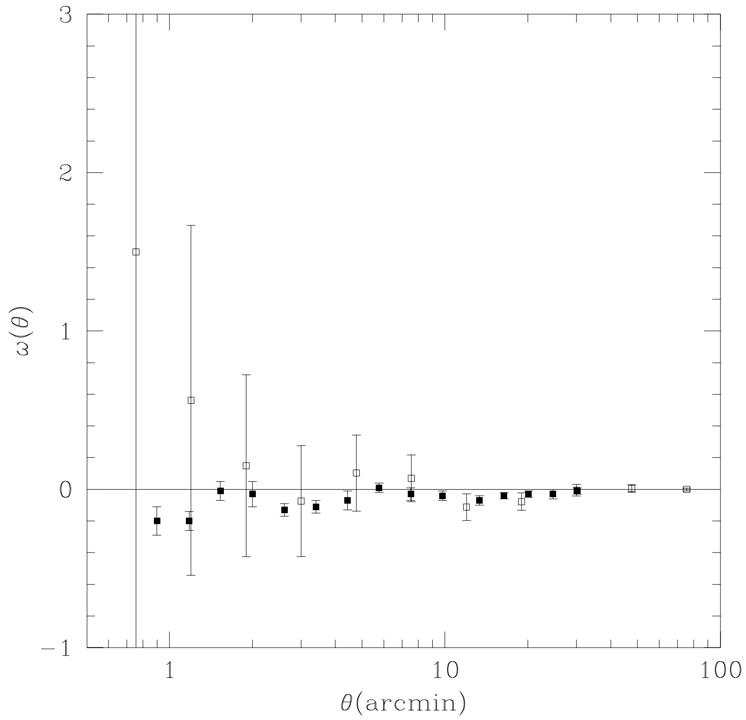

Figure 5.11: A comparison of the cross-correlation results of UVX QSOs and galaxy clusters from BFS88 and from the analysis of the 2dF UVX catalogue discussed in the text. The solid squares are the BFS88 data while the open squares are the cross-correlation of 2dF UVX candidates ($18.25 \le b_{\rm J} \le 21.0$) with APM clusters ($R_{\rm APM} \ge 40$).

are ~ 200kms^{-1}, so we produce Monte-Carlo simulations with velocity dispersions of 200 and 400kms^{-1} and constant density planes with $\Sigma = 0.0$ and $0.02h$ g cm^{-2}. Fig. 5.12 shows how the clustering amplitude in these simulations changes with redshift. The extreme case of $\Sigma = 0.02h$ g cm^{-2} and $\sigma = 400$kms^{-1}, which can contribute ~ -0.02, can account for most of the negative signal found for QSOs at $z < 1.5$, while it cannot account for the negative correlation found at higher z. This has no effect on the rejection of high clustering amplitude models in Chapter 2, but does make the models with low clustering amplitude more consistent with the data.

5.6 Conclusions

We look at the correlation of QSOs and foreground galaxy clusters and interpret the measured anti-correlation in terms of statistical gravitational lensing. We come to the following conclusions:

1) The velocity dispersion required to fit the BFS88 result, allowing for stellar contamination in the UVX sample, is $\sigma = 1286^{+72}_{-91}$kms^{-1}. If a uniform density sheet is added to the mass profile we require $\sigma = 1205^{+85}_{-108}$kms^{-1} and $\Sigma_{\rm c} = 0.0779 \pm 0.0232h$ g cm^{-2}. The velocity dispersion found is similar to that of rich galaxy

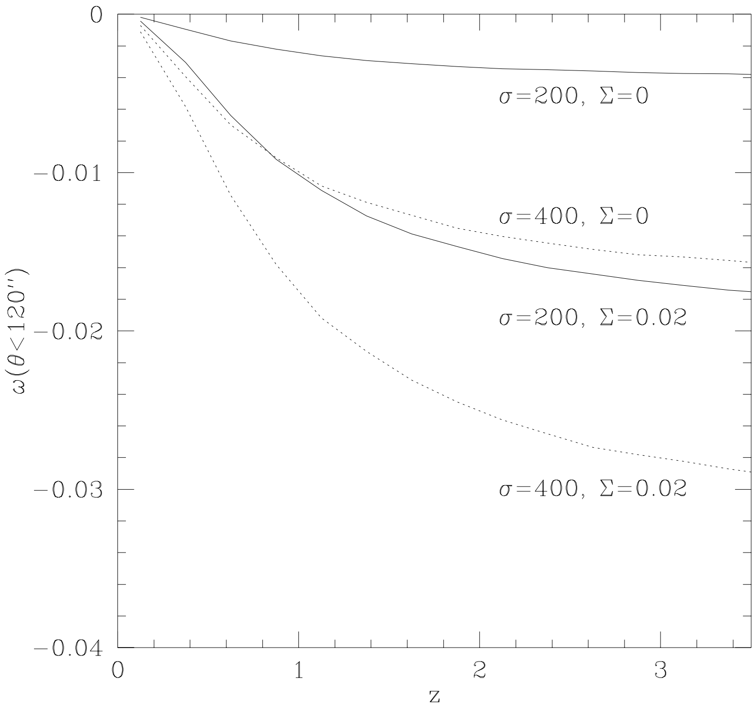

Figure 5.12: Estimated angular cross-correlation function of QSOs with faint, $b_J < 23$, galaxies due to lensing, as a function of QSO redshift. The correlation amplitude is measured within 120″ from Monte-Carlo simulations, with velocity dispersions 200 and 400kms^{-1} and planes with zero, and $\Sigma = 0.02h$ g cm^{-2} mass surface densities.

clusters, although the majority of clusters in the sample will be poor clusters so the values we find are larger than the values expected from other mass estimates. The density in the plane is larger than expected from estimates based on the known clustering properties of galaxy clusters, a value of $\sim 0.02h$ g cm^{-2} being the largest expected density in an $\Omega_0 = 1$ universe. An offset in the measured clustering at large scales ($\sim 20 - 30'$) in BFS88 would allow a more reasonable model, with $\sigma \sim 600$kms^{-1} to fit the data.

2) We test the lensing model with the 2dF UVX catalogue and the ACO and APM cluster catalogues. No significant correlation is found between the two data sets, only rich APM clusters ($R_{\rm APM} \geq 45$) and faint UVX objects show any sign of anti-correlation, although this is not strongly significant. At scales larger than $\sim 1\ h^{-1}$ Mpc the correlation function is zero in all cases. This last point does suggest that the uniform density plane is not an appropriate model to use as we would expect to see a signal on $\sim 10 - 20\ h^{-1}$ Mpc scales. In fact, the large planar density found using the two component model with the BFS88 data is inconsistent with the 2dF UVX/rich cluster data on these large scales.

3) The results found in Chapter 2 are not significantly affected by the inclusion of gravitational lensing. Lensing can account for most of the anti-correlation seen at low ($z < 1.5$) redshift, making a contribution of ~ -0.02. The high clustering amplitude models in Chapter 2 are still ruled out, while the low amplitude models

become more consistent with the data.

We show that it is possible to interpret the anti-correlation of QSOs and foreground clusters as an effect due to gravitational lensing. Not only this, we also find that the small anti-correlation found in Chapter 2 between QSOs and $b_J < 23$ galaxies can be mostly explained by lensing. Generally, cluster masses predicted by the data are higher than expected from other mass estimates. Combining lensing with a small dust component in clusters could reduce the masses required to reasonable levels.

The 2dF QSO survey will produce a large homogeneous catalogue in the magnitude range $17 \leq b_J \leq 21$, allowing a full test of the lensing hypothesis. The present stellar contamination, which is particularly dominant at bright magnitudes, combined with the relatively small number of clusters in the survey area restricts our ability to detect the characteristic features of lensing. The completed redshift survey will not have the problem of contamination, and this, combined with a variety of cluster catalogues of varying richness, will allow us to find the positive and negative signals which are the unambiguous indication of gravitational lensing.

Chapter 6

Spectroscopic Observations of UVX QSO Candidates

6.1 Introduction

In this chapter we describe preliminary spectroscopic observations of the UVX catalogue discussed in Chapter 4. Two separate investigations were undertaken to ascertain the effectiveness of the UVX catalogue at selecting QSOs. Observations were carried out using the 2-degree Field (2dF) (Taylor, 1995) and FLAIR-II (Parker & Watson, 1995) fibre-optic, multi-object spectroscopy systems at the AAT and UKST respectively.

First, the catalogue was sub-divided into a bright and a faint portion; the bright sample containing all UVX objects with b_J magnitude in the range $17.0 \leq b_J < 18.25$, while the faint sample covered the range $18.25 \leq b_J \leq 21.0$. The bright sample was observed using FLAIR, while for the faint sample the 2dF instrument was used. The primary aims of obtaining the FLAIR data were to reduce the amount of scattered light from bright objects in the 2dF spectrograph, and secondly, to test the effectiveness of the FLAIR system at obtaining QSO spectra. Below we will first discuss observations of the bright FLAIR sample, followed by the faint 2dF sample in Section 6.3. These sections will include a discussion of the various properties of the samples, including completeness and contamination rates. Our conclusions are given in Section 6.4.

This survey is still in progress, with further data being obtained during the writing of this thesis. The data presented here constitute a small fraction of the final sample, and have been primarily used to estimate the effectiveness of the survey. We also have the opportunity at this time to make improvements to the catalogue, based on the spectroscopic results in this chapter.

Table 6.1: Details of the FLAIR observations of QSO survey fields.

field name	RA (B1950)	Dec (B1950)	exposure time(s)	No. of QSO candidates
f411-b1	00 46 00	-30 00 00	8×3000	64
f469-b1	23 00 00	-30 00 00	9×3000	75

6.2 The Bright FLAIR QSO Sample

6.2.1 Observations and the FLAIR-II instrument

Two fields were observed using FLAIR over a period of 3 nights. The field f411-b1 was observed on the night of the 13/9/96, while the field f469-b1 was observed over the two nights 12-13/10/96 (Observers M. Hartley and K. Russell). Two plate holders are available to position fibres, the first with 73 fibres and the second with 92. The fibres are $6.7''$ (100μm) in diameter. Field f411-b1 was observed with the first plate holder, while field f469-b1 used the second. FLAIR has a semi-manual fibre positioning system. Fibres are fed into a floor mounted (so highly stable) spectrograph. The FLAIR detector is a 400×578 thinned, back-illuminated EEV CCD, with a read-out noise of $\simeq 11e^-$ and a gain of $\simeq 1e^-$/ADU. A 250B grating was used giving a resolution of 6.3Å/pixel. Bias frames were taken at the beginning of each night, followed by mercury-cadmium (Hg-Cd) and neon (Ne) arcs. A number of 3000 second exposures were obtained on our survey fields, (see Table 6.1). On both fields a number of fibres (~ 10) were allocated to the night sky. At the end of the night further arcs were taken along with dome flat-fields. Observing conditions were bad, with cirrus and poor seeing, during the night of the 13/9/96 (f411-b1 field).

6.2.2 FLAIR data reduction

The FLAIR data were reduced using the IRAF astronomical reduction package according to Drinkwater & Holman (1996) . The object, flat-field and arc frames were de-biased, overscan corrected and trimmed using the **imred.ccdred.ccdproc** task. Flat-fields were then median combined using **flatcombine**, with a 4σ clipping to remove CREs. The Hg-Cd and Ne arcs taken at the beginning of the night were added together using **imarith**, those taken at the end of the night were combined separately. The object frames were averaged together in groups of 2 or 3 using **imcombine**. The algorithm CRREJECT was used with a high threshold $\simeq 7\sigma$ in order to remove CREs. This threshold removes almost all of the CREs while not removing any real data from the spectra. The frames were combined in groups of 2 or 3, so that images combined together have similar seeing, and there is not a significant shift in the position of the spectra. The final reduced spectra can then be summed at a later stage.

Spectral extraction was performed using the **imred.specred.dofibers** package. This is a multi-task package which automatically traces each fibre aperture along the CCD and extracts the spectra. It then extracts the flat-field spectra and uses these, summed in the dispersion direction, to normalize the fibre throughput. The next stage is to wavelength calibrate the spectra. **dofibers** matches the arc lines to an input list of line wavelengths and produces a polynomial fit to each individual arc spectrum. These fits are then used to wavelength calibrate the object spectra. Finally, **dofibers** median combines the sky spectra and subtracts the composite sky spectra from the object spectra.

This process resulted in set of sky subtracted, wavelength calibrated, object spectra; spectra of the same object were then combined using the **scombine** task.

6.2.3 Spectroscopic results

We now discuss the spectra obtained from the FLAIR observations. The spectra were identified by eye using the `REDSHIFT` program written by Dr. K. Glazebrook. The stellar spectra were classified according to an approximate spectral type. Objects which were possible QSOs, but did not show definite broad emission lines were classified as QSO?. The quality of QSO redshifts were also categorized; (1) signifies a certain redshift with two or more strong lines, (2) signifies a probable redshift with one strong line and one or more low signal-to-noise lines, (3) signifies an uncertain redshift, with only one strong line or only low signal-to-noise lines. This should be only be taken as a guide, as QSOs which show only Mg II emission were generally classified as having a class (1) redshift.

Table 6.2 shows the composition of the FLAIR sample. A total of 139 FLAIR spectra were obtained from the two pointings. We discuss the galactic and non-galactic components of the sample below. We should first note that the total number of candidates in the f411 and f469 fields is 76 and 158 respectively, so less than half of the QSO candidates in the f469 field were observed, candidates which were observed being chosen at random. The difference in the number of candidates in the two fields is due to several effects. Photometric zero-point errors and the position of f469 closer to the galactic plane contribute to this difference. The dominant effect however, appears to come from the broadening of the stellar locus at bright magnitudes in f469 (see Fig. 4.7).

Galactic stars

The majority of objects identified are found to be halo subdwarfs. Most lie in the spectral classification range $\sim A0$ to $G5$, although 2 are identified as K stars. All

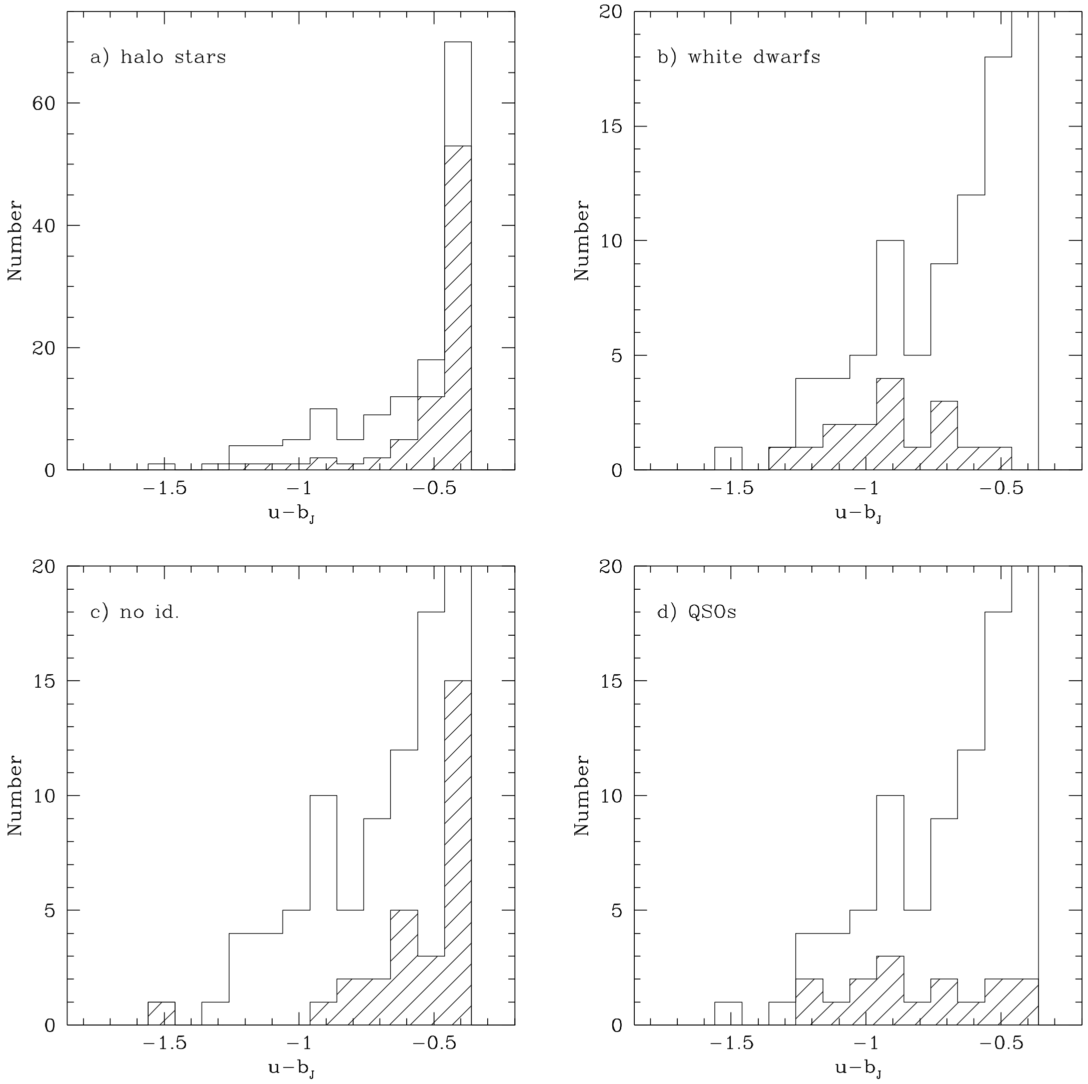

Figure 6.1: Histograms of the colour distribution of the components of the FLAIR sample. The shaded histograms show the distributions for the a) halo stars, b) white dwarfs, c) objects with no identification and d) QSOs respectively. The unshaded histogram in each case is for reference and shows the colour distribution of all observed objects. The two CVs are included in the white dwarf plot and the one QSO? ($u - b_{\rm J} = -0.53$) is included in the QSO plot.

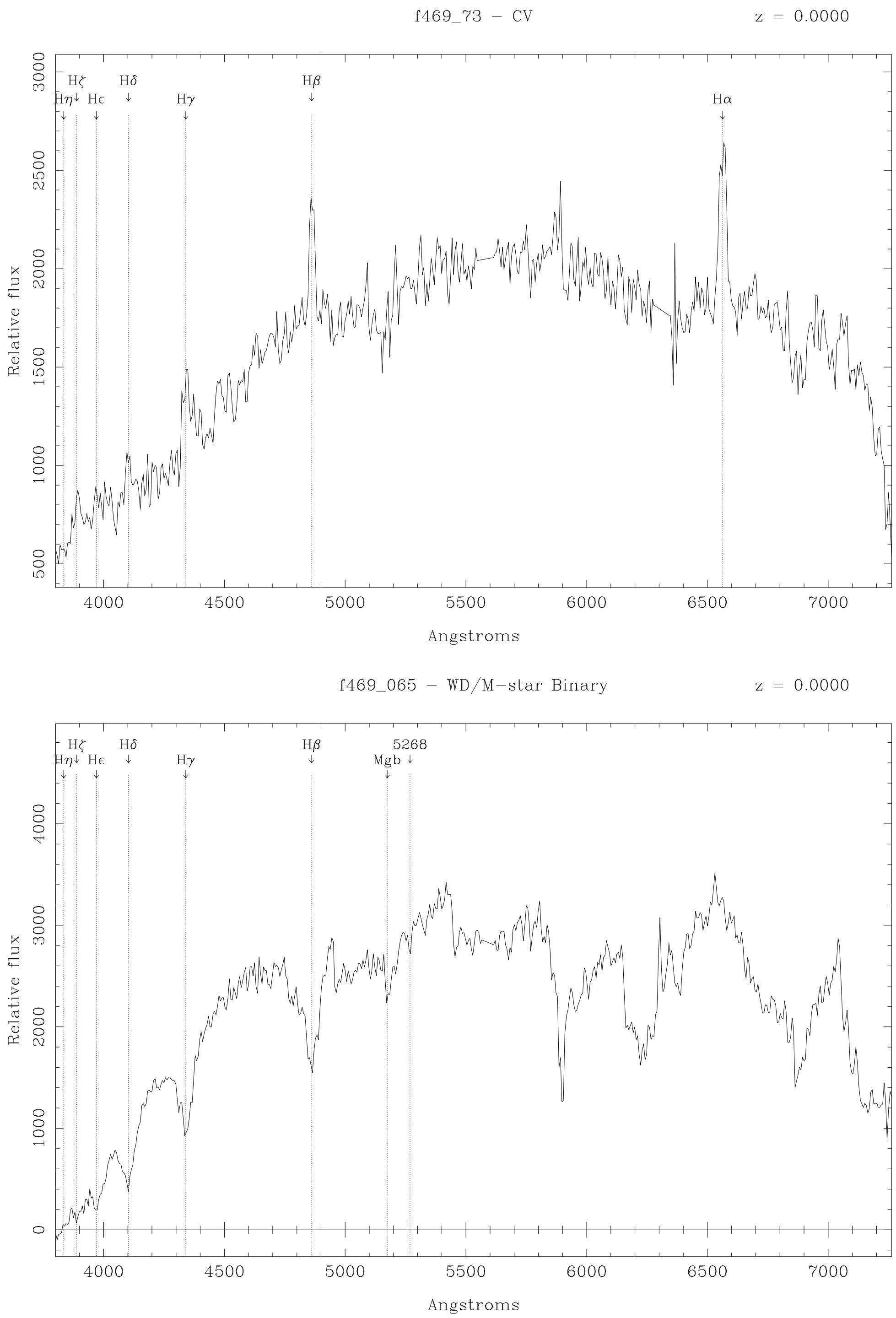

Figure 6.2: FLAIR spectra of a cataclysmic variable (top) and a DA white dwarf/M-star binary system (bottom).

Table 6.2: The composition of the FLAIR bright QSO sample.

	Number		
Identification	f469	f411	**Total**
subdwarf	53	25	**78**
White dwarf	8	7	**15**
CV	1	1	**2**
QSO	7	8	**15**
BAL QSO	0	0	**0**
QSO?	0	1	**1**
NL Galaxy	0	0	**0**
No id.	6	23	**29**
Total	75	64	**139**

these objects would generally be expected to have colours of $U-B\sim 0$ or redder, so are likely to have been added into the sample through photometric errors. The colour distribution of halo stars, shown in Fig. 6.1a, is strongly peaked at the red limit of our selection, demonstrating that these stars do not in any way form a complete sample. Almost all the remaining stars (15) are white dwarfs (WD). Fig 6.1b shows that these objects have blue colours and are therefore likely to form a complete sample. 12 of these show only hydrogen Balmer absorption lines and therefore belong to the DA class of white dwarfs. Of these, two objects f411_075 and f469_046 show evidence of core emission or line splitting in Hβ (f411_075 and f469_046), Hγ (f411_075) and Hδ (f411_075). This is possibly Zeeman splitting induced by strong magnetic fields, although the signal-to-noise is not sufficient to measure the effect. The remaining 3 WDs comprise a DAO WD, showing evidence of He II absorption, a DAB WD with neutral Helium absorption lines and one peculiar object showing broad hydrogen Balmer lines at the blue end of the spectrum ($\lambda < 5000$Å), but molecular absorptions bands at the red end of the spectrum (Fig. 6.2), usually associated with an M class star. This is most likely to be a WD(DA)/M-star binary system. Finally, we find two stellar objects with hydrogen Balmer emission lines. These are cataclysmic variables (CVs), which are accreting white dwarfs, and have colours similar to that of WDs (see Fig. 6.2).

QSOs

We find 15 QSOs in the two fields and one further QSO? object; spectra and details of these are listed in Appendix A. Their colour distribution is shown in Fig. 6.1d. Of the 15 confirmed QSOs only one is outside of the redshift range $0.3 < z < 2.2$. The magnitude and redshift distributions of these objects are shown in Fig. 6.3. We will show and discuss a combined number-magnitude relation for the FLAIR

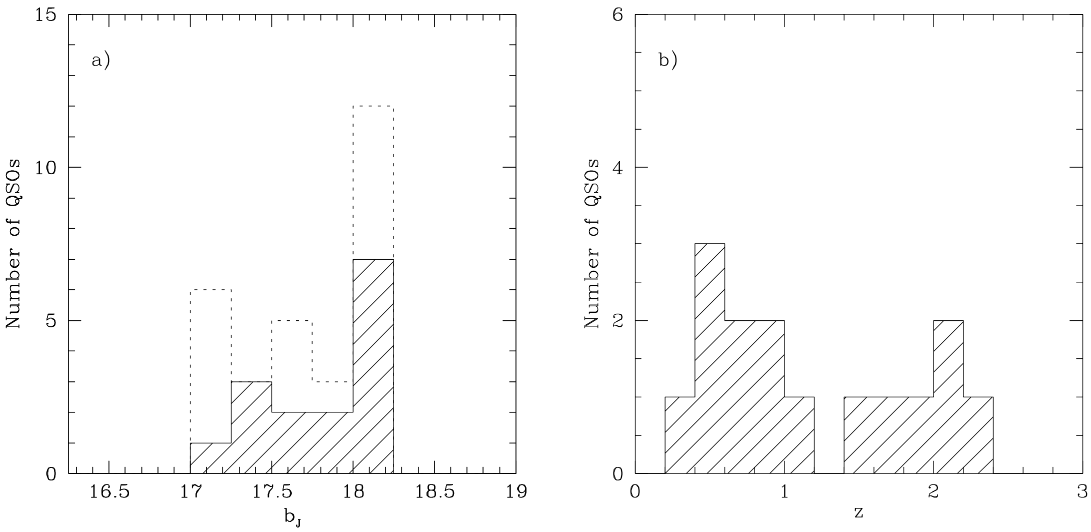

Figure 6.3: Distribution of QSOs in the FLAIR sample as a function of a) magnitude and b) redshift. The shaded histogram shows the QSO distributions in both cases. The dotted histogram in a) shows the distribution of unidentified sources.

and 2dF samples in Section 6.3.4. The redshift distribution is weighted towards low redshift, as we would expect in a bright QSO sample (see the LBQS $N(z)$ in Fig. 3.1). The LBQS (Hewett et al., 1995) shows a surface density of QSOs of 0.90 deg^{-2} between $b_{\rm J} = 17.0$ and 18.25, over the redshift range $0.3 < z < 2.2$. Considering the fraction of candidates observed in each field we find that the *effective* areas of the two fields are 20.86 and 10.62 deg^2 for the f411 and f469 fields respectively. The density of QSOs we find over the range $0.3 < z < 2.2$ is therefore 0.44 ± 0.12 QSOs per sq. deg, a factor of 2 less than found in the LBQS, with f411 and f469 having densities of 0.34 ± 0.13 and 0.66 ± 0.25 deg^{-2} respectively.

The LBQS has been shown to be extremely effective at selecting QSOs (Hewett et al., 1995) and there are several reasons for our lower density. First, even in this magnitude range we expect $\sim 10 - 15\%$ incompleteness from photometric errors and variability (due to our relatively blue UVX selection threshold). Second, a high fraction of these bright QSOs are found at low redshift. The UVX selection technique is not so effective at low redshift as these objects become both redder than the QSOs at higher redshift and are no longer classified as point sources; both these effects being primarily due to the increasing effect of the host galaxy at low redshift. Third, it is of course possible that there is a residual offset between the LBQS and 2dF $b_{\rm J}$ magnitude systems, which could cause this difference in number density. An offset of 0.1 mag could cause a 20% reduction in the measured QSO density.

We note that the f469 field QSO density is within 1σ of the expected value from the LBQS. The f411 field, which shows a particularly low density of QSOs, contains a high number of unidentified spectra. Over one third of the spectra could not be positively identified, these being mostly at the faint end of the sample where a higher fraction of QSOs is expected (as demonstrated in Fig. 6.3). There are 16 previously known QSOs in the f411 field which lie in the redshift and magnitude intervals $0.3 < z < 2.2$ and $17.0 < b_J < 18.25$. Of these, two are classed as merged objects on the APM scans and are not included in the survey (both are at low redshift, $z \sim 0.3 - 0.4$). One further object is slightly too red to fall within our colour selection (with $u - b_J = -0.35$). Of the remaining 13 QSOs we have obtained spectra of 11 with FLAIR. Of these we classify 6 as certain QSOs, one as QSO? and four have no identification. If we include these objects in our calculation of QSO surface density we find the f411 density to be 0.58 ± 0.17 deg^{-2} (for $0.3 < z < 2.2$), a number much more consistent with the f469 field and closer to the LBQS result. The f469 data show that the UKST/FLAIR, with adequate observing conditions, can obtain $> 90\%$ identifications from our UVX catalogue. This combination can obtain QSO densities consistent with the LBQS.

6.3 The Faint 2dF QSO Sample

6.3.1 Observations with the 2-degree Field instrument

The 2-degree Field instrument is a multi-fibre spectroscopic system which utilizes the wide field of view provided by a 4-component optical corrector. The corrector produces a field of two degrees diameter with some cost in terms of broad band imaging quality. However, for multi-fibre spectroscopy with fibres of $\sim 2''$ diameter ($2.16''$ at the field centre, $2.0''$ at the edges), the small loss due to variations across the field (mostly due to a Chromatic Variation in Distortion), is more than compensated by the increased field of view. There are two field plates onto which the fibres are positioned using a robotic positioner and magnetic buttons. The two field plates provide a substantial reduction in overheads by allowing the positioner to reconfigure one field while the other is being observed. 400 fibres can be positioned on each field, with two identical spectrographs receiving 200 fibres each. The spectrographs use thinned 1024×1024 Tektronix CCDs and there are a variety of low and medium resolution gratings available. Further details of the instrument can be found in the 2dF user manual (Bailey, 1996).

Our observations were carried out during a time of science verification testing. At this time the instrument had only 200 fibres per plate and one spectrograph with an engineering grade CCD (with diminished blue response). We use the 300B grating which has a dispersion of 178.8Å/mm. In order to make effective use of telescope time we combine our observations with those of the 2dF Galaxy Redshift Survey Project. Thus on average each field of 400 fibres will contain ~ 135 fibres observing QSO candidates, ~ 245 fibres observing galaxies and a further ~ 20 fibres on blank sky positions. In the current mode (only 200 fibres) we observe ~ 65 QSO candidates per 2dF pointing. We observed 7 individual fields, 4 were in the Southern (SGP) strip and 3 were in the Northern (NGP) strip. One field (NGP298) contained 3 very bright, $b_J \sim 9$ mag, stars which had been mis-classified as galaxies by the 2dF Galaxy Survey team. Contamination by these objects caused approximately half of

Table 6.3: Details of the 2dF observations of QSO survey fields.

UKST field	field name	RA (B1950)	Dec (B1950)	exposure time(s)	No. of QSO candidates	comments
f417	SGP238	03 08 43.8	-27 42 01	2×1800	26	
f417	SGP463	03 11 31.8	-32 11 58	3×1800	50	
f417	SGP392	03 12 51.9	-30 42 15	2×1800	70	
f853	NGP298	09 53 27.3	+00 23 56	3×1800	72	Bright stars
f853	NGP242	09 56 36.7	-00 56 40	3×1800	69	270R grating
f854	NGP361	10 11 03.6	+01 44 38	3×1800	59	low S/N
f466	SGP246	21 44 36.5	-29 12 20	4×1800	73	

the spectra to be unusable in this field. Another field (NGP242) was observed using the 270R grating rather than the 300B. Table 6.3 gives details of these observations. While the Southern fields used the catalogue limits described in Chapter 4, the Northern fields used a somewhat brighter, $b_J = 20.75$, magnitude limit with a redder selection limit of $u - b_J = -0.3$. The aim of these fields was to help assess the effect that altering our survey limits has on completeness and contamination.

For each field a number of 1800s exposures were taken of the candidate objects. As well as these, helium-neon-copper-argon arc exposures where taken, usually at both the beginning and end of a run of object exposures. Dome flats were taken to measure the individual fibre throughputs using a quartz lamp. Approximately 20 fibres were given over to blank sky positions for each field.

6.3.2 2dF data reduction

An eventual goal of the 2dF facility is to have a pipe-line processing system which will produce fully reduced spectra. At the time of this thesis the pipe-line software was still in the development stage, therefore the **IRAF dofibers** task was used to perform the spectroscopic data reduction. This task is described above in Section 6.2.2, and here we will outline points which are peculiar to the 2dF data set. First, the spectrograph is located on the top end ring of the telescope. While reducing losses due to long lengths of optical fibre this makes the instrument less stable than the FLAIR spectrograph. Therefore, it is not straightforward to combine multiple exposures taken at different times, due to non-linear shifts in the relative positions of the spectra. In cases where this is a problem we have combined our object spectra after extraction rather than before. This method has the disadvantage of being less effective at CRE rejection. In practice, for all fields where shifts in spectra positions were a significant problem, we had at least 3 exposures from which a median could be taken to remove CREs. A second point is that the current CCD has several cosmetic

Table 6.4: The composition of the 2dF QSO sample. The numbers of objects identified are listed for individual UKST fields and for the SGP (f417 and f466) and NGP (f853) samples.

	Number			
Identification	f417	f466	**SGP**	**NGP**
subdwarf	10	20	**30**	**44**
White dwarf	8	2	**10**	**1**
CV	1	1	**2**	**0**
QSO (inc. BALs)	82	32	**114**	**38**
BAL QSO	3	1	**4**	**0**
QSO?	2	1	**3**	**2**
NL Galaxy	25	11	**36**	**6**
No id.	18	6	**24**	**19**
Total	146	73	**219**	**110**

defects including bad columns. These were interpolated across using the task **fixpix**, and a note was made of these columns in the arc spectra so any line which contained cosmetic defects was not used to calculate the wavelength calibration.

6.3.3 Spectroscopic results

A total of 419 spectra have been obtained from the seven fields listed in Table 6.3, this includes 31 spectra which were contaminated by scattered light from the bright stars in the NGP298 field, leaving 388 spectra. We analyse the data from the Northern and Southern fields separately.

In the four SGP fields we obtained a total of 219 spectra of UVX QSO candidates. Identification was carried out by eye using the `REDSHIFT` program and spectra were classified as described in Section 6.2.3. In the 3 NGP fields we obtained 200 spectra. Field NGP361 has low signal-to-noise and, due to poor observing conditions, less than half the spectra could be classified; this field was left out of the following analysis. The 31 spectra contaminated by scattered light from the three bright stars were also removed from the sample leaving a total of 110 spectra in the two remaining NGP fields. The compositions of the SGP and NGP samples are shown in Table 6.4 and below we discuss the individual components of these samples.

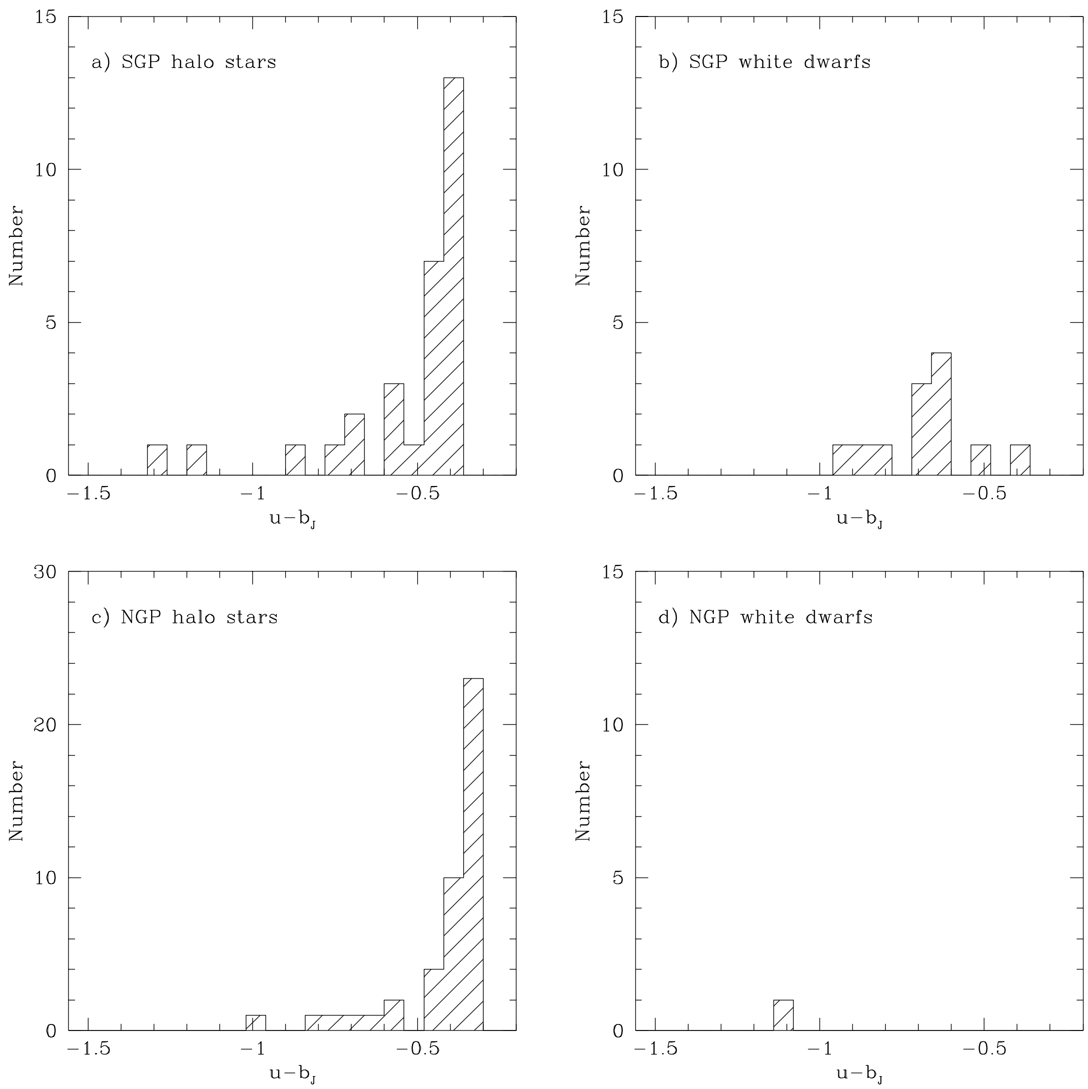

Figure 6.4: Colour distribution of stars found in the 2dF samples. a) SGP halo stars, b) SGP white dwarfs, c) NGP halo stars and d) NGP white dwarfs.

Galactic stars

Out of a total of 219 spectra the SGP sample contains 42 stellar objects, the majority of these (30 objects, 15% of the 195 classified spectra) being galactic halo subdwarfs in the range $\sim A0-G5$. Fig 6.4 shows that the majority of halo stars are close to the red limit of our selection, as in the brighter FLAIR sample. Ten of the remaining stars are WDs, mostly of the DA variety, easily recognizable from their broad hydrogen Balmer lines. Two of these WDs appear to be of the rarer DAB type, which have weak HeI lines present in their spectra. The remaining two galactic sources are CVs. The 24 unclassified spectra comprise faint objects with low signal-to-noise, these being mostly located near the faint limit of our survey, or objects which show a strong continuum flux with no emission or absorption features visible. Many of these are likely to be subdwarfs as these objects are by far the most difficult to classify, generally having only weak absorption lines. The remaining continuum sources could be BL Lac objects, or possibly DC (continuum) WDs.

In the NGP fields we find a significantly higher fraction of halo subdwarfs, as expected, given the redder limits. There are 44 (48%) subdwarfs out of a total of 91 classified spectra. The vast majority of these appear to be A, F and G stars although in the NGP242 field, for which the 270R grating was used, stellar classification is more difficult since the Ca II H and K lines are not visible. We find two objects which appear to be WD/M-star binaries in the NGP242 field, although the R270 grating only allows us to see the Hβ absorption feature. One normal DA white dwarf was found in the NGP sample. Of the 44 subdwarfs, 22 have $u-b_{\rm J}$ colours between –0.36 and –0.3, thus the stellar contamination is doubled by moving the colour limit 0.06 mag redder.

QSOs and emission line galaxies

The SGP sample of 219 spectra resulted in the identification of 114 QSOs (excluding 2 QSO?s). The QSO spectra and details of individual objects are given in Appendix B. All of the QSOs were identified on the basis of their broad ($>1000{\rm kms^{-1}}$) emission lines, particularly the Mg II(λ2798Å), C III](λ1909Å), C IV(λ1549Å) and Lyα+N V(λ1240Å) lines. The lowest redshift QSOs could also be identified by their broad Balmer emission lines. Several other weaker lines were also observed in a number of spectra, including the Si IV(λ1397Å), C II(λ2326Å) and [Ne V](λ3426Å) lines. Here we will discuss a number of objects of particular interest. The lowest redshift QSO is TQ392_258 at a redshift of 0.213. This object has an apparent magnitude of $b_{\rm J}=20.99$, and is therefore the faintest object in the catalogue with an absolute magnitude of $M_{\rm b_J}=-19.54$ (throughout this section we will assume $H_0=50{\rm kms^{-1}Mpc^{-1}}$ and $\Omega_0=1$). The absolute magnitude in the $b_{\rm J}$ band, $M_{\rm b_J}$, is found using

$$M_{\rm b_J}=b_{\rm J}-5\log(d_L)+2.5(1+\alpha)\log(1+z)-25 \qquad (6.1)$$

where d_L is the luminosity distance to the QSO, which for $\Omega_0 = 1$ is given by

$$d_L = \frac{2c}{H_0}[(1+z) - (1+z)^{1/2}] \tag{6.2}$$

For the K-correction we use a spectral slope of $\alpha = -0.5$. A further 12 objects have $M_{b_J} > -23$, all below $z = 0.8$. Therefore 11% of the QSO sample could be classified as Seyferts. The highest redshift QSO is at $z = 2.684$ and has $b_J = 18.53$, implying an absolute magnitude of $M_{b_J} = -27.39$, the most luminous source in the sample. Five QSOs show broad absorption line (BAL) features with evidence of broad absorption in Mg II, C IV and Lyα+N V. These objects comprise $4.3 \pm 2.0\%$ of the total sample, consistent with previous QSO surveys (Boyle et al., 1990). Several of the highest redshift QSOs show Lyα absorption at redshifts below that of the QSO. TQ462_271 ($z = 2.684$) and TQ463_254 ($z = 2.667$) are the most prominent examples, and merit further investigation with high resolution spectroscopy to measure the redshifts and hydrogen columns of the absorbing systems.

As well as QSOs, 36 narrow emission line (NL) galaxies were found in this sample. These objects show strong hydrogen Balmer, [O II](λ3727Å) and [O III](λ4959Å, λ5007Å) lines, indicators of significant star formation. The majority of these objects are red, $u - b_J > -0.5$, and faint, $b_J > 20.6$, and range in redshifts from $z \sim 0.1$ to ~ 0.5. These objects are small compact star-forming galaxies which have been classified as stars in our analysis; their relatively red colours suggest that this sample of galaxies is likely to be highly incomplete. NL galaxies form 18% of the classified sample, compared to 4% found in the Durham/AAT QSO survey (Boyle et al., 1990). This discrepancy is partly due to the differing magnitude limits of the two samples, as most narrow line galaxies are found near to the faint limit of the survey. We note in Chapter 4 that the 2dF QSO survey limit of $b_J = 21$ mag is, on average, slightly deeper (by ~ 0.25 mag) than the Durham/AAT sample. 22 of the NL galaxies were found fainter than $b_J = 20.75$.

The NGP fields contain 40 objects classified as QSOs, two of which are QSO?s. These QSOs range in redshift from $z = 0.235$ to 2.558. No BAL QSOs are found in this sample, which is consistent with the fraction found in the SGP sample. Four QSOs (11%) have absolute magnitudes fainter than $M_{b_J} = -23.0$ and so would be classified as Seyferts. The NGP sample contains fewer narrow line galaxies the SGP sample; only 6 are identified. Using common selection criteria, $b_J \leq 20.75$ and $u - b_J \leq -0.36$, the SGP sample would contain 14 (9%) NL galaxies while the NGP sample would contain only 3 (4%).

6.3.4 Properties of the QSO sample

We now go on to look at the statistical properties of the 2dF QSO sample, in order to ascertain the completeness of the sample and compare it to other QSO surveys. First, the redshift distributions, $n(z)$, of the SGP and NGP samples are shown in Fig 6.5. Overplotted on the redshift distributions is a polynomial fit to the Durham/AAT sample (Shanks & Boyle, 1994) normalized to the numbers of QSOs

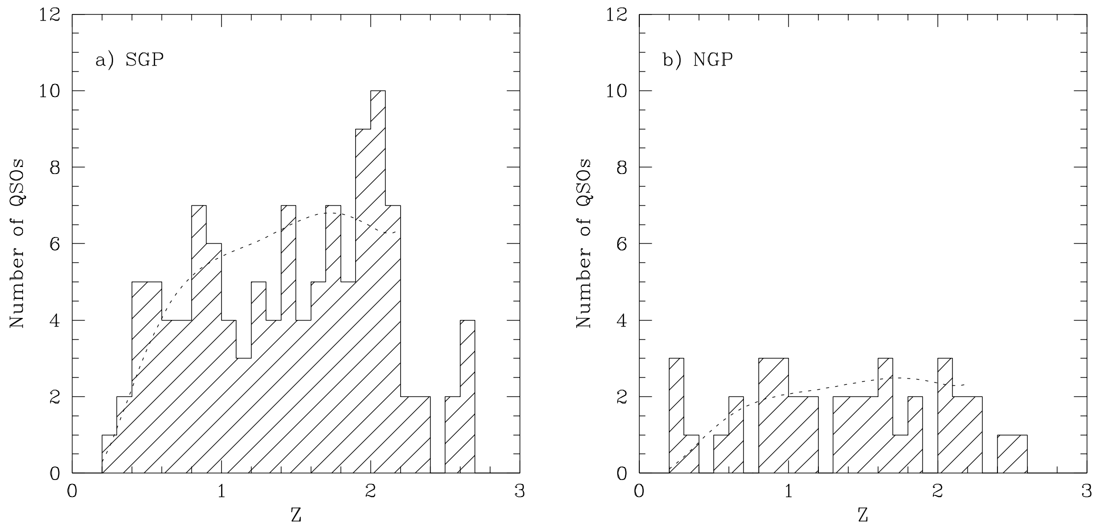

Figure 6.5: The distribution of QSOs as a function of redshift in the a) SGP and b) NGP samples. The dotted lines show a polynomial fit to the Durham/AAT sample at $z < 2.2$ normalized to the number of QSOs in each sample.

Table 6.5: Number densities of QSOs in individual UKST fields. Densities are given in deg^{-2}.

field	No. of cands.	effective area	No. of QSOs	No. of QSOs $0.3 < z < 2.2$	QSO density	QSO density $0.3 < z < 2.2$
f417	146	2.55	82	73	32.2 ± 3.6	28.6 ± 3.4
f466	73	0.85	32	30	37.5 ± 6.6	35.2 ± 6.4
f853	110	2.11	38	31	18.0 ± 2.4	14.7 ± 3.0

in each plot. A χ^2 test comparing the SGP and NGP to the Durham/AAT survey finds reduced χ^2 of 0.63 and 0.58 for the SGP and NGP respectively. The most noticeable feature of the $n(z)$ is the sudden fall off at $z = 2.2$, expected due to the changing colours of the QSO population near this redshift.

We calculate the surface number density of QSOs in both the samples. The SGP data is taken from 2 different UKST field areas, f466 and f417. The limiting magnitudes in the two fields were $b_J = 21.06$ and $b_J = 20.92$ for f466 and f417 respectively (the difference is due to plate-edge zero point corrections being used). Each 2dF pointing only observed a fraction of the UVX candidates within the 2° diameter field, due to the collaboration with the 2dF Galaxy Redshift Survey and only having 200 fibres available. We therefore calculate the effective area of each 2dF pointing based on the fraction of UVX candidates observed. The effective areas for each field, along with the calculated QSO densities, are given in Table 6.5.

The f466 field shows the highest number density of QSOs at 37.5 ± 6.6 deg^{-2}, while the f417 field has a lower density of 32.2 ± 3.6 deg^{-2}. In order to compare the two fields, we reject all QSOs fainter than $b_{\rm J} = 20.92$. The number density in f466 then becomes 32.8 ± 6.2 or 30.5 ± 6.0 ($0.3 < z < 2.2$), which is more consistent with the values found in the f417 field. Combining the f466 and f417 fields at this limit we have 110 QSOs (99 within $0.3 < z < 2.2$) in an effective area of 3.40 deg^2 which is then a surface density of 32.3 ± 3.1 or 29.1 ± 2.9 ($0.3 < z < 2.2$) deg^{-2}. $b_{\rm J} = 20.92$ is equivalent to $b = 21.17$ (b being the magnitude system used in the Durham/AAT QSO Survey). The number density of QSOs found in the Durham/AAT sample was 36.7 deg^{-2} at a limit of $b = 21$. The slope of the integrated number counts in this region is ~ 0.28 (Boyle et al., 1988b) and therefore we expect 40.9 deg^{-2} at $b = 21.17$. So we appear to be selecting only $71.1 \pm 7.1\%$, which is lower than, but not inconsistent with, the $\sim 80\%$ predicted in Chapter 4. At $b_{\rm J} = 21$ this completeness corresponds to a QSO density of 30.6 deg^{-2}, compared to ~ 34 deg^{-2} estimated from previously known QSOs.

Before we discuss this result any further we will similarly analyse the NGP data, which have a brighter magnitude limit, $b_{\rm J} = 20.75$, and a redder colour selection, $u - b_{\rm J} = -0.3$. Table 6.5 contains the calculated QSO density in the NGP f853 field. The number density of QSOs, at 18.0 ± 2.4 deg^{-2} (and 14.7 ± 3.0 for $0.3 < z < 2.2$), is lower than the SGP data, where the density is 28.5 ± 2.9 (26.2 ± 2.8 for $0.3 < z < 2.2$) for $b_{\rm J} < 20.75$. It is also below the number density found in the Durham/AAT survey, which is 36.7 deg^{-2} at this limit.

More information regarding the expected completeness of the sample can be obtained from analysis of the colour distribution of the identified QSOs (shown in Fig. 6.6). The distribution peaks bluer than our UVX limit, which allows us to fit a Gaussian profile to the colour distribution of SGP QSOs over the range $0.3 < z < 2.2$. Integrating this function to the colour selection limit of $u - b_{\rm J} = -0.36$ we find that 85.1% of QSOs should be selected, under the assumption, of course, that the Gaussian distribution is a reasonable description of the data. This number is much more consistent with the expected completeness obtained in Chapter 4. Three QSOs in the NGP data set have colours $u - b_{\rm J} > -0.36$, two of which are within the redshift range $0.3 < z < 2.2$. They therefore constitute $7.9 \pm 4.6\%$ or $6.5 \pm 4.6\%$ ($0.3 < z < 2.2$) of the total NGP sample, whereas from the Gaussian fit to the SGP data we would expect this to be 3.8%, which, considering the large error, is obviously consistent.

We can combine the FLAIR and 2dF data sets to construct the differential number magnitude relation for our sample; this is shown in Fig. 6.7 and compared to the LBQS and Durham/AAT surveys. The data clearly show the break in the number-magnitude relation at $b_{\rm J} \simeq 19$, which is present in the LBQS and Durham/AAT data, but also shows an under-density compared to these surveys. Our analysis of previously known QSOs in Chapter 4 predicts a completeness of $\sim 80\%$, where the incompleteness is due to photometric errors and variability. The QSO density measured from spectroscopic data in the SGP region is consistent with this. The NGP data show significantly lower QSO densities, but these data in particular are of vari-

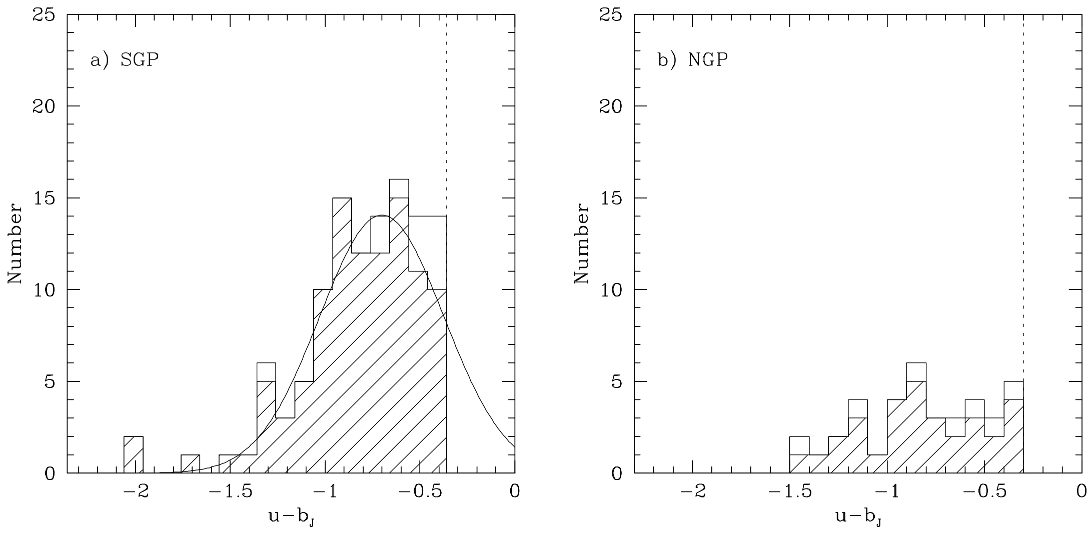

Figure 6.6: The distribution of QSOs as a function of $u - b_J$ colour for a) the SGP and b) the NGP samples. The shaded histograms show QSOs in the redshift range $0.3 < z < 2.2$ while the unshaded histogram includes those QSOs detected outside of these redshift limits. The dotted lines show the colour selection limits in each case (-0.36 for the SGP fields and -0.3 for the NGP fields). Note that the bins in the two plots are offset with respect to one another by 0.06 mag so as to make the bin nearest to the colour limit complete. a) shows a Gaussian fit (peak at -0.7 and width 0.328) to the colour distribution of QSOs within $0.3 < z < 2.2$.

able quality (17% of candidates were not identified). Further data, currently being obtained using the 2dF facility, should produce a more uniform data set. The levels of completeness determined here and in Chapter 4 drive a continued investigation, aimed at improving the candidate catalogue used in the 2dF QSO Survey. Below, in our conclusions, we will outline one possible way to make these improvements.

6.4 Conclusions

We have made preliminary spectroscopic observations of UVX QSO candidates from the UVX catalogue discussed in Chapter 4. The observations have been carried out using both the 2-degree Field facility at the AAT and the FLAIR system at the UKST. Bright ($17 < b_J < 18.25$) candidates were observed using FLAIR and fainter ($18.25 < b_J < 21.0$) candidates were observed using 2dF. 139 spectra were obtained from FLAIR and 419 from 2dF. The aim of this investigation was to test the effectiveness of the UVX catalogue at selecting QSOs, in terms of both completeness and contamination.

As well as QSOs, the samples also contain significant numbers of both galactic stars and narrow emission line galaxies. The galaxies lie at the faint and red limits of the sample and as such form a highly incomplete sample. This is also the case for

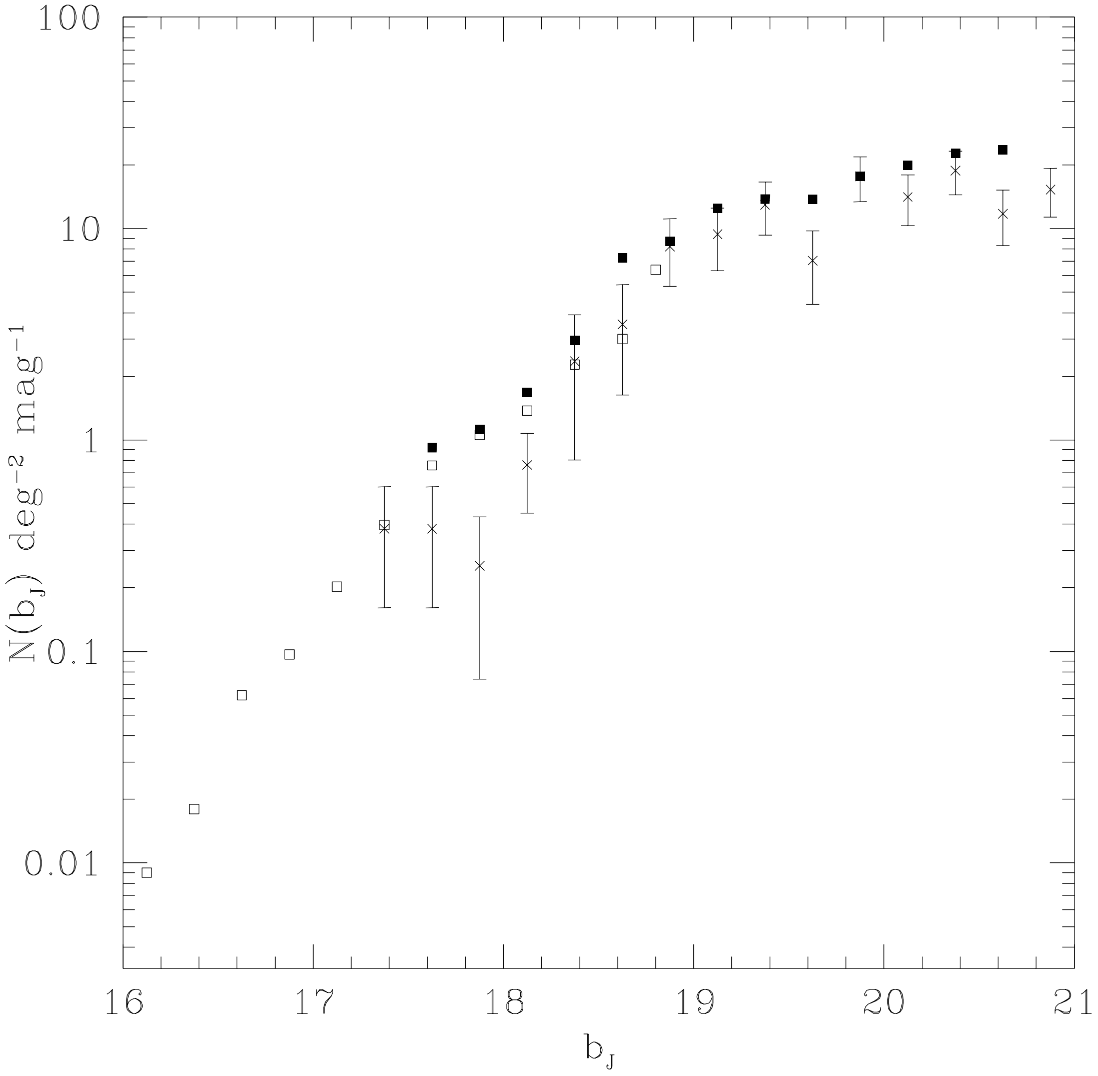

Figure 6.7: The number magnitude relation for the combined FLAIR and 2dF (SGP only) data (crosses). The points without errors are the LBQS (open squares) and the Durham/AAT (filled squares) survey. The Durham/AAT survey has been converted from the b magnitude system to b_J using the conversion in Eq. 4.10.

the majority of galactic stars, which are halo subdwarfs (A, F and G stars) scattered into our colour limits by photometric errors. Apart from these objects we also find 28 hot white dwarfs, which due to their bluer colours do form a complete sample. Most of these objects are DA white dwarfs, dominated by broad hydrogen Balmer lines. Four of these objects show evidence of helium absorption, either neutral (DAB WDs) or ionized (DAO). Three of the WDs show broad molecular absorption features at $\sim 6000 - 7000$Å, these are WD/M-star binary systems. Four CVs were also found, being easily distinguishable by their hydrogen Balmer emission lines. The number of WDs found implies that the completed survey will contain ~ 2000 WDs, which will be invaluable to the study of galactic structure.

The combined data set found a total of 167 QSOs. In particular the SGP subsample of the 2dF observations contains 114 QSOs, that is 50% of the sample were positively identified as QSOs. The contamination comes mainly from halo subdwarfs at bright magnitudes, but at fainter magnitudes, $18.25 \leq b_{\mathrm{J}} \leq 21.0$, we find approximately equal numbers of NL galaxies and subdwarfs. The increased number of NL galaxies is most likely to be due to the star-galaxy separation becoming less accurate at $b_{\mathrm{J}} \sim 21$. The use of a faint limit of $b_{\mathrm{J}} = 20.75$, and a colour limit of $u - b_{\mathrm{J}} \leq -0.3$ reduces the number of NL galaxies but increases the number of subdwarfs, so that the total contamination is greater.

Exact quantitative analysis of the amount of incompleteness is vital in assessing the effectiveness of the 2dF QSO survey. This is somewhat hindered by the inhomogeneous nature of the current data, particularly in the case of the currently available data in the NGP region of the survey and the f411-1b FLAIR data. Given the measured densities of QSOs, the *current estimates* suggest a completeness in the SGP of $71.1 \pm 7.1\%$, which corresponds to a QSO surface density at $b_{\mathrm{J}} = 21$ of ~ 30 deg^{-2}.

These levels of completeness give a QSO density which is lower than expected. We would like a high QSO density as the statistics of QSO clustering are strongly dependent on the density of QSOs in the sample. From Chapter 4 we aimed for $\sim 80\%$ completeness (~ 35 deg^{-2}), although even this could be improved. Any improvement which could increase the completeness of the catalogue without dramatically increasing the level of contamination should be carefully investigated. An obvious option is to include a third colour into our selection process; deep UKST r plates have recently become available in all of the NGP survey region and almost all of the SGP survey region. Fig 6.8 shows a $u - b_{\mathrm{J}}$ vs. $b_{\mathrm{J}} - r$ diagram for the f411 field which contains many previously known QSOs. The magnitude limits used are $18.25 < b_{\mathrm{J}} < 20.75$, the brighter faint limit is used because of the r plate limit of $r \sim 21$. Of the 153 known QSOs which we detect in our stellar catalogue, only 123 (80%) are selected using the standard $u - b_{\mathrm{J}} \leq -0.36$ selection, while introducing a second selection criterion based on both colours can increase this number to 142, that is, 93% completeness. It is clear that a multi-colour selection can select QSOs which have $u - b_{\mathrm{J}}$ colours which are close to the stellar locus. The addition of a third band effectively reduces the scatter from photometric errors and variability, while also constraining the stellar locus into a smaller area on the colour-colour

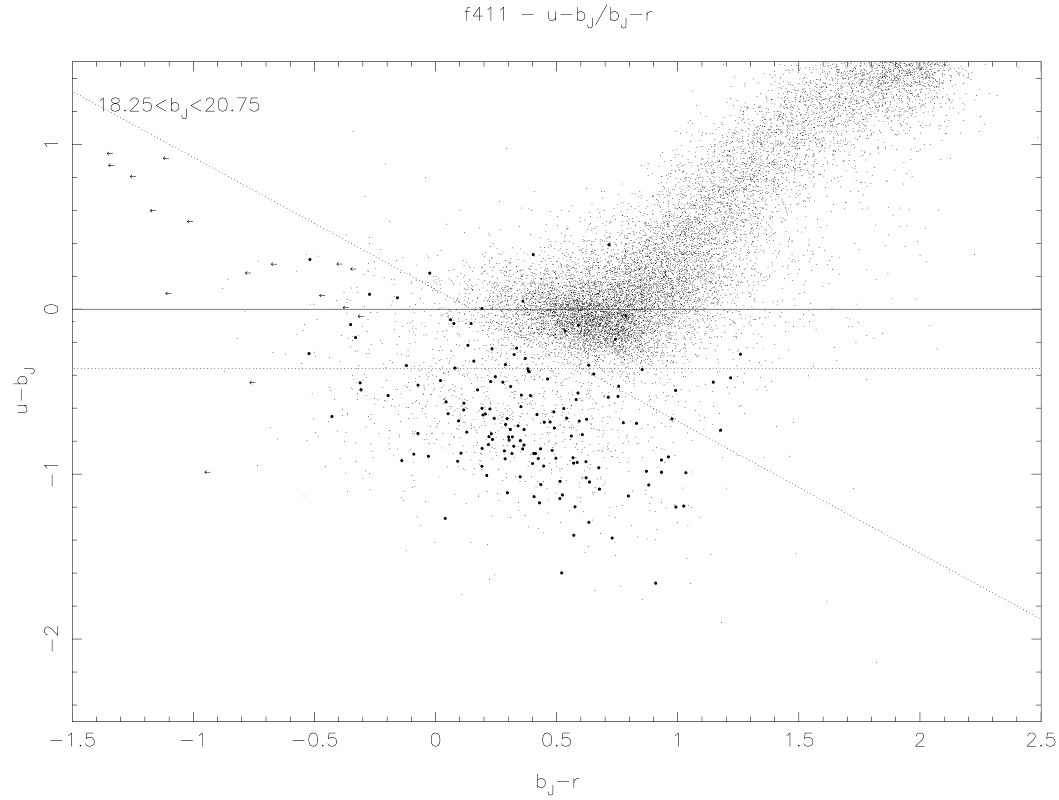

Figure 6.8: A test of QSO selection using a multi-colour selection in the f411 field, all stellar objects in the range $18.25 < b_J < 20.75$ are marked. Known QSOs are indicated with large points, and arrows indicate upper limits on r magnitudes. The dotted lines indicate two selections, the horizontal line showing the $u - b_J \leq -0.36$ UVX selection and the diagonal line shows a colour selection chosen to lie blueward of the stellar locus.

plane than is possible on the colour-magnitude plane. Hence, QSOs are less likely to be scattered into the stellar locus. The number density of candidates is still only at the level of 63 per deg^2 (this density includes objects with only upper limits in the r band). This would allow us, at a limiting magnitude of $b_J \sim 20.75$, to obtain high completeness, while still retaining a low contamination rate of $< 50\%$. The loss in QSOs due to a limit 0.25 mag brighter is more than compensated for by the increased completeness. Based on the results so far obtained, we intend to extend the test observations of the 2dF QSO survey to objects which have been selected by this multi-colour process, and hence continue to improve the quality of the 2dF QSO Survey input catalogue.

Chapter 7

Conclusions

Our aim in this thesis has been to use the clustering of QSOs as a probe of cosmology. We are particularly interested in making new estimates of the parameters which govern the form and evolution of large-scale structure in the Universe. We have used QSO catalogues that are already available to obtain initial results, and we have then begun the process of constructing a new, large, QSO catalogue which will allow more definitive answers to our questions.

7.1 QSO Environments

A first important question to be answered before we make cosmological inferences is: how do QSOs trace the mass distribution? In Chapter 2 we address this question by cross-correlating a sample of ~ 150 QSOs from optically and X-ray selected catalogues with faint, $b_J < 23$, galaxies. These data allow us to probe the galaxy clustering environment of QSOs out to $z \sim 1.5$. Far from giving a positive correlation, the QSO-galaxy cross-correlation function is marginally negative even at $z < 1.5$ (-0.027 ± 0.020 at $< 120''$). Colour information shows that the anti-correlation is most significant between the QSOs and the red galaxy population.

We have therefore constructed a model to predict the QSO-galaxy cross-correlation. To do this we need to know the form of the $N(z)$ distribution of $b_J < 23$ galaxies; fortunately this is now well constrained from Keck data (Cowie et al., 1995). Clustering evolution is also included in the model. A case in which QSOs exist in rich cluster environments is comfortably ruled out by comparing our model to the data. The cross-correlation function is more consistent with a 'normal' galaxy environment. If the small anti-correlation is interpreted as an effect of gravitational lensing, then this conclusion is not altered. In this case, the data are only $\sim 1\sigma$ below the low clustering amplitude models, while the high amplitude models are still comfortably rejected. We therefore conclude that QSOs do not trace a highly biased distribution, such as galaxy clusters. The results are in line with previous observations of radio-quiet QSOs at lower redshift (Ellingson et al., 1991; Boyle & Couch, 1993; Smith et al., 1995) which suggest that QSOs tend to exist in *average* galaxy environments and are not highly biased.

7.2 Evolution of QSO Clustering

In Chapter 3, several presently available QSO surveys were combined to place constraints on cosmology from the evolution of their clustering properties. We used the LBQS, Durham/AAT, CFHT and ESO/AAT QSO surveys, a total of > 1500 QSOs over the redshift range $0.3 < z < 2.2$. This combined data set has a clustering amplitude $\bar{\xi}(10\ h^{-1}\ \mathrm{Mpc}) = 0.83 \pm 0.29$ for $\Omega_0 = 1$ at $\bar{z} = 1.27$. On larger scales, from $\sim 100 - 1000\ h^{-1}$ Mpc, the limit on a detected signal in ξ is ± 0.025.

A model of clustering evolution which includes the effect of bias was used to estimate the expected QSO clustering amplitude at the present day. The measured clustering amplitude at high redshift could then be compared to present day galaxy clustering and the clustering of low redshift Seyfert galaxies. The maximum present day QSO correlation length is $r_0 = 9.23 \pm 1.11$ (for $\gamma = -1.8$), assuming $\Omega_0 \leq 1$ and that galaxies are not anti-biased on $\sim 10\ h^{-1}$ Mpc scales. If the low redshift Seyferts and high redshift QSOs are from a similarly clustered population, the best fit is a slowly evolving model, which implies low Ω_0 and/or high bias for both galaxies and QSOs. By contrast, comparisons of QSO clustering to the CMB measurements of *COBE*, using CDM-type power spectra suggest relatively low bias. Although this might be taken as evidence for a low Ω_0 model, the statistics still allow an $\Omega_0 = 1$ world model with $b_{q\rho} \simeq b_{g\rho} \simeq 2$. The 2dF QSO Redshift survey will be needed to make further progress on these questions.

7.3 Lensing of QSOs by Galaxy Clusters

Various authors have noted the apparent correlation between nearby galaxies and distant QSOs. This is most easily interpreted in terms of gravitational lensing. We consider the anti-correlation found by Boyle et al., (1988) in terms of gravitational lensing in Chapter 5. Using an isothermal sphere lens model, the required velocity dispersion is $\sigma = 1286^{+72}_{-91}\mathrm{kms}^{-1}$. With an isothermal sphere plus uniform density plane, the velocity dispersion is $\sigma = 1205^{+85}_{-108}\mathrm{kms}^{-1}$, while the plane density is $\Sigma_c = 0.0779 \pm 0.0232h\ \mathrm{g\ cm}^{-2}$. Both these values are considerably larger than expected for the poor clusters and groups used by BFS88. We extend this investigation to the UVX catalogue prepared for the 2dF QSO redshift survey, in combination with the ACO (Abell et al., 1989) and APM (Dalton et al., 1997) cluster catalogues. Due to the small number of clusters available, no significant result was found. We find that the anti-correlation between QSOs and faint, $b_J < 23$, galaxies in Chapter 2 can also be interpreted as due to gravitational lensing. Similarly, in this case, an extreme model is required to account completely for the anti-correlation. The existence of a small amount of dust in clusters could reduce estimated masses, bringing them into line with other cluster mass estimates.

A more convincing test will be possible, given the full 2dF QSO catalogue (without contamination) and a complete galaxy catalogue across the survey area. This should allow us to test whether the large masses found from statistical lensing investigations are indeed correct.

7.4 The 2-degree Field QSO Redshift Survey

Chapters 4 and 6 are concerned with preparing a new QSO redshift survey which is currently being undertaken using the 2dF facility at the AAT. This survey is expected to obtain redshifts for $\sim$ 25000 QSOs, over an order of magnitude larger than current QSO surveys. Chapter 4 discusses the production of the UVX catalogue which forms the basis of the candidate selection in the Southern portion of the survey. The survey is based on UKST photographic plates in b_J and u, scanned by APM. These have been corrected for field effects and calibrated using CCD sequences obtained in each UKST field. Several tests have been carried out in order to determine the photometric accuracy of the catalogue. Estimates of completeness, based on previously known QSOs in our survey area, suggest that the survey will be $\sim$ 80% complete over the redshift range $0.3 < z < 2.2$. This corresponds to a QSO surface density of ~ 34 deg^{-2} at a magnitude limit of $b_J = 21$.

In Chapter 6 we analyse the first spectroscopic observations of the UVX catalogue. Observations of bright candidates, with $17 \leq b_J < 18.25$, have been made using the FLAIR instrument on the UKST. The fainter candidates have been observed using the 2dF facility at the AAT. The combined data set contains 167 QSOs. In particular, the Southern 2dF observations contain 114 QSOs, that is, 50% of the candidates observed. The estimated completeness of this data is $71.1 \pm 7.1\%$, lower, although not significantly, than predicted in Chapter 4. A possible solution to the general problem of incompleteness is to include UKST r plates in our candidate selection process. We demonstrate that in one field, which contains a number of previously known QSOs, selection based on $b_J - r$ and $u - b_J$ colours increases the completeness from 80% to 93%. This is obviously a significant improvement and observations to test the new UBR catalogue are currently underway.

7.5 The Future: Science from the 2dF QSO Redshift Survey

The 2dF QSO Redshift Survey will allow a wide ranging and detailed investigation of the Universe at high redshift. The primary scientific aims are:

- To measure the power spectrum of density fluctuations from small scales (a few Mpc) to the large scales sampled by *COBE*, $\sim 1000\ h^{-1}$ Mpc.
- To measure the rate of QSO clustering evolution, in order to constrain Ω_0 and QSO bias.
- To apply geometric tests to measure the cosmological constant, Λ.

As described in Chapter 1, we expect the power spectrum to turn over to $P(k) \sim k$ on the largest scales. On the scales probed we should see this effect in the 2dF QSO Survey. We will be able to compare the shape of the QSO power spectrum to a wide range of theoretical models. Matching the QSO power spectrum to CMB measurements on large scales should also allow a *direct* measurement of QSO bias. Chapter 3 shows how Ω_0 and bias can be constrained from clustering evolution using a relatively small sample of QSOs. The 2dF sample will allow accurate measurements of these parameters. The measurement of the cosmological constant uses a geometric test (Alcock & Pacynski, 1979; Phillipps, 1994; Ballinger et al., 1996) similar to that outlined in Chapter 3, which uses the fact that when the wrong cosmology is assumed, clustering is distorted from its average spherical distribution. The distortion is particularly sensitive to the value of the cosmological constant.

The 2dF QSO Redshift Survey will supply us with a picture of the Universe to a fraction of its current age. The ability to *look back in time* over great distances gives us new opportunities to further our understanding of the Universe and the physical processes which control its evolution.

Bibliography

Abell, G. O., Corwin, H. G., & Olowin, R. P. (1989). *ApJS*, 70, 1.

Alcock, C. & Pacynski, B. (1979). *Nature*, 283, 358.

Almaini, O. (1996). *PhD Thesis*, University of Durham.

Andreani, P. & Cristiani, S. (1992). *ApJ*, 398, L13.

Antonucci, R. (1993). *ARAA*, 31, 473.

Bade, N., Fink, H. H., Engels, D., Voges, W., Hagen, H. J., Wisotzki, L., & Reimers, D. (1995). *AAS*, 110, 469.

Bailey, J. (1996). *2dF User Manual*, Anglo-Australian Observatory.

Ballinger, W. E., Peacock, J. A., & Heavens, A. F. (1996). *MNRAS*, 282, 877.

Bardeen, J. M., Bond, J. R., Kaiser, N., & Szalay, A. S. (1986). *ApJ*, 304, 15.

Barrow, J. D., Bhavsar, S. P., & Sonoda, D. H. (1984). *MNRAS*, 210, 19P.

Bastian, U. & Roeser, S. (1993). *Positions and Proper Motions - South*, Astronomisches Rechen-Institut, Heidelberg.

Baugh, C. M. & Efstathiou, G. (1993). *MNRAS*, 265, 145.

Bennett, C. L. et al (1994). *ApJ*, 436, 423.

Blair, M. & Gilmore, G. (1982). *PASP*, 94, 742.

Boyle, B. J. (1986). *PhD Thesis*, University of Durham.

Boyle, B. J. & Couch, W. J. (1993). *MNRAS*, 264, 604.

Boyle, B. J., Fong, R., & Shanks, T. (1988a). *MNRAS*, 231, 897.

Boyle, B. J., Fong, R., Shanks, T., & Peterson, B. A. (1987). *MNRAS*, 237, 987.

Boyle, B. J., Fong, R., Shanks, T., & Peterson, B. A. (1990). *MNRAS*, 243, 1.

Boyle, B. J., Griffiths, R. E., Shanks, T., Stewart, G. C., & Georgantopoulos, I. (1993). *MNRAS*, 260, 49.

Boyle, B. J., Jones, L. R., & Shanks, T. (1991). *MNRAS*, 251, 482.

Boyle, B. J. & Mo, H. J. (1993). *MNRAS*, 260, 925.

Boyle, B. J., Shanks, T., & Peterson, B. A. (1988b). *MNRAS*, 235, 935.

Broadhurst, T. J., Ellis, R. S., Koo, D. C., & Szalay, A. S. (1990). *Nature*, 343, 726.

Bruzual, A. G. & Charlot, S. (1993). *ApJ*, 405, 538.

Burstein, D. & Heiles, C. (1982). *AJ*, 87, 1165.

Chen, J. S. (1984). *AA*, 134, 306.

Clowes, R. G. & Savage, A. (1983). *MNRAS*, 204, 385.

Cowie, L. L., Hu, E. M., & Songaila, A. (1995). *Nature*, 377, 603.

Crampton, D., Cowley, A. P., & Hartwick, F. D. A. (1987). *ApJ*, 314, 129.

Crampton, D., Cowley, A. P., & Hartwick, F. D. A. (1989). *ApJ*, 345, 59.

Crampton, D., Schade, D., & Cowley, A. P. (1985). *AJ*, 90, 987.

Cristiani, S., franca, F. L., Andreani, P., Gemmo, A., Goldschmidt, P., Miller, L., Vio, R., Barbieri, C., Bodini, L., Iovino, A., Lazzarin, M., Clowes, R., Macgillivray, H., Gouiffes, C., Lissandrini, C., & Savage, A. (1995). *AASup*, 112, 347.

Cristiani, S., Trentini, S., Franca, F. L., Aretxage, I., Andreani, P., Vio, R., & Gemmo, A. (1996). *AA*, 306, 395.

Dalton, G. B., Croft, R. A. C., Efstathiou, G., Sutherland, W. J., Maddox, S. J., & Davis, M. (1994). *MNRAS*, 271, L47.

Dalton, G. B., Sutherland, W. J., Maddox, S. J., & Efstathiou, G. (1997). *MNRAS*, in press.

Dawe, J. A. & Metcalfe, N. (1982). *PASA*, 4, 466.

de Grijp, M. H. K., Miley, B. K., & Lub, J. (1987). *AASup*, 70, 95.

Drinkwater, M. & Holman, B. (1996). *FLAIR Data Reduction with IRAF*, Anglo-Australian Observatory.

Efstathiou, G., Bond, J. R., & White, S. D. M. (1992). *MNRAS*, 258, 1P.

Efstathiou, G. & Rees, M. J. (1988). *MNRAS*, 230, 5P.

Ellingson, E., Yee, H. K. C., & Green, R. F. (1991). *ApJ*, 371, 49.

Ferguson, H. C. (1993). *MNRAS*, 263, 343.

Foltz, C. B., Chaffee, F. H., Hewett, P. C., MacAlpine, G. M., Turnshek, D. A., Weymann, R. J., & Anderson, S. F. (1987). *AJ*, 94, 1423.

Fry, J. N. (1996). *ApJ*, 461, L65.

Georgantopoulos, I. (1991). *PhD Thesis*, University of Durham.

Georgantopoulos, I. & Shanks, T. (1994). *MNRAS*, 271, 773.

Georgantopoulos, I., Stewart, G. C., Shanks, T., Boyle, B. J., & Griffiths, R. E. (1996). *MNRAS*, 280, 276.

Goldschmidt, P. & Miller, L. (1991). *In: The space distribution of quasars; Proceedings of the Workshop.*, page 212.

Gott, J. R. & Gunn, J. E. (1974). *ApJ*, 190, L105.

Gott, J. R. & Turner, E. L. (1977). *ApJ*, 216, 357.

Graham, J. A. (1982). *PASP*, 94, 244.

Gregg, M. D., Becker, R. H., White, R. L., Helfand, D. J., Mcmahon, R. G., & Hook, I. M. (1996). *AJ*, 112, 407.

Guth, A. (1981). *Phys. Rev.*, D23, 347.

Hamilton, A. J. S. (1993). *ApJ*, 417, 19.

Hamilton, A. J. S., Kumar, P., Lu, E., & Matthews, A. (1991). *ApJ*, 374, L1.

Hawkins, M. R. S. (1986). *MNRAS*, 219, 417.

Hawkins, M. R. S. & Veron, P. (1995). *MNRAS*, 275, 1102.

Hawkins, M. R. S. & Veron, P. (1996). *MNRAS*, 281, 348.

Hewett, P. C., Foltz, C. B., & Chaffee, F. H. (1993). *ApJ*, 406, L43.

Hewett, P. C., Foltz, C. B., & Chaffee, F. H. (1995). *AJ*, 109, 1499.

Hintzen, P., Romanishin, W., & Valdes, F. (1991). *ApJ*, 366, 7.

Hoyle, F. & Burbidge, G. (1996). *AA*, 309, 335.

Hubble, E. (1929). *Proc.N.A.S.*, 15, 168.

Hutchings, J. B., Crampton, D., & Johnson, A. (1995). *AJ*, 109, 73.

Jones, L. R., Fong, R., Shanks, T., Ellis, R. S., & Peterson, B. A. (1991). *MNRAS*, 249, 481.

Kaiser, N. (1984). *ApJ*, 284, L9.

Kaiser, N. (1987). *MNRAS*, 227, 1.

Kolb, E. W. & Turner, M. S. (1990). *The Early Universe*, Addison-Wesley.

Koo, D. C., Kron, R. G., & Cudworth, K. M. (1986). *PASP*, 98, 285.

Kormendy, J. & Richstone, D. (1995). *ARAA*, 33, 581.

Kron, R. G. (1980). *ApJS*, 43, 305.

Landolt, A. U. (1983a). *AJ*, 88, 439.

Landolt, A. U. (1983b). *AJ*, 88, 853.

Lilje, P. B. & Efstathiou, G. (1988). *MNRAS*, 231, 635.

Lilly, S. J., Tresse, L., Hammer, F., Crampton, D., & Fevre, O. L. (1995). *ApJ*, 455, 108.

Limber, D. N. (1953). *ApJ*, 117, 134.

Loeb, A. (1993). *ApJ*, 403, 542.

Loeb, A. & Rasio, F. A. (1994). *ApJ*, 432, 52.

Loveday, J., Maddox, S. J., Efstathiou, G., & Peterson, B. A. (1995). *ApJ*, 442, 457.

Madau, P., Ferguson, H. C., Dickinson, M. E., Giavalisco, M., Steidel, C. C., & Fruchter, A. (1996). *MNRAS*, 283, 1388.

Maddox, S. J. (1988). *PhD Thesis*, University of Cambridge.

Maddox, S. J., Sutherland, W. J., Efstathiou, G., & Loveday, J. (1990). *MNRAS*, 243, 692.

Mather, J. C. et al (1990). *ApJ*, 354, L37.

Metcalfe, N., Shanks, T., Campos, A., Fong, R., & Gardner, J. P. (1996). *Nature*, 383, 236.

Metcalfe, N., Shanks, T., Fong, R., & Jones, L. R. (1991). *MNRAS*, 249, 498.

Mo, H. J. & Fang, L. Z. (1993). *ApJ*, 410, 493.

Mo, H. J., Jing, Y. P., & Borner, G. (1992). *ApJ*, 392, 452.

Narayan, R. (1989). *ApJ*, 339, L53.

Osmer, P. S. (1981). *ApJ*, 247, 762.

Osmer, P. S. & Hewett, P. C. (1991). *ApJS*, 75, 273.

Park, C., Vogeley, M. S., Geller, M. J., & Huchra, J. P. (1994). *ApJ*, 431, 569.

Parker, Q. A. & Watson, F. G. (1995). *in Maddox S.J., Aragon-Salamanca A., eds, Wide Field Spectroscopy and the Distant Universe*, World Scientific, 33.

Peebles, P. J. E. (1980). *The Large-Scale Structure of the Universe*, Princeton.

Peebles, P. J. E. (1984). *ApJ*, 284.

Peebles, P. J. E. (1993). *Principles of Physical Cosmology*, Princeton.

Penzias, A. A. & Wilson, R. W. (1965). *ApJ*, 142, 419.

Phillipps, S. (1994). *MNRAS*, 269, 1077.

Pozzetti, L., Bruzual, G., & Zamorani, G. (1996). *MNRAS*, 281, 953.

Ratcliffe, A. (1996). *PhD Thesis*, University of Durham.

Ratcliffe, A., Shanks, T., Parker, Q. A., & Fong, R. (1997). *MNRAS*, in press.

Rees, M. J. (1984). *ARAA*, 22, 471.

Roche, N. (1994). *PhD Thesis*, University of Durham.

Roche, N., Shanks, T., Georgantopoulos, I., Stewart, G. C., Boyle, B. J., & Griffiths, R. E. (1995). *MNRAS*, 273, L15.

Roche, N., Shanks, T., Metcalfe, N., & Fong, R. (1996). *MNRAS*, 280, 397.

Savage, A. & Bolton, J. G. (1984). *MNRAS*, 188, 599.

Savage, A., Trew, A. S., Chen, J. S., & Weston, T. (1984). *MNRAS*, 207, 393.

Schmidt, M. (1963). *Nature*, 197, 1040.

Schmidt, M. & Green, R. F. (1983). *ApJ*, 269, 352.

Schramm, N. D. (1991). *Physica Scripta*, T36, 22.

Shanks, T. & Boyle, B. J. (1994). *MNRAS*, 271, 753.

Shanks, T., Boyle, B. J., Griffiths, R. E., Stewart, G. C., Georgantopoulos, I., & Almaini, O. (1997). *In preparation*.

Shanks, T., Fong, R., & Boyle, B. J. (1983a). *Nature*, 303, 156.

Shanks, T., Fong, R., Boyle, B. J., & Peterson, B. A. (1987). *MNRAS*, 227, 739.

Shanks, T., Fong, R., Green, M. R., Clowes, R. G., & Savage, A. (1983b). *MNRAS*, 203, 181.

Shanks, T., Georgantopoulos, I., Stewart, G. C., Pounds, K. A., Boyle, B. J., & Griffiths, R. E. (1991). *Nature*, 353, 315.

Shaver, P. A., Wall, J. V., Kellerman, K. I., Jackson, C. A., & Hawkins, M. R. S. (1996). *Nature*, 384, 439.

Small, T. A. & Blandford, R. D. (1992). *MNRAS*, 259, 725.

Smith, R. J. (1997). *PhD Thesis*, University of Cambridge.

Smith, R. J., Boyle, B. J., & Maddox, S. J. (1995). *MNRAS*, 277, 270.

Stevenson, P. R. F. (1985). *PhD Thesis*, University of Durham.

Stevenson, P. R. F., Fong, R., & Shanks, T. (1988). *MNRAS*, 234, 801.

Stocke, J. T., Morris, S. L., Gioia, I. M., Maccacaro, T., Schild, R., Wolter, A., Fleming, T. A., & Henry, J. P. (1991). *ApJS*, 76, 813.

Tadros, H. & Efstathiou, G. (1995). *MNRAS*, 276, L45.

Tadros, H. & Efstathiou, G. (1996). *MNRAS*, 282, 1381.

Taylor, K. (1995). *in Maddox S.J., Aragon-Salamanca A., eds, Wide Field Spectroscopy and the Distant Universe*, World Scientific, 15.

Tucker, D. L., Oemler, A., Kirshner, R. P., Lin, H., Shectman, S. A., Landy, S. D., Schechter, P. L., Muller, V., Gottlober, S., & Einasto, J. (1997). *MNRAS*, 285, L5.

Turner, E. L., Ostriker, J. P., & Gott, J. R. (1984). *ApJ*, 284, 1.

Tyson, J. A. (1986). *AJ*, 92, 691.

Veron, P. (1983). *in Quasars and Gravitational Lenses; The 24th Liege Astrophysical Symposium.*

Veron, P. & Hawkins, M. R. S. (1995). *AA*, 296, 665.

Veron-Cetty, M. P. & Veron, P. (1996). *Quasars and Active Galactic Nuclei (7th Ed.)*, ESO Scientific Report.

Warren, S. J., Hewett, P. C., Irwin, M. J., McMahon, R. G., & Bridgeland, M. T. (1987). *Nature*, 325, 131.

Warren, S. J., Hewett, P. C., Irwin, M. J., & Osmer, P. S. (1991). *ApJS*, 76, 1.

Weinberg, S. (1972). *Gravitation and Cosmology*, Wiley.

Williams, R. E. et al (1996). *AJ*, 112, 1335.

Wisotzki, L., Koehler, T., Groote, D., & Reimers, D. (1996). *AASup*, 115, 227.

Wu, X. P. (1994). *AA*, 286, 748.

Wu, X. P. & Fang, L. Z. (1996). *ApJ*, 461, L5.

Wu, X. P., Fang, L. Z., Zhu, Z. H., & Qin, B. (1996). *ApJ*, 471, 575.

Yee, H. K. C. & Green, R. F. (1984). *ApJ*, 280, 79.

Yee, H. K. C. & Green, R. F. (1987). *ApJ*, 319, 28.

Zitelli, V., Mignoli, M., Zamorani, G., Marano, B., & Boyle, B. J. (1992). *MNRAS*, 260, 925.

Zombeck, M. V. (1990). *Handbook of Space Astronomy and Astrophysics*, Cambridge.